



University of Kentucky  
UKnowledge

---

Theses and Dissertations--Mechanical  
Engineering

Mechanical Engineering

---

2012

## A FILTER-FORCING TURBULENCE MODEL FOR LARGE EDDY SIMULATION INCORPORATING THE COMPRESSIBLE "POOR MAN'S" NAVIER--STOKES EQUATIONS

Joshua Strodtbeck

University of Kentucky, [Joshua.Strodtbeck@gmail.com](mailto:Joshua.Strodtbeck@gmail.com)

[Right click to open a feedback form in a new tab to let us know how this document benefits you.](#)

---

### Recommended Citation

Strodtbeck, Joshua, "A FILTER-FORCING TURBULENCE MODEL FOR LARGE EDDY SIMULATION INCORPORATING THE COMPRESSIBLE "POOR MAN'S" NAVIER--STOKES EQUATIONS" (2012). *Theses and Dissertations--Mechanical Engineering*. 13.

[https://uknowledge.uky.edu/me\\_etds/13](https://uknowledge.uky.edu/me_etds/13)

This Doctoral Dissertation is brought to you for free and open access by the Mechanical Engineering at UKnowledge. It has been accepted for inclusion in Theses and Dissertations--Mechanical Engineering by an authorized administrator of UKnowledge. For more information, please contact [UKnowledge@lsv.uky.edu](mailto:UKnowledge@lsv.uky.edu).

## **STUDENT AGREEMENT:**

I represent that my thesis or dissertation and abstract are my original work. Proper attribution has been given to all outside sources. I understand that I am solely responsible for obtaining any needed copyright permissions. I have obtained and attached hereto needed written permission statements(s) from the owner(s) of each third-party copyrighted matter to be included in my work, allowing electronic distribution (if such use is not permitted by the fair use doctrine).

I hereby grant to The University of Kentucky and its agents the non-exclusive license to archive and make accessible my work in whole or in part in all forms of media, now or hereafter known. I agree that the document mentioned above may be made available immediately for worldwide access unless a preapproved embargo applies.

I retain all other ownership rights to the copyright of my work. I also retain the right to use in future works (such as articles or books) all or part of my work. I understand that I am free to register the copyright to my work.

## **REVIEW, APPROVAL AND ACCEPTANCE**

The document mentioned above has been reviewed and accepted by the student's advisor, on behalf of the advisory committee, and by the Director of Graduate Studies (DGS), on behalf of the program; we verify that this is the final, approved version of the student's dissertation including all changes required by the advisory committee. The undersigned agree to abide by the statements above.

Joshua Strodbeck, Student

Dr. James McDonough, Major Professor

Dr. James McDonough, Director of Graduate Studies

A FILTER-FORCING TURBULENCE MODEL FOR LARGE EDDY  
SIMULATION INCORPORATING THE COMPRESSIBLE “POOR MAN’S”  
NAVIER–STOKES EQUATIONS

---

DISSERTATION

---

A dissertation submitted in partial  
fulfillment of the requirements for  
the degree of Doctor of Philosophy  
in the College of Engineering at the  
University of Kentucky

By  
Joshua P. Strodbeck  
Lexington, Kentucky

Director: Dr. J.M. McDonough, Professor of Mechanical Engineering  
Lexington, Kentucky 2012

Copyright© Joshua P. Strodbeck 2012

## ABSTRACT OF DISSERTATION

### A FILTER-FORCING TURBULENCE MODEL FOR LARGE EDDY SIMULATION INCORPORATING THE COMPRESSIBLE “POOR MAN’S” NAVIER–STOKES EQUATIONS

A new approach to large-eddy simulation (LES) based on the use of explicit spatial filtering combined with backscatter forcing is presented. The forcing uses a discrete dynamical system (DDS) called the compressible “poor man’s” Navier–Stokes (CPMNS) equations. This DDS is derived from the governing equations and is shown to exhibit good spectral and dynamical properties for use in a turbulence model. An overview and critique of existing turbulence theory and turbulence models is given. A comprehensive theoretical case is presented arguing that traditional LES equations contain unresolved scales in terms generally thought to be resolved, and that this can only be solved with explicit filtering. The CPMNS equations are then incorporated into a simple forcing in the OVERFLOW compressible flow code, and tests are done on homogeneous, isotropic, decaying turbulence, a Mach 3 compression ramp, and a Mach 0.8 open cavity. The numerical results validate the general filter-forcing approach, although they also reveal inadequacies in OVERFLOW and that the current approach is likely too simple to be universally applicable. Two new proposals for constructing better forcing models are presented at the end of the work.

KEYWORDS: CFD, LES, turbulence modeling, filtering

Author’s signature: Joshua P. Strodtbeck

Date: November 9, 2012

A FILTER-FORCING TURBULENCE MODEL FOR LARGE EDDY  
SIMULATION INCORPORATING THE COMPRESSIBLE “POOR MAN’S”  
NAVIER–STOKES EQUATIONS

By  
Joshua P. Strodtbeck

Director of Dissertation: J.M. McDonough

Director of Graduate Studies: J.M. McDonough

Date: November 9, 2012

Dedicated to my dear wife, Laura.

## ACKNOWLEDGMENTS

I would like to acknowledge Pieter Buning and Ethan Romander, who were of tremendous help in patiently fielding questions from me regarding some intricacies of the OVERFLOW source code. I would also like to acknowledge two presenters at the 2012 Dayton-Cincinnati AIAA Symposium, whose names I have since lost, who suggested reformulating my model as a forcing function rather than an additive term.





## TABLE OF CONTENTS

Acknowledgments . . . . .	iii
Table of Contents . . . . .	v
List of Figures . . . . .	viii
List of Tables . . . . .	xi
Chapter 1 Introduction . . . . .	1
Chapter 2 Foundations in Turbulence Theory . . . . .	5
2.1 Governing equations . . . . .	6
2.2 Basic Tools . . . . .	8
2.2.1 Kovasznay decomposition . . . . .	8
2.2.2 Statistical tools . . . . .	10
2.2.3 Spectral analysis . . . . .	14
2.3 Dynamical systems view of turbulence . . . . .	17
2.3.1 Mathematics of dynamical systems . . . . .	17
2.3.2 The Ruelle-Takens theory of turbulence . . . . .	20
2.3.3 Turbulent length scales . . . . .	21
2.3.4 Turbulent “dissipation” . . . . .	24
2.3.5 Dynamics of Euler turbulence . . . . .	26
2.4 Shock-Turbulent Interaction . . . . .	29
2.5 Conclusions on the nature of turbulence . . . . .	32
Chapter 3 Computational Simulation of Turbulent Flows . . . . .	35
3.1 Mathematical issues in CFD . . . . .	36
3.1.1 Nonlinearity . . . . .	36
3.1.2 Aliasing . . . . .	37
3.2 Turbulence modeling . . . . .	40
3.2.1 RANS modeling . . . . .	41
3.2.2 Large eddy simulation . . . . .	46
3.2.3 Implicit and explicit filtering . . . . .	49
3.2.4 Aliasing in traditional LES . . . . .	52
3.2.5 Eddy viscosity in LES . . . . .	54
3.2.6 Structural modeling . . . . .	57
3.2.7 Dealiased LES equations . . . . .	58
3.2.8 A critique of deconvolution . . . . .	63
3.3 Summary and conclusions . . . . .	65
Chapter 4 The Compressible Poor Man’s Navier–Stokes Equations . . . . .	69

4.1	Analysis . . . . .	71
4.2	Bifurcation analysis . . . . .	79
4.2.1	Bifurcation behavior and PSD analysis . . . . .	80
4.2.2	Regime maps . . . . .	87
4.3	Sensitivity to initial conditions . . . . .	95
4.4	SGS model functions . . . . .	99
4.4.1	Leith's stochastic backscatter model . . . . .	104
4.4.2	Chasnov's $\eta - F$ model . . . . .	105
4.4.3	Laval and Dubrulle's LQL model . . . . .	106
4.4.4	A new CPMNS-based model . . . . .	108
4.5	Summary and conclusions . . . . .	112
Chapter 5	OVERFLOW . . . . .	113
5.1	Governing equations and features . . . . .	114
5.2	Chimera overset interpolation . . . . .	115
5.3	WENOM shock capturing . . . . .	119
5.4	Parallelization and performance tests . . . . .	121
5.4.1	Model problem . . . . .	122
5.4.2	Results . . . . .	123
5.5	Summary and conclusions . . . . .	125
Chapter 6	Computations . . . . .	127
6.1	HAMR filtering . . . . .	128
6.1.1	Low-pass filtering . . . . .	130
6.1.2	High-pass filtering . . . . .	133
6.1.3	Shock detection . . . . .	135
6.2	Homogeneous, isotropic, decaying turbulence . . . . .	140
6.2.1	Initial and boundary conditions . . . . .	141
6.2.2	Numerical method . . . . .	142
6.2.3	Results and analysis . . . . .	143
6.3	Mach 2.9 compression ramp with turbulent boundary layer . . . . .	153
6.3.1	Geometry, grid, and methods . . . . .	158
6.3.2	Results and analysis . . . . .	163
6.4	Turbulent flow over an open cavity . . . . .	174
6.4.1	Geometry, grid, and methods . . . . .	176
6.4.2	Results and analysis . . . . .	177
6.5	Summary and conclusions . . . . .	180
Chapter 7	Final Conclusions and Future Work . . . . .	183
7.1	Summary . . . . .	183
7.2	Assessment of the filter-forcing model . . . . .	185
7.3	Open problems . . . . .	187
7.3.1	Ideal filtering . . . . .	187
7.3.2	Shock modeling . . . . .	187
7.4	Proposal 1: Helmholtz-decomposed forcing . . . . .	188

7.5	Proposal 2: Self-similarity . . . . .	189
7.6	Conclusion . . . . .	190
	Appendix A Source Code . . . . .	192
	Bibliography . . . . .	199
	Vita . . . . .	211

## LIST OF FIGURES

2.1	The three regimes of truncated inviscid turbulence on a log-log scale. . . . .	27
3.1	544x725 image filtered to 136x182 and deconvolved back to the original resolution using Lanczos-3 for both operations. Image is public domain [94].	66
3.2	PSDs of the original 544x725 image and its deconvolution. . . . .	66
4.1	CPMNS bifurcation diagram for $\beta_i = \beta$ for all $i$ with zoom in . . . . .	82
4.2	Logistic map bifurcation diagram with zoom in . . . . .	82
4.3	CPMNS bifurcation diagram for $\beta_1 = \beta$ , $\beta_2 = 0.99\beta$ , $\beta_3 = 0.98\beta$ , $\alpha = (0.0001, 0.0002, 0.00013)$ with zoom in . . . . .	83
4.4	PSDs, time series, and phase portraits for $\beta =$ (a) (0.928458, 0.919173, 0.909889) (b) (0.92874, 0.919453, 0.910165) (c) (0.928176, 0.918894, 0.909612), (d) (0.9556, 0.5844, 0.854), (e) (0.9444, 0.5154, 0.32). In (a), (b), and (c), $\alpha_i = 0.0001 \forall i$ , while in (d) and (e), $\alpha = (0.0001, 0.002, 0.0013)$ . . . . .	85
4.5	Time series and phase portraits for $\beta = (0.93, 0.85, 0.41)$ . . . . .	88
4.6	Regime map of $\beta_3$ vs. $\beta_1 = \beta_2$ , $\alpha_i = 0.0001$ . . . . .	90
4.7	Close-up of regime map of $\beta_3$ vs. $\beta_1 = \beta_2$ , $\alpha_i = 0.0001$ . . . . .	91
4.8	$\xi$ vs. $\beta$ . . . . .	93
4.9	$\alpha$ vs. $\beta$ . . . . .	94
4.10	$\beta_T$ vs. $\beta$ . . . . .	95
4.11	$\eta$ vs. $\beta$ . . . . .	96
4.12	$\zeta$ vs. $\beta$ . . . . .	97
4.13	Basin of attraction for $\beta_i = 0.945$ and $\alpha_i = 0.0001$ for all $i$ . . . . .	100
4.14	Basin of attraction for $\beta = (0.92, 0.94, 0.93)$ and $\alpha = (0.0001, 0.002, 0.0013)$ . . . . .	101
4.15	PSD, time series, and phase portrait for initial conditions detected as noisy quasiperiodic (a) and broadband with fundamental (b) . . . . .	102
4.16	Lyapunov exponent $\lambda$ vs. $\beta$ . . . . .	102
5.1	Close-up of overset grid features for a 24 degree shock ramp featuring a trip wire . . . . .	117
5.2	Overlapping 1-D grids with a ghost point (red) created by chimera interpolation . . . . .	118
5.3	Density contours for the initial condition . . . . .	123
5.4	Processing speed versus number of cores . . . . .	124
6.1	Transfer functions for the $(d^2)^n$ filters featured in OVERFLOW versus scaled wavenumber $k$ . . . . .	129
6.2	Transfer function for low-pass (solid) and high-pass (dashed) filters versus scaled wavenumber $\omega$ . . . . .	132

6.3	Real (solid) and imaginary (dashed) components of the transfer function for the 2 <sup>nd</sup> point away from the boundary versus scaled wavenumber $\omega$ . . . . .	133
6.4	Real (solid) and imaginary (dashed) components of the transfer function for the 3 <sup>rd</sup> point away from the boundary versus scaled wavenumber $\omega$ . . . . .	135
6.5	Discrete signal $u$ featuring a smoothed, discontinuous jump. . . . .	137
6.6	Difference between $u$ and $\bar{u}$ , where $\bar{u}$ is filtered with the HAMR scheme without any shock detection . . . . .	137
6.7	Contours of $ \mathbf{u}_{hi} $ for a Mach 2.9 compression ramp with no shock detection. Note the pronounced oscillations on both sides of the shock wave and its reflection. . . . .	139
6.8	Contours of $ \mathbf{u}_{hi} $ for a Mach 2.9 compression ramp with simple shock detection using $F_{smooth} = 0.2$ . Note the elimination of oscillations near the shock wave, although turbulent regions are still effectively captured. . . . .	139
6.9	Decay of mean kinetic energy over time . . . . .	145
6.10	Evolution of rms divergence versus time . . . . .	145
6.11	Evolution of the skewness of $\partial_x u_1$ in time . . . . .	146
6.12	Evolution of $\kappa'$ in time . . . . .	147
6.13	Decay of rms $ \mathbf{f} $ versus time. . . . .	148
6.14	Contour plots of $\rho$ for DNS at $t = 0.36$ and $t = 4.02$ . Note the loss of small-scale structure and increase in overall smoothness as the solution evolves in time. . . . .	149
6.15	Contour plots of density at $t = 2.2$ for (a) $C_{PMNS} = 0$ , (b) $C_{PMNS} = 50$ , (c) $C_{PMNS} = 100$ , and (d) DNS filtered and downsampled to the $65^3$ grid . . . . .	150
6.16	PSDs of the velocity field $t = 2.2$ for, $C_{PMNS} = 0$ , $C_{PMNS} = 50$ , $C_{PMNS} = 100$ , and both raw and downsampled DNS results . . . . .	151
6.17	PSDs of the solenoidal velocity field $t = 2.2$ for, $C_{PMNS} = 0$ , $C_{PMNS} = 50$ , and both raw and downsampled DNS results . . . . .	152
6.18	PSDs of the dilatational velocity field $t = 2.2$ for, $C_{PMNS} = 0$ , $C_{PMNS} = 50$ , and both raw and downsampled DNS results . . . . .	152
6.19	Sketch of the key features of the shock structure near a compression ramp . . . . .	154
6.20	Time-averaged pressure for an oscillating shock . . . . .	157
6.21	Experimental results (o), Sinha's modified $k - \epsilon$ (---) and $k - \omega$ (-.-), and fit of Eq. (6.27) (-). Observe how the shape of the $\sin^{-1}$ function is a better match to the experimental results than anything produced by the eddy viscosity models. Figure adapted from [157]. . . . .	157
6.22	Mesh A for the 24 degree shock ramp. Every 4 <sup>th</sup> point is displayed. . . . .	159
6.23	Mesh B for the 24 degree shock ramp. Note the coarse region containing the ramp. Every 4 <sup>th</sup> point is displayed. . . . .	160
6.24	Close-up of the overlap zone between the fine and the coarse regions of Mesh B. . . . .	160
6.25	Close-up of the shock corner. . . . .	160
6.26	Fine grid for Mesh A with similarity region outlined. . . . .	162
6.27	Velocity profile of incoming boundary layer. . . . .	164
6.28	Close-up of mean separation zone on Grid A, where coloring is by velocity magnitude. . . . .	166

6.29	Close-up of mean separation zone on Grid B, where coloring is by velocity magnitude. . . . .	166
6.30	Wall pressure in the interface between the fine grid (blue) and coarse grid (red) for Mesh B. Note the discontinuity between the zones and the immediate beginning of an adverse pressure gradient in the coarse zone. .	167
6.31	Contours of mean velocity for OVERFLOW's 5 <sup>th</sup> -order filtering with no turbulence model on an earlier mesh. Note the very long, thin separation zone and Gibbs phenomena upstream of the shock. . . . .	167
6.32	Mean wall pressure for OVERFLOW's 6 <sup>th</sup> -difference filtering (black) versus the HAMR scheme (red) on an earlier mesh. The black curve is not as smooth due to being computed with fewer total time steps. . . . .	168
6.33	Density gradient contours for 6 <sup>th</sup> -difference filtering versus the HAMR scheme with shock detection. . . . .	168
6.34	Mean wall pressure for the Grid B versus the experimental results of Ringuette et al. ( $Re_\theta = 2400$ ) [135] and Settles et al. ( $Re_\theta = 67,200$ ) [153]. Image adapted from [135] . . . . .	170
6.35	Numerical schlieren of Mach 2.9 ramp from Wu and Martin. [139] Used with permission. . . . .	171
6.36	Density gradient contours for Mesh A with, beginning from the top, $C_{PMNS} = 0, 1,$ and $5.$ . . . . .	172
6.37	Density gradient contours for Mesh B with (a) $C_{PMNS} = 0,$ (b) $1,$ (c) $2,$ and (d) $5,$ the last of which diverged. . . . .	173
6.38	Major features of an open cavity flow. Contours are of mean velocity magnitude. . . . .	175
6.39	Overset mesh for the open cavity. Every fourth grid point is displayed. .	177
6.40	Contours of forcing for $C_{PMNS} = 1.$ . . . . .	178
6.41	Pseudoschlierens of the open cavity simulation for $C_{PMNS} =$ a) $0,$ b) $1,$ c) $5,$ and d) $10.$ . . . . .	179
6.42	Wall $C_p$ on the floor of the open cavity for $C_{PMNS} = 0, 1, 5,$ and $10$ compared with the experiments of Plentovich et al. [140], where we have assumed the different spanwise locations recorded by Plentovich were obtained by moving the walls of the experimental apparatus. . . . .	181

## LIST OF TABLES

5.1	Time per step in seconds for the coarse, medium, and fine meshes . . . .	124
6.1	Parameters for the DNS and LES runs on the periodic cube. Note that for the runs with filtering, but no explicit CPMNS model, $C_{PMNS}$ is assigned a value of 0 . . . . .	143
6.2	Upstream boundary layer properties for the compression ramp . . . . .	166

## Chapter 1. Introduction

The simulation of turbulent flows remains a critical problem in modern computational fluid dynamics (CFD). Many engineering and naturally occurring flows are turbulent, ranging across such situations as planetary boundary layers, jet engine combustors, rocket nozzles, and pipe flows. However, due to nonlinearities in the Navier–Stokes equations (NSEs), direct numerical simulation (DNS) requires that the computational grid must be resolved down to the finest coherent structures. Furthermore, under-resolution is not only inaccurate, but numerically unstable. For turbulent flows, this requires resolution down to the Kolmogorov dissipation scale, which is the length scale at which viscous dissipation overwhelms nonlinearities. The ratio of the dissipation scale to the largest scale of coherent structure, called the integral scale, is  $\mathcal{O}(Re^{3/4})$ , where  $Re$  is the integral scale Reynolds number. Thus, a 3-D grid resolving all scales of the flow requires  $\mathcal{O}(Re^{9/4})$  grid points. Also the time step is generally proportional to the grid size; this means that the overall computational work required for a certain period of time grows like  $\mathcal{O}(Re^3)$ . Because turbulent Reynolds numbers are frequently  $\mathcal{O}(10^6)$  or greater, this typically makes DNS prohibitively expensive for flows of engineering interest, even on modern supercomputers.

The reality of the infeasibility of using DNS for simulating engineering flows for the foreseeable future has led to the need for turbulence modeling. Generally, turbulence models fall into two types: Reynolds averaged Navier–Stokes (RANS) models and large-eddy simulation (LES) models. RANS models sidestep the fact that turbulence is an intrinsically unsteady phenomenon by attempting to predict only the Reynolds or time-averaged flow by solving time-averaged equations. However, the Reynolds averaging technique introduces a closure problem, which must be dealt with by means of a model. In general, RANS models are limited in their applicability, and different



models have been developed for different types of flows. In particular, RANS models tend to be poor at dealing with turbulent transition, highly separated flows, and moving boundaries. One explanation for the limitations of RANS modeling is that it must capture the entire frequency spectrum of turbulence, ultimately frustrating the search for a universal RANS turbulence model.

LES modeling differs from RANS modeling in that it is intended to capture the unsteady phenomena that can be resolved by the grid, while handling the effects of subgrid-scale (SGS) phenomena by means of a model. This includes traditional LES [1], which filters the governing equations and relies on an “eddy viscosity”, implicit LES (ILES) [2], which relies on built-in numerical dissipation to achieve stability, and structural models [3], which attempt to reconstruct estimates of SGS quantities in order to return information to the large scale. The vast majority of RANS and LES methods rely on artificial dissipation to handle the effects of SGS fluctuations. But because turbulence is due to nonlinear interactions, although it does act to enhance dissipative properties of the flow, its mathematical characteristics are substantially different from true, linear dissipation. Thus, although the popular dissipative methods are relatively stable and can produce usable results for certain classes of flows, reliance on dissipation intrinsically limits these methods, especially in the case of transition to turbulence. In Chapter 3, we will present a detailed, mathematical explanation and critique of both RANS and LES methods and present an argument for the necessity of using an explicit filter to compute LES solutions.

Currently, the simulation of more complex flow situations, such as chemically reacting flows and multiphase flows, is gaining industrial significance. However, the critical phenomena of these flows happen at the SGS level, and traditional dissipative models do not provide the information needed to simulate such phenomena. This has led researchers to investigate new types of models. One class of models is coupled to traditional dissipative turbulence models, and uses the turbulence model terms

in order to construct SGS quantities. See, for example, the Lagrangian-Langevin dispersion model investigated by Berrouk et al. [4]. Another approach is to rely on the SGS estimates provided by a structural model. Rather than modeling turbulence as dissipation, these models use dissipation primarily to achieve numerical stability, and use some kind of model to directly simulate SGS fluctuations. For example, A.R. Kerstein’s one-dimensional turbulence (ODT) uses a stochastic process to simulate SGS mixing [5]. J. Domaradzki’s subgrid-scale estimation model estimated SGS quantities, then used these to estimate the SGS stress tensors in the LES equations [6]. This class of models has the advantage of simultaneously attacking the traditional flow-related problems of dissipative models, while also providing a model of SGS quantities suitable for application to situations such as the mixing of chemical species.

Compressible turbulence introduces another layer of complication for turbulence modeling. The compressible Navier–Stokes equations (CNSEs) include additional terms in the mass and momentum equations, and include an energy equation as well. The averaging and filtering techniques used to produce RANS and LES equations produce additional nonlinear terms beyond those of the usual stress tensors familiar to incompressible LES researchers. Further, compressible turbulence interacts with shock waves at high Mach number and can be shown to violate some of the assumptions undergirding classic eddy viscosity models [7]. For example, scalar eddy viscosity models rely on an assumption of local isotropy, an assumption that has been shown to be false by Schmitt [8]. They also assume turbulence is an essentially dissipative mechanism that transfers energy from large to small scales, while the analysis of Kraichnan shows that locally, net energy transfer can be in the reverse direction [9].

The model presented in this current work is of the latter type. In particular, it is an extension to the compressible NSEs of an older turbulence model by McDonough and Yang [10]. The same techniques used to formulate this model, called the “poor

man’s Navier–Stokes” (PMNS) equations after the terminology of Frisch [11], will be applied to the compressible NSEs, hence the name, compressible “poor Man’s Navier–Stokes” (CPMNS) equations. The SGS model takes the form of a discrete dynamical system (DDS), as opposed to the aforementioned random models (more explanation of dynamical systems will be given in Chapter 2). A DDS is a natural choice for a SGS model, as the NSEs themselves can be viewed as a dynamical system, according to the theory of Ruelle and Takens [12]. Moreover, dynamical systems exhibit bifurcation behavior; that is, their time-evolution behavior changes qualitatively as certain parameters, called bifurcation parameters, are increased. For example, the logistic map, a commonly studied DDS, exhibits steady-state, periodic, subharmonic, and chaotic behavior as its bifurcation parameter is increased. In the case of the compressible NSEs, three relevant bifurcation parameters are the Reynolds number  $Re$ , the Mach number  $M$ , and the Peclet number  $Pe$ . We will show in Ch. 4 that the bifurcation parameters of the CPMNS equations produce physically realistic bifurcation sequences, a desirable characteristic that a stochastic model cannot match.

In the latter portion of Ch. 4, we develop a forcing function to be used as a backscatter model. A pure backscatter model is a natural choice to be used in conjunction with an explicit filter, and we give a detailed discussion of prior research in forcing methods. This forcing method is implemented in the OVERFLOW compressible CFD code, and we discuss the features, advantages, and shortcomings of this package in Ch. 5. In Ch. 6, this model is applied to two different flows: decay of homogeneous, isotropic turbulence in a periodic cube, and turbulent boundary layer flow over a Mach 2.9 compression ramp. We show that in both cases, the backscatter model enhances the performance of the LES. In Ch. 7, we summarize our findings, outline some open problems, and present two alternative strategies for developing better forcing functions.

## Chapter 2. Foundations in Turbulence Theory

In this chapter, we present a summary of compressible turbulence theory and the basic techniques of turbulence modeling. A solid theoretical foundation serves as both a foundation for modeling and for critiquing existing models. This is necessary, as researchers in the field of turbulence modeling employ a variety of competing theories. The fact is that despite decades of research, no universally applicable, reliable turbulence model has yet been constructed, nor has any single general approach to turbulence modeling even become universally accepted. When such a large knowledge gap exists in a field, it is incumbent upon scientists to refrain from taking the core assumptions behind any technique for granted, and by the same token it is necessary to explicitly state what assumptions, simplifications, and theories are being employed. Fluid turbulence remains one of the great unsolved problems of physics, and were it solved, there would be no need for this discussion. We present our judgment of which theoretical and analytical techniques we believe shed the most light on the nature of turbulence with the goal of explicitly clarifying to the reader why we have chosen the particular turbulence modeling technique presented in Chapter 4.

In this chapter, then, we will present an overview of compressible turbulence theory, beginning with the statistical and mathematical tools used to discuss and analyze both physical turbulence and the Navier–Stokes equations. The Kovasznay decomposition is used to separate the flow into pressure, entropy, and vorticity modes. Statistics are used both to characterize turbulent flow data and to construct popular turbulence models. Spectral analysis is used to analyze physical data, to decompose the NSEs, to build turbulence models, and to construct and study numerical solution methods. We then continue to give a basic discussion of chaotic dynamical systems and their application to the NSEs, a critical paradigm shift in the theory of turbulence

with significant consequences for turbulence modeling. Shock-turbulent interaction is the last topic discussed, as it is an issue unique to compressible turbulence and poses challenges that researchers most familiar with incompressible turbulence may not be aware of. Finally, we summarize the discussion in this chapter and present our conclusions on the nature of turbulence and how it relates to turbulence modeling.

## 2.1 Governing equations

Turbulence in engineering flows is assumed to obey the continuum hypothesis; that is, that turbulent fluid behaves like a continuous medium. In physical terms, this means that we assume that the smallest length scales on which turbulent dynamics operate are much greater than the mean free path of the molecules of the fluid. This is a non-trivial assumption, though it is now generally accepted that the governing equations contain everything necessary for turbulence. But even still, there are flow situations where the continuum hypothesis does not necessarily hold, such as hypersonic wakes at high altitudes [13]. These situations must be handled using statistical mechanics and the Boltzmann equation, which is outside the scope of the problem approached here. Within the continuum regime, compressible, flow with no body forces or source terms is governed by the following equations for mass, momentum, and energy:

$$\partial_t \rho + \partial_j (\rho u_j) = 0, \quad (2.1a)$$

$$\partial_t (\rho u_i) + \partial_j (\rho u_j u_i) = -\partial_i p + 2\partial_j (\mu S_{ij}) + \partial_i \mu_v \partial_j u_j, \quad (2.1b)$$

$$\partial_t (\rho e_0) + \partial_j (\rho e_0 + p) u_j = \partial_j \sigma_{ij} u_i - \partial_j q_j, \quad (2.1c)$$

where

$$\sigma_{ij} = 2\mu S_{ij} + \mu_v S_{kk} \quad (2.2)$$

and

$$S_{ij} = \frac{1}{2} (\partial_j u_i + \partial_i u_j), \quad (2.3)$$

where  $u_i$  is the velocity component in the  $i^{\text{th}}$  direction,  $\rho$  is the density,  $\mu$  is the dynamic viscosity,  $\mu_v$  is the second viscosity,  $e_0$  is the stagnation energy,  $p$  is the pressure,  $q_j$  is the heat flux, and repeated indices indicate summation. Pressure is related to energy by

$$\rho e_0 = \frac{p}{\gamma - 1} + \frac{1}{2}\rho u_i u_i \quad (2.4)$$

and to static temperature  $T$  and  $\rho$  by the equation of state

$$p = \rho R T, \quad (2.5)$$

where  $R$  is the ideal specific gas constant and  $\gamma$  is the specific heat ratio. The formula for heat flux is

$$q_j = -\kappa \partial_j T, \quad (2.6)$$

where  $\kappa$  is the thermal conductivity. Computations in this work make use of the Stokes hypothesis,

$$\mu_v = -\frac{2}{3}\mu, \quad (2.7)$$

although we note that this hypothesis is not in general true for polyatomic gases [14]. However, the software used in the present research does not have a model of second viscosity, nor is there a generally accepted model, although it can indeed have significant effects on turbulence dynamics, as seen in the DNS flame experiments of Fru et al. [15].

Although turbulence modeling of the compressible Navier–Stokes equations (NSEs) is the focus of this work, for a preliminary investigation of some of the core mathematical issues of turbulence, it will helpful at times to consider the incompressible NSEs, as they are much simpler and still have the essential nonlinearities that lead to turbulence. The incompressible NSEs are given in non-conservative form by

$$\partial_i u_i = 0 \quad (2.8a)$$

$$\partial_t u_i + u_j \partial_j u_i = -\partial_i p + \nu \partial_{jj} u_i, \quad (2.8b)$$

where  $\nu$  is the kinematic viscosity.

## 2.2 Basic Tools

In studying the properties of turbulent flows, several mathematical tools are traditionally used. As these tools are important both in interpreting experimental data presented in the literature and in traditional turbulence models, they will be defined here. We divide these methods into three general classes: the Kovasznay decomposition, statistical tools, and spectral analysis. Each of these tools gives unique insights into the nature of compressible turbulence and the challenges an LES model must overcome.

### 2.2.1 Kovasznay decomposition

We have referred before to information being transferred through a compressible flow via three mechanisms: advection, acoustic waves, and entropy waves. This idea of information transmission can be justified in both physical and mathematical terms. From a physical, somewhat heuristic standpoint, we can think of “information” as a change in conditions at a particular point in or subset of the flow field and its “transmission” as the propagation of these effects. Physically, these effects can be observed to propagate in a compressible medium as flow particles advect downstream, and as both acoustic and entropy waves propagate at the speed of sound through the medium. Mathematically, information transmission is fundamentally embedded in the concept of a partial differential equation (PDE), as differential operators define the way solution variables at different points in the domain interact with each other. Further, information transmission can be associated with analytical and numerical solution techniques. The method of characteristics, which looks at how certain quantities remain constant along particular paths and is associated with compression wave propagation, has been invaluable in both the theoretical analysis and numerical computation of compressible flows. Thus because of both mathematical and physical considerations, decomposing the flow field into modes associated with the three

aforementioned mechanisms intuitively seems like a productive route of analysis.

In a 1953 paper [16] and with Chu in 1958 [17], Kovasznay developed a decomposition of the compressible flow field into vortical, acoustic, and entropic modes. Here, we follow the discussion of Garnier et al. [7]. The linear decomposition used to develop this approach bears a great deal of similarity to the tools of linear perturbation analysis used in PDE theory to study small deviations of nonlinear systems from equilibrium, of which classical instability analysis in fluid dynamics is an example. By assuming the turbulent fluctuations are small relative to the mean flow field, the flow variables are expanded as

$$\mathbf{u} = \sum_{m=0}^{\infty} \epsilon^m \mathbf{u}_m \quad (2.9a)$$

$$\rho = \sum_{m=0}^{\infty} \epsilon^m \rho_m \quad (2.9b)$$

$$p = \sum_{m=0}^{\infty} \epsilon^m p_m \quad (2.9c)$$

$$s = \sum_{m=0}^{\infty} \epsilon^m s_m, \quad (2.9d)$$

where  $\epsilon \ll 1$ ,  $(\mathbf{u}_0, \rho_0, p_0, s_0)$  is the mean flow field, and  $(\mathbf{u}_m, \rho_m, p_m, s_m)$  is referred to as the  $m^{\text{th}}$ -order fluctuating flow field. By assuming the fluctuations are small, the high-order terms can be dropped and the expansions applied to the NSEs. The the individual fluctuations and thus the equations themselves can then decomposed into vorticity, entropy, and acoustic modes. The equation for the vorticity mode is given by

$$\begin{aligned} \partial_t \boldsymbol{\omega}_\omega &= \nu_0 \nabla^2 \boldsymbol{\omega}_\omega, \\ p_\omega &= 0, s_\omega = 0, \nabla \times \mathbf{u}_\omega = \boldsymbol{\omega}_\omega, \nabla \cdot \mathbf{u}_\omega = 0, \end{aligned} \quad (2.10)$$

where the  $\omega$  subscript denotes the vorticity mode of the first-order fluctuating variable. Because the fluctuating vorticity component of velocity is divergence-free, this is also referred to as the solenoidal component.



Both the entropy and acoustic modes are dilatational; i.e., they are vorticity-free. The equation for the entropy mode is given by

$$\begin{aligned}\partial_t s_e &= \kappa_0(\gamma - 1)\nabla^2 p_e + \kappa_0\nabla^2 s_e \\ p_e &= 0, \boldsymbol{\omega}_e = 0, \nabla \cdot \mathbf{u}_e = \partial_t s_e,\end{aligned}\tag{2.11}$$

and the equation for the acoustic mode is given by

$$\begin{aligned}\partial_{tt} p_a &= +a_0^2\nabla^2 p_a + \kappa_0\gamma\partial_t(\nabla^2 p_a) \\ \partial_t s_a - \kappa_0\nabla^2 s_a &= \kappa_0(\gamma - 1)\nabla^2 p_a \\ \boldsymbol{\omega}_a &= 0, \nabla \cdot \mathbf{u}_a = \partial_t s_a - \partial_t p_a,\end{aligned}\tag{2.12}$$

where  $a_0$  is the mean speed of sound, and the  $e$  and  $a$  subscripts denote the entropy and acoustic modes of first-order fluctuations, respectively. The vorticity and entropy modes are both associated with advection at the speed of the fluid, while the acoustic mode is associated with pressure waves traveling at the speed of sound. Note that by construction, the decomposition  $(\mathbf{u}_\omega, \mathbf{u}_e + \mathbf{u}_a)$  is a Helmholtz decomposition into solenoidal and dilatational modes. Interactions among the modes can be studied by including higher-order terms [17]. These are not listed here, but their existence is sufficient to establish that not only does compressibility affect the overall dynamics of turbulence, but that the solenoidal (i.e., “incompressible”) and dilatational modes interact. This leads to the conclusion that the solenoidal mode may not simply be separated from the dilatational mode and treated with techniques that are sufficient for incompressible flow.

### 2.2.2 Statistical tools

Statistical descriptions of turbulence are natural for the analysis of experimental data, as it is relatively simple to compute statistics for large data sets. *Reynolds averaging*, or time averaging, is one of the oldest statistical tools for measuring turbulent flows, used for both incompressible and compressible flows. The Reynolds average is defined

by

$$\bar{f}(\mathbf{x}) = \lim_{T \rightarrow \infty} \frac{1}{T} \int_0^T f(\mathbf{x}, t) dt. \quad (2.13)$$

When applied to turbulence modeling, researchers generally assume that the time average is independent of the initial conditions. This is known as the ergodic hypothesis, which Foias et al. demonstrated is true for incompressible flows under certain assumptions [18]. The Reynolds average leads naturally to the *Reynolds decomposition*,

$$f(\mathbf{x}, t) = \bar{f}(\mathbf{x}) + f'(\mathbf{x}, t), \quad (2.14)$$

where  $\bar{f}$  and  $f'$  are referred to as the mean and fluctuating variables. Often in the literature,  $\bar{f}$  is replaced by  $F$ . In compressible flows, momentum and velocity are not interchangeable, which leads naturally to *Favre averaging*, also known as density-weighted or mass-weighted averaging. This technique has been found to be useful in the context of compressible flows and is defined by

$$\tilde{f}(\mathbf{x}) = \frac{\overline{\rho f}}{\bar{\rho}}. \quad (2.15)$$

This leads to the *Favre decomposition*,

$$f(\mathbf{x}, t) = \tilde{f}(\mathbf{x}) + f''(\mathbf{x}, t). \quad (2.16)$$

Favre averaging is also used to define the turbulent Mach number  $M_t$ , by

$$M_t = \frac{\sqrt{\widetilde{u_i'' u_i''}}}{a}, \quad (2.17)$$

where  $a = \sqrt{\gamma R \tilde{T}}$  is the mean speed of sound,  $\gamma$  is the specific heat ratio, and  $R$  is the specific gas constant. The two forms of averaging are not equivalent for compressible flows, though they clearly are in the incompressible case. In particular,  $\bar{f}' = 0$  and  $\tilde{f}' \neq 0$ , while  $\widetilde{f''} = 0$ , and  $\bar{f}'' \neq 0$ . Favre variables are particularly useful, since mean streamlines are tangent to the density-weighted average velocity vector, which is not true for the Reynolds-averaged velocity vector for the compressible case.

Reynolds averaging combined with the ideas of the Kovaszny decomposition lead naturally to separating familiar turbulence statistics from incompressible flows into solenoidal and dilatational components. In particular, we define the solenoidal dissipation rate by

$$\bar{\varepsilon}_s = \frac{\tilde{\mu}}{\bar{\rho}} \widetilde{\omega_i'' \omega_i''}, \quad (2.18)$$

and the dilatational dissipation rate is given by

$$\bar{\varepsilon}_d = \frac{4}{3} \frac{\tilde{\mu}}{\bar{\rho}} \widetilde{(\partial_i u_i'')^2}. \quad (2.19)$$

We will define the solenoidal and dilatational kinetic energies,  $K_s$  and  $K_d$ , in terms of spectra in Sec. 2.2.3. The Reynolds and Favre decompositions can be applied to the NSEs, and then filtering applied to the equations themselves, to give the Reynolds-averaged Navier–Stokes (RANS) equations, which express the variables in terms of their means and moments. Details of the derivation and simplifying assumptions can be found in [19]. The equations for mass, momentum, and energy are given by:

$$\partial_j(\bar{\rho} \tilde{u}_j) = 0, \quad (2.20a)$$

$$\partial_j(\bar{\rho} \tilde{u}_j \tilde{u}_i) = -\partial_i \bar{p} + (\tilde{\mu} + \tilde{\mu}_v) \partial_i \partial_j \tilde{u}_j + \tilde{\mu} \partial_j \partial_j \tilde{u}_i + \partial_j \bar{\rho} \widetilde{u_i'' u_j''}, \quad (2.20b)$$

$$\partial_j(\bar{\rho} \tilde{u}_j \tilde{h}) = \overline{u_j \partial_j p} + \overline{\sigma_{ij} S_{ji}} - \partial_j \bar{\rho} c_p \widetilde{u_j'' T''}, \quad (2.20c)$$

where  $h = c_p T$  is the specific enthalpy,  $T$  is the temperature, and  $c_p$  is the specific heat capacity at constant pressure. Here, unlike Wilcox [20], we have omitted time derivatives, since time-averaging eliminates them. They may be restored by using ensemble rather than time averaging; however, ensemble averaging is significantly more complex to rigorously define in such a way that it is always equivalent to the time average, especially when the long-term behavior is dependent on initial conditions.

There are many equivalent formulations of the energy equation, since the equation of state and specific heat relations allow equivalent transformations among a variety of variables. Note the presence of two covariance terms,  $\bar{\rho} \widetilde{u_i'' u_j''}$  and  $\widetilde{u_j'' T''}$  and two

correlations,  $\overline{u_j \partial_j p}$  and  $\overline{\sigma_{ij} S_{ji}}$ . This means the RANS equations are not a closed system and cannot be directly solved. This will be discussed in more detail in Section 3.2.1. However, the RANS equations do introduce a number of terms that are useful for experimentation and validation of turbulence models. In particular, the velocity covariance tensor  $\widetilde{u''_i u''_j}$  in Eq. (2.20b) is called the *Reynolds stress tensor* (RST), and components of it can be computed whenever time series for two velocity components at a point in space are known. In the literature, the RST is often denoted by

$$\tau_{ij} = \widetilde{u''_i u''_j} \quad (2.21)$$

for compressible flows, and by

$$\tau_{ij} = \overline{u'_i u'_j} \quad (2.22)$$

for incompressible flows.

It is important to emphasize here that outside of fluid dynamics, statistical quantities have proven to be of very little use to the academic mathematics community in the formal study of the solutions of classical, deterministic PDEs (although they are of course essential for studying random and stochastic differential equations). Many mathematical techniques familiar to fluid dynamicists, such as linear perturbation theory, the method of characteristics, Sobolev spaces, and harmonic analysis, have proved quite productive in the study of deterministic PDEs, but attempts to characterize solutions in terms of statistical moments are noticeably absent from both graduate textbooks on PDE theory (such as Evans [21]) and journal publications. Foias et al. do in fact prove some interesting results about the statistics of the incompressible NSEs, such as boundedness and well-definedness, and prove Kolmogorov's scaling laws under certain assumptions, but even their lengthy discussion does not contain any of the groundwork that would be necessary for closing the RANS equations. In fact, there is a crucial distinction to be made between statistically characterizing solutions of a PDE and applying averaging to a PDE to write it in terms

of more statistical moments than one has equations for. The former is actually an application of measure theory, which is a very productive mathematical concept. The latter eliminates information from the system, replacing a closed system of equations with an unclosed one.

### 2.2.3 Spectral analysis

We include all uses of the Fourier transform in both continuous and discrete space under the general category of spectral analysis. We begin with the cube  $\Omega = [-\pi, \pi]^3$  with periodic boundary conditions, which is a common domain for studying the characteristics of homogeneous, isotropic turbulence. The set  $L^2(\Omega)$  of square-integrable functions on  $\Omega$  has the orthonormal Fourier basis set,

$$\{\phi_{\mathbf{k}}(\mathbf{x}) = e^{i\mathbf{k}\cdot\mathbf{x}} \mid \mathbf{k} \in \mathbb{Z}^3, \mathbf{x} \in \Omega\}, \quad (2.23)$$

and the Fourier transform is defined by the volume integral,

$$\hat{u}_{i,\mathbf{k}}(t) = \frac{1}{8\pi^3} \int_{\Omega} u(\mathbf{x})\phi(\mathbf{x})dV \quad (2.24)$$

Note that here and below,  $i = \sqrt{-1}$  when not used as an index. A common assumption is that  $u_i$  is an  $L^2$  function, so we can expand it in a Fourier series:

$$u_i(\mathbf{x}, t) = \sum_{\mathbf{k}} \hat{u}_{i,\mathbf{k}}(t)\phi_{\mathbf{k}}(\mathbf{x}), \quad (2.25a)$$

where  $\mathbf{k}$  is often referred to as the wavenumber (or wave vector). This technique can be generalized to any domain for which there exists a set of functions that form a complete orthogonal system, which can then be used as a basis set. Readers familiar with the finite element method know that this is the analytical basis of that technique. In this work, however, we restrict our investigations to the periodic basis in Eq. (2.23).

Fourier series can be applied to a PDE to obtain a Galerkin expansion, which transforms a PDE into a system of infinitely many ordinary differential equations (ODEs), as long as all the relevant derivatives of the solution exist in  $L^2$  in at least

weak form. For the NSEs, this requires that the solutions exist in the Sobolev space  $H^1$ , which is a subset of  $L^2$ . Although this has not been formally proven in three space dimensions, it is a necessary condition for the existence of solutions, so any discussion of finding numerical solutions must assume this. Given a general PDE for a scalar  $u$ ,

$$\partial_t u = L(u) + B(u, u), \quad (2.26)$$

where  $L$  and  $B$  are linear and bilinear operators, respectively, applying a Fourier expansion provides

$$\frac{d}{dt} \sum_k \hat{u}_k(t) \phi_k(x) = \sum_k \hat{u}_k(t) L(\phi_k(x)) + \sum_{l,m} \hat{u}_l(t) \hat{u}_m(t) B(\phi_l(x), \phi_m(x)). \quad (2.27)$$

The linear operator  $L$  has the Fourier representation  $\sum_j A_j (ik)^{n_j}$  where  $A_j$  is a scalar constant,  $n_j$  is an integer, and  $j = \{0, 1, \dots, J\}$ , leading to the simplification

$$\frac{d}{dt} \sum_k \hat{u}_k(t) \phi_k(x) = \sum_{j,k} A_j (ik)^{n_j} \hat{u}_k(t) \phi_k(x) + \sum_{l,m} \hat{u}_l(t) \hat{u}_m(t) B(\phi_l(x), \phi_m(x)). \quad (2.28)$$

Applying the Hermitian inner product  $\int_{\Omega} (\cdot) \phi_{-k} dx$  to both sides then provides the infinite set of ODEs,

$$\frac{d}{dt} \hat{u}_k = \sum_j A_j (ik)^{n_j} \hat{u}_k + \sum_{l,m} \hat{u}_l \hat{u}_m \int_{\Omega} B(\phi_l, \phi_m) \phi_{-k}, \quad k \in \mathbb{Z}, \quad (2.29)$$

where the  $(x)$  and  $(t)$  notation has been suppressed. This technique can easily be extended to a system of PDEs for a vector of solutions  $\mathbf{u}$ . In particular, note the term produced by the bilinear operator,

$$\sum_{l,m} \hat{u}_l \hat{u}_m \int_{\Omega} B(\phi_l, \phi_m) \phi_{-k},$$

causes the system of ODEs to be coupled across all Fourier modes. Galerkin expansions of linear PDEs do not have such terms, meaning that exact solutions for the individual Fourier coefficients can be found independently without solving for any other coefficients. This clearly is not the case for nonlinear PDEs. We will not provide

Galerkin expansions of the NSEs in this section, as it is more useful to derive them in the following sections where they provide more immediate contextual relevance.

The Fourier series can also be applied to discrete signals. The discrete Fourier transform (DFT) for a vector  $\{f_n\}_{n=0}^{N-1}$  is given by

$$F_k = f_n \exp\left(\frac{-(2\pi i)nk}{N}\right), \quad k = 0, \dots, N-1. \quad (2.30)$$

The power spectral density (PSD) estimate is then given by

$$P_0(F) = \frac{1}{N^2} |F_0|^2, \quad (2.31a)$$

$$P_k(F) = \frac{1}{N^2} (|F_k|^2 + |F_{N-k}|^2), \quad k = 1, \dots, \left(\frac{N}{2} - 1\right), \quad (2.31b)$$

$$P_{N/2}(F) = \frac{1}{N^2} |F_{N/2}|^2. \quad (2.31c)$$

When  $f_n$  is a velocity signal sampled in time or space, the PSD gives (modulo  $\rho|\Omega|$ ) the kinetic energy per unit space or time stored at each temporal or spatial frequency. This observation allows us to decompose the kinetic energy into solenoidal and dilatational components without actually computing a Helmholtz decomposition of the velocity field. Given a discrete solution, we define  $P_k(W)$  and  $P_k(D)$  to be the PSDs of vorticity and divergence, respectively. Then the solenoidal and dilatational kinetic energy dissipation rates are estimated by

$$\bar{\varepsilon}_s \approx 2|\Omega| \frac{\bar{\mu}}{\bar{\rho}} \sum P_k(W), \quad (2.32)$$

and

$$\bar{\varepsilon}_d \approx \frac{4|\Omega|}{3} \frac{\bar{\mu}}{\bar{\rho}} \sum P_k(D). \quad (2.33)$$

Since spatial differentiation in Fourier space is equivalent to multiplication by  $ik$ , we can compute the solenoidal kinetic energy by

$$K_s = |\Omega| \sum \frac{P_k(W)}{k^2}. \quad (2.34)$$

and the dilatational kinetic energy by

$$K_d = |\Omega| \sum \frac{P_k(D)}{k^2}. \quad (2.35)$$

We then define  $E_s(k) = P_k(W)/k^2$  and  $E_d(k) = P_k(D)/k^2$  to be the solenoidal and dilatational energy spectra, respectively.

In the rest of this work, Galerkin expansions and Fourier series will be critical tools for the study of turbulence, analysis of discrete data, study and critique of turbulence modeling techniques, and the derivation of the CPMNS equations.

### 2.3 Dynamical systems view of turbulence

Since O. Reynolds' original pipe flow experiments [22], the mechanics of transition from laminar to turbulent flow have occupied special attention of researchers. While transition to turbulence has been a studied problem for over a century, foundations were not laid for a solid theory of transition to turbulence until the development of dynamical systems theory in the second half of the 20<sup>th</sup> century. Generally speaking, dynamical systems theory is a means of investigating time-evolution equations in terms of the transformation of their solution states from one moment in time to the next. In particular, the theory is well-suited to describing qualitative changes from one kind of dynamic behavior to another. This section presents a technical definition of dynamical systems, the notion of bifurcation behavior, strange attractors, and chaos. The section proceeds to give an overview of the length scales typically associated with turbulent behavior and discusses the idea of so-called "turbulent dissipation" with an overview of the dynamics of conservative, Euler turbulence.

#### 2.3.1 Mathematics of dynamical systems

Before proceeding further with this discussion, we quote here Frisch's definition of a dynamical system [11]:

**Definition 1** *A dynamical system is a quadruplet  $(\Omega, \mathcal{A}, P, G_t)$ . The set  $\Omega$  is called the probability space.  $\mathcal{A}$  is a  $\sigma$ -algebra of  $\Omega$ .  $P$ , the probability*



measure, maps  $\mathcal{A}$  to the real numbers between 0 and 1 and satisfies

$$P(A) \geq 0 \quad \forall A \in \mathcal{A}, \quad P(\cup_i A_i) = \sum_i P(A_i), \quad P(\Omega) = 1, \quad (2.36)$$

where  $\{A_i\}$  is any enumerable set of disjoint sets  $\in \mathcal{A}$ . The time-shifts,  $G_t$ , are a family of operators depending on a variable  $t \geq 0$  which can be either continuous or discrete. The  $G_t$ s satisfy the semi-group property

$$G_0 = I, \quad G_t G_{t'} = G_{t+t'} \quad (2.37)$$

and conserve the probability:

$$P(G_t^{-1}A) = P(A), \quad \forall t \geq 0, \quad \forall A \in \mathcal{A} \quad (2.38)$$

In other words,  $G_t$  maps  $\Omega$  into itself. Another way of saying this is that it evolves an initial condition,  $\omega_0 \in \Omega$ , in time. A dynamical system may be either discrete or continuous, depending on whether the state evolves continuously or in discrete steps. A common example of a discrete dynamical system is the logistic map:

$$x_{n+1} = \beta x_n(1 - x_n). \quad (2.39)$$

Time-dependent partial differential equations (PDEs) may be viewed as continuous. In the case of the NSEs,  $\Omega$  is the set of all instantaneous flow fields for a given domain, initial conditions, and boundary conditions, and  $G_t$  is the solution operator for the NSEs.

An important feature of dynamical systems theory is the notion of bifurcation behavior. A thorough investigation of bifurcation theory is beyond the scope of this work, but the relevant elements of it will be presented here. Following Seydel [23], we begin with a system of ODEs,

$$\dot{\mathbf{y}} = \mathbf{f}(\mathbf{y}, \lambda), \quad (2.40)$$

where  $\dot{\mathbf{y}}$  indicates differentiation of  $\mathbf{y}$  with respect to time. Note that the system is autonomous, i.e., it does not explicitly depend on  $t$ . Here,  $\lambda$  is the *bifurcation*

*parameter* of the system, and in this simple case, we are considering a system with only one parameter. Bifurcation theory investigates how the behavior of systems change as the parameters are varied, such as a transition from steady-state equilibria to periodic limit cycles. In general, analytical investigation of bifurcation behavior involves examining the eigenvalues and other characteristics of the Jacobian matrix of  $\mathbf{f}, \mathbf{f}_{\mathbf{y}}$ . For the incompressible NSEs, the bifurcation parameter is  $Re$ , but the compressible NSEs have three such parameters:  $Re$ ,  $M$ , and  $Pe$ .

While there are various kinds of bifurcations, one of the most well-studied, the Hopf bifurcation, which is a transition from a steady equilibrium to a periodic oscillation, was demonstrated by E. Hopf for  $n$ -dimensional systems of the type of ODEs seen in Eq. (2.40) [24]. Hopf's theorem, which describes and predicts this elementary bifurcation behavior is given below:

**Theorem 1** *Assume, given a system as in Eq. (2.40), that the following hold for some  $(\mathbf{y}_0, \lambda)$*

1.  $\mathbf{f}(\mathbf{y}_0, \lambda_0) = 0$  for some pair  $(\mathbf{y}_0, \lambda_0)$ .
2.  $\mathbf{f}_{\mathbf{y}}(\mathbf{y}_0, \lambda_0)$  has a simple pair of purely imaginary eigenvalues  $\mu(\lambda_0) = \pm i\beta$  and no other eigenvalue with zero real part.
3.  $d[\Re(\mu(\lambda_0))]/d\lambda \neq 0$ .

*Then there is a birth of periodic limit cycles at  $(\mathbf{y}_0, \lambda_0)$ , and the initial period of the oscillation is*

$$T_0 = \frac{2\pi}{\beta}.$$

Of course, the NSEs are PDEs, not ODEs, so this theorem cannot be directly applied to them. But it is useful to see that a qualitative change in the dynamical behavior of a system is associated with a definite, quantifiable change in the intrinsic properties of the associated differential equations. In the case of a Hopf bifurcation, it is the birth

of a new pair of imaginary eigenvalues. In fact, Hopf bifurcations can be generalized to PDEs in the sense of a new pair of complex conjugate eigenvalues, an important distinction being that PDEs such as the NSEs have infinitely many eigenvalues.

### 2.3.2 The Ruelle-Takens theory of turbulence

Dynamical systems theory has proved a fruitful basis for investigating the nature of turbulence. The Landau-Hopf theory of turbulence, which was widely accepted until the 1970s, posited successive Hopf bifurcations with incommensurate frequencies (also known as quasiperiodicity) as the route from laminar to turbulent flow [25], similar to how the logistic map reaches chaos after an infinite number of subharmonic bifurcations. This theory was superseded in the 1970s by the Ruelle–Takens theory of turbulence [12]. Ruelle and Takens made use of a new aspect of dynamical systems theory, that of a *strange attractor*, to describe turbulence. To understand the concept of an attractor, consider the ODEs in Eq. (2.40) again. The attractor is the set of all  $\mathbf{y}(t)$  that the solution tends to as  $t \rightarrow \infty$ . The simplest attractor is the steady-state case, which is a single point in  $\mathbb{R}^n$  for the case of a system of ODEs, and the final solution field in the case of a PDE with a steady-state solution. In the case of a limit cycle, it is the entire orbit that the solution traces. A quasiperiodic attractor, such as Landau hypothesized characterizes turbulence, is a torus. In contrast to these regular sets, a *strange attractor* is a highly irregular set, usually with fractal dimension, associated with chaotic behavior. More detail can be found in specific literature on chaos, e.g., Peitgen et al. [26].

The Ruelle–Takens theory of turbulence essentially looks at the bifurcation sequence as a transition from one type of attractor to another as the parameter  $Re$  increases, with turbulence itself being associated with a strange attractor. In a 1978 paper with Newhouse [27], they argued that a small perturbation in  $Re$  away from a quasiperiodic attractor may lead to a strange attractor, thus the appropriate bifurca-

tion sequence leading to turbulence would lead from one quasiperiodic mode directly to chaos, rather than the infinite succession of quasiperiodic bifurcations as in the Landau theory. This sequence has been observed in numerous experiments, e.g., those of Wan and Coney [28]. However, it is important to note that the 1978 paper does not say that quasiperiodic behavior must always give way to chaotic behavior, simply that it is highly probable. Thus, observations of slightly modified sequences, such as the sequence of two period-doubling bifurcations between quasiperiodicity and chaos recorded by Yoo and Han [29], are consistent with the 1978 theory.

In general, most turbulence models, especially those widely used in engineering practice, are constructed without incorporating many if any of the important insights of the dynamical systems view of turbulence. This is a major shortcoming that the CPMNS equations are intended to address.

### 2.3.3 Turbulent length scales

Three length scales, originally developed for incompressible flow, are generally associated with turbulence. They are (1) the integral scale, (2) the Taylor microscale, and the (3) the dissipation or Kolmogorov scale. This theory was originally developed for incompressible turbulence, but, as the compressible NSEs also have advective and dissipative terms, the terminology has also been used in the context of compressible turbulence. A brief description of these length scales is given here; fuller discussion including derivations can be found in standard works on turbulence, such as Tennekes and Lumley [30].

1. The *integral scale*,  $\ell_0$ , is the largest length scale associated with coherent turbulent structure. It can be thought of as the approximate thickness of a turbulent boundary layer, or the approximate width of a turbulent jet. The integral scale is estimated by

$$\ell_0 \sim LRe^{-1/2}, \quad (2.41)$$

where  $L$  is the length scale of the flow, and  $Re$  is the large-scale Reynolds number. In terms of the equations, this is the length scale where viscous diffusion has little influence on the overall dynamics of the turbulence, i.e., the turbulence is a wholly nonlinear phenomenon. This length scale is associated with its own Reynolds number,  $Re_\ell = u_{rms}\ell/\nu$ , where  $u_{rms}$  is the rms velocity fluctuation.

2. The *Taylor microscale*,  $\lambda_T$ , is the length scale associated with interaction between both nonlinear dynamics and viscosity. It can be thought of as the length scale where viscosity begins to affect the dynamics of the turbulent eddies, and is estimated by the formula,

$$\lambda_T \sim \ell_0 Re_\ell^{-1/2} \quad (2.42)$$

The Taylor microscale also has its own associated Reynolds number,  $Re_\lambda = u\lambda_T/\nu$ .

3. Finally, the *Kolmogorov microscale*,  $\eta_K$  is the smallest length scale associated with turbulence. This is the scale at which the dissipation rate of the turbulent eddies dominates the dynamics of the behavior. It is estimated by

$$\eta_K \sim 15^{-1/4} Re_\lambda^{-1/2} \lambda_T \quad (2.43)$$

The portion of the spectrum between the integral scale and Taylor microscales, where nonlinearities dominate the dynamics of the flow, is generally referred to as the *inertial subrange*. For incompressible, homogeneous, isotropic turbulence, A.N. Kolmogorov argued that the energy spectrum in this range obeys a power law,  $k^{-5/3}$  [31], in the limit  $Re \rightarrow \infty$ . But as we will see below, this law does not apply generally to compressible turbulence. However, the length scales in general will be useful. Because these length scales are simply estimates, and because these estimates are derived from terms that occur in both the compressible and incompressible NSEs, they can be applied to compressible turbulence as well as incompressible turbulence. These

estimates will be important later on for constructing parameters for the CPMNS equations.

Attempts to construct a theory for the spectral decay of compressible turbulence kinetic energy in the inertial subrange corresponding to Kolmogorov's  $k^{-5/3}$  law are still an area of active research. From a physical standpoint, it is natural to expect that the dissipative characteristics of turbulence should be affected by compressibility. Lighthill [32] argued that in both turbulent and laminar compressible flows, energy is radiated away from a point by acoustic mode waves and ultimately converted to heat via acoustic attenuation. Thus, compressibility effects act like a source of additional dissipation and ought to make the spectral decay steeper than the  $k^{-5/3}$  law for incompressible turbulence. Attempts to derive a spectral decay law have been presented by Zakharov and Sagdeev in [33], and by Kadomtsev and Petviashvili in [34], where they argued for an approximate  $k^{-2}$  scaling.

The shock thickness is another length scale is often mentioned in the context of compressible turbulence, and those familiar with this field should find it to be conspicuous in its absence from this text. This is because at high Mach numbers, the thickness of a shock wave in a physical flow is a result of the breakdown of continuum mechanics in the shock, and this work is concerned specifically with modeling unresolved dynamical behavior of the NSEs. In contrast to physical shock thickness, the thickness of a shock wave generated by the viscosity terms in the NSEs at moderate Mach numbers is generally significantly smaller than the physical shock thickness[35], and is zero in inviscid flows. In fact, Ruggeri [36] has proven that for general hyperbolic conservation laws with added dissipation (such as the NSEs), there exists a critical velocity beyond which shocks must be discontinuous, i.e., the analytical shock thickness is zero even for high-Mach NSE flows. That physical flows exhibit nonzero shock thickness shows that, at least in the interior of the shock, the continuum hypothesis breaks down, and the NSEs are no longer an adequate model.

In the absence of any model of the breakdown of the continuum hypothesis in a CFD simulation, the numerical shock thickness is almost entirely a result of the shock-capturing method and the grid resolution, not any accurate physics or mathematics. The more accurate the solution method, then, the more closely the shock thickness approaches a value smaller than the real, physical scale. Therefore, the CFD researcher should always keep in mind that discrepancies between CFD and experimental results in the immediate vicinity of shock waves could be due not to any inadequacy in the mesh resolution or the numerical method, but could arise from the fact that NSEs themselves are an imperfect model of real-world compressible fluid dynamics. For those interested in non-continuum modeling of the internal dynamics of shock waves, we refer them to the work of Carlson et al. [37], who created a statistical model exhibiting excellent agreement with argon shock tube experiments, as a starting point.

### 2.3.4 Turbulent “dissipation”

The turbulent kinetic energy dissipation rate arises naturally from Reynolds-averaging the dissipative term in the kinetic energy equation. See, e.g., the classic derivation of Wilcox [38], where he derived the incompressible turbulent kinetic energy equation,

$$\partial_t K + \bar{u}_j \partial_j K = \tau_{ij} \partial_j \bar{u}_i - \rho \varepsilon + \partial_j \left[ \mu \partial_j K - \frac{1}{2} \overline{\rho u'_i u'_i u'_j} - \overline{p' u'_j} \right], \quad (2.44)$$

where  $K$  is the turbulent kinetic energy,  $\tau_{ij}$  is the RST as in Eq. (2.22), and  $\varepsilon$  is the turbulent kinetic energy dissipation rate. This derivation is exact, and no additional hypotheses are made. It can be easily seen from a Galerkin expansion of the NSEs that the effect of dissipation grows like the square of the wavevector length, and that the nonlinear terms lead to interactions between the small and large scales that would otherwise not exist. So it is reasonable to conclude that turbulence enhances dissipation through the transfer of kinetic energy from large to small scales, where the energy is more rapidly dissipated by the viscous terms.

Although these observations are entirely correct, this has led to incorrect descriptions of turbulence itself as “dissipation.” In mathematics, dissipation is formally defined in terms of dynamical systems, and an understanding of this definition makes it clear why it is incorrect to refer to turbulence as dissipative. One of the first formal definitions was given by Willems [39]. We will not give a thorough explanation of his formalism here due to it requiring a significant extension of the definitions in the previous section that goes beyond the scope of this work. However, it is straightforward to discuss it in a less formal way.

Willems considers a dynamical system that has a quantity  $Q$  that can be both “supplied” and “stored,” where the storage is by definition a nonnegative scalar, e.g., the total mass in a volume. Willems then defines a dissipative system as one in which

$$S(Q_0) + \int_{t_0}^t \dot{Q} \geq S(Q_t), \quad (2.45)$$

for all time  $t$ , where  $S$  is the storage function and  $\dot{Q}$  is the net rate of supply of  $Q$ , e.g., the net flow of mass across the boundary of a volume. In the case of strict equality, the system is said to be lossless, i.e., conservative. However, this definition results in frictionless and isentropic systems being defined as “dissipative,” which is non-intuitive for engineers and physicists, so we will use the term to refer only to those systems where strict equality does not hold for all  $t$ . Eckmann [40] uses a phase space definition, defining a dissipative system as one in which the phase space volumes (the measure of the set of all future possible states) contracts in time, eventually reaching a set of measure zero. This is not as general as Willems’ definition, since it does not include randomly forced systems; however, it is equivalent to Willems’ definition when strict inequality holds and forcing is either absent or deterministic.

A consequence of either definition is that Hamiltonian mechanics (which are a transformation of Lagrangian mechanics) are unable to describe dissipation, i.e., conservation laws are by definition not dissipative. See, e.g., Derks and van Groeson



[41] for a discussion of dissipation and Hamiltonian systems in the context of the Korteweg-de Vries equation. In the context of fluid dynamics, the Euler equations are a Hamiltonian system, as demonstrated by Olver [42], but the full NSEs are not, due to the presence of the viscous term. Therefore, the nonlinear mechanics leading to turbulence are non-dissipative.

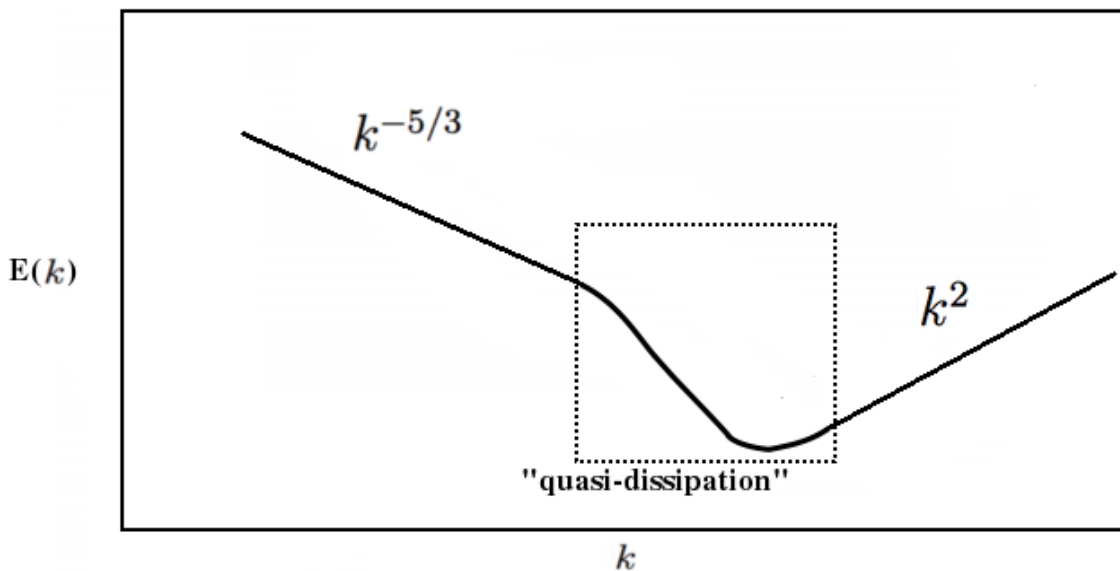
### 2.3.5 Dynamics of Euler turbulence

Although it receives somewhat less attention due to its nonphysical characteristics, the dynamics of so-called “inviscid turbulence” have been studied since at least the numerical experiments of Basdevant and Sadourney [43], who used very low-fidelity simulations of two-dimensional inviscid turbulence to evaluate the validity of the ergodic hypothesis, which states that two states  $\mathbf{q}(t_1)$ ,  $\mathbf{q}(t_2)$  in a turbulent flow eventually become uncorrelated in the limit  $(t_2 - t_1) \rightarrow \infty$ . More recent and more relevant numerical experiments are those of Bos and Bertoglio [44] and Cichowlas et al. [45], whose numerical experiments of three-dimensional spectrally truncated incompressible Euler turbulence showed that inviscid turbulence exhibits a transient inertial subrange with approximate  $k^{-5/3}$  scaling, thus confirming that the inertial subrange in turbulence is due to the conservative nonlinear terms and is largely independent of dissipation.

Even in the case of Euler turbulence, however, Cichowlas et al. refer to “effective dissipation” acting on the low wavenumbers. This is not true mathematical dissipation. Rather, what they are referring to is the fact the energy at some of the low- $k$  modes is eventually and permanently transferred to the higher modes, which maintain a statistical equilibrium, i.e., the phase space volumes cease decaying. Further, the energy is globally conserved, so this is not a dissipative system. Bos and Bertoglio are more careful, referring only to a “quasi-dissipative regime” that has some superficial spectral similarities to dissipation.

The experiments mentioned above have some important dynamics. Both use truncated spectral methods which are conservative in their formulation. In the statistically stationary limit, truncated inviscid turbulence actually exhibits  $k^2$  scaling, which is of course nothing like physical turbulence. But what Cichowlas et al. [43] observed was that when beginning with a single-mode initial condition, during the transient evolution of the flow to the statistically stationary state, the spectrum exhibits the regimes depicted in Fig. 2.1. The low- $k$  wavenumbers exhibit  $k^{-5/3}$  scaling, while  $k^2$  scaling occupied only the highest wavenumbers. Between these two regimes lies a buffer regime, termed “quasi-dissipative” by Bos and Bertoglio[44] due to its tendency to decay to the  $k^2$  region.

Figure 2.1: The three regimes of truncated inviscid turbulence on a log-log scale.



Eventually, the  $k^2$  behavior propagates to the lowest mode and occupies the entire spectrum. Moreover, the speed of this behavior’s evolution and its spectral range depends on the number of modes used in the simulation, as was shown on experiments with 256, 512, 1024, and 1600 modes by Cichowlas et al. [45], and further extended by Bos and Bertoglio [44], who used an EDQNM closure model to investigate as many as 32768 modes. If we denote  $k_Q(N, t)$  to be the boundary wavenumber between the

quasi-dissipative and  $k^2$  behaviors for an  $N$ -mode spectral truncation of the Euler equations, then  $k_Q(N, t)$  is a decreasing function of  $N$  and  $t$  based on numerical observations, i.e., the  $k^2$  behavior takes over the spectrum more quickly for lower-order truncations. Essentially, the high-frequency  $k^2$  regime acts like an energy sink primarily for the quasi-dissipative regime, although there is some absorption of energy from the  $k^{-5/3}$  regime as well.

The numerical experiments above have led us to the following hypotheses for incompressible turbulence, which are analogous to K41 theory with Galerkin truncations in place of viscosity:

- *H1.* For any fixed  $t$ ,  $\lim_{N \rightarrow \infty} k_Q(N, t) = \infty$ .
- *H2.* In the limit of infinite time, the system represented by the limiting case in *H1* exhibits a global energy spectrum,  $E(k) = \frac{K_0}{\zeta(5/3)} k^{-5/3}$ , where  $K_0$  is the energy of the initial condition integrated over the domain, and  $\zeta(s)$  is the Riemann zeta function.

This hypothesis is justified both by the fact that the limiting case is equivalent to the limiting case of K41 theory, and by the fact that a global  $k^2$  behavior is mathematically impossible due to the divergence of the series, and it therefore must be an artifact of truncation rather than the limiting case.

In light of the fact that the nonlinear dynamics of turbulence are conservative, *not* dissipative, these two hypotheses (and, by extension, K41 theory) are equivalent to claiming that in the  $k^{-5/3}$  energy spectrum, the transfer of energy from low- $k$  to high- $k$  wavenumbers, or “effective dissipation”, is in balance with the backscatter. The evolution of truncated Euler turbulence with a single-mode initial condition leads us to a description of turbulence as the sub-dissipation scale, “energy-starved” modes absorbing energy primarily from modes in the Taylor scale and above, while backscatter keeps the inertial subrange in a kind of “approximate equilibrium.” Moreover,

the behavior of all but the highest- $k$  modes in the inertial subrange is in the short term not significantly affected by the energy-starved modes.

In light of this spectral theory, the physical viscosity of the NSEs, which acts mainly high wave numbers, as can be seen by the Fourier expansion of Laplacian,  $\partial_{xx}u = -\sum_k k^2 \hat{u}_k \phi_k$ , “empties” the high- $k$  modes of energy, so that the energy supplied to them from lower modes is not balanced with an equilibrium-sustaining backscatter. But the dissipation itself is due entirely to the physical viscosity (and note that in the CNSEs, the energy equation contains additional dissipative terms). Thus, while it is tempting to look at the empirical fact that turbulence enhances dissipation, observe the fact that the RANS momentum equations differ structurally from the NSEs only due to the inclusion of the RST, and conclude that turbulence is an essentially dissipative mechanism, this is incorrect. The RST arises entirely due to applying Reynolds averaging to the nonlinear, conservative Euler terms, so it is incorrect to view these terms or the nonlinear mechanics of the NSEs in general as dissipative.

## 2.4 Shock-Turbulent Interaction

We have established in Section 2.2.1 that compressibility affects the dynamics of turbulence. In particular, the presence of a dilatational mode that is absent in incompressible flow shows this. The Kovasznay decomposition shows analytically that compressibility effects not only exist, but interact with the “incompressible” (i.e. solenoidal) dynamics. Thus we expect shock waves to have a significant effect on the dynamics of turbulence. From a physical standpoint, shock waves increase the entropy of the flow and thus ought to contribute to turbulent dissipation. They also compress turbulent eddy structures in the direction normal to the shock and stretch them in the direction parallel to the shock. To understand this phenomenon, recall that a shock wave reduces only the normal component of the velocity of an

incoming flow, while leaving the tangential components unchanged. The effect of this is that shock waves induce anisotropy in the turbulence behind the shock, even if the incoming turbulence field is isotropic, as confirmed in experiments by Hesselink and Sturtevant [46]. This has significant consequences for turbulence modeling, as it means any compressible turbulence model relying on a local isotropy assumption will necessarily break down in the presence of shock waves.

Linear interaction analysis (LIA) of the Kovasznay decomposition of compressible turbulence provides more theoretical insight into the phenomenon of shock-induced distortions in the turbulent field. Depending on the Mach number and angle of incidence, an incoming wave can be refracted, phase shifted, and generate new waves behind the shock. For example, when an entropy wave with wavenumber  $\mathbf{k}$  is refracted through a shock wave by some angle  $\alpha$ , it generates a vorticity wave propagating at  $\alpha_v < \alpha$  at wavenumber  $\mathbf{k}$ , combined with a pressure wave, also propagating at  $\alpha_v$ , but with a different wavenumber  $\mathbf{k}_p$  [19], which then propagate downstream of the shock. While a more general analysis can be found in Fabre et al. [47], it suffices for our purposes to observe from this that the composition, orientation, and spectral characteristics of incoming turbulence will significantly affect the characteristics of the turbulence field behind the shock wave. The linear interaction analysis by Jamme et al. [48] of DNS results for shock-turbulence interaction at  $M = 1.5$  showed that the shock wave tended to amplify both streamwise and transverse turbulent stress components  $\widetilde{u_i'^2}$  of incoming pure vorticity and vorticity/entropy modal waves, while it tended to attenuate the turbulent stress for pure entropy waves. Thus in the presence of shock waves, both experimental and theoretical considerations negate the local isotropy hypothesis.

An important phenomenon of shock-turbulence interaction is the eddy shocklet. Shocklets occur over a wide range of supersonic Mach numbers and are generally associated with coherent eddies that have relatively large spatial and coherent scales.

Eddy shocklets have been observed experimentally, for example, in the compressible shear layer experiments of Papamoschou [49]. DNS studies by Lee et al. [50] found that eddy shocklets have the characteristics of a usual shock wave. In this study, the shocklets were found to have a very large local effect on turbulent dissipation rate, several orders of magnitude larger than the dissipation due to turbulent stress. However, because shocks are matched by expansions in such a flow, they have a net  $\mathcal{O}(10\%)$  effect on the global turbulent dissipation rate of the flow. In general, strong local effects can have effects on phenomena such as boundary layer development, flow separation, and other flow characteristics critical to the macroscopic quantities important for engineering flows.

Shock corrugation refers to the distortion of the shock front caused by interaction with the irregular, turbulent flow field. Lee et al. [50] used both linear perturbation analysis and DNS to demonstrate that the shock wave interacts with the Taylor microscales of the flow, significantly reducing them as the flow passed through the shock. The DNS experiments of Grube et al. [51] showed that the smallest length scales associated with the shock corrugation correspond with the microscales of the turbulent flow, and that the distortion of the shock wave has a significant effect on the location and behavior of the shock-turbulence interaction. Thus to accurately capture shock-turbulence interaction, DNS-like grid resolution near the shock wave is necessary. Garnier et al. [7] identify three levels of grid resolution near the shock:

1. The microscopic level resolves all length scales of the corrugated shock and corresponds to DNS resolution.
2. The mesoscopic level resolves some features of the corrugated shock and the near field downstream of the shock.
3. The macroscopic level does not resolve any of the shock corrugation.

Both the mesoscopic and macroscopic levels under-resolve the shock-turbulence inter-

action and therefore require turbulence models. The investigation of Bermejo-Moreno et al. [52], where several subgrid scale interaction models were compared against DNS and LES without a model, found that in the absence of an explicit turbulence model, LES greatly over-predicts the Reynolds stresses and kinetic energy downstream of the shock. Introducing a turbulence model, such as the eddy viscosity of Vreman et al. [53], improved the correspondence of LES and DNS results. However, the numerical method used in that work discretized a form of the filtered equations that is prone to aliasing. As we will see in Sec. 3.2.3 there is an aliasing problem associated with the standard LES formulation that many researchers do not directly engage; this aliasing error is very likely the source of the phenomena that are typically mitigated by dissipative turbulence models.

Furthermore, there are additional physics governing the interaction of shocks and turbulence that are currently not well-understood. Because physical shock waves do not obey continuum mechanics within the shock, any effects that this breakdown might have on turbulence cannot be captured in an NSE-based simulation, regardless of the mesh resolution. Furthermore, Donzis [35] has argued that the ratio of the shock thickness to Kolmogorov dissipation scale is a key parameter in the behavior of shock-turbulent interactions and accounts for the differences between predictions and experiments. Because the NSEs alone cannot capture the shock thickness accurately [36], this leads to the expectation that some intrinsic deviations between simulation and experiment will always arise in purely NSE-based simulations, especially at high Mach number and temperature.

## 2.5 Conclusions on the nature of turbulence

In this chapter, we have developed the theory of compressible turbulence with a view toward the construction of turbulence models. Any researcher in this field requires a solid theoretical foundation, but simply being acquainted with the wealth

of mathematical tools is not enough. The construction of a turbulence model requires a judgment about just what exactly the nature of turbulence is. Whether or not this judgment is made explicitly, it must be made, and when it is explicit, it can be critiqued and the premises of a model reexamined. For example, in the view of Prandtl and Boussinesq, turbulence consisted of discrete eddies randomly mixing with each other. This led to mixing-length models which have been almost wholly discarded as this view of turbulence has been discarded.

The view of turbulence taken in this work is strictly mathematical. That is, we view turbulence as a phenomenon completely described and contained within the Navier–Stokes equations themselves. The numerical simulation of turbulent flows under the continuum hypothesis, then, is a matter of numerically solving the NSEs. Although the mathematical community has yet to provide the theorems necessary to definitively establish this view, it is partially validated by the many successes of DNS in both incompressible and compressible turbulence. Of course, turbulent phenomena can and do happen in contexts where the NSEs no longer hold, but we are limiting the investigations of this work to contexts where we can reasonably assume the governing assumptions of the NSEs hold everywhere outside the internal structure of shocks. This view is further validated by the fact that some of the most productive tools in the investigation of the nature of turbulence have been the same tools that mathematicians use to study, derive, and characterize solutions of general partial differential equations of various classes and types.

To state succinctly the theory of turbulence on which this work relies, a turbulent flow is the evolution in time of the Navier–Stokes equations as a chaotic dynamical system, driven by the conservative, nonlinear interactions of the entire spectrum, and controlled by the dissipative, linear terms in the energy and momentum equations. This rather abstract definition, which eschews any language of physical phenomena, is deliberate; by the time we have gotten to the point of writing a CFD code, the



question of how to construct governing equations out of the physical system has already been answered, hopefully correctly. As we will see in the following chapter, the need for turbulence modeling arises not due to the NSEs, but the difficulty in computing numerical solutions of them in a computationally feasible way. Therefore, the model in this work will be based on this mathematical concept rather than the more physical concepts of turbulent eddies, vortical structures, and the like.

### Chapter 3. Computational Simulation of Turbulent Flows

Since the inception of the discipline of computational fluid dynamics, turbulence has posed a fundamental obstacle to obtaining reliable, accurate solutions of computational flow problems. In this chapter, we will outline the fundamental issues associated with attempting to compute solutions of the NSEs for flows of engineering interest, the common techniques associated with solving them, and the issues associated with those techniques.

In Sec. 3.1, the mathematical issues associated with numerically solving the NSEs are presented, including the coupling different length scales and the aliasing problem, both of which are associated with nonlinearities. The instabilities induced by aliasing require the use of some kind of artificial dissipation. Traditionally, because turbulence has been viewed as a mechanism of dissipation (whether in a statistical sense or otherwise), dissipation has been introduced into the computations by adding an artificial viscosity term, which derived from quantities resolved by the numerical method, to the equations themselves. This dissipative term is then supposed to emulate the mechanisms of turbulence. However, this is hardly the only approach to turbulence modeling. In general, a turbulence model is any means of attempting to simulating the effects of fluctuations that are not directly computed by solving the NSEs. As we will see below, there are two main classes of turbulence models: Reynolds averaged Navier–Stokes (RANS), discussed in Sec. 3.2.1, and large-eddy simulation (LES) models, discussed in Sec. 3.2.2. In these sections, we will present an overview of both RANS and LES modeling and the strengths and shortcomings associated with popular modeling strategies. The LES section in particular is a detailed, thorough discussion of current technique, and a criticism of existing methods in the context of aliasing. Finally, we will summarize our findings and their implications for turbulence

in Sec. 3.3.

### 3.1 Mathematical issues in CFD

In general, directly solving a system of PDEs using a finite difference (FD), finite volume (FV) or finite element method requires resolving the computational mesh down to the smallest scales necessary to resolve all solution phenomena. For steady-state, laminar flow, such direct numerical simulation (DNS) is already frequently done using modern computers, as the characteristic structures of the flow are relatively large. However, for turbulent flow, the computational grid must be resolved down into the Kolmogorov dissipation scale. Thus, if a computational grid is to be resolved down to the dissipation scale for compressible turbulence, based on the Kolmogorov scaling, it will require  $\mathcal{O}(Re^{9/4})$  grid points. Moreover because the time step is generally proportional to  $Re^{-3/4}$ , the total arithmetic necessary to solve the equations over a fixed length of time grows like  $\mathcal{O}(Re^3)$ . This makes DNS of all but very simple turbulent flows infeasible on current computers, and thus useless for engineering applications for the foreseeable future.

#### 3.1.1 Nonlinearity

The fundamental problem posed by turbulent CFD can be seen by looking at a Galerkin expansion of the incompressible momentum equations, Eq. (2.8b). Suppose our domain of interest  $\Omega$  is the cube,  $[-\pi, \pi]^3$ , and we have periodic boundary conditions. Then the set of complex exponential functions  $\{\phi_{\mathbf{k}}(\mathbf{x}) = e^{i\mathbf{k}\cdot\mathbf{x}}\}$ , where  $\mathbf{k} \in \mathbb{Z}^3$ , is an orthonormal basis for the Hilbert space  $L^2$  on the cube. Consider the scaled, incompressible momentum equation

$$\partial_t u_i + u_j \partial_j u_i = -\partial_i p + \frac{1}{Re} \partial_{jj} u_i. \quad (3.1)$$

Now, applying the techniques discussed in Sec. 2.2.3, we have the Galerkin system,

$$\frac{d}{dt}\hat{u}_{i,\mathbf{k}} + \sum_{\mathbf{m}} ik_j \hat{u}_{j,\mathbf{m}} \hat{u}_{i,\mathbf{k}-\mathbf{m}} = ik_i \hat{p}_{\mathbf{k}} - \frac{1}{Re} k_j k_j \hat{u}_{i,\mathbf{k}}, \quad \mathbf{k} \in \mathbb{Z}^3. \quad (3.2)$$

Contrast this with a Galerkin expansion of the heat equation on the same domain,  $\partial_t u = \kappa \partial_{jj} u$ , given by

$$\frac{d}{dt}\hat{u}_k = -\kappa k_j k_j \hat{u}_k. \quad (3.3)$$

From Eq. (3.2), we can see that the behavior of the Fourier coefficients of the NSEs is coupled across the various modes due to the nonlinear terms, while the behavior of each mode in the linear heat equation is independent of any other mode. Moreover, this coupling extends across the entire basis set, so we cannot *a priori* discard any wavenumbers when constructing a solution or attempting to characterize its behavior. In other words, the high-frequency phenomena affect the low-frequency phenomena and vice-versa; there is an explicit coupling among all length scales of turbulent behavior. Domaradzki et al. showed that for a given wavenumber,  $k$ , almost all the energy transfer occurs over the range  $[0.5k, 2k]$  [54]. K41 theory says that eventually, the viscous term will overwhelm the nonlinear terms and render the energy negligible beyond some point in the spectrum. For accurate DNS, then, all wavenumbers corresponding to wavelengths longer than the beginning of the Kolmogorov dissipation scale must be resolved.

### 3.1.2 Aliasing

Aliasing is a fundamental issue in discrete solutions of the Navier–Stokes equations. The problems associated with it arise entirely due to the nonlinear interactions and are therefore not an issue in the solutions of linear PDEs. One of the most comprehensive treatments of aliasing applied to numerically solving the NSEs was presented in the context of spectral methods employing discrete Fourier coefficients by Canuto et al. [55], but their work can be easily generalized to other discrete methods. Following

their discussion, we consider an  $L^2$  function  $u$  defined on  $[0, 2\pi]$  and discretized into  $N$  evenly spaced nodes,

$$x_j = \frac{2\pi j}{N}, \quad j = 0, \dots, N-1. \quad (3.4)$$

The DFT of a discrete signal  $\{u(x_j)\}_{j=0}^N$  is given by

$$\tilde{u}_k = \frac{1}{N} \sum_{j=0}^{N-1} u(x_j) e^{ikx_j}. \quad (3.5)$$

The  $N/2$ -degree trigonometric interpolant of  $u$ , also known as the discrete Fourier series of  $u$ , is then defined by

$$I_N u(x) = \sum_{k=-N/2}^{N/2-1} \tilde{u}_k e^{ikx}. \quad (3.6)$$

Note that  $I_N u(x_j) = u(x_j)$ . There is an exact relationship between the DFT and the Fourier coefficients of  $u$ ,

$$\tilde{u}_k = \hat{u}_k + \sum_{\substack{m=-\infty \\ m \neq 0}}^{\infty} \hat{u}_{k+Nm}, \quad -N/2 \leq k \leq N/2 - 1. \quad (3.7)$$

Because of this relationship, the class of modes with wavenumbers  $k + Nm$  are considered to be aliased with mode  $k$  on a grid with  $N$  points. The  $k^{\text{th}}$  discrete Fourier coefficient of  $u(x_j)$  thus depends on all the Fourier coefficients of  $u$  whose modes alias with mode  $k$ . This leads naturally to the definition of aliasing error,  $R_N u(x)$ , which is defined as the difference between the discrete Fourier series and the truncated continuous Fourier series,

$$\begin{aligned} R_N u(x) &= I_N u(x) - P_N u(x) \\ &= \sum_{k=-N/2}^{N/2-1} (\tilde{u}_k - \hat{u}_k) \phi_k \\ &= \sum_{k=-N/2}^{N/2-1} \left( \sum_{\substack{m=-\infty \\ m \neq 0}}^{\infty} \hat{u}_{k+Nm} \right) \phi_k. \end{aligned} \quad (3.8)$$

This definition of aliasing can be easily extended to any discretized form of polynomial interpolation with orthogonal basis functions. While applying this same analysis to the finite volume (FV) discretization of the NSEs on an arbitrary structured grid is not feasible in general, it is easy to see that FV methods are themselves equivalent to discretized polynomial interpolation and therefore can be expressed as a continuous truncation (such as a truncated Fourier series) plus an aliasing error term. While we cannot assume this aliasing error will in general be orthogonal to the continuous truncation error, it is still a useful concept because aliased spectral methods applied to the NSEs display non-physical oscillations and numerical instabilities at large Reynolds number [56], much like what is seen in any FV method. The important conclusion from this is that unresolved scales can cause errors in resolved scales.

Aliasing is a particular issue in solutions of the Navier–Stokes equations due to the nonlinear terms. Consider  $u^2$  on the aforementioned grid. We have

$$\widehat{u^2}_k = \sum_{l=-\infty}^{\infty} \widehat{u}_l \widehat{u}_{(k-l)}. \quad (3.9)$$

Then the aliasing error associated with this nonlinear term is

$$\begin{aligned} R_N u^2(x) &= \sum_{k=-N/2}^{N/2-1} \left( \sum_{\substack{n=-\infty \\ n \neq 0}}^{\infty} \widehat{u^2}_{k+Nn} \right) \phi_k \\ &= \sum_{k=-N/2}^{N/2-1} \left( \sum_{\substack{n=-\infty \\ n \neq 0}}^{\infty} \sum_{l=-\infty}^{\infty} \widehat{u}_l \widehat{u}_{(k+Nn-l)} \right) \phi_k. \end{aligned} \quad (3.10)$$

What is critical to note here is that while the aliasing in Eq. (3.8) is generated exclusively by modes that are both unresolved and alias with the resolved modes, *all* modes contribute to the aliasing error on Eq. (3.10). This issue can be illustrated in a different way by looking at the discrete Fourier series:

$$(I_N u(x))^2 = \sum_{k=-N}^{N-2} \left( \sum_{l=-N/2}^{N/2-1} \widetilde{u}_l \widetilde{u}_{(k-l)} \right) e^{ikx}. \quad (3.11)$$

Here we see that the square of the discrete Fourier series, which corresponds to the numerical solution method, contains unresolved modes itself. These modes will then alias with the resolved modes in the construction of  $u^2$ , requiring special treatment. Intuitively, nonlinear PDEs should experience some kind of compounding error problem not exhibited by linear PDEs.

In a more thorough analysis of the aliasing errors arising from the incompressible NSEs, Canuto et al. [56] identify the presence of “parasitic modes” apparent in Eq. (3.11) due to aliasing that negatively affect the accuracy of the solution and are amplified as the solution evolves. Ultimately, these modes must be eliminated by filtering, whether by an explicit numerical filter or implicitly via the numerical method itself. While the details of the derivation are obviously not directly applicable to finite-volume methods for the compressible NSEs, the fundamental observation that aliasing due to unresolved modes is compounded and propagated by the nonlinear terms, thus requiring artificial dissipation, is generally applicable to all numerical solution methods.

The infeasibility of DNS for turbulent flows on engineering scales has led to a variety of attempts to compute desired quantities via other techniques. In the first section, we will give a technical definition of aliasing error and the instabilities it induces. We will return to the concepts in this section repeatedly throughout the course of this work, as it is essential to understanding the challenges and pitfalls of CFD, so it must be read carefully.

## **3.2 Turbulence modeling**

The following discussion of the various methods and techniques of turbulence modeling is somewhat lengthy, but it is necessary. The modeling approach presented in this work is a significant departure from previous methods, and the full rationale behind it requires a complete discussion and critique of the existing state of the art. Because

there are so many different approaches to turbulence modeling, it is not trivial to state a universally applicable definition of the problem turbulence modeling is supposed to solve, and thus it is easy to neglect it. On a similar note, certain assumptions have become so universal that they are often not stated explicitly or formally justified, but given the lack of any universal turbulence model, re-examination of those assumptions remains appropriate. In science, when the predictions of models do not match the data, the theories behind those models must be continually scrutinized.

### 3.2.1 RANS modeling

RANS modeling attempts to predict only time-averaged flow quantities by solving the RANS equations and thus does not require resolution of any of the turbulent flow structures at all. But as discussed in Section 2.2.2, the RANS equations are unclosed and thus do not admit solutions. Thus the RST and all other quantities containing fluctuating components must be modeled. Applying a Fourier expansion to the fluctuating component of the Reynolds decomposition shows that the turbulence model must capture the entire spectrum of unsteady behavior:

$$f'(\mathbf{x}, t) = f(\mathbf{x}, t) - \bar{f}(\mathbf{x}) = \sum_{\mathbf{k} \in \mathbb{N}^3} (\hat{f}_{j,\mathbf{k}}(t) - \hat{f}) \phi_{\mathbf{k}}(\mathbf{x}),$$

with a similar relationship holding for the Favre decomposition. In other words, a RANS model must capture the effects of fluctuations on every scale from the integral scale down to the dissipation scale; it is thus inappropriate to refer to a RANS model as a “subgrid scale model.” The additional covariance tensors and correlations make RANS modeling for compressible flows significantly more complex than for incompressible flows. For the purposes of explanation and critique, then, we restrict our discussion to the RANS equations for incompressible flows, which are given by

$$\partial_j \bar{u}_j = 0, \tag{3.12a}$$

$$\partial_j (\bar{u}_j \bar{u}_i) = -\partial_i \bar{p} + \mu \partial_j \partial_j \bar{u}_i + \partial_j \overline{u'_i u'_j}. \tag{3.12b}$$



Here, only the incompressible RST,  $\overline{u'_i u'_j}$ , must be modeled. However, the fact that the incompressible RANS equations have fewer degrees of freedom than the compressible case does not make the closure problem any more tractable. In both cases, the equations must be closed via turbulence models, all of which rely to one degree or another on further heuristic assumptions and empirical constants.

The RST is generally simplified by means of the Boussinesq hypothesis [8]. He thus proposed that the RST is proportional to the deviatoric stress tensor, leading to the relation:

$$\overline{u'_i u'_j} = 2\mu_{T,ij} \left( \overline{S}_{ij} - \frac{\delta_{ij}}{3} \overline{S}_{kk} \right), \quad (3.13)$$

where  $\mu_{T,ij}$  is called the *eddy viscosity*, and  $S_{kk} = 0$  for incompressible flows. However, note in this original formulation,  $\mu_{T,ij}$  is a tensor, which makes it rather complex to estimate, even assuming such an estimate can be found. To simplify this, Prandtl drew on the kinetic theory of gases, which had recently been applied with much success to molecular viscosity, substituting turbulent eddies for gas molecules and a mixing length for mean free path, and thus proposed a scalar eddy viscosity,  $\mu_T$ . An immediate weakness apparent in this approach is that unlike molecules and mean free paths, neither eddies nor mixing lengths are well-defined in a turbulent flow.

The Boussinesq hypothesis is the foundation of nearly all RANS and LES turbulence models used in commercial applications, including the RANS  $k-\epsilon$ ,  $k-\omega$ , and Spalart–Allmaras (SA) [57] turbulence models, and variants of the LES Smagorinsky–Lilly model [1] [58]. A notable exception is the Reynolds stress model (RSM), which is a second-order closure model that uses transport equations to solve for the RST directly. However, the RSM creates new terms that also must be closed, and some implementations use an eddy viscosity to close the higher-order terms, such as that of Lien and Leschziner [59].

Most RANS models assume local isotropy, i.e.,  $\mu_T$  is approximately scalar. But as we saw in Section 2.4, we can expect turbulent flows with shock waves to be highly

anisotropic behind the shock. Not only that, but the linear perturbation analysis that originally led to this expectation is independent of length scale, suggesting that isotropy will not even hold in a local sense. Further, while homogeneous, isotropic turbulence is an important tool in the development of turbulence theory, flows of engineering interest usually include boundary layers, wakes, and other shear mechanisms, which produce anisotropic turbulence. In fact, anisotropy is critical to the study of boundary layers. The effects of roughness on boundary layer anisotropy have been studied by Shafi and Antonia [60], where they found that increased roughness tends to decrease anisotropy; and the effects of suction on anisotropy have been studied by Djenidi et al. [61], where they found that suction alters the structure of the boundary layer anisotropy. Antonia and Djenidi then joined with Spalart to do a fairly detailed DNS study of the anisotropy structure of a turbulent boundary layer with a view toward constructing more effective RANS models [62].

While the Boussinesq hypothesis seems reasonable from the aforementioned physical analogy to the kinetic theory of gases, it must be understood that while the kinetic theory of gases starts with the random motion of gas molecules, turbulent flow is a deterministic phenomenon. Further, an eddy is not a discrete, well-defined, physical object; it is a subjectively defined temporary structure in the velocity field and is thus not amenable to a kinetic theory of its own. On a closer look, then, the physical rationale of the Boussinesq hypothesis is not self-evident. A mathematical analysis shows that nonlinear interactions of fluctuating terms and dissipative terms are unlike.

Consider the Boussinesq hypothesis applied to cross-strain terms  $i \neq j$ . In the case of isotropic, homogeneous turbulence, the eddy viscosity will be constant, so we have

$$\partial_j \overline{u'_i u'_j} = \mu_T \partial_j (\partial_j \bar{u}_i + \partial_i \bar{u}_j). \quad (3.14)$$

We proceed by applying Fourier expansion to both sides. For the left-hand side of

Eq. (3.14) we have:

$$\begin{aligned}
\partial_j \overline{u'_i u'_j} &= \partial_j (\overline{\hat{u}_{i,\mathbf{k}} \hat{u}_{j,\ell}} - \overline{\hat{u}_{i,\mathbf{k}} \hat{u}_{j,\ell}}) \phi_{\mathbf{k}} \phi_{\ell} \\
&= \partial_j (\overline{\hat{u}_{i,\mathbf{k}} \hat{u}_{j,\ell}} - \overline{\hat{u}_{i,\mathbf{k}} \hat{u}_{j,\ell}}) \phi_{\mathbf{k}+\ell}, \\
&= i(k_j + \ell_j) (\overline{\hat{u}_{i,\mathbf{k}} \hat{u}_{j,\ell}} - \overline{\hat{u}_{i,\mathbf{k}} \hat{u}_{j,\ell}}) \phi_{\mathbf{k}+\ell},
\end{aligned}$$

where summation is over  $j$ ,  $\mathbf{k}$  and  $\ell$ .

Applying the same process to the right-hand side of Eq. (3.14), we have

$$\begin{aligned}
\mu_T \partial_j (\partial_i \bar{u}_j + \partial_j \bar{u}_i) &= \hat{\mu}_T \partial_j (\partial_i \bar{\hat{u}}_{j,\mathbf{k}} \phi_{\mathbf{k}} + \partial_j \bar{\hat{u}}_{i,\mathbf{k}} \phi_{\mathbf{k}}) \\
&= -\hat{\mu}_T (k_i k_j \bar{\hat{u}}_{j,\mathbf{k}} + k_j k_i \bar{\hat{u}}_{i,\mathbf{k}}) \phi_{\mathbf{k}},
\end{aligned}$$

where, as before, summation is over  $j$  and  $\mathbf{k}$ . Thus the Boussinesq hypothesis is equivalent to claiming that

$$i(k_j + \ell_j) (\overline{\hat{u}_{i,\mathbf{k}} \hat{u}_{j,\ell}} - \overline{\hat{u}_{i,\mathbf{k}} \hat{u}_{j,\ell}}) \phi_{\mathbf{k}+\ell} = -\mu_T (k_i k_j \bar{\hat{u}}_{j,\mathbf{k}} + k_j k_i \bar{\hat{u}}_{i,\mathbf{k}}) \phi_{\mathbf{k}} \quad (3.15)$$

However, it is clear from this expression that the left-hand side contains interactions of different wavenumbers, while the right-hand side does not. The effect of differentiation is quite different as well. On the left-hand side, we have the imaginary value  $i(k_j + \ell_j)$ , while on the right-hand side, we have the negative real values  $-k_i k_j$  and  $-k_j k_i$ . The right-hand side is thus clearly dissipative, but no such conclusion is apparent for the left-hand side. Moreover, Galerkin truncation of this system provides

$$\frac{i \left( \overline{\hat{u}_{i,\ell} \hat{u}_{j,\mathbf{k}-\ell}} - \overline{\hat{u}_{i,\ell} \hat{u}_{j,\mathbf{k}-\ell}} \right)}{(k_i \bar{\hat{u}}_{j,\mathbf{k}} + k_j \bar{\hat{u}}_{i,\mathbf{k}})} = -\mu_T \quad \forall \mathbf{k} \in \mathbb{Z}^3, \quad (3.16)$$

which reduces the hypothesis to a claim that there is a constant relationship between any pair of mean Fourier coefficients and sub-series of nonlinear interactions across the entire spectrum. In this simplified case, then, we can see that there is substantial mathematical rationale to expect the Boussinesq hypothesis to not hold.

While the above analysis suggests that the Boussinesq hypothesis will not, in general, be exactly satisfied for global turbulence, it may validly be argued that it

is only a model, and therefore needs only to be satisfied approximately to within the needs of engineering applications. In fact, RANS turbulence models based on the Boussinesq hypothesis have been employed successfully to predict meaningful quantities to within engineering tolerances, such as the pressure distributions at low angles of attack in Mittal's numerical results for a NACA airfoil [63]. Based on the success of this kind of modeling in certain types of flows, it is then not unreasonable to think that it might be successfully applied to all turbulent flows, as long as the right kinds of models can be found, or if perhaps the right parameters for existing models can be found. But as early as 1976, Kraichnan [64] advanced a detailed theoretical argument for the inability of a scalar eddy viscosity to correctly capture the energy transfer between large and small scales, and his 1987 work suggests further difficulties with this basic approach. The analysis of Schmitt [8] answers the question of approximate satisfaction by using DNS, experimental, and LES data. Drawing from the basic linear constitutive equation,

$$\mathbf{R} = -2\mu_T \mathbf{S}, \quad (3.17)$$

where  $\mathbf{R}$  is the RST and  $\mathbf{S}$  is the deviatoric stress tensor, he applies a tensor product  $\rho_{RS}$ , defined by

$$\rho_{RS} = \frac{|\mathbf{R} : \mathbf{S}|}{\|\mathbf{R}\| \|\mathbf{S}\|}, \quad (3.18)$$

where  $\mathbf{A} : \mathbf{B} = \text{tr}(\mathbf{AB}) = A_{ij}B_{ij}$  is the Frobenius inner product, and  $\|\cdot\|$  is the Frobenius norm. The Frobenius inner product is simply the usual vector dot product when  $\mathbf{A}$  and  $\mathbf{B}$  are vectors, and the quantity  $\rho_{RS}$  reduces to the cosine of the angle between them in this case. Further, it has the property

$$\rho_{RS}(\mathbf{A}, \mathbf{B}) = 1 \text{ iff } \mathbf{A} = a\mathbf{B} \text{ for some } a \in \mathbb{R}.$$

Thus the Boussinesq hypothesis can be exactly satisfied for a given turbulent flow field if and only if  $\rho_{RS} = 1$  everywhere. However, this function allows a tolerance

to be set for where the Boussinesq hypothesis is approximately satisfied; Schmitt chose the value  $\rho_{RS} = \cos(\pi/4) \approx 0.71$  as the cutoff. In the case of DNS data for an annular pipe flow, Schmitt found that the Boussinesq hypothesis is valid near the wall, but in the main flow,  $\rho_{RS} < 0.7$ . Only a small region in LES data for flow past a square cylinder, and likewise for experimental data for a double annular jet, were found to approximately satisfy the Boussinesq hypothesis. Therefore, not only do current eddy viscosity models fail in these regions of the flow, but Schmitt [8] has shown experimentally that no such models can be found for many flows of interest.

There are many more variations on RANS modeling, which we will not discuss in depth here. One particular example is unsteady RANS (URANS), which is the application of traditional RANS models to unsteady flows. The justification of this technique is often weak. For a typical example, Iaccarino et al. [65] make an off-hand appeal to ensemble averaging, but do not produce any analysis to further justify this approach. Johansen et al. [66] appeal to a filter with a spectral cutoff, but this is indistinguishable from LES. The theoretical and experimental weaknesses of RANS modeling are why we are pursuing more effective LES in this work. Further, the criticisms of the Boussinesq hypothesis are valid in any context, and they are why the turbulence model presented in this work does not rely on an eddy viscosity of any kind.

### 3.2.2 Large eddy simulation

Large eddy simulation (LES) is a simulation method designed to directly compute the unsteady phenomena resolved by the grid, while modeling the subgrid-scale (SGS) effects. Due to the nonlinear effects of aliasing, a dissipative filter to attenuate high-wavenumber content is necessary for stable solution of the NSEs on a coarse mesh. Nearly all LES methods used today use some kind of spatial dissipation. Further, finite volume and finite difference methods rely on Taylor series approximations, which

may not be accurate on a coarse mesh. Recall that the second-order finite difference expansion of  $\partial_x u$  is

$$\frac{u(x+h) - u(x-h)}{2h} = \partial_x u + h^2 \partial_x^3(\xi), \quad (3.19)$$

where  $\xi \in [x-h, x+h]$ . Typically the error term is written  $\mathcal{O}(h^2)$  and assumed to be small, but this is only the case when high-order derivatives are small. But for turbulent solutions of the NSEs, this may not be the case. Further, because so little is known about turbulent solutions to the NSEs, we do not even know if high-order derivatives exist, let alone whether the Taylor series converges everywhere or has a sufficiently large radius of convergence for finite difference approximations to be valid. A properly constructed filter can eliminate these issues.

To filter the variables, a filter kernel  $G_\Delta(\mathbf{x}, t)$  is chosen along with associated filter width,  $\Delta$ , where  $\Delta$  is assumed to be smaller than the solution domain. Typically,  $G_\Delta$  is a  $C^\infty$  function with compact support on  $\mathcal{B}_\Delta(\mathbf{x})$ , the ball of radius  $\Delta$  centered about  $\mathbf{x}$ . The filtered variable is then defined by

$$\bar{f}_\Delta = G_\Delta * f = \int_{\mathcal{B}_\Delta(\mathbf{x})} f(\boldsymbol{\xi}, t) G_\Delta(\mathbf{x} - \boldsymbol{\xi}, t) d\boldsymbol{\xi}, \quad (3.20)$$

$$f'_\Delta = f - \bar{f}_\Delta, \quad (3.21)$$

and spatial Favre filtering is defined in a natural way;

$$\tilde{f}_\Delta = \frac{\bar{\rho} f_\Delta}{\bar{\rho}_\Delta}, \quad (3.22)$$

$$f''_\Delta = f - \tilde{f}(\mathbf{x})_\Delta. \quad (3.23)$$

If  $\hat{G}_k = 0$  for  $k > k_{max}$ , where  $k_{max}$  is the largest wavenumber that can be resolved accurately on the mesh (on a uniform mesh with spacing  $h$ , this is the Nyquist wavenumber,  $k_N = \pi/h$ ), and  $\Delta$  is sufficiently large, both  $\bar{f}$  and  $\tilde{f}$  will have convergent Taylor series on the computational mesh and not have any of the high frequency content that causes aliasing. In engineering CFD,  $\Delta$  is typically not constant and

is instead a function of the local mesh resolution. However, note that solvers for structured meshes typically transform the equations into generalized coordinates in which the mesh is uniform. Details of this transformation are given in Section 5. For this section, it suffices to point out that the NSEs in generalized coordinates have the same structural nonlinearities and numerical issues as the NSEs in rectangular coordinates, the analysis we do here is generally applicable.

Traditional LES methods use a filtered set of equations derived by applying the LES and Favre decompositions, filtering the governing equations, and following a similar procedure used to derive the RANS equations. However, because the filter kernel has compact support, no differential terms are eliminated. One form of the LES equations is given by Gatski as [67]

$$\partial_t \bar{\rho} + \partial_j (\bar{\rho} \tilde{u}_j) = 0, \quad (3.24a)$$

$$\partial_t (\bar{\rho} \tilde{u}_i) + \partial_j (\bar{\rho} \tilde{u}_j \tilde{u}_i) = -\partial_i \bar{p} + (\tilde{\mu} + \tilde{\mu}_v) \partial_i \partial_j \tilde{u}_j + \tilde{\mu} \partial_j \partial_j \tilde{u}_i + \partial_j \bar{\rho} \widetilde{u_i'' u_j''}, \quad (3.24b)$$

$$\partial_t (\bar{\rho} \tilde{e}) + \partial_j (\bar{\rho} \tilde{u}_j \tilde{h}) = \overline{u_j \partial_j p} + \overline{\sigma_{ij} S_{ji}} - \partial_j \bar{\rho} c_p \widetilde{u_j'' T''}, \quad (3.24c)$$

where the  $\Delta$  subscript is suppressed. Observe that, due to some of the simplifications, this form of the LES equations is identical to the RANS equations in Eqs. (2.20a)–(2.20c) with the addition of time derivative terms. Because of this, the LES equations have the same closure issues that the RANS equations do, and, like in RANS modeling, researchers into new LES techniques typically employ the Boussinesq hypothesis in order to achieve closure. But unlike RANS methods,  $u''$  is truly a SGS quantity, so a LES model need not capture the entire spectrum. Though we will not provide details of these models here, the Smagorinsky [1], dynamic [68], and WALE [69] turbulence models are common eddy viscosity models used in engineering applications and most commonly included in commercial CFD packages. Thus, the criticisms in Section 3.2.1 apply to traditional LES modeling as well. In addition, a recurring problem in eddy viscosity methods is excessive dissipation. For example,

in transitional flows, they tend to damp out unstable modes and prevent them from developing into turbulence.

### 3.2.3 Implicit and explicit filtering

Despite the use of spatial filtering to derive the LES equations, no such filter is typically used in numerical solution procedures. Instead, the usual approach is to present the LES equations along with equations for the SGS model, simply discretize this system, and assume that the nodal variables represent filtered quantities. For example, while the dynamic model of Germano et al. [68] uses an explicit spatial filter to compute parameters for the SGS model, it does not actually low-pass filter the flow variables. Arguably, omitting an explicit filtering in the solution procedure is equivalent to assuming that the finite mesh support and low-pass characteristics of the discrete differencing operators act as a filter.

The assumption that discretization acts as a filter is explicitly stated in implicit LES (ILES). ILES methods employ neither explicit turbulence modeling nor explicit filtering. Rather, dissipation is introduced into the simulation via the discretization of the equations, and it is argued that this numerical dissipation acts as both filter and model [2]. The amount of dissipation needed in a grid cell is often estimated from the large scale flow using some kind of deconvolution scheme, such as the “approximate deconvolution” scheme of Adams and Stolz [70]. This dissipation estimate is then built into the truncation error of the local, spatial discretization. While ILES has been more successful than traditional LES at modeling turbulent transition (see, e.g., Hickel et al. [71], the numerical experiments of Thornber et al. [72] indicate that ILES is still too dissipative to correctly model turbulent decay. In fact, ILES shares the fundamental assumption of the Boussinesq hypothesis that the effects of nonlinear SGS interactions on the large scale are dissipative. Thus the same kind of rationale based on Eq. (3.15) still holds, as the effects of nonlinear interactions can be seen to



be quite different from those of dissipation when viewed in Fourier space. Thus we expect that this approach alone will never be adequate for SGS turbulence modeling.

While the problems with assuming turbulence is purely dissipative have been discussed previously, there is a more subtle problem with assuming spatial discretization acts as a filter. Lund [73] showed that the filtering associated with discretization is strictly one-dimensional, so each term in the NSEs has a unique filter associated with the direction of the spatial derivative. This nonuniform approach means that there is no well-defined three-dimensional filter equivalent to the ILES technique, so that ILES methods cannot be viewed as rigorously providing a solution to the filtered NSEs.

A second problem associated with the the lack of explicit filtering is the aliasing associated with the under-resolved nonlinear terms. In practice, the spurious oscillations associated with aliasing tend to be damped out by the artificial dissipation typically provided by the turbulence model. The aliasing problem can be seen by applying LES filtering methods to the Burgers equation with unity Reynolds number,

$$\partial_t u = -\frac{1}{2}\partial_x u^2 + \partial_{xx} u. \quad (3.25)$$

Applying filtering provides

$$\partial_t \bar{u} = -\frac{1}{2}\partial_x \bar{u}^2 + \partial_{xx} \bar{u} + \varepsilon_c, \quad (3.26)$$

where  $\varepsilon_c$  is the commutation error,

$$\varepsilon_c = \left( -\frac{1}{2}\overline{\partial_x u^2} + \overline{\partial_{xx} u} \right) - \left( -\frac{1}{2}\partial_x \bar{u}^2 + \partial_{xx} \bar{u} \right). \quad (3.27)$$

Here, we assume that  $\varepsilon_c = \mathcal{O}(\Delta^n)$ , where  $n$  is the order of the spatial discretization we intend to use in the numerical method, an assumption we will later justify. A typical assumption in LES is that the filtering operation eliminates all modes above  $k_{max}$ , so for the purposes of the present analysis, we assume that  $\overline{(\cdot)}$  is a sharp spectral cutoff

filter, i.e.,

$$\bar{u} = \sum_{|k| \leq k_{max}} \hat{u}_k \phi_k. \quad (3.28)$$

Suppression of the commutation error and Galerkin expansion reveals that the filtered equations contain no unresolvable modes and are thus not subject to aliasing, although note that all contribute to the filtered nonlinear term:

$$\frac{d}{dt} \hat{u}_k = \frac{ik}{2} \sum_{l \in \mathbb{Z}} \hat{u}_l \hat{u}_{k-l} - k^2 \hat{u}_k, \quad |k| \leq k_{max}. \quad (3.29)$$

In practice, then, properly implemented numerical solutions of the filtered equation should be stable. In fact, we will show in Chapter 6 that filtering alone increases the kinetic energy decay rate of homogeneous, isotropic turbulence. But note that the summations include interactions where two high- $k$  modes interact to form a low- $k$  mode. In actual LES computations, this information does not exist. Under-resolved discretization of the filtered equations does not introduce aliasing, but rather eliminates high wavenumber interactions at the lower modes. If we introduce the nonlinear filter error,

$$\hat{\varepsilon}_{f,k} = ik \sum_{|l| > k_{max}} \hat{u}_l \hat{u}_{k-l}, \quad |k| \leq k_{max}, \quad (3.30)$$

we can decompose the expansion into the form suitable for numerical solution,

$$\frac{d}{dt} \hat{u}_k = \frac{ik}{2} \sum_{l=-k_{max}}^{k_{max}} \hat{u}_l \hat{u}_{k-l} - k^2 \hat{u}_k + \hat{\varepsilon}_{f,k}, \quad |k| \leq k_{max}. \quad (3.31)$$

Reconstituting this in physical space then provides

$$\partial_t \bar{u} = -\frac{1}{2} \partial_x \bar{u}^2 + \partial_{xx} \bar{u} + \varepsilon_f, \quad (3.32)$$

where  $\varepsilon_f$  is the filter error,

$$\varepsilon_f = \frac{1}{2} \partial_x \left( \overline{\bar{u}^2} - \bar{u}^2 \right) \quad (3.33)$$

Equation (3.32) features errors due to the effects of filter truncation on the nonlinear terms, but it still does not generate aliasing-related errors. While we have worked this out in detail only for the Burgers equation in Eq. (3.25), the same rationale holds for the full compressible NSEs.

### 3.2.4 Aliasing in traditional LES

A common assumption is that  $\overline{\overline{u^2}}$  in Eq. (3.32) is impossible to evaluate and therefore must be replaced by  $\overline{u^2} + (\overline{\overline{u^2}} - \overline{u^2})$ , resulting in the form,

$$\partial_t \overline{u} = -\frac{1}{2} \partial_x \overline{u^2} + \partial_{xx} \overline{u} + \frac{1}{2} \partial_x \left( \overline{u^2} - \overline{\overline{u^2}} \right) + \varepsilon_f. \quad (3.34)$$

For example, Sagaut explicitly states regarding the incompressible LES equations [74],

“But the  $\overline{\overline{u_i u_j}}$  term cannot be calculated directly because it requires a second application of the filter.”

The unstated assumption behind this claim is that filtering is being done implicitly. For the incompressible momentum equations, this leads to the form

$$\partial_t \overline{\mathbf{u}} + \nabla \cdot (\overline{\mathbf{u}} \overline{\mathbf{u}}^T) = -\nabla p + \frac{1}{Re} \nabla^2 (\overline{\mathbf{u}}) + \nabla \cdot \boldsymbol{\tau}, \quad (3.35)$$

where  $\boldsymbol{\tau}$  is the familiar Leonard decomposition [75] given by

$$\tau_{ij} = L_{ij} + C_{ij} + R_{ij} \quad (3.36)$$

$$L_{ij} = \overline{\overline{u_i u_j}} - \overline{u_i} \overline{u_j} \quad (3.37)$$

$$C_{ij} = \overline{\overline{u_i u'_j}} + \overline{\overline{u'_j u_i}} \quad (3.38)$$

$$R_{ij} = \overline{\overline{u'_i u'_j}}. \quad (3.39)$$

The problem with this form is that  $\nabla \cdot (\overline{\mathbf{u}} \overline{\mathbf{u}}^T)$  is not supported on the computational mesh, as discussed below, so the Leonard decomposition actually introduces the problem it purports to solve. As should be fairly clear, if an explicit filtering operation is performed, there is no issue whatsoever with applying it as many times as is necessary for a given method. If explicit filtering is used, the Leonard stress  $L_{ij}$ , is unnecessary, and only the cross tensor,  $C_{ij}$ , and the Reynolds subgrid tensor,  $R_{ij}$ , should be modeled.

An additional issue is that the Leonard decomposition is not Galilean invariant. In 1986, Germano proposed a modification [76],

$$\tau_{ij} = L_{ij}^0 + C_{ij}^0 + R_{ij}^0 \quad (3.40)$$

$$L_{ij}^0 = \overline{\overline{u_i u_j}} - \overline{\overline{u_i}} \overline{\overline{u_j}} \quad (3.41)$$

$$C_{ij}^0 = \overline{\overline{u_i u'_j}} + \overline{\overline{u_j u'_i}} - \overline{\overline{u_i}} \overline{\overline{u'_j}} - \overline{\overline{u_j}} \overline{\overline{u'_i}} \quad (3.42)$$

$$R_{ij}^0 = \overline{\overline{u'_i u'_j}} - \overline{\overline{u'_i}} \overline{\overline{u'_j}}. \quad (3.43)$$

Note that when the filtering operation is an exact spectral cutoff, the Germano modification is equivalent to the original Leonard decomposition.

To see the aliasing issue with traditional LES modeling, we return to our discussion of the LES Burgers equation, Eq. (3.34). The usual technique is to replace  $\frac{1}{2} \partial_x (\overline{u^2} - \overline{\overline{u^2}}) + \varepsilon_f$  with a turbulence model,  $\partial_x M(\overline{u})$ , regarding which we currently make no assumptions other than support on the computational mesh. Galerkin expansion of this new system now provides

$$\frac{d}{dt} \widehat{u}_k = ik \sum_{|l| \leq k_{max}} \widehat{u}_l \widehat{u}_{k-l} - k^2 \widehat{u}_k + ik \widehat{M(\overline{u})}_k, \quad |k| \leq k_{max}, \quad (3.44a)$$

$$0 = ik \sum_{|l| \leq k_{max}} \widehat{u}_l \widehat{u}_{k-l}, \quad |k| > k_{max}. \quad (3.44b)$$

We can see from Eq. (3.44b) that the traditional LES equations contain high wavenumber terms that will cause aliasing, and so the system Eqs. (3.44a)–(3.44b) cannot be accurately solved on the mesh. By the logic discussed in Section 3.1.2, terms in Eq. (3.44b) will alias with terms in Eq. (3.44a), so that a discrete numerical method actually approximates the system

$$\frac{d}{dt} \widehat{u}_k = ik \sum_{\substack{|l| \leq k_{max} \\ n \geq 0}} \widehat{u}_l \widehat{u}_{(k-l+n k_{max})} - k^2 \widehat{u}_k + ik \widehat{M(\overline{u})}_k, \quad |k| \leq k_{max}. \quad (3.45)$$

Therefore in the absence of explicit filtering, the discretization scheme and  $M(\overline{u})$  must provide enough dissipation to completely eliminate all of the parasitic modes

in the nonlinear summation, in addition to providing a simulation of interactions with unresolved wavenumbers. But since most implicitly filtered LES models are not constructed with a view toward specifically eliminating the aliasing error above, they tend to be excessively dissipative.

Thus we see from a careful analysis of aliasing that by introducing the SGS terms with the goal of creating a system of equations that resemble the NSEs with filtered variables, the aliasing problem that filtering is meant to solve is reintroduced in a different form. In our view, this makes the traditional LES equations inadequate to perform the task for which they were originally constructed.

### 3.2.5 Eddy viscosity in LES

Typical formulations of  $M(\bar{u})$  employ the Boussinesq hypothesis, given by [77]

$$\overline{u_i u_j} - \bar{u}_i \bar{u}_j - \frac{1}{3} (\overline{u_k u_k} - \bar{u}_k \bar{u}_k) \delta_{ij} - \bar{u}_k \bar{u}_k = -2\nu_e \bar{S}_{ij}. \quad (3.46)$$

We restrict our analysis to the incompressible equations for simplicity's sake, but the arguments in this section can be easily extended to compressible turbulence. As in RANS,  $\nu_e$  is assumed to not be constant throughout the flow. In fact, we cannot even assume it constant in the case of homogeneous, isotropic turbulence because it is based on local, subgrid-scale turbulent behavior, which cannot be assumed to be statistically uniform in space at any given  $t$ . However, we can assume  $\nu_e$  is fully resolved on the grid; i.e., there is no wavenumber content beyond  $k_{max}$ . Assume, then, that the filter is a spectral cutoff filter at  $k_{max}$ . If we consider only the case  $i = j = 1$ , an eddy viscosity model must satisfy the relationship

$$\frac{2}{3} (\overline{u^2} - \bar{u}^2) = -2\nu_e \partial_x \bar{u}, \quad (3.47)$$

where  $u = u_1$  and  $\nu_e$  is the eddy viscosity. Galerkin expansion of Eq. (3.47) provides

$$\frac{2}{3} \left( \sum_{l+m=k} \widehat{u}_l \widehat{u}_m - \sum_{\substack{l+m=k \\ |l|, |m| \leq k_{max}}} \widehat{u}_l \widehat{u}_m \right) = -2 \sum_{\substack{l+m=k \\ |l|, |m| \leq k_{max}}} m \widehat{\nu}_{e,l} \widehat{u}_m, \quad k \in \mathbb{Z} \quad (3.48)$$

$$\frac{2}{3} \left( \sum_{\substack{l+m=k \\ |l|, |m| > k_{max}}} \widehat{u}_l \widehat{u}_m \right) = -2 \sum_{\substack{l+m=k \\ |l|, |m| \leq k_{max}}} m \widehat{\nu}_{e,l} \widehat{u}_m, \quad k \in \mathbb{Z}. \quad (3.49)$$

From this expansion we see the questionable character of the Boussinesq hypothesis even in the context of LES. The left-hand side contains exclusively multiplication of high-frequency modes, but the right-hand side contains exclusively dissipation of the low-frequency modes. No interactions between the high and the low frequencies whatsoever are involved. However, the problem is not nearly so intractable as the RANS case, since resolved modes do exist (recall that in RANS no spatial modes are resolved), and eddy viscosity models only need to introduce small amounts of dissipation in order to stabilize the numerical procedure and produce reasonably accurate simulations of the large-scale flow.

Another issue with eddy viscosity is that dissipation can only be used to model energy transfer strictly from large scales to small scales, but DNS results for incompressible turbulent flows as early as those presented by Piomelli et al. [78] exhibit substantial inverse transfer of energy from small to large scales, which is known as “backscatter.” Hence, an effective turbulence model for LES must be able to capture this phenomenon. The dynamic model [68] is capable of producing backscatter, but its creation of negative viscosities results in a mathematically ill-posed problem that causes numerical instabilities unless special treatments, such as the Lagrangian dynamic model of Meneveau et al. [79], are used. In fact, in the absence of explicit filtering, where the dynamic model returns eddy viscosities near zero, it is allowing aliasing to supply the backscatter, and negative eddy viscosities actually amplify aliasing. However, because LES eddy viscosity models apply limited, local dissipa-

tion, they are better able to capture transient phenomena of the flow than any RANS model.

The traditional LES approach is understandable in its historical context, as the theoretical foundations of large-eddy simulation were not well developed when Leonard introduced his tensor decomposition in 1976 [75]. Lele would not provide thorough analysis of low-dissipation Padé filtering in the context of CFD until 1996, Vasilyev et al. [80] did not formally address and solve the critical mathematical issues associated with explicit filtering until 1998, and Canuto would not publish the first edition of his work on spectral methods [81], with its important discussion of aliasing, until 1988. In fact, when Smagorinsky introduced his eddy viscosity model in 1963 [1], he did not filter the governing equations at all, but rather constructed a simple model of the atmosphere using a combination of mathematical and physical reasoning. His model was thus formulated not based on any numerical or spectral properties of the filtering, but simply based on the physically intuitive Boussinesq hypothesis.

Further, early attempts to analyze the LES equations involved assuming that  $\overline{\overline{u_i u_j}} \approx \overline{u_i} \overline{u_j}$ . In 1970, for example, Deardorff [82] made this assumption, in addition to assuming a “top-hat” filter with support on a small cube in attempting to analyze the LES equations. Likewise, Clark et al. followed this assumption in 1979 [83]. This assumption is false, and the Leonard decomposition can be viewed as a correction to this error. In neither case did these authors engage in a rigorous spectral analysis of the SGS tensor, so the Leonard decomposition was reasonable in this context. However, in the light of all the previously discussed knowledge of aliasing and filtering developed since then, we argue that this traditional approach is clearly inadequate and should be abandoned.

### 3.2.6 Structural modeling

The problems with eddy viscosity based turbulence models have led to a variety of alternative approaches, one of the more common being constructing subgrid-scale information from the resolved flow field. Following the terminology of Garnier et al. [7], we refer to this general class of techniques as structural modeling. Two fairly common approaches to structural modeling are scale similarity modeling, such as the models of Bardina et al. [84] and Liu et al. [85], and deconvolution models, such as that of Adams and Stolz [70]. Further need for good structural models has arisen as multi-species flow simulations have become more common. Dispersion of solid particles, chemical kinetics, and other such phenomena depend on small-scale fluctuating velocities and therefore require reconstruction of SGS quantities, whether via a structural turbulence model or by an *ex post facto* reconstruction, such as the stochastic Langevin model of Dehbi [86].

A type of structural model of particular interest due to its direct applicability to SGS mixing in multiphase or multi-fluid flows is synthetic velocity modeling. In these models, the fluctuating variables are directly constructed. An early example of a synthetic velocity model is Domaradzki's subgrid-scale estimation (SSE) model [6]. The SSE model works by estimating a SGS velocity field via construction from the large scales, using a method similar to the deconvolution methods employed in ILES. The turbulent stress tensor of the LES momentum equations (3.24b) is then directly constructed from this estimated SGS velocity field.

In incompressible LES, Kerstein's linear eddy model [87] is a synthetic velocity model that has been extensively developed. LEM simulates SGS fluctuations by combining a one-dimensional heat equation with a stochastic mixing process; thus both dissipation and nonlinear interactions are modeled. This model has been incorporated into a full LES model, one-dimensional turbulence (ODT) [88]. ODT has been incorporated into full LES simulations by Schmidt et al. with considerable success [5],



although it also shows significant dissipation as the resolution of the grid decreases. This is likely due to the fact that it still handles very small scales with an eddy viscosity.

Attempts at inducing backscatter via random forcing functions were introduced in the 1990s by Leith [89] and Chasnov [90] with reasonable success. Although this has not been a particularly popular method, the basic idea continues to be used and modified with some success. A more recent example that has exhibited fairly good agreement with DNS results is the LES–Langevin model of Laval and Dubrulle [91], although the dissipative component of this model was provided by a Smagorinsky-type eddy viscosity. We will provide extensive detail and analysis of these models in Sec. 4.4, as the model presented in this work is based on backscatter forcing.

In this work, we are presenting a turbulence model that is a combination of scale similarity, synthetic velocity and forcing; in particular, the fluctuations from the synthetic velocity will be used to supply the “randomness” of the forcing, and a general scale-similarity argument will be used to provide the magnitude. However, we will see that the model used to construct the synthetic velocities is deterministic, not random, and further has favorable characteristics that make it an attractive choice to use in the context of turbulence modeling.

### **3.2.7 Dealiased LES equations**

We have shown above that the bilinear term in traditional constructions of the LES equations introduces numerical aliasing error when discretized. This aliasing is traditionally suppressed via a highly dissipative, eddy viscosity-based turbulence model. Because of these considerations, it is our view that explicit filtering is an indispensable component of LES. This leads us to reconsider the original application of the filtering operation to the NSEs. In particular, the filtering of the NSEs must be done in such a way as to be consistent with the numerical implementation of explicit filtering. We

begin by filtering the governing equations, Eqs. (2.1a)–(2.1c):

$$\partial_t \bar{\rho} + \partial_j \overline{(\rho u_j)} = 0, \quad (3.50a)$$

$$\partial_t \overline{(\rho u_i)} + \partial_j \overline{(\rho u_j u_i)} = -\partial_i \bar{p} + \partial_j \bar{\sigma}_{ij}, \quad (3.50b)$$

$$\partial_t \overline{(\rho e_0)} + \partial_j \overline{(\rho e_0 + p) u_j} = \partial_j \bar{\sigma}_{ij} u_i - \partial_j \bar{q}_j, \quad (3.50c)$$

where the commutation error  $\varepsilon_c$  has been suppressed. As in traditional LES, we will solve for the filtered conserved variables  $\{\bar{\rho}, \overline{\rho u_i}, \overline{\rho e_0}\}$ , but we will not employ the usual technique that creates the SGS terms. Instead, we define high frequency interactions (HFIs) by

$$HFI_i = \partial_j \left( \overline{\rho u_j \tilde{u}_i} - \overline{\rho u_j u_i} \right) \quad (3.51)$$

$$HFI_e = \partial_j \left( \overline{\sigma_{ij} u_i} - \overline{\sigma_{ij} \tilde{u}_i} - \overline{(\rho e_0 + p) u_j} + \overline{(\rho e_0 + p) \tilde{u}_j} \right). \quad (3.52)$$

In the case of  $HFI_i$ , this term is just the derivative of the cross and Reynolds subgrid stress tensors for compressible flows. However, we are deliberately eschewing the language of stress tensors because we believe, based on the discussions in Ch. 2.3.4, that it is fundamentally misleading and leads to the sorts of physical analogies behind ideas such as the Boussinesq hypothesis. In particular, so-called “SGS turbulent stress” is not a physical phenomenon; it is a mathematical artifact that arises from filtering the NSEs, and both its magnitude and its spectral character depends entirely on the filtering operation chosen. Thus we are viewing these as error terms associated with the filtering operation rather than physical phenomena to be modeled via a linear stress-strain relationship or something else along those lines.

Continuing by substituting the HFI terms, we get

$$\partial_t \bar{\rho} + \partial_j \overline{(\rho u_j)} = 0, \quad (3.53a)$$

$$\partial_t \overline{\rho u_i} + \partial_j \overline{\rho \tilde{u}_j \tilde{u}_i} = -\partial_i \bar{p} + \partial_j \bar{\sigma}_{ij} + HFI_i, \quad (3.53b)$$

$$\partial_t \overline{\rho e_0} + \partial_j \overline{(\rho e_0 + p) \tilde{u}_j} = \partial_j \overline{\sigma_{ij} \tilde{u}_i} - \partial_j \bar{q}_j + HFI_e, \quad (3.53c)$$

where the HFI terms can be modeled. This system is similar in structure to the filtered Burgers equation, Eq. (3.32). Assuming that the filtering operation approximates a spectral cutoff, the HFI terms take the form of the error term in Eq. (3.30) and contain the entirety of interaction of the high wavenumber content with the low-pass filtered variables. There are two important differences from Eqs. (3.24a)–(3.24c), namely, that all bilinear operators are filtered, and discretization of this system minus the HFI error terms creates no aliasing. Therefore in the absence of a turbulence model, numerical solutions of this system should be stable. This leads to the conclusion that any properly anti-aliased solution procedure for the compressible NSEs on an under-resolved mesh with no turbulence model, in fact, returns a solution for Eqs. (3.53a)–(3.53c) minus the HFI error terms, rather than Eqs. (3.24a)–(3.24c). In this view, it is these error terms that must be modeled to increase solution accuracy, not the usual SGS tensor.

To show that the system above is equivalent to filtering the solution at each time step, we return to the Burgers equation in Eq. (3.25),

$$\partial_t u = -\frac{1}{2}\partial_x u^2 + \partial_{xx}u.$$

Partial discretization with forward Euler time step provides

$$u^{(n+1)} = \Delta t \left[ -\partial_x (u^{(n)})^2 + \partial_{xx}u^{(n)} \right] + u^{(n)}. \quad (3.54)$$

Applying a discrete filter operator  $G$  to the solution at time step  $(n + 1)$  gives

$$Gu^{(n+1)} = \Delta t \left[ -\partial_x G (u^{(n)})^2 + \partial_{xx}Gu^{(n)} \right] + Gu^{(n)} + \Delta t\epsilon_c. \quad (3.55)$$

where  $\Delta t$  is the time step and  $\epsilon_c$  is the discrete commutation error. Thus we can see that filtering the solution at time step  $(n + 1)$  is equivalent to solving the filtered equations up to the commutation error. However, since we will be filtering at each time step, then we have

$$Gu^{(n+1)} = \Delta t \left[ -\partial_x G (Gu^{(n)})^2 + \partial_{xx}G^2u^{(n)} \right] + Gu^{(n)} + \Delta t(\epsilon_c + \epsilon_f), \quad (3.56)$$

where  $\epsilon_f$  is the discrete filter error caused by filtering at the previous time step. Defining  $G$  such that  $G(u) \rightarrow \bar{u}$  in the limit of infinite mesh resolution, as the time step and mesh size go to zero, this system becomes

$$\partial_t \bar{u} = -\partial_x \bar{u}^2 + \partial_{xx} \bar{u} + \epsilon_c + \epsilon_f,$$

which is just Eq. (3.32) with the commutation error included, and  $\epsilon_f$  is the HFI term.

The commutation error associated with a discrete filter can be controlled to be arbitrarily small. Let  $W$  be a vector of filter weights,

$$W = [w_{-N}, \dots, w_0, \dots, w_N], \quad (3.57)$$

where  $2N + 1$  is the stencil size,  $\sum w_l = 1$ , and the filtering operation is defined by

$$\bar{u}_j = \sum_{l=-N}^N w_l u_{j+l}. \quad (3.58)$$

Then the  $n^{\text{th}}$  moment of  $W$  is defined by

$$M^n(W) = \sum_{l=-N}^N l^n w_l. \quad (3.59)$$

Vasilyev et al. [80] showed that for a discrete derivative operator,  $\epsilon_c = \mathcal{O}(\Delta^m)$ , where

$$m = \min\{n \mid M^n(W) \neq 0\}. \quad (3.60)$$

In the case of Padé filters constructed of two weight vectors,  $W_1$  and  $W_2$ , they showed that

$$m = \min\{n \mid M^n(W_1) - M^n(W_2) \neq 0\}. \quad (3.61)$$

This provides an easy method for constructing filters with small commutation error. If this error is of the same or higher order than the discretization scheme, no significant effects on global solution accuracy are introduced.

It is fairly easy to see that the numerical implementation of the filtering operation by filtering after each time step is dissipative by restricting our discussion to the

Euler equations on a periodic cube,  $\Omega = [0, 2\pi]^3$ . Recall from Sec. 2.3.4 that the Euler equations are a conservative system, so that kinetic energy in the cube must be constant in time. Furthermore, the truncated Galerkin system is conservative as well. Suppose we use a truncated Galerkin method to solve the system, with truncation wavenumber  $k_{max}$ . Now suppose the filtering operation is a spectral cutoff at  $k_{max}/2 < k_N < k_{max}$ .

The Galerkin expansion of the Euler equations with the pressure Poisson equation is given by

$$\frac{d}{dt}\hat{u}_{i,\mathbf{k}} = - \sum_{\mathbf{m}} ik_j \hat{u}_{j,\mathbf{m}} \hat{u}_{i,\mathbf{k}-\mathbf{m}} + ik_i \hat{p}_{\mathbf{k}} \quad (3.62)$$

$$p_{\mathbf{k}} = \sum_{\mathbf{m}} m_i (m_j - k_j) u_{i,\mathbf{m}} u_{j,\mathbf{k}-\mathbf{m}}, \quad (3.63)$$

where  $i^2 = -1$  when not used as a subscript index, and all wavenumbers are bounded by  $k_{max}$ . Now suppose we begin with an initial condition  $\mathbf{u}_0$  such that  $\hat{u}_{\mathbf{k},i}(0) = 0$  for all  $k_i > k_N$ , i.e.,  $\bar{\mathbf{u}}_0 = \mathbf{u}_0$ . Then at  $t = 0$ , the summations in the system in Eqs 3.62–3.63 are only over  $\mathbf{m}$  such that  $\|\mathbf{m}\|_{\infty} \leq k_N$  and  $\|\mathbf{k} - \mathbf{m}\|_{\infty} \leq k_N$ . Because the system is conservative,

$$\frac{d}{dt}K \equiv \frac{1}{2} \frac{d}{dt} \int_{\Omega} u_i u_i dV = \frac{1}{2} \sum \hat{u}_{i,\mathbf{k}} \hat{u}_{i,-\mathbf{k}} = 0. \quad (3.64)$$

What we can see from the above analysis is that initially, the evolution of energy at modes above  $k_N$  after a single time step is due entirely to the low- $k$  modes, and the conservative nature of the system means therefore that the energy at those low- $k$  modes must initially decay. But applying the filtering operation eliminates all the energy accumulated at the high- $k$  modes. Assuming, based on the results discussed in Sec. 2.3.5, that “energy-starved” modes in a truncated system immediately absorb energy from the low- $k$  modes, for this implementation,

$$\frac{d}{dt}K < 0, \quad (3.65)$$

and the system is dissipative. This logic can be extended to any conservative numerical formulation of the Euler equations, such as finite-volume methods, since the DFT can be used to define and investigate the spectral content of those methods as well.

In FD and FV methods, there is an additional complication to consider. By waiting until the end of the time step to apply the filter, the nonlinear term induces a small amount of aliasing error which the filter must eliminate. But this aliasing propagates throughout all wavenumbers, so appropriate filtering must induce at least some attenuation at every mode, and a mere spectral cutoff is therefore likely to be inadequate, as we will see in Sec. 3.2.8. Therefore, if a numerical FV or FD method is formulated such that it is conservative in the inviscid fluxes, even a perfect dealiasing filter turns a conservative system into a dissipative system. Moreover, if the dealiasing filter has a transfer function that completely attenuates the highest wavenumbers, these high- $k$  modes are “energy-starved” at the beginning of the next time step. Based on the results for inviscid turbulence in Sec. 2.3.5, the nonlinear dynamics alone should be enough to transfer energy to these modes and cause the evolution of a proper inertial subrange. This leads to the conclusion that in the context of a proper implementation of Eqs. (3.53a)–(3.53b), the numerical implementation of filtering should induce excessive dissipation, and the sole role of any turbulence model should be to supply backscatter.

### **3.2.8 A critique of deconvolution**

The above discussion leads logically to a critique of the concept of deconvolution, first developed by Adams and Stolz in their approximate deconvolution method (ADM) [70], interpreted further by Mathew et al. in 2003 [92], and slightly modified by Mathew et al. in 2006 [93]. These latter authors argued in their 2003 publication (and we agree with this argument) that ADM is nearly equivalent to an explicit filtering procedure that can be done in a single step after each discrete time integration. The

basic concept revolves around a filter  $G$  and an approximate inverse  $Q$  such that  $QGu \approx u$  on the resolved scales of the flow. Applying their method to Eq. (3.25), we get

$$\partial_t Gu + \frac{1}{2} G \partial_x (QGu)^2 = \partial_{xx} Gu. \quad (3.66)$$

The problem with this method is subtle, but is apparent based on the previous discussion. Recall that parasitic modes are created by the nonlinear term alone. Now suppose  $G$  is some “optimal” filter kernel that applies the minimal filtering necessary to eliminate all aliasing error on the given mesh. Then for any approximate inversion  $Q$  such that  $1 \geq T_{QG}(k) \geq T_G(k)$ , where the  $T$ s are filter transfer functions (this is what is typically meant by an approximate inverse), the  $Q$  anti-filtering operation simply re-introduces parasitic modes.

In the 2006 variant of the Mathews deconvolution technique [93], the equations are reformulated as

$$\partial_t QGu + \frac{1}{2} \partial_x (QGu)^2 = \frac{1}{2} \partial_x \left( ((QG)^2 u)^2 - (QGu)^2 \right) + \partial_{xx} QGu, \quad (3.67)$$

which they present as a “completely non-heuristic LES model,” which is an accurate statement. Because they are filtering at each time step, this formulation is not exact, and the discrete filter must converge to some continuous filter in the limit of infinite mesh resolution and zero time step. Due to this and the fact that their method effectively dealiased their solutions, we argue based on the previous discussion that the correct formulation of the continuous equations their discrete method corresponds to is

$$\partial_t QGu + \frac{1}{2} \partial_x QG(QGu)^2 = \frac{1}{2} \partial_x QG \left( (QG^2 u)^2 - (QGu)^2 \right) + \partial_{xx} QGu, \quad (3.68)$$

where filter and commutation errors have been suppressed.

Because the discrete implementation of  $QG$  is already close to a spectral cutoff, the differences between the transfer functions of  $QG$  and  $(QG)^2$  are marginal and,

as can be expected, so are the differences in the respective solutions. In the limiting case of a true spectral cutoff,  $QG = QG^2$ , this method returns to the equations seen in Eq. (3.32). The fundamental problem with all deconvolution methods of this type is that without resorting to any heuristic model, assuming the method is properly dealiased, the best they can do is solve Eqs. (3.53a)–(3.53b) without the HFI terms. Otherwise, all that is accomplished is insufficient attenuation of parasitic modes. In fact, the 2006 variant tends to under-dissipate, and it does not attenuate the low- $k$  modes at all, suggesting that in fact the filter is not sufficiently removing aliasing.

The fundamental conceptual problem with deconvolution can best be seen when applied to image filtering. Even when exact knowledge of the method used to filter from  $N$  data points to  $M < N$  data points is used, this process cannot be inverted and does not reconstruct any lost high-frequency information. Fig. 3.1 shows an image [94] that has been downsampled to one-fourth resolution using the Lanczos-3 kernel, then deconvolved back to the original resolution using the exact same kernel. Clearly, the high-frequency information lost in the original downsampling has not been restored, and PSDs of representative vectors from both images confirm that, as seen in Fig. 3.2. Deconvolution methods thus cannot restore missing SGS information, and at best simply provide a high-quality, low-pass filtering that dealiases the solution while minimizing unnecessary attenuation of the resolved modes.

### 3.3 Summary and conclusions

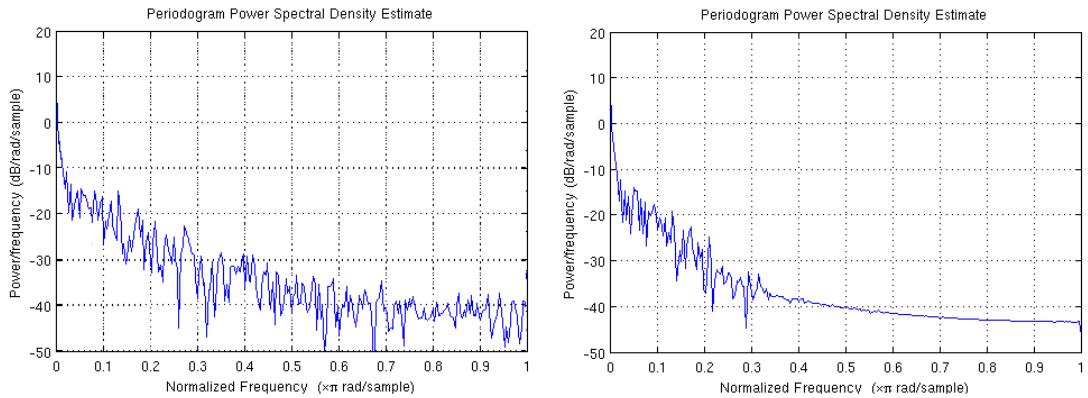
The above discussion allows us to concisely answer the question of what exactly the purpose of a turbulence model is. Put succinctly, the purpose of a turbulence model is to counteract the errors induced by inadequacies of the numerical method used for solving the NSEs. This makes turbulence modeling materially different from other types of physical modeling. For example, the Boussinesq approximation for thermal convection is a model, but it corrects the inability of the incompressible NSEs to



Figure 3.1: 544x725 image filtered to 136x182 and deconvolved back to the original resolution using Lanczos-3 for both operations. Image is public domain [94].



Figure 3.2: PSDs of the original 544x725 image and its deconvolution.



respond to temperature gradients. Newton’s laws of motion are useful models of all kinds of phenomena at sub-relativistic and super-quantum scales, but completely inadequate in those two latter ranges. In fact, the NSEs themselves are a model of the bulk motion of fluid molecules, one that has proved to be quite adequate for generating accurate simulations of turbulence. A turbulence model, by contrast, is essentially low-fidelity approximation of the information lacking from the numerical implementation of a mathematical system.

In this light, the task of RANS modeling appears to be borderline intractable. The inadequacy is in the construction of the RANS equations themselves, which cannot be viewed as a truncation of the NSEs and cannot even hypothetically be solved

analytically. Unlike the LES equations, the RANS equations cannot be viewed as equivalent to an under-resolved numerical method plus an error term. Since the original idea is to compute solutions of the NSEs in a statistical sense only, the task of a RANS model is to reconstruct the statistical information that has been destroyed by the Reynolds averaging process, information that is completely independent of the number of degrees of freedom in the solution method.

The task of turbulence modeling in the case of large-eddy simulation is thus fairly straightforward. If  $N_{DNS}$  degrees of freedom are necessary to obtain an accurate solution for a given set of parameters, but the computer in question is only capable of solving systems of size  $N_{LES} \ll N_{DNS}$ , then the inadequacy in the numerical method is simply insufficiently many degrees of freedom in the system and the resulting large truncation error feeding on itself via the nonlinear terms. As seen in Section 3.2.7, LES equations can be constructed based on the assumption of a spectral cutoff filter, and it can be shown that even solving this system requires  $N_{DNS}$  degrees of freedom due to the HFI terms. Further, it was demonstrated that the HFI terms cause aliasing error on an under-resolved mesh, and removal of this error via explicit filtering results in a dissipative system that transfers energy from large to small scales, but has no inverse transfer. Then in the context of dealiased LES, the sole purpose of any turbulence model is to supply backscatter. In the limit  $N_{LES} = N_{DNS}$ , the truncation error vanishes and with it, any concern for modeling.

This view of the LES closure problem, combined with the modern knowledge that the NSEs are sufficient to produce turbulence on their own, naturally leads away from the kind of physical rationale underlying eddy viscosity modeling and toward methods grounded more in the NSEs themselves. Indeed, techniques that are useful in general PDE theory and analysis have been very productive in studying the theory of turbulence and are in turn useful for numerical methods. However, it is important to understand that even in the case of LES, a closure problem exists. The information

in a high-degree system simply is not, by definition, contained in a low-degree system. Note that this is a separate problem from the issue of the construction of the low-degree solution, such as the construction of an ideal mesh. Adaptive meshing, such as the SCALES method, significantly improves LES results without introducing new degrees of freedom, even more so when used in conjunction with a turbulence model [95]. Eq. (3.29) shows that accurate solutions of the filtered NSEs require the same amount of information as DNS on an ideal mesh due to the nonlinear terms. Because this information is entirely absent from the resolved-scale computations, some degree of heuristic modeling is necessary to improve the performance of an under-resolved solution method.

## Chapter 4. The Compressible Poor Man’s Navier–Stokes Equations

In the first section of this chapter, we present a brief background of the “poor man’s” Navier–Stokes equations. In Sec. 4.1, the CPMNS equations are derived from the compressible NSEs. A detailed derivation of the discrete, coupled momentum and energy equations is provided, along with formulas for the bifurcation parameters in terms of the fundamental parameters of the flow. A full numerical analysis of the bifurcation behavior of the system is presented in Sec. 4.2, with attention given to each bifurcation parameter. Dynamical behavior is characterized using an automated tool that processes the power spectral densities (PSDs) of the time series generated as bifurcation parameters are varied. Color-coded regime maps are presented to demonstrate the range of dynamical behavior achieved by the CPMNS equations as the different momentum and energy bifurcation parameters are varied. Section 4.3 shows the response of the CPMNS equations to initial conditions, demonstrating they are truly chaotic. Sensitivity to initial conditions is quantitatively demonstrated using numerically computed Lyapunov exponents. In the final section, we present a survey and discussion of existing forcing techniques and construct the forcing function we use in this work.

This chapter presents work published earlier by Strodtbeck et al. [96]. We describe the motivation behind the CPMNS equation, give a complete derivation, and present the results of numerical experiments on the bifurcation behavior. The CPMNS equations are a discrete dynamical system, a simple and famous example of which is the logistic map. This map is a classical and well-studied example of a discrete dynamical system (DDS), given by

$$a^{(n+1)} = \beta a^{(n)} (1 - a^{(n)}), \quad (4.1)$$

where  $\beta$  is the bifurcation parameter. A complete overview of this map will not be

given here, as this has been accomplished elsewhere (see, for example, May, [97]). Of particular interest is that increasing  $\beta$  leads to transitions in dynamical behavior, so that steady behavior gives way to periodicity, and eventually to chaos through subharmonic bifurcations, with recurring “windows” of periodic behavior between regions of chaos. Similarity between the bifurcation behavior of the logistic map as  $\beta$  increases and behavior of the 2-D Navier–Stokes equations (NSEs) as  $Re$  increases was observed in the 1990s by Pulliam and Vastano [98]. This led Hylin and McDonough [99] to incorporate the logistic map in constructing subgrid-scale (SGS) models for large-eddy simulation (LES). However, despite some surface similarities, there are substantial differences between bifurcation characteristics of the logistic map and the NSEs. The logistic map does not exhibit quasiperiodic behavior, and it transitions to chaos via a sequence of period-doubling bifurcations, neither of which are uniformly consistent with observed transitional behavior in physical fluid turbulence.

The aforementioned inadequacies and others motivated McDonough and Yang [10] to propose use of a different DDS as a SGS model. This DDS, called the “poor man’s Navier–Stokes (PMNS) equation” (following the terminology of Frisch [11]) was derived directly from a Galerkin expansion of the NSEs and has the form of three logistic maps coupled via additional nonlinear terms. McDonough and Huang showed that the 2-D PMNS equations exhibit the full range of dynamical behavior seen in physical fluid turbulence [100]. Initial LES experiments for a buoyant plume presented by McDonough and Yang [10] and small-scale simulations of combustion have also been performed using the PMNS equations and show good agreement with experimental data, although comprehensive studies have yet to be completed.

In view of the successes of the incompressible PMNS equations, in this chapter we will use similar techniques applied to the compressible NSEs to obtain a discrete dynamical system, which will be referred to as the compressible PMNS or CPMNS equations. Attention will be given to fundamental differences from the derivation

and formulation of the original PMNS equations. It will be further shown that the CPMNS equations exhibit the same range of dynamical behavior as the full compressible Navier–Stokes equations and the original PMNS equations, and that their bifurcation behavior corresponds to observed physical turbulence. To this end, bifurcation diagrams, regime maps, and time series will be presented and analyzed.

#### 4.1 Analysis

In this section, the CPMNS equations will be derived from the compressible NSEs (CNSEs) in a manner similar to that presented in [100] for the incompressible case. Because we are deriving a model for small-scale fluctuations, we assume  $(\mathbf{x}, t) \in \Omega \times [t_0, t_f]$ , where  $\Omega \subset \mathbb{R}^3$  is a typical grid cell, and  $[t_0, t_f]$  is a typical LES time step. The CNSEs can be scaled to give, in dimensionless, non-conservative form,

$$\partial_t \rho + \partial_j(\rho u_j) = 0, \quad (4.2a)$$

$$\partial_t u_i + u_j \partial_j u_i = -\frac{1}{M^2} \partial_i T + \frac{1}{\rho Re} \left( \partial_j \partial_j u_i + \frac{\mu + \lambda}{\mu} \partial_i \partial_j u_j \right), \quad (4.2b)$$

$$\begin{aligned} \partial_t T + u_j \partial_j T &= -(\gamma - 1) T \partial_j u_j \\ &+ (\gamma - 1) \frac{M^2}{2\rho\mu Re} \sigma_{ij} (\partial_j u_i + \partial_i u_j) + \frac{1}{Pe} \partial_j \partial_j T, \end{aligned} \quad (4.2c)$$

where repeated indices indicate summation,  $1 \leq i, j \leq 3$ ,  $u_i$  are the velocity components,  $\rho$  is density,  $T$  is temperature,  $\mu$  is the dynamic viscosity,  $\lambda$  is the second viscosity coefficient,  $\gamma$  is the specific heat ratio,  $R$  is the gas constant,  $\sigma_{ij} = [\mu(\partial_j u_i + \partial_i u_j) + \delta_{ij} \lambda \partial_k u_k]$  represents the components of the viscous stress tensor, and  $\delta_{ij}$  is the Kronecker delta function. The equations are scaled using velocity scale  $U$ , length scale  $L$ , density scale  $D$ , temperature scale  $\gamma T_\infty$ , and time scale  $L/U$ . This leads to the non-dimensional numbers,  $Re = ULD/\mu$  (Reynolds number),  $Pe = UL/\alpha$  (Peclet number), where  $\alpha$  is the thermal diffusivity, and  $M = U/\sqrt{\gamma RT_\infty}$  (Mach number). This particular form of the energy equation was derived by applying the ideal gas equation of state  $p = \rho RT$ , where  $p$  is pressure, and the linear internal

energy relationship  $e = RT/(\gamma - 1)$  to the internal energy equation as found in Gatski [67].

Before applying a Galerkin procedure to the CNSEs, we must first discuss our treatment of the density. The CPMNS equations, like the original PMNS equations, will be derived by first truncating a Galerkin expansion of the NSEs to a single, arbitrary wave vector. On the other hand, because  $\rho$  appears in the denominator of the compressible NSEs, simple truncation creates difficulties. From a practical standpoint, fluctuation of the truncated density between 0 and 1 will lead to numerical instabilities, as is clear from Eqs (4.2b) and (4.2c). However, recall that our goal with the CPMNS equations is to derive a DDS to serve as the core of a SGS turbulence model for use in a LES method, so we will employ some simplifications on the small scales. To this end, we will make the following two assumptions:

1. The grid cell will be small enough that variations in density across the cell will be small; i.e., at any given time  $t_{ref}$ ,  $\int_{\Omega} \rho(\mathbf{x}, t_{ref}) \approx |\Omega| \rho(\mathbf{x}, t_{ref}) \forall \mathbf{x} \in \Omega$ . This is not true in general for supersonic flows featuring shock waves; however, modern shock-capturing methods dissipate shocks across several grid cells, so this is an acceptable first-order approximation within the context of any practical numerical simulation.
2. The time interval is small enough that temporal turbulent fluctuations in the SGS density will be small relative to the local average density; i.e., the effect of SGS density fluctuations will be dominated by velocity and energy derivatives in the momentum and energy equations. This can be seen because  $\rho$  appears in the denominator of Eqs. (4.2b) and (4.2c). If we decompose  $\rho = \rho_0 + (dt)\rho_1 + (dt)^2\rho_2 + \dots$ , where  $\rho_0$  is some local reference density (such as a time-filtered quantity), on a small enough time interval  $dt$ , we expect the fluctuating terms

to be small enough that

$$\frac{1}{\rho} = \frac{1}{\rho_0 + (dt)\rho_1 + (dt)^2\rho_2 + \dots} = \frac{1}{\rho_0} + \mathcal{O}(dt).$$

Combined, these two assumptions will allow us to effectively treat  $\rho$  as a constant in the context of deriving the CPMNS equations. Recalling that the CNSEs have already been scaled to dimensionless form, this means that we will set  $\rho = 1$  and omit the density equation. However, these assumptions do not mean we are assuming there are no turbulent density fluctuations; rather, we are assuming that the effect of density fluctuations on temperature and velocity are small enough to be neglected. But because spatial derivatives can be large even while fluctuating quantities themselves are small, Eq. (4.2a) implies that velocity fluctuations can have a significant effect on density fluctuations. Since the CPMNS equations are to be used as a SGS turbulence model, coupling with the large scales will require enforcing global conservation laws. Thus, we intend to modify density as part of the global coupling routine, rather than with a direct SGS model. This is analogous to the approach taken with the incompressible PMNS equations, where the divergence-free mass conservation law is not used in the construction of the DDS, but rather is used to enforce global mass conservation on the model output via a projection method.

To construct the CPMNS equations, we assume solutions of the NSEs exist as  $L^2$  functions on the grid cell, so that a Fourier representation exists for velocity and temperature:

$$u_i(\mathbf{x}, t) = \sum_k^{\infty} a_{i,\mathbf{k}}(t)\varphi_{\mathbf{k}}(\mathbf{x}), \quad (4.3a)$$

$$T(\mathbf{x}, t) = \sum_k^{\infty} e_{\mathbf{k}}(t)\varphi_{\mathbf{k}}(\mathbf{x}). \quad (4.3b)$$

Here,  $\{\varphi_{\mathbf{k}}(\mathbf{x})\}$ , is an unspecified, countable, orthonormal set of basis functions, which we assume to be complete in  $L^2(\Omega)$ . We assume that elements of  $\{\varphi_{\mathbf{k}}(\mathbf{x})\}$  have the



wave-like properties:

$$\tilde{\varphi}_{\mathbf{k}} \equiv \frac{1}{k_i} \partial_i \varphi_{\mathbf{k}}, \quad (4.4)$$

$$C_{\mathbf{k}} \tilde{\varphi}_{\mathbf{k}} \in \{\varphi_{\mathbf{k}}(\mathbf{x})\}, \quad (4.5)$$

$$\partial_i \partial_j \varphi_{\mathbf{k}} = -k_i k_j \varphi_{\mathbf{k}}, \quad (4.6)$$

where  $C_{\mathbf{k}}$  is some normalization constant. This basis will be used to apply a Galerkin procedure to the momentum equation as follows.

First, substitute Eqs. (4.3a) and (4.3b) into Eq. (4.2b) and apply the wave-like property of the basis functions to the spatial derivatives to obtain:

$$\begin{aligned} \sum_{\mathbf{k}} \dot{a}_{i,\mathbf{k}} \varphi_{\mathbf{k}} + \sum_{l,\mathbf{m}} m_j a_{j,l} a_{i,\mathbf{m}} \varphi_l \tilde{\varphi}_{\mathbf{m}} \\ = \sum_{\mathbf{k}} \left( -\frac{1}{M^2} k_i e_{\mathbf{k}} - \frac{1}{Re} \left( |\mathbf{k}|^2 a_i + \frac{\mu + \lambda}{\mu} k_i k_j a_j \right) \right) \varphi_{\mathbf{k}}, \end{aligned} \quad (4.7)$$

where “ $\dot{\cdot}$ ” indicates differentiation with respect to time. Next, multiply both sides by  $\varphi_{\mathbf{k}}$  and integrate over the domain  $\Omega$ . Orthonormality gives

$$\begin{aligned} \dot{a}_{i,\mathbf{k}} + \sum_{l,\mathbf{m}} m_j a_{j,l} a_{i,\mathbf{m}} \int_{\Omega} \varphi_{\mathbf{k}} \varphi_l \tilde{\varphi}_{\mathbf{m}} = -\frac{1}{M^2} k_i e_{\mathbf{k}} \\ - \frac{1}{Re} \left( |\mathbf{k}|^2 a_{i,\mathbf{k}} + \frac{\mu + \lambda}{\mu} k_i k_j a_{j,\mathbf{k}} \right), \quad i, j = 1, 2, 3. \end{aligned} \quad (4.8)$$

To simplify notation, we define

$$A_j = k_j \int_{\Omega} \varphi_{\mathbf{k}}^2 \tilde{\varphi}_{\mathbf{k}} \quad (4.9)$$

and truncate the system to a single mode  $\mathbf{k}$ , yielding

$$\dot{a}_i + A_j a_i a_j = -\frac{1}{M^2} k_i e - \frac{1}{Re} \left( |\mathbf{k}|^2 a_i + \frac{\mu + \lambda}{\mu} k_i k_j a_j \right), \quad (4.10)$$

where the  $\mathbf{k}$  subscript is suppressed. Note that in the case of  $\Omega$  being a cube with periodic or zero Dirichlet boundary conditions, the conditions in Eqs. (4.4)–(4.6) imply that sines and cosines are the basis functions, so  $A_j = 0$ . However, because our

domain is approximately a single grid cell in a turbulent flow, boundary conditions will be neither periodic nor zero everywhere, so we do not expect  $A_j = 0$ .

To arrive at a discrete equation, Eq. (4.10) is discretized according to a simple forward Euler scheme with time step  $\tau$ , as follows:

$$a_i^{(n+1)} = a_i^{(n)} - \tau \left[ \frac{k_i}{M^2} e^{(n)} + \frac{1}{Re} \left( |\mathbf{k}|^2 a_i + \frac{\mu + \lambda}{\mu} k_i k_j a_j^{(n)} \right) + A_j a_i^{(n)} a_j^{(n)} \right]. \quad (4.11)$$

Rearranging to combine all  $a_i$  terms yields the following for the momentum equations:

$$\begin{aligned} a_i^{(n+1)} = & a_i^{(n)} \left( \frac{1 - \tau |\mathbf{k}|^2 / Re}{\tau A_i} - a_i^{(n)} \right) \tau A_i \\ & - \tau \left[ \frac{k_i}{M^2} e^{(n)} + \left( \frac{\mu + \lambda}{\mu} \frac{1}{Re} k_i k_j a_j^{(n)} + A_j a_i^{(n)} a_j^{(n)} \right) (1 - \delta_{ij}) \right]. \end{aligned} \quad (4.12)$$

If we define the parameter

$$\epsilon_i = \frac{1 - \frac{\tau |\mathbf{k}|^2}{Re}}{\tau A_i},$$

apply the scaling  $a_i \rightarrow \epsilon_i a_i$ , and divide both sides by  $\epsilon_i$ , we get

$$\begin{aligned} a_i^{(n+1)} = & \epsilon_i \tau A_i a_i^{(n)} (1 - a_i^{(n)}) \\ & - \tau \left[ \frac{k_i}{M^2 \epsilon_i} e^{(n)} + \left( \frac{\mu + \lambda}{\mu} \frac{1}{Re} \frac{\epsilon_j}{\epsilon_i} k_i k_j a_j^{(n)} + \epsilon_j A_j a_i^{(n)} a_j^{(n)} \right) (1 - \delta_{ij}) \right]. \end{aligned} \quad (4.13)$$

The purpose of the scaling is to obtain the term  $\beta_i a_i^{(n)} (1 - a_i)$ , which is the right-hand side of the logistic map and the core of the original PMNS equations. This approach contrasts with McDonough's assumption  $1 - \tau |\mathbf{k}|^2 / Re = \tau A_j$  [100] and results in slightly different formulation of several of the bifurcation parameters below. To further simplify, we assume  $\int_{\Omega} \varphi_{\mathbf{k}}^2 \tilde{\varphi}_{\mathbf{k}} = 1$ , and we introduce local, directional Reynolds numbers  $Re_i$  in order to more effectively model anisotropic turbulence. Thus we can express the coefficients of Eq. (4.13) as bifurcation parameters:

$$\beta_i = 1 - \frac{\tau |\mathbf{k}|^2}{Re_i}, \quad (4.14a)$$

$$\xi_{ij} = (1 - \delta_{ij}) \frac{\tau \epsilon_j}{Re_i \epsilon_i} \frac{\mu + \lambda}{\mu} k_i k_j, \quad (4.14b)$$

$$\alpha_i = \frac{\tau k_i}{M^2 \epsilon_i}. \quad (4.14c)$$

This leads to the discrete momentum equation,

$$a_i^{(n+1)} = \beta_i a_i^{(n)} (1 - a_i^{(n)}) - \beta_j a_i^{(n)} a_j^{(n)} (1 - \delta_{ij}) - \xi_{ij} a_j^{(n)} - \alpha_i e^{(n)}. \quad (4.15)$$

We can apply the same procedure to the energy equation. The steps are analogous to those used to derive the momentum equation, so we give each term from Eq. (5.1c) with the analogous term after single-mode truncation and defining  $\Phi = \int_{\Omega} \tilde{\varphi}_{\mathbf{k}}^2 \varphi_{\mathbf{k}}$ :

$$\partial_t T \rightarrow \dot{e} \quad (4.16a)$$

$$u_j \partial_j T \rightarrow a_j e A_j \quad (4.16b)$$

$$-(\gamma - 1) T \partial_j u_j \rightarrow -(\gamma - 1) a_j e A_j \quad (4.16c)$$

$$\mu (\partial_j u_i + \partial_i u_j)^2 \rightarrow \mu (k_j a_i + k_i a_j)^2 \Phi \quad (4.16d)$$

$$\delta_{ij} \lambda \partial_k u_k (\partial_i u_j + \partial_j u_i) \rightarrow 2 \lambda k_i k_j a_i a_j \Phi \quad (4.16e)$$

$$\frac{1}{Pe} \partial_j \partial_j T \rightarrow -\frac{|\mathbf{k}|^2}{Pe} e. \quad (4.16f)$$

Simplifying, we have the single-mode energy equation:

$$\dot{e} + \gamma a_j e A_j = \Phi \frac{(\gamma - 1) M^2}{2 Re} \left[ (k_j a_i + k_i a_j)^2 + \frac{2 \lambda}{\mu} k_i k_j a_i a_j \right] - \frac{|\mathbf{k}|^2}{Pe} e. \quad (4.17)$$

Forward Euler discretization in all but the dissipative term and applying the  $a_i \rightarrow \epsilon_i a_i$  scaling gives

$$e^{(n+1)} \left( 1 + \frac{\tau}{Pe} |\mathbf{k}|^2 \right) = e^{(n)} + \tau \left\{ \Phi \frac{(\gamma - 1) M^2}{Re} \left[ \frac{1}{2} (k_j \epsilon_i a_i^{(n)} + k_i \epsilon_j a_j^{(n)})^2 + \frac{\lambda}{\mu} k_i k_j \epsilon_i \epsilon_j a_i^{(n)} a_j^{(n)} \right] - \gamma \epsilon_j a_j^{(n)} e^{(n)} A_j \right\} \quad (4.18)$$

Here, the dissipative term has been treated implicitly because numerical experiments revealed that explicit treatment caused severe stability problems, as is true rather

generally for linear diffusion. Next, we define the following bifurcation parameters:

$$\beta_T = \frac{\tau |\mathbf{k}|^2}{Pe}, \quad (4.19a)$$

$$\zeta_{ij} = \frac{\tau \lambda \Phi(\gamma - 1) M^2 \epsilon_i \epsilon_j k_i k_j}{\mu Re}, \quad (4.19b)$$

$$\eta_{ij} = k_i \epsilon_j \sqrt{\frac{\tau \Phi(\gamma - 1) M^2}{2 Re}}, \quad (4.19c)$$

which allows us to write the discrete energy equation as

$$e^{(n+1)} = [ e^{(n)}(1 - \gamma \beta_j a_j^{(n)}) + 2 \left( \eta_{ji} \eta_{ji} (a_i^{(n)})^2 + \eta_{ij} \eta_{ji} a_i^{(n)} a_j^{(n)} \right) + \zeta_{ij} a_i^{(n)} a_j^{(n)} ] / (1 + \beta_T). \quad (4.20)$$

We can then combine Eqs. (4.15) and (4.20) into the following DDS, to which we will refer as the CPMNS equations:

$$a_i^{(n+1)} = \beta_i a_i^{(n)} (1 - a_i^{(n)}) - \beta_j a_i^{(n)} a_j^{(n)} (1 - \delta_{ij}) - \xi_{ij} a_j^{(n)} - \alpha_i e^{(n)}, \quad (4.21a)$$

$$e^{(n+1)} = [ e^{(n)}(1 - \gamma \beta_j a_j^{(n)}) + 2 \left( \eta_{ji} \eta_{ji} (a_i^{(n)})^2 + \eta_{ij} \eta_{ji} a_i^{(n)} a_j^{(n)} \right) + \zeta_{ij} a_i^{(n)} a_j^{(n)} ] / (1 + \beta_T), \quad (4.21b)$$

where summation in the momentum equation is over  $j$  alone.

Certain modifications and assumptions must be made to achieve the desired range of dynamical behavior. Although the formula for  $\beta_i$  constrains its value to be less than unity, chaotic behavior requires the value to range as high as four; hence, we will apply a multiplier of four to the term,  $\beta_i a_i^{(n)} (1 - a_i^{(n)})$ , as done in [97]. Thus, the system that will be used in actual computations for the present work is given as follows:

$$a_i^{(n+1)} = 4\beta_i a_i^{(n)} (1 - a_i^{(n)}) - \beta_j a_i^{(n)} a_j^{(n)} (1 - \delta_{ij}) - \xi_{ij} a_j^{(n)} - \alpha_i e^{(n)}, \quad (4.22a)$$

$$e^{(n+1)} = [ e^{(n)}(1 - \gamma \beta_j a_j^{(n)}) + 2 \left( \eta_{ji} \eta_{ji} (a_i^{(n)})^2 + \eta_{ij} \eta_{ji} a_i^{(n)} a_j^{(n)} \right) + \zeta_{ij} a_i^{(n)} a_j^{(n)} ] / (1 + \beta_T), \quad (4.22b)$$

As with the original PMNS equations, the CPMNS equations retain all the essential symmetries and nonlinearities of the original NSEs. As shown below, this leads to

similar dynamical behavior. Observe that there are 28 total bifurcation parameters. This would seem to present a closure problem similar to that of other turbulence models; however, all the bifurcation parameters can be expressed in terms of flow-related quantities, such as local Reynolds numbers and characteristic wavenumbers. In contrast to typical turbulence models, where the model constants must be calibrated from experimental data, the bifurcation parameters of the CPMNS equations are dynamic, and the principal issue will be determining how to compute these from the large-scale results.

It might seem unexpected that a discrete map could serve as the basis of a turbulence model, as the CNSEs are a continuous system. However, consider the case of the Lorenz equations [101] and the Hénon map. The former set of equations is likewise a single-mode truncation of fluid flow equations, although in the case of Lorenz, the system to be truncated is already a simplification of the original NSEs based on 2-D convection assumptions. Further, the Lorenz equations are still a continuous system of ODEs, whereas the CPMNS equations are a discrete system. However, recall that the Hénon map [102] is a DDS that generates the Poincaré section for a simplified model of the Lorenz attractor. Hénon constructed a discrete map that mimicked the way the Lorenz equations stretch, fold, and contract a volume. Thus there is an important theoretical link between continuous and discrete dynamical systems. We can then envision the CPMNS equations as mimicking a single topological cycle of a turbulent fluid flow on a small parcel of fluid, although clearly, the action is much more complicated than that modeled by the Hénon map.

As an aside, a similar discrete equation can be derived for the density equation, but this is not done here, as we assumed from the beginning that the fluctuations in  $\rho$  are small enough to be neglected when deriving the CPMNS equations. In fact, this assumption was motivated by early numerical experiments, which did incorporate density. However, these early versions of the CPMNS equations exhibited stability

problems due to the linearity of the density equation. Further, retaining coupling with a density equation in order to arrive at a DDS requires additional assumptions which are more difficult to justify. However, despite the omission of a density equation, there are still non-trivial differences from the original, incompressible PMNS equations, as there are additional dissipative terms in the momentum equation and coupling with the energy equation.

## 4.2 Bifurcation analysis

In this section we present results obtained by varying the bifurcation parameters in the momentum and energy equations. Regimes are identified on the basis of their power spectral densities (PSDs) using the same automated tool employed in [100]. This tool analyzes the PSDs of velocity series produced by the system and assigns a label based on the spectral peaks. PSDs with only one peak are periodic, those with multiple commensurate frequencies are subharmonic, and those with incommensurate peaks are quasiperiodic. In addition, if there are non-smooth intervals in between spectral peaks, the tool adds the description of being “broadband” or “noisy.” The regime maps presented thus give a broad overview of the kind of dynamical behavior that can be exhibited by the CPMNS equations and a qualitative understanding of the transition behavior. In addition to this, we present details of representative behavior from each regime in the form of time series, phase portraits, bifurcation diagrams, and PSDs.

Calculations were performed on a single Pentium IV processor at the University of Kentucky. All results were obtained using 64-bit Fortran. A typical run consisted of  $2 \times 10^4$  iterations with the last 5000 iterations subjected to statistical analysis. A standard radix-2 FFT with 2048 points was used to compute PSDs characterizing the solution regimes. Early experiments showed that 2048 points were sufficient to generate the regime maps while still keeping computation time low.

### 4.2.1 Bifurcation behavior and PSD analysis

As mentioned before, the CPMNS equations exhibit the same range of dynamical behavior as the original PMNS equations. Because of the relatively high computational cost required to calculate traditional measures of chaos such as Lyapunov exponents and fractal dimension, the automated tool employed characterizes dynamical behavior based on PSD of the time series of  $a_1$  (due to coupling, all components tend to exhibit the same behavior) and identifies the following solution regimes: steady, periodic, periodic with different fundamental frequency, subharmonic, phase-locked, quasiperiodic, noisy subharmonic, noisy phase-locked, noisy quasiperiodic with fundamental, noisy quasiperiodic without fundamental, broadband with fundamental, broadband with different fundamental, broadband without fundamental, and divergent. In this section, we present some representative time series with their PSDs to illustrate how the tool works. Note that here, noisiness in the PSD reflects the behavior of the DDS itself and may be associated with strange attractors, in contrast to inherent instrumental noise at high- $k$  modes in experimental results.

In the following numerical experiments,  $\beta_i$  were varied, while the other bifurcation parameters for the CPMNS equations were, except when otherwise specified, defined using values that maintained stability over significant ranges of  $\beta_i$ :

$$\alpha_i = 1 \times 10^{-4} \quad (4.23a)$$

$$\xi_{ij} = 0.005(1 - \delta_{ij}) \quad (4.23b)$$

$$\zeta_{ij} = 0.03 \quad (4.23c)$$

$$\eta_{ij} = 0.01 \quad (4.23d)$$

$$\mathbf{a}^{(0)} = (0.1041, 0.1022, 0.1053) \quad (4.23e)$$

$$e^{(0)} = 0.01 \quad (4.23f)$$

$$\beta_T = 0.55 \quad (4.23g)$$

$$\gamma = 1.4 \quad (4.23h)$$

for all  $i$  and  $j$ .

The bifurcation diagrams in this section were created by plotting the last 400 steps of 60,000 iterations against the value of  $\beta_i$  used to generate that particular sequence. Of course, the number of potential bifurcation diagrams is infinite since the DDS depends on more than one parameter. We chose to exhibit two such diagrams in order to stress the similarity to and differences with the bifurcation diagram for the logistic map.

Figure 4.1 shows a bifurcation diagram for the above parameters where  $\beta_1 = \beta_2 = \beta_3 = \beta$  and other parameters as given above, corresponding to isotropic turbulence, scaled for direct comparison with the logistic map. There are some notable similarities between this bifurcation diagram and that of the logistic map, seen in Figure 4.2. First, Figure 4.1 shows a period-doubling Feigenbaum bifurcation sequence associated with the logistic map, in this case on the interval  $4\beta \in [3, 3.633]$ . Note that in the close-up views presented, a structure similar to the logistic map bifurcation sequence is revealed. Observe also that there are bifurcation parameter values, such as  $4\beta = 3.636$ , where chaos transitions temporarily back to periodicity. This is reminiscent of turbulent-to-laminar transitions observed experimentally by Patel and Head [103]. It is also similar to the “periodic windows” of the logistic map. This is to be expected, as the logistic map serves as the core of the CPMNS equations.

There are also a number of structural dissimilarities between the bifurcation sequence for the logistic map and the bifurcation sequence for CPMNS shown in Figure 4.1. There is a prominent discontinuity in Figure 4.1 at  $\beta = 3.633$ , while the bifurcation diagram in Figure 4.2 appears to be continuous. Further, this discontinuity appears after only one period-doubling bifurcation, while the logistic map continues a period-doubling sequence until chaos is reached.

We next considered a bifurcation diagram for a case of mild anisotropy. Figure 4.3 shows one such example, where  $\beta_1 = \beta$ ,  $\beta_2 = 0.99\beta$ ,  $\beta_3 = 0.98\beta$ ,  $\alpha =$



(0.0001, 0.0002, 0.00013), and other parameters as given above. In this case, the structural dissimilarity with Figure 4.2 is more apparent, and there are additional dissimilarities with Figure 4.1 as well. In this particular case, the first bifurcation happens at approximately 3.038, and there are multiple discontinuities at higher values of  $\beta$ .

Figure 4.1: CPMNS bifurcation diagram for  $\beta_i = \beta$  for all  $i$  with zoom in

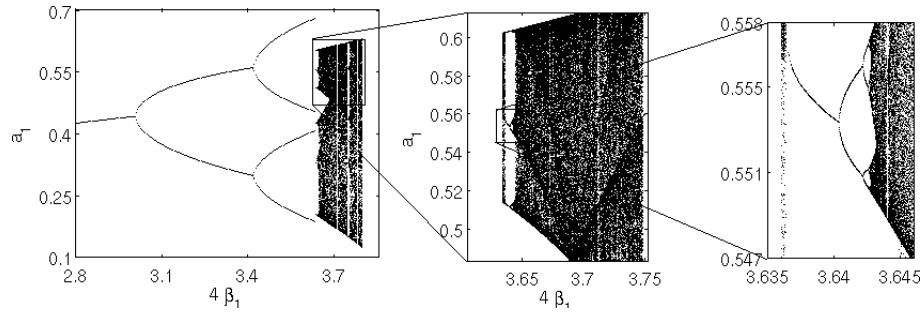


Figure 4.2: Logistic map bifurcation diagram with zoom in

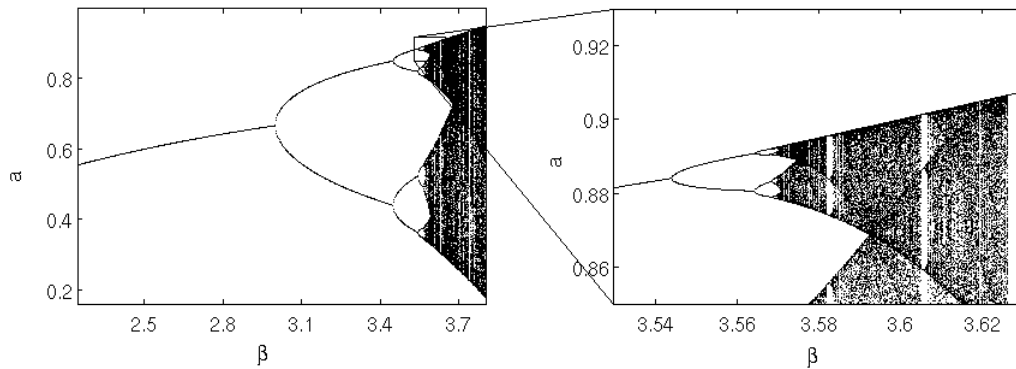
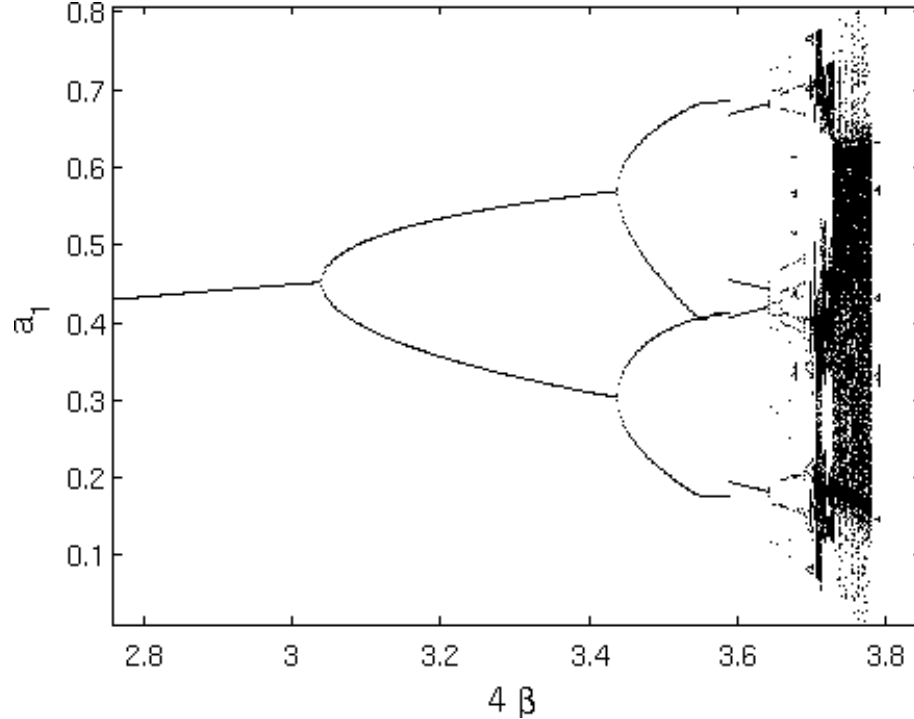


Figure 4.4 shows the PSDs, time series and phase portraits of various types of signals along with 80 representative steps of the associated time series. Note the values in (d) and (e) correspond to much stronger anisotropy than in the first three images. For the two corresponding phase portraits, the insets stretch the vertical axis so that the structure may be seen more clearly. PSDs and the corresponding phase portraits were constructed from the same 2048-point series for the given values of  $\beta_i$  and  $\alpha_i$ . Dynamical behavior is established from the PSDs by analyzing the character

Figure 4.3: CPMNS bifurcation diagram for  $\beta_1 = \beta$ ,  $\beta_2 = 0.99\beta$ ,  $\beta_3 = 0.98\beta$ ,  $\alpha = (0.0001, 0.0002, 0.00013)$  with zoom in



of the spectral peaks. Periodic and subharmonic behavior is characterized by spikes tens of decibels over the noise at commensurate frequency intervals. Quasiperiodic behavior has spectral peaks at incommensurate frequencies, while strict broadband behavior has no observable spectral peaks.

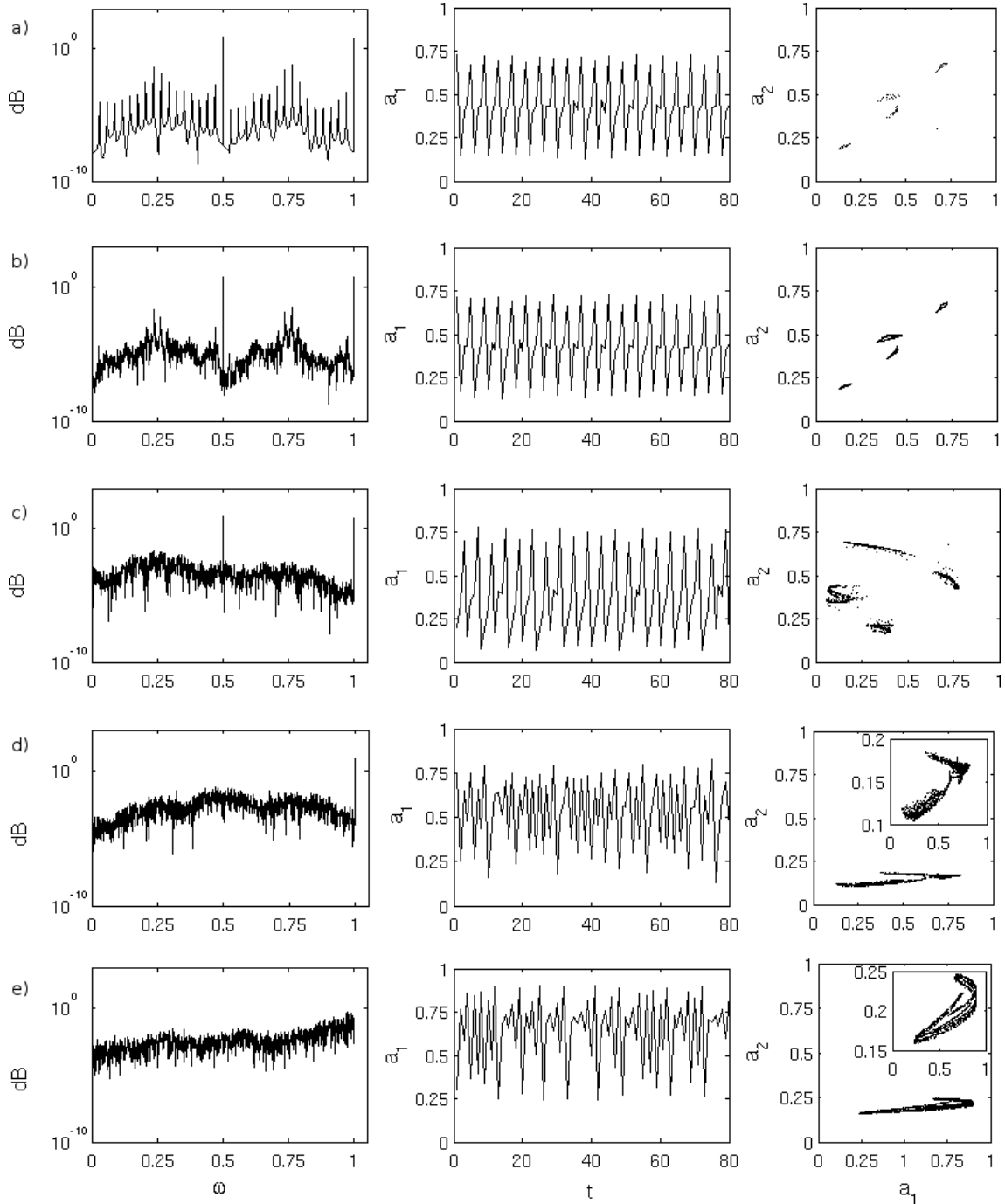
Here, we focus on noisy signals, as the existence of periodic and subharmonic behavior can be easily established from the bifurcation diagrams. The phase portraits further help identify the dynamical behavior. In order, the PSDs correspond to (a) quasiperiodic (with a previous subharmonic bifurcation), (b) noisy quasiperiodic with fundamental frequency, (c) noisy subharmonic, (d) broadband with fundamental frequency and (e) pure broadband. In terms of real fluid turbulence, both subharmonicity and quasiperiodicity have been observed experimentally as transition stages to turbulence. See, for example, the results of Takeda [104]. The former is the main constituent of Feigenbaum sequences for quadratic maps, and the latter is a funda-

mental stage in the Ruelle and Takens bifurcation sequence. Despite the fact that time series corresponding to quasiperiodic flow can be rather complicated, the flow is not yet turbulent; in particular, it is not sensitive to initial conditions. The noisy subharmonic and broadband with fundamental frequency are reminiscent of the turbulent mixing layers found in Van Dyke [105], in which large-scale structures appear to follow a periodic (or nearly periodic) law, while the small-scale turbulent fluctuations are clearly non-periodic. Likewise in the same book, the wake of a turbulent cylinder is shown to shed large, coherent turbulent structures in a nearly periodic fashion.

Note that as the PSDs become more broadband-like, new structures appear in the time series. The quasiperiodic (a), noisy quasiperiodic (b), and noisy subharmonic (c) cases show similar, fairly regular time series, while the broadband with fundamental (d) and pure broadband (e) cases are both highly irregular and non-repeating. The subharmonic frequency can be seen in the nearly alternating amplitudes in the time series of (a), (b), and (c). Note especially the intermittency in the pure broadband signal. Intermittency is an important characteristic of physical turbulence, so a subgrid-scale synthetic velocity model ought to be able to exhibit this behavior as well. Finally, observe that the time series are fairly similar for most of the broadband behavior, suggesting that modeling using the CPMNS equations will be fairly forgiving—a desirable feature, as the bifurcation parameters must be computed dynamically from imperfect numerical data (typically obtained via some form of deconvolution of resolved-scale calculations) in full LES.

The noise in the above PSDs is not quite white noise, as the PSDs are not completely flat. As the phase portraits demonstrate, the noisy signals exhibit the kind of behavior commonly associated with chaotic dynamical systems, as there is clear structure in each phase portrait. This is consistent with the fact the CPMNS equations are a set of algebraic maps and therefore are a deterministic system. Further, recalling

Figure 4.4: PSDs, time series, and phase portraits for  $\beta =$  (a) (0.928458, 0.919173, 0.909889) (b) (0.92874, 0.919453, 0.910165) (c) (0.928176, 0.918894, 0.909612), (d) (0.9556, 0.5844, 0.854), (e) (0.9444, 0.5154, 0.32). In (a), (b), and (c),  $\alpha_i = 0.0001 \forall i$ , while in (d) and (e),  $\alpha = (0.0001, 0.002, 0.0013)$



that the CPMNS equations themselves were derived from the NSEs, the occurrence of noisy signals after a brief transition through subharmonic and quasiperiodic regimes is generally consistent with the theory of Ruelle and Takens that the transition to physical turbulence corresponds to a relatively short bifurcation sequence to chaos as  $Re$  increases in the NSEs [12], although there are many more bifurcations in the discrete system. Recalling that the attractor for a continuous quasiperiodic dynamical system is a torus, note that the attractor for the quasiperiodic discrete series appears to be a number of closed “rings.” Fundamental frequencies can be associated with clear divisions of the attractor into 2 or more discrete pieces, while the phase portrait corresponding to the pure broadband signal in (e) is not divided into multiple distinct pieces.

When at least two of the three  $\beta_i$ s are equal, there is a tendency for the corresponding  $a_i$ s to lock, as was also observed in the 2-D case [100]; i.e., for some  $N$  and  $i, j$  pair such that  $\beta_i = \beta_j$ ,  $a_i^{(n)} = a_j^{(n)}$  for all  $n > N$ . However, this phenomenon was observed to occur exclusively for  $\beta_i = \beta_j$ , which is unlikely to ever hold in a real simulation, as it would require the velocity components and length scales to be exactly equal in each of the two directions. Nevertheless, it is interesting to see why this occurs. Suppose  $\beta = \beta_2 = \beta_3$ ,  $\alpha = \alpha_2 = \alpha_3$ ,  $\xi = \xi_{21} = \xi_{31}$ , and  $\xi^* = \xi_{32} = \xi_{23}$ . Substituting these into Eq. (4.22a) yields:

$$a_2^{(n+1)} = \beta a_2^{(n)}(1 - a_2^{(n)}) - \beta_1 a_1^{(n)} a_2^{(n)} - \beta a_3^{(n)} a_2^{(n)} - \xi a_1^{(n)} - \xi^* a_3 - \alpha e^{(n)}, \quad (4.24)$$

$$a_3^{(n+1)} = \beta a_3^{(n)}(1 - a_3^{(n)}) - \beta_1 a_1^{(n)} a_3^{(n)} - \beta a_2^{(n)} a_3^{(n)} - \xi a_1^{(n)} - \xi^* a_2 - \alpha e^{(n)}. \quad (4.25)$$

Subtracting (4.24) from (4.25) then provides:

$$\begin{aligned} a_2^{(n+1)} - a_3^{(n+1)} &= 4\beta \left[ a_2^{(n)} \left( 1 - a_2^{(n)} \right) - a_3^{(n)} \left( 1 - a_3^{(n)} \right) \right] + (\xi^* - \beta_1 a_1^{(n)}) \left( a_2^{(n)} - a_3^{(n)} \right) \\ &= \left( 4\beta + \xi^* - \beta_1 a_1^{(n)} \right) \left( a_2^{(n)} - a_3^{(n)} \right) - 4\beta \left( \left( a_2^{(n)} \right)^2 - \left( a_3^{(n)} \right)^2 \right) \\ &= \left( 4\beta \left( 1 - a_2^{(n)} - a_3^{(n)} \right) + \xi^* - \beta_1 a_1^{(n)} \right) \left( a_2^{(n)} - a_3^{(n)} \right) \end{aligned}$$

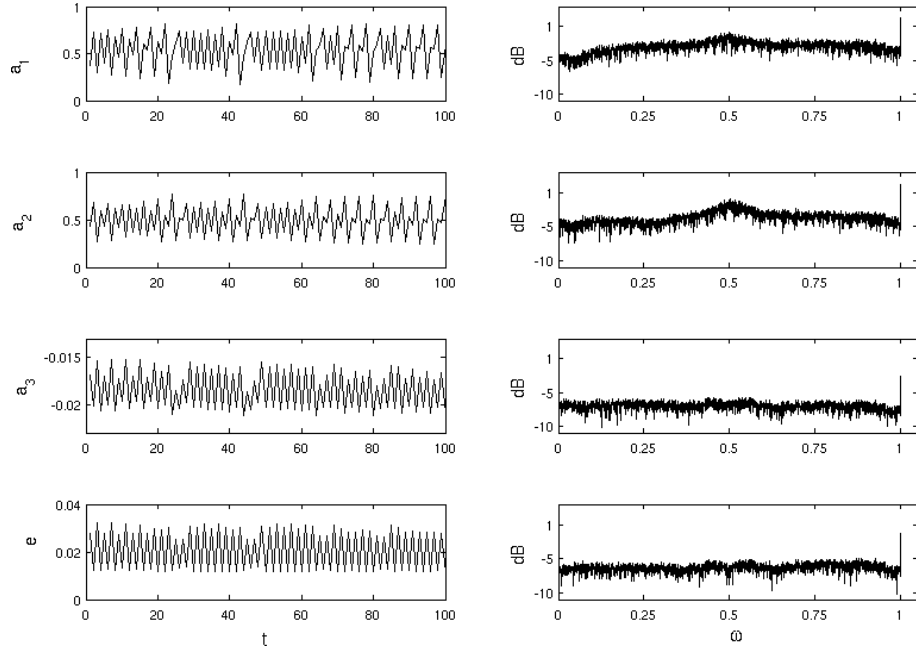
If  $\left|4\beta \left(1 - a_2^{(n)} - a_3^{(n)}\right) + \xi^* - \beta_1 a_1^{(n)}\right| < 1$ , this will be a contractive map leading to  $a_2$  and  $a_3$  converging together. This inequality is clearly within the realm of possibility, as we expect  $|a_i|$ ,  $\xi_{ij}$ , and  $\beta_i$  all to be less than unity. It has been observed over the course of numerical experiments that even mild anisotropy in  $\beta_i$  and  $\alpha_i$  is sufficient to prevent locking, so we do not expect this to occur in full simulations.

Figure 4.5 shows 100 representative time steps and PSDs for all three components of  $\mathbf{a}$  and  $e$  for  $\boldsymbol{\beta} = (0.93, 0.85, 0.41)$  and  $\boldsymbol{\alpha} = (0.0001, 0.002, 0.0013)$ , which corresponds to anisotropic, broadband behavior with a single fundamental frequency. Note that the time series for both  $a_1$  and  $a_2$  exhibit recurring, intermittent, small oscillations that appear to be absent in the signal of  $a_3$ . However, there is no obvious, qualitative difference in the PSDs of the three signals, suggesting that there is no reliable way to determine intermittency of a signal from the PSD alone. Also, the  $e$  series is entirely negative with a significantly smaller absolute value than that of any of the  $a_i$ s, which are positive. In general, velocity series tend to be positive, although some very small negative velocity series have been observed. This means that in implementation, the effect of this model will be to add kinetic energy into the flow if the final result receives the same sign as the large-scale velocity component, suggesting that an equivalent amount of thermal energy ought to be subtracted in order to maintain conservation of energy. At the same time, nearly uniform positivity of velocity components suggests the need for a transformation (e.g., subtracting their mean values) permitting both signs as occurs in physical turbulent flows.

### 4.2.2 Regime maps

While the above analysis is instructive for understanding core characteristics of the CPMNS equations, unlike the logistic map, there are 28 potential bifurcation parameters to be investigated. In this section, we present 2-D regime maps of bifurcation behavior for bifurcation parameters of both the momentum and energy equations.

Figure 4.5: Time series and phase portraits for  $\beta = (0.93, 0.85, 0.41)$ .



These regime maps were produced automatically using an algorithm designed to characterize solutions based on their power spectra.

#### 4.2.2.1 Momentum parameters

The regime map in Figure 4.6 illustrates that the CPMNS equations exhibit the same range of dynamical behavior as a real fluid flow. In particular, transitions between regimes moving in the direction of increasing  $\beta$  correspond to real transitional behavior: steady behavior gives way to periodic, which becomes subharmonic, and then transitions through several quasiperiodic and broadband regimes before reaching a distinct, yellow, fully broadband (chaotic) regime and finally diverging. There does, however, seem to be significantly less phase-locked behavior than in the incompressible case, and often this does not appear as an Arnol'd tongue. Another interesting characteristic of this regime map is that periodic behavior can transition directly to quasiperiodic (as in the incompressible case [100]) without first passing through a subharmonic bifurcation, which is the Ruelle and Takens bifurcation sequence [12].

Figure 4.7 shows a close-up view of the boxed region of the regime map depicted in Figure 4.6. Note that there is not a definite boundary between zones. Rather, the different regime zones are interspersed in a manner suggestive of fractal zonal boundaries. This establishes that the bifurcation sequence is far more complex than a simple progression from stationary to broadband, but in fact shifts back and forth among several regimes, including even periodic behavior, before finally settling on pure broadband behavior, similar to what can be seen with the incompressible PMNS equations, and analogous to experimental results in the incompressible case, e.g., Gollub and Benson [106].

A key concern of implementing the CPMNS equations as part of a LES SGS model is maintaining stability. As can be seen in the figures already presented, the divergent (black) zone does not have a clearly defined, regular boundary, so it is important to determine an appropriate maximum value for  $\beta$  that guarantees stability, but also includes the full range of dynamical behavior. There are sizable “noisy” bands when the  $\beta_i$  are large, which is consistent with physical turbulence, since  $\beta \rightarrow 1$  as  $Re \rightarrow \infty$ . Although there are black bands of instability for smaller values of  $\beta$ , it should be noted that in actual implementation, the CPMNS equations are to be used as a turbulence model and thus would be turned off when there are no chaotic subgrid-scale fluctuations to be modeled, i.e., when  $\beta_i \lesssim 0.7$ . In general, we see that  $\beta_i > 0.9$  must hold for at least one  $i$  in order to see noisy behavior, and this criterion was implemented in simulations.

Figure 4.8 is a regime map for  $\beta$  vs.  $\xi$ . Here  $\xi_{ij} = \xi$  for all  $i$  and  $j$ , and  $\beta_i = \beta$  for all  $i$ . Observe that in Eq. (4.14b),  $\xi$  is associated with the dissipative terms in the NSEs and is inversely proportional to  $Re$ . The regime map shows the expected behavior that as  $\xi$  increases, the bifurcation sequence is shifted, requiring larger values of  $\beta$  to transition. But note that for  $\xi > 0.26$ , the regime map shows that no broadband behavior is exhibited at all, and the CPMNS equations are almost



Figure 4.6: Regime map of  $\beta_3$  vs.  $\beta_1 = \beta_2$ ,  $\alpha_i = 0.0001$

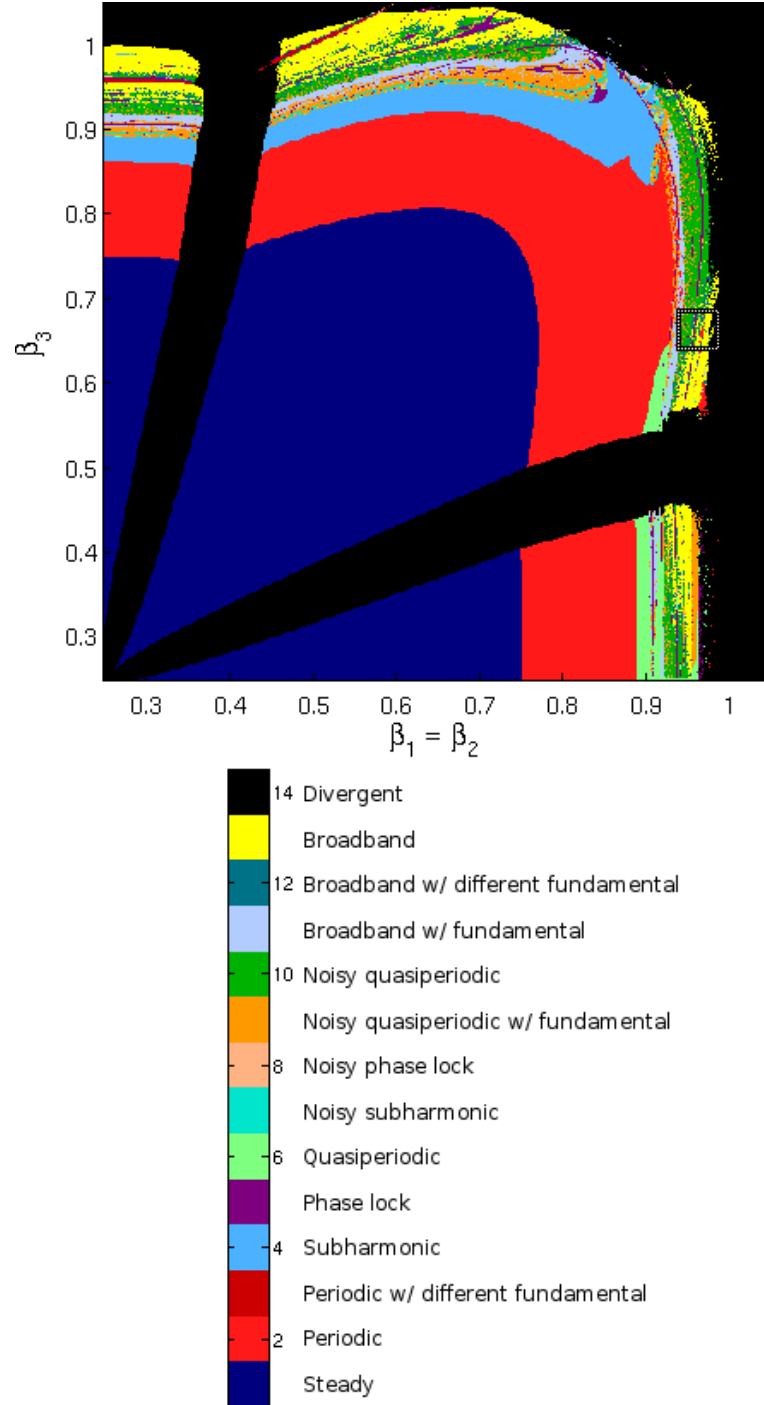
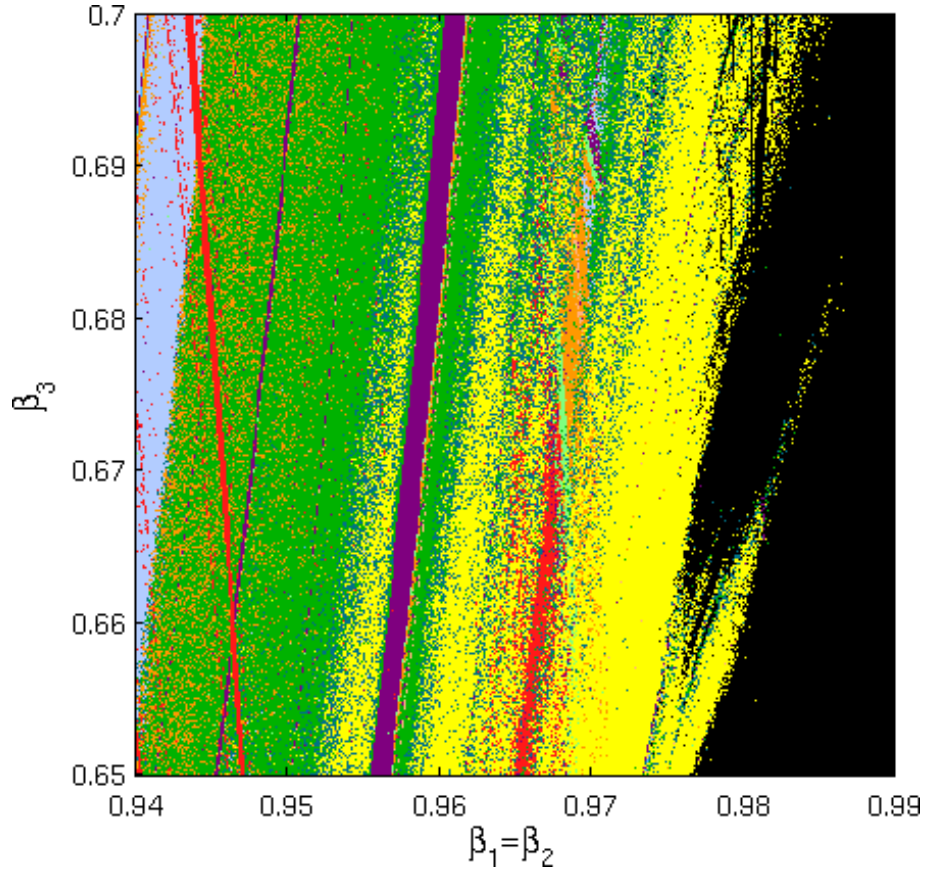


Figure 4.7: Close-up of regime map of  $\beta_3$  vs.  $\beta_1 = \beta_2$ ,  $\alpha_i = 0.0001$



completely unstable. Linear terms tend to destabilize a DDS, as when the coefficients are large enough, they simply amplify the variable and result in diverging to  $\pm\infty$ . It appears from this map that limiting  $\xi < 0.1$  captures the desired dynamical behavior. Also, note that as  $\xi$  increases, the stable zone is bounded below by an increasing value of  $\beta$ . In the code used in this work, a check to ensure that  $\xi_{ij} < 0.26$  was implemented.

Figure 4.9 shows the interaction between  $\beta$  and the coefficient on the energy term,  $\alpha$ , where  $\alpha_i = \alpha$  for all  $i$ . As  $\alpha$  increases, at first, the bifurcation sequence appears to be compressed; i.e., a higher value of  $\alpha$  results in a lower value of  $\beta$  corresponding to the same point in the bifurcation sequence. Increasing  $\alpha$  corresponds to decreasing the square of the Mach number, which is consistent with experimental results, such as older experiments of Demetriades [107], and more recent experiments, such as those of Chen et al. [108], which indicate that increasing Mach number has

an overall stabilizing effect on a flow. But note also that as  $\alpha$  increases past 3, totally different dynamical behavior emerges. Instead of the usual transition to periodicity, steady-state behavior gives way immediately to quasiperiodicity, or periodicity with a different fundamental frequency, with Arnol'd tongue-shaped zones of phase-locked behavior. While interesting from a purely mathematical point of view, this zone has less in common with physical turbulence, so we exclude this zone from modeling, and therefore implement a check on  $\alpha_i$  to ensure that it is always less than three. Furthermore, note the lower bound on  $\beta$  increases, so stability is also an issue in the zone of large  $\alpha$ . Numerically, flow simulation of very low  $M$  tends to be unstable as well.

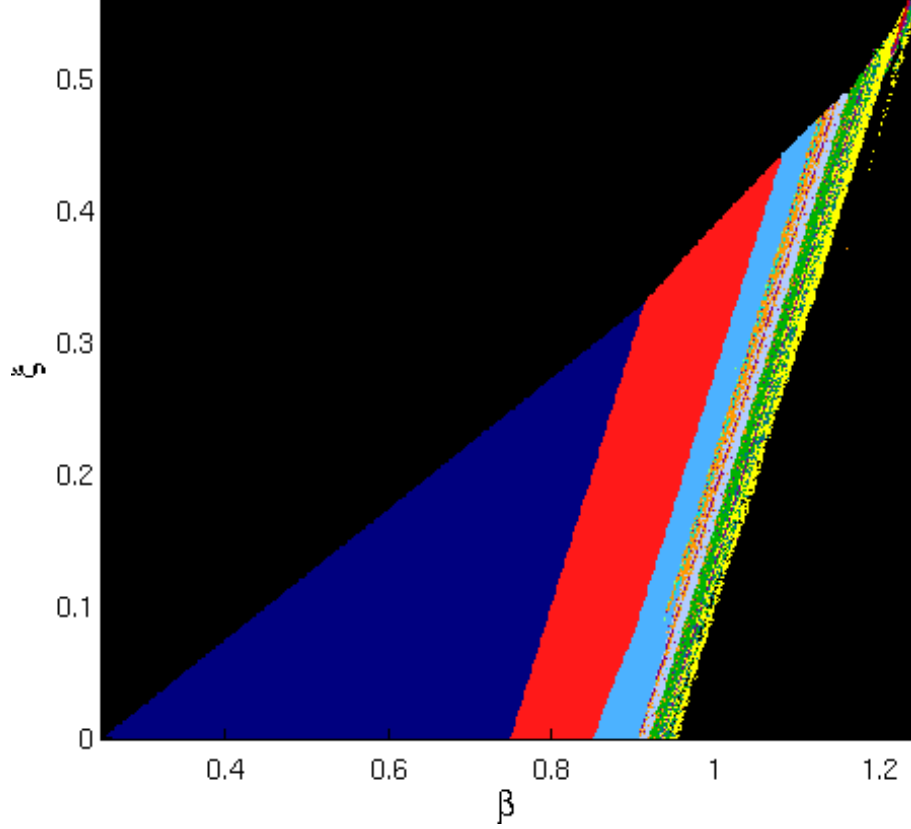
Finally, note that in all the regime maps, the bifurcation sequence frequently passes through a subharmonic region before transitioning to quasiperiodicity and then broadband chaos. This contrasts with the bifurcation sequence of Ruelle and Takens [12], where periodicity immediately transitions to quasiperiodicity. Rather, what is seen has more in common with the Feigenbaum bifurcation sequence and the results in [98], although the bifurcation diagram in Figure 4.3 shows that the subharmonic bifurcations are not necessarily of the period-doubling type.

#### 4.2.2.2 Energy parameters

In this section, each regime map is created by varying a given parameter of the discrete energy equation while simultaneously varying  $\beta$  in the discrete momentum equation (recall that  $\beta_i = \beta$  for all  $i$ ), with the other parameters given in Eq. (4.23). For all  $i$  and  $j$ ,  $\eta_{ij} = \eta$ , and  $\zeta_{ij} = \zeta$ . The presence of an energy equation is one of the main differences between the CPMNS equations and the original incompressible PMNS equations [100], so its effects on the bifurcation sequence are of key interest.

As seen in Figure 4.10, the parameter  $\beta_T$  has very little overall effect on the bifurcation sequence. This is because, as it appears in the denominator of the discrete

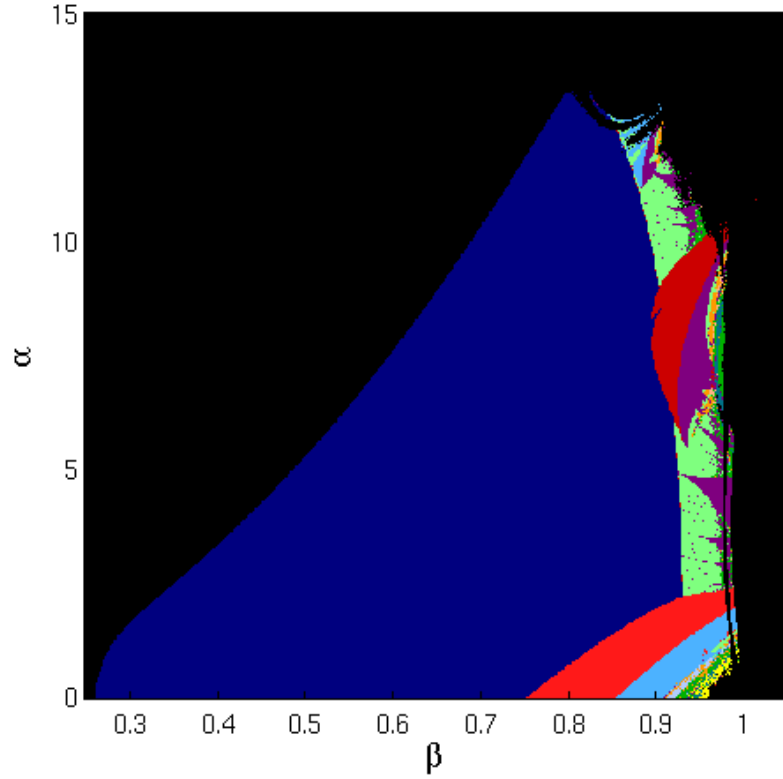
Figure 4.8:  $\xi$  vs.  $\beta$



energy equation Eq. (4.22b), increasing it simply reduces the influence of  $e^{(n)}$  on the overall system, i.e.,  $e^{(n)} \rightarrow 0$  as  $\beta_T \rightarrow \infty$ . Observe that this corresponds to  $Pe \rightarrow 0$  as seen in Eq. (4.19a), but note also that the denominator of the energy equation is bounded below by unity, which eliminates the ability of  $\beta_T$  to destabilize the CPMNS equations as it decreases. As seen in Figures 4.11 and 4.12, all the energy parameters with the most influence on the bifurcation behavior of the system lie in the numerator. Note also the similarity of Figure 4.12 with Figure 4.11, likely due to both coefficients operating on second-order terms.

As in the case of the momentum parameters, the behavior of the energy equation is qualitatively similar to that of physical turbulence. Note in Eqs. (4.19b) and (4.19c), that increasing  $\zeta_{ij}$  and  $\eta_{ij}$  corresponds to increasing Mach number or decreasing Reynolds number, both of which have the physical effect of delaying the

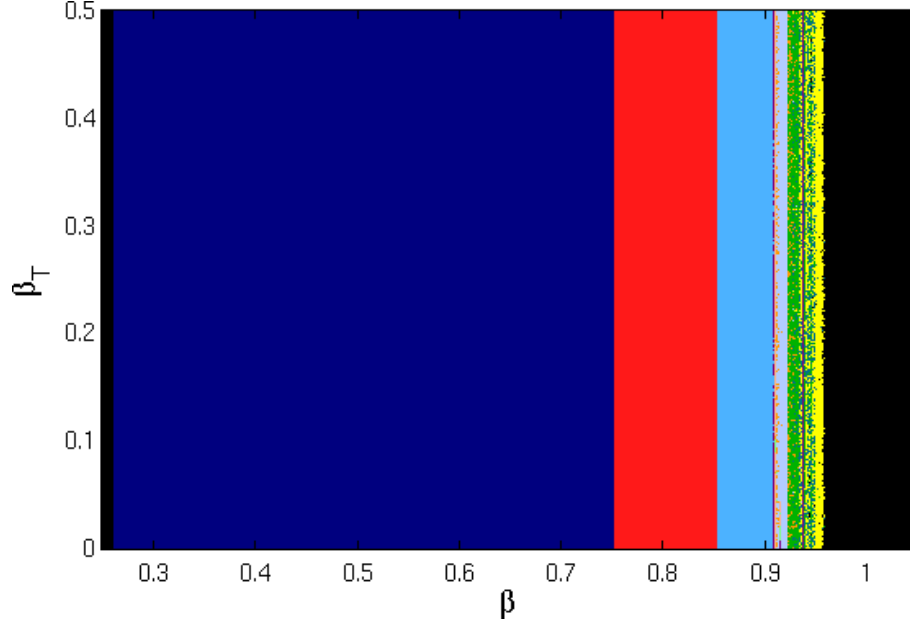
Figure 4.9:  $\alpha$  vs.  $\beta$



onset of turbulence. In particular, both  $\zeta_{ij}$  and  $\eta_{ij}$  are associated with the viscous stress tensor term in the original PDE, which is dissipative due to the presence of second derivatives. But unlike in the momentum equation, this term results in a second-order nonlinearity in the discrete energy equation due to multiplication of  $\sigma_{ij}$  by  $(\partial_j u_i + \partial_i u_j)$  in the original PDE. However, we can see in Figure 4.11 that increasing  $\eta$  still delays the the onset of chaos. As in the case of  $\alpha$ , increasing  $\eta$  sufficiently results in completely different dynamical behavior. In this case, steady-state becomes quasiperiodic and then simply diverges. But for  $\eta < 10$ , we see the usual bifurcation sequence. The regime map for  $\zeta$  in Figure 4.12 appears to be a simple transformation of that of  $\eta$  in Figure 4.11, the main difference being that the range on  $\zeta$  is several orders of magnitude larger than that of  $\eta$ . The similarity of regime maps is unsurprising, since both coefficients correspond to second-order terms. Since  $\zeta$  also

corresponds to viscous stress tensor, the above comments regarding  $\eta$  are applicable to  $\zeta$  as well.

Figure 4.10:  $\beta_T$  vs.  $\beta$

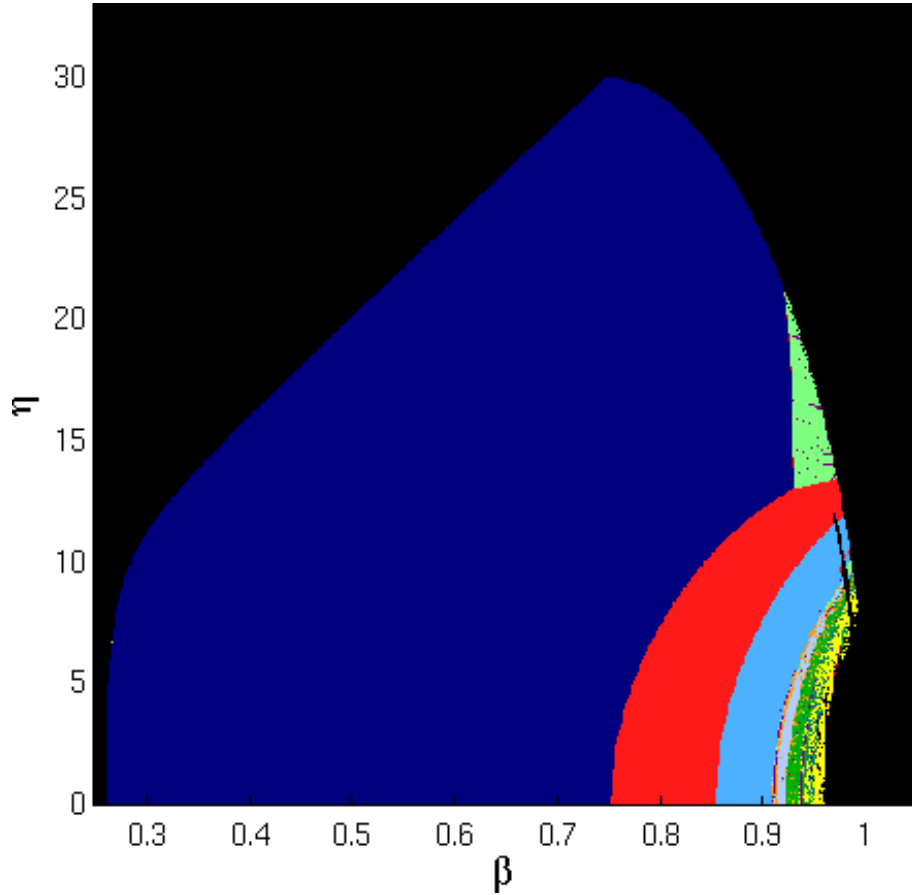


In earlier experiments, the discrete energy equation was derived from the total energy equation without making the simplification of subtracting out the kinetic energy equation. This resulted in a third-order equation, with the third-order terms being associated with the viscous stress tensor. However, this third-order system exhibited dynamics contrary to observed physical behavior. As the  $\eta$  and  $\zeta$  coefficients (which were formulated differently from Eqs. (4.19c) and (4.19b), but were still associated with viscous terms) increased, corresponding to  $M$  increasing and  $Re$  decreasing, the bifurcation sequence was compressed, and the onset of chaos happened more rapidly. Thus Eq. (4.2c) is preferable for our purposes than the total energy equation.

### 4.3 Sensitivity to initial conditions

As with any DDS, an important question is the size and location of basins of attraction. If the basin of attraction has low fractal dimension or small measure, then it

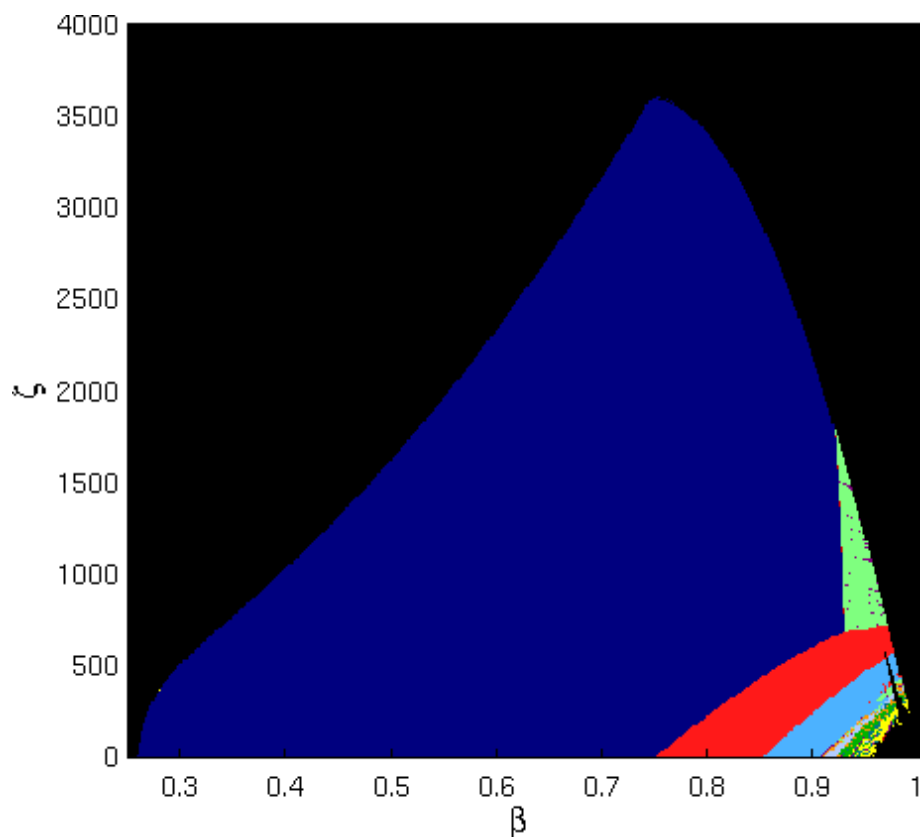
Figure 4.11:  $\eta$  vs.  $\beta$



may be a difficult or even intractable problem to ensure that initial conditions for use in a real simulation lie in the basin. Of particular interest as well is determining whether all initial conditions for a given set of bifurcation parameters lead to the same dynamical behavior. At a minimum, for use as the basis of a turbulence model, it is necessary that the initial conditions lead to similar dynamical behavior, i.e., the PSDs exhibit similar characteristics.

In these numerical experiments, we investigate two cases of highly different “noisy” behavior to see how initial conditions affect each one. Figure 4.13 is the basin of attraction for  $\beta_i = 0.945$  and  $\alpha_i = 0.0001$  for all  $i$ , which corresponds to an isotropic broadband region and is very close to the divergent zone. Figure 4.14 is the attracting basin for  $\beta = (0.92, 0.94, 0.93)$  and  $\alpha = (0.0001, 0.002, 0.0013)$ , which the

Figure 4.12:  $\zeta$  vs.  $\beta$



automated tool identified as a noisy quasiperiodic region. The basin in Figure 4.13 has a sparse structure, likely due to it being so close to the divergent region to begin with, which suggests that it may have small or vanishing Lebesgue measure. By contrast, Figure 4.14 shows a clearly positive-measure basin with multiple solution regimes interspersed. In a real simulation, initial conditions will be set by results from the previous time step, so we expect overall stability.

Close inspection of Figure 4.14 shows five colors, corresponding to noisy quasiperiodic with and without fundamental frequency, broadband with and without fundamental, and broadband with different fundamental. The immediate question, then, is whether these represent truly different dynamical behavior, or whether the automated tool simply is inconsistent in classifying signals that are close to one kind of behavior or another. Numerical investigation of initial conditions that the regime map algo-



rithm associated with each dynamical behavior was performed to determine whether different initial conditions lead to truly different numerical behavior, or whether this is due to marginal selection criteria in the algorithm. Sample results are shown in Figure 4.15. The PSDs and time series are quite similar, and, importantly, the phase portraits appear nearly identical. While time series (b) has two large intermittency bursts not seen in (a), this is due to the relatively small sample shown here, and these structures can be seen in (a) in other regions of the time series. The two time series shown each begin exactly  $4 \times 10^4$  iterations from their respective initial conditions to illustrate the sensitivity to initial conditions. Upon further investigation, these observations proved true of a variety of initial conditions, regardless of how the tool had labeled them. This indicates that the multiple colors in the basins of attraction are due to the selection algorithm itself, not to the behavior of the CPMNS equations, as categorizing a noisy signal has a subjective element, such as deciding exactly how large a spike at the end of a PSD qualifies as retention of the fundamental frequency. In this particular case, note the two small bumps in each PSD and how it gradually rises at the end. Whether or not the tool detected the bumps as incommensurate frequencies determined whether or not it classified the signal as noisy quasiperiodic or broadband, and whether or not it detected the rise at the end determined whether or not it classified the signal as having a fundamental frequency. Therefore, interspersions of different noisy regimes in Figure 4.6 may also be due to the selection algorithm rather than entirely to fundamental mathematical properties of the DDS. For modeling purposes, this indicates that different initial conditions will not lead to significantly different dynamical behavior, emphasizing once again that the CPMNS equations will be robust as a turbulence model.

Both cases used to generate Figures 4.13 and 4.14 exhibited sensitivity to initial conditions. Lyapunov exponents  $\lambda_L$  were estimated numerically using an algorithm described by Peitgen et al. [109], based on the formula

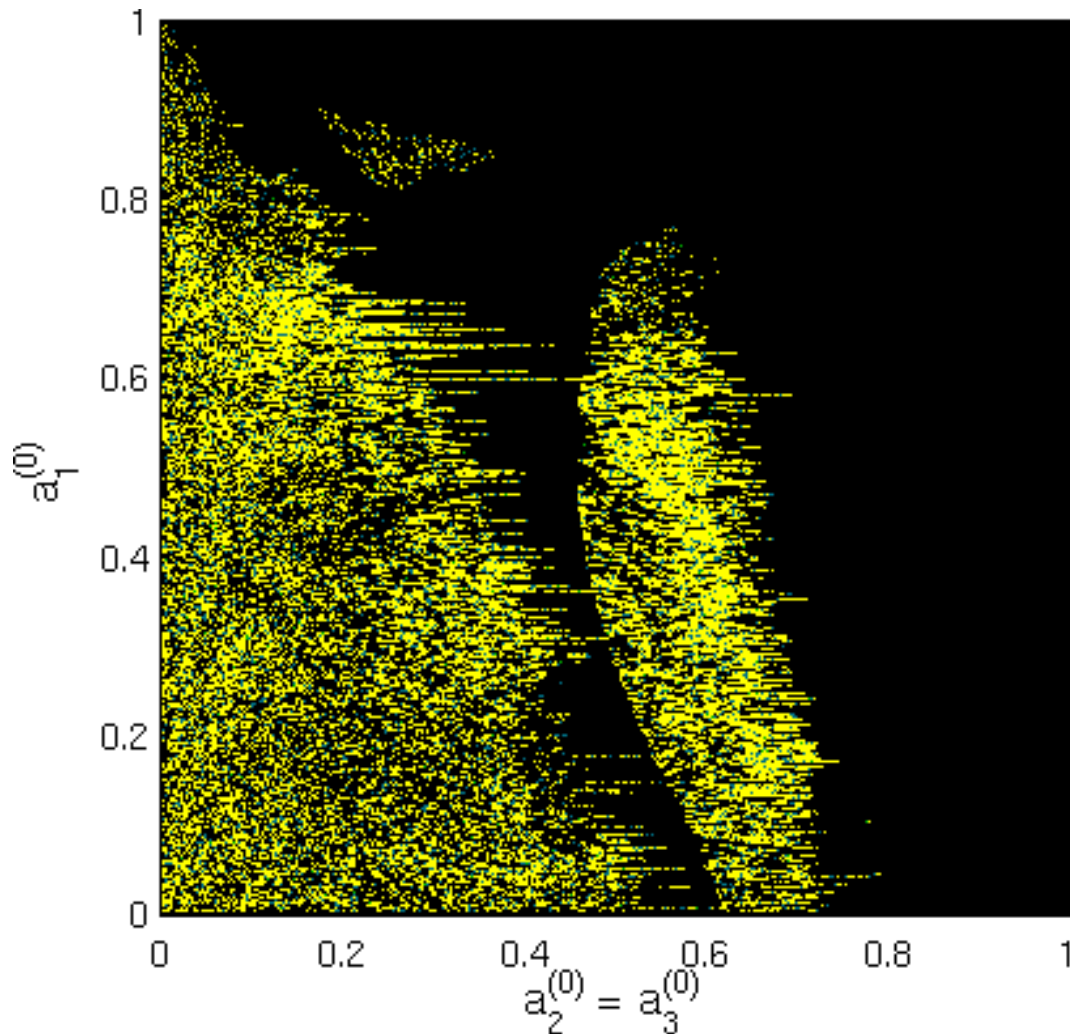
$$\lambda_L \approx \frac{1}{N} \sum_{n=1}^N \ln \left| \frac{\mathbf{a}^{(n,\varepsilon)} - \mathbf{a}^{(n)}}{\varepsilon} \right|, \quad (4.26)$$

where  $\mathbf{a}^{(n,\varepsilon)}$  is computed from the previous time step using  $\mathbf{a}^{(n-1)} + \varepsilon$ , and  $\varepsilon$  is an error term. For these computations,  $N = 5 \times 10^5$ , and  $\varepsilon = 3 \times 10^{-5}$ . The isotropic case corresponding to Figure 4.13 exhibited a Lyapunov exponent  $\lambda_L = 0.939$ , while the anisotropic case corresponding to Figure 4.14 had  $\lambda_L = 0.930$ . Both Lyapunov exponents were computed using  $5 \times 10^5$  iterations. Initial DNS experiments by Schwarz et al. [110] suggest values of  $\lambda_L$  in this range, although current computing power was insufficient to complete the numerical experiments. Figure 4.16 shows the growth of  $\lambda_L$  as  $\beta = \beta_1 = \beta_2 = \beta_3$  and  $\alpha_i = 0.0001$  for all  $i$  increases. The sharp drops correspond to transitions from chaos to periodicity in the bifurcation sequence. Clearly, infinitely many such diagrams can be generated for the anisotropic case, depending on what relationships among the different  $\beta_i$  are chosen.

#### 4.4 SGS model functions

In Sec. 3.2.3, we argued that adequate explicit filtering will on its own eliminate aliasing and provide a stable solution procedure. Thus we expect numerical solution of the dealiased NSEs, Eqs. (3.53a)–(3.53c), to be numerically stable. In fact, Mathew et al. [93], whose method could be considered a solution of the aforementioned equations without any turbulence model, and whose filtering method was close to a spectral cutoff (which we suspect does not sufficiently dealias numerical results), reported that decreasing mesh resolution merely led to the eventual disappearance of turbulent structures rather than the instability normally associated with the lack of a turbulence model. In the DNS experiments of Huang and Leonard [111], which used a Fourier method with grid-shift dealiasing, reducing the number of modes from 256 to 128 had the effect of increasing the decay rates of various turbulence quantities. Further, experiments with homogeneous, isotropic turbulence on a cube, detailed in Section

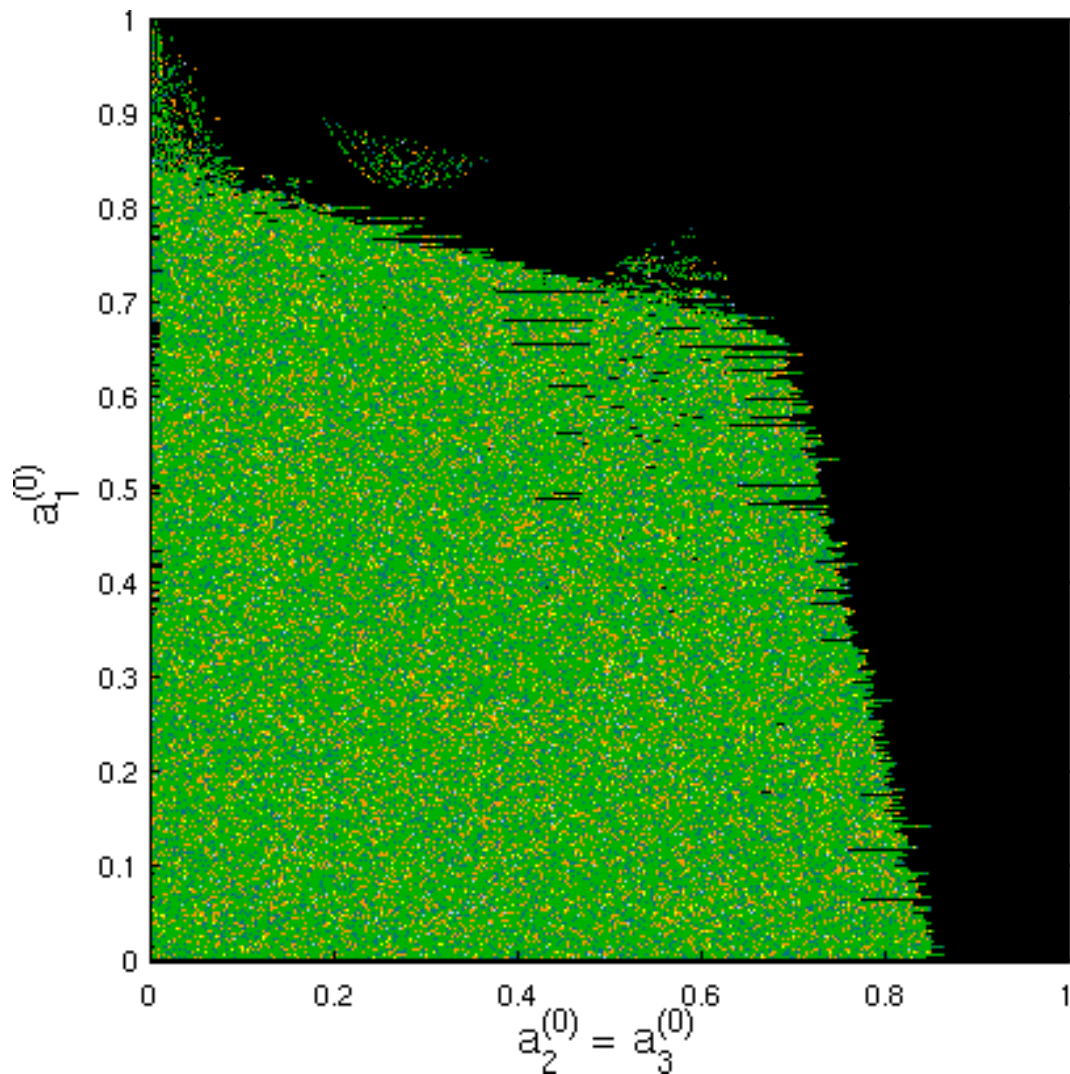
Figure 4.13: Basin of attraction for  $\beta_i = 0.945$  and  $\alpha_i = 0.0001$  for all  $i$



6.2, revealed that the low-dissipation HAMR scheme [112], which we have used as an explicit filter, by itself increases the turbulent kinetic energy decay rate. As we will see in Ch. 5, Fig. 6.31 shows the dissipation caused by a 5<sup>th</sup>-order differencing filter on a shock ramp is far in excess of what is needed. This leads to the conclusion that in the presence of filtering sufficiently dissipative to eliminate aliasing entirely, a model of the HFI error terms in Eqs. (3.53a)–(3.53c) needs to be entirely responsible for providing backscatter. The question, then, is how exactly to do this.

Simple additive methods have been used with a significant degree of success in ODTLES [5] and by McDonough and Yang in LES of a buoyant plume [10]. However,

Figure 4.14: Basin of attraction for  $\beta = (0.92, 0.94, 0.93)$  and  $\alpha = (0.0001, 0.002, 0.0013)$



both of these models involve the construction of a small-scale velocity field, which is then mass-conserved by projecting it to a divergence-free subspace and added to the large-scale solution. Clearly, this method is not viable for the compressible equations, since compressible flows are not divergence-free. Further, a second projection significantly increases the total computation time of the LES due to the required Poisson solve. The problem with any additive model is that any modification of the flow field no longer satisfies the governing equations. While this is not as severe an issue in incompressible LES, as just about any mass-conserved field within reason can

Figure 4.15: PSD, time series, and phase portrait for initial conditions detected as noisy quasiperiodic (a) and broadband with fundamental (b)

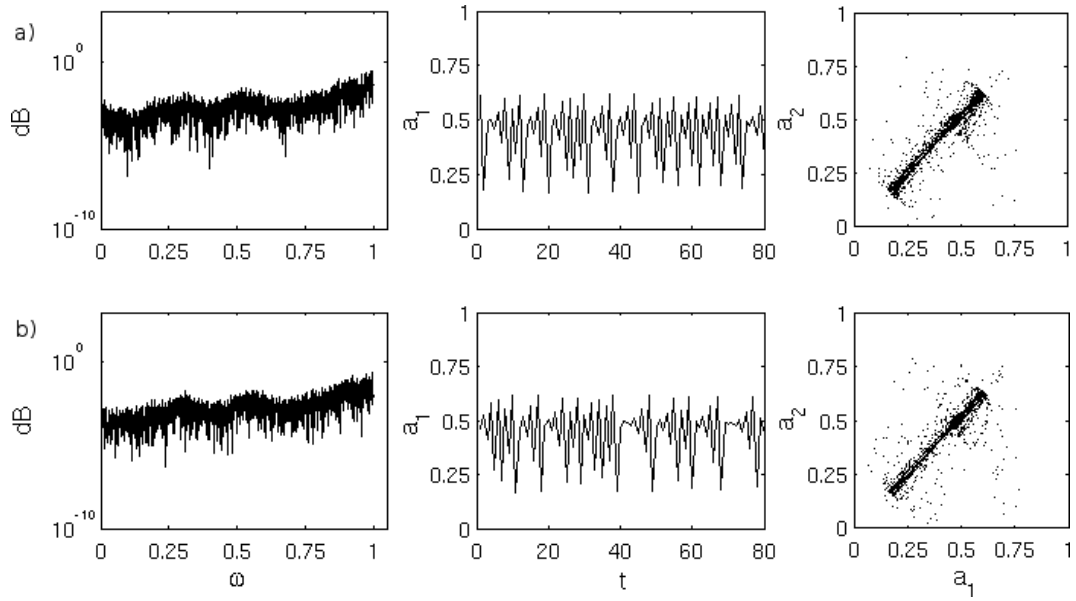
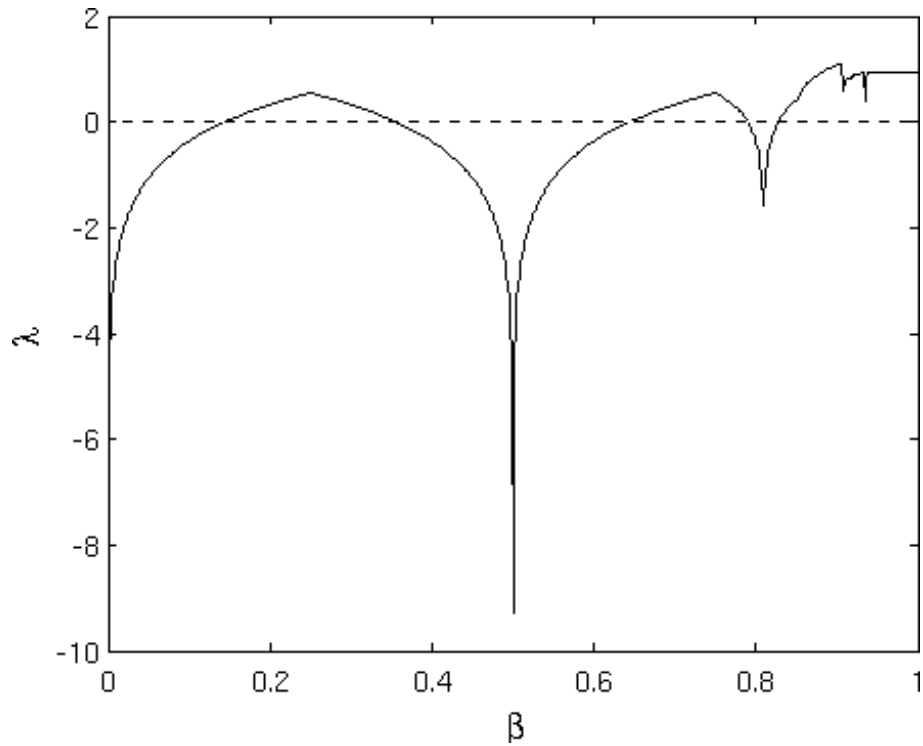


Figure 4.16: Lyapunov exponent  $\lambda$  vs.  $\beta$



serve as an initial condition, it is a significant issue in compressible LES. In DNS, constructing initial conditions that do not result in rapid divergence to instability is nontrivial, and in both DNS and LES, generating inlet turbulence for compressible flows is an active area of research, as can be seen in the review of Tabor and Baba-Amadi [113]. Thus we would expect any additive method to potentially introduce instability. Indeed, in the course of this work, various attempts to construct an additive method for compressible flows without introducing additional PDEs proved to be numerically unstable. Inevitably, unless the modifications were so small as to induce no significant variation in the flow statistics, they would cause negative pressures to build somewhere in the flow domain.

It is tempting to attempt to build an approximation to the HFI terms, restated here for momentum,

$$HFI_i = \partial_j \left( \overline{\rho u_j \tilde{u}_i} - \overline{\rho u_j u_i} \right).$$

However, as discussed in Sec. 3.3, the fundamental issue is insufficiently many degrees of freedom. It is important to keep in mind that no information about the HFI error terms is resolved on the grid; we have explicitly constructed them to contain exclusively all of the error associated with filtering and under-resolution. Attempts to directly estimate these terms from the resolved scale, such as the SSE model of Domaradzki and Saiki, have met with limited success [3].

This led to consideration of formulating the turbulence model as a backscatter-inducing forcing function instead. Attempts at inducing backscatter via random forcing functions were introduced in the 1990s by Leith [89] and Chasnov [90] with reasonable success. Although this has not been a particularly popular method, the basic idea continues to be used and modified with some success. A more recent example that has exhibited fairly good agreement with DNS results is the LES–Langevin model of Laval and Dubrulle [91]. We discuss each of these models below.

#### 4.4.1 Leith's stochastic backscatter model

The stochastic backscatter model of Leith, proposed in [114] and [89], is perhaps the earliest example of forcing used as a turbulence model. Motivated by the observations of experimentalists that energy transfer is not strictly from large to small scales, he proposed the addition of an isotropic backscatter forcing vector  $\mathbf{f}$  to the traditional Smagorinsky model,

$$f_i = \rho \partial_i \phi_i \quad (4.27)$$

$$\phi_i = C_b |\mathbf{S} dt|^{3/2} \left( \frac{\Delta}{dt} \right)^2 g, \quad (4.28)$$

where  $g$  is a Gaussian random number with unit variance and zero mean,  $C_b$  is an adjustable constant,  $dt$  is the time step,  $\mathbf{S}$  is the deviatoric stress tensor, and  $\Delta$  is the filter width. The exponents were arrived at via dimensional scaling arguments. This model was applied to a plane shear mixing layer in a compressible flow of  $M = 0.25$  with reasonably good predictions of the evolution of the width.

Leith's implementation has a few intrinsic limitations. There are the usual shortcomings associated with the Smagorinsky model and traditional LES equations, which we will not repeat, as they have been discussed in detail in Chapter 3. The use of a two-dimensional computation is questionable as well, although the dynamics of geophysical turbulence tends to follow 2D patterns.

The main issues are with the model itself. First, turbulence is non-Gaussian, so the best that can be achieved with such a model is a Gaussian approximation to turbulence. Second, the forcing is isotropic, while both physical and NSE turbulence are frequently anisotropic. Third, differentiating the non-smooth  $\phi_i$  resulted in  $f_i$  inducing the accumulation of numerical errors, possibly due to the aliasing problem that exists in traditional implementations of LES. To avoid this issue, Leith smoothed the forcing potential  $\phi_i$  using an unspecified filter. However, filtering has the effect of attenuating high wavenumbers, and it is precisely the effect of unresolved scales

on all resolved wavenumbers that a backscatter model must capture.

Leith appears to have abandoned this model. There have been no further publications of computations performed with it since 1990, and in a 1996 publication on stochastic modeling of chaotic systems [115], this model is not even mentioned. This suggests that the model proved to be inadequate upon further investigation.

#### 4.4.2 Chasnov's $\eta - F$ model

Chasnov, drawing in part on inspiration from Leith, introduced a random backscatter model in the context of a spectral method [90]. Like Leith, he introduced a forcing model as a means of augmenting the traditional Smagorinsky model. He posed his argument as a conceptual improvement over eddy viscosity modeling a net transfer of energy from low to high wavenumbers by arguing that energy cascade and backscatter should be modeled as separate effects, where the former can be provided by eddy viscosity,  $\eta$ , and the latter should be provided by random forcing  $f$  defined by a spectrum  $F$ . Chasnov's eddy viscosity, in contrast to typical Smagorinsky-type models used in finite-volume methods, is wavenumber-dependent, increasing somewhat at the higher wave numbers.

Chasnov defines  $\eta$  and  $F$  in terms of integrals of the energy spectrum,  $E$ , by deriving them from Kraichnan's eddy-damped quasinormal Markovian model (EDQNM) [9] of the momentum equation. The formulas are given by

$$\eta_k = \frac{1}{k^2} \int_{k_{max}}^{\infty} dp \int_{p-k}^p dq \theta_{kpq} \left( \frac{p^2}{q} (xy + z^3) E(q) + \frac{q^2}{p} (xz + y^3) E(p) \right) \quad (4.29)$$

$$F_k = \int_{k_{max}}^{\infty} dp \int_{p-k}^p dq \theta_{kpq} \frac{k^3}{pq} (1 - 2y^2 z^2 - xyz) E(q) E(p), \quad (4.30)$$

where  $\theta$  is a damping rate and  $x, y$ , and  $z$  are the cosines of the angles of the triangle with side lengths  $k, p$ , and  $q$ .

A comprehensive overview of EDQNM theory is beyond the scope of this work and would likely require a chapter of its own. Briefly, it is an attempt to provide closure



for ensemble averaging in the spectral domain, and like many other closure methods, it uses artificial dissipation to do so. That said, good agreement with experimental results has been achieved using it, both by Chasnov and others, such as Park and Mahesh [116].

By tuning the Kolmogorov constant, which is embedded in the construction of  $\theta$ , the  $\eta - F$  model was able to more closely match the  $k^{-5/3}$  energy spectrum than an eddy viscosity alone. However, it required constants well in excess of experimental observations. A further weakness of the  $\eta - F$  approach is its spectral formulation. For LES of flows of engineering interest, spectral and pseudo-spectral methods are rare, and many of the most popular codes use FV methods. Thus forcing with a carefully tuned spectrum may not have any applicability to practical LES.

It is worth noting that to achieve the  $k^{-5/3}$  spectrum, the spectral eddy viscosity,  $\eta$ , had near-zero values throughout low- $k$  spectrum, only rising to significantly large values in the last  $\sim 50\%$  of the resolved spectrum. This gives it a spectral dissipation profile similar to that of the HAMR scheme of Liu et al. [112]. Contrast this with the Smagorinsky eddy viscosity [1], where the spectral damping profile is simply the spectrum of the strain rate magnitude, and thus can be expected to contain significant low- $k$  damping.

Much like Leith, Chasnov appears to have ceased development of this turbulence model. None of his recent publications have anything to do with LES, and he appears to have ceased research into turbulence entirely in 2001. However, the fact that a combination of damping and forcing was able to capture the Kolmogorov spectrum provides positive reinforcement for this general approach.

#### 4.4.3 Laval and Dubrulle's LQL model

Laval and Dubrulle [91] proposed a model making use of Langevin equations for inducing backscatter. Their model is constituted in terms of the inviscid NSEs and

includes both a sharp cutoff filter and an eddy viscosity. They identify forcing from the small scales as the key feature missing from purely dissipative models and employ stochastic forcing in order to simulate the effects of the unresolved scales on the large scales. The Langevin Quasi-Linear (LQL) formulation of their model is given by

$$\partial_t \bar{u}_i = \overline{\bar{u}_j \partial_j \bar{u}_i} + \bar{l}_i = -\partial_i \bar{p} + \partial_j (\mu + \mu_t) \partial_j \bar{u}_i \quad (4.31)$$

$$\partial_t l_i = -\frac{1}{\tau} + \zeta_i + \xi \quad (4.32)$$

$$\zeta_i = -\bar{u}_j \partial_j f_i - f_j \partial_j \bar{u}_i \quad (4.33)$$

$$f_i = \partial_j (\bar{u}_i \bar{u}_j - \overline{\bar{u}_i \bar{u}_j}) \quad (4.34)$$

where  $\tau$  is a time scale,  $\mu_t$  is an eddy viscosity, and  $\xi$  is a Gaussian random variable with zero mean and adjustable variance chosen to be of the order of the velocity magnitude without injecting additional energy.

Their experiments on isotropic turbulence exhibited good agreement with DNS results. In particular, the addition of the forcing showed a good match with the time evolution of spectral characteristics of decaying isotropic turbulence, and a good match for the energy transfer characteristics of forced isotropic turbulence. As expected, it was significantly less dissipative than a pure eddy viscosity model and more closely matched the Kolmogorov energy spectrum than either the Smagorinsky or spectral eddy viscosity methods used for comparison.

The spectral matches are particularly interesting considering the non-Gaussian nature of turbulence. However, the probability density function of the velocity increments and gradients of randomly forced Burgers equation is not Gaussian [117], so it is likely that the “feeding” of a random forcing through the NSE discrete solution operators breaks the Gaussian behavior (although this is not something we have so much as sketched a proof for, it could be an interesting task for an enterprising mathematician to demonstrate whether a Gaussian distribution can be recovered by some transformation of the results from a numerical solution of Gaussian-forced NSEs).

While the results of Laval and Dubrulle suggest that the use of Langevin equations for a forcing model could prove a very fruitful route of inquiry, there are two immediate criticisms of this approach.

1. It employs a sharp spectral cutoff filter, which does not dealias the low wavenumbers; an eddy viscosity would probably be unnecessary if the filter provided proper dealiasing.
2. The term  $f_i$  cannot be accurately computed on the under-resolved mesh, and any numerical formulation of it will consist almost entirely of aliasing error. Thus the forcing term is mostly a perturbation of numerical aliasing error.

Using aliasing to model turbulence is perhaps not a particularly important issue in homogeneous, isotropic turbulence, since both aliasing and SGS quantities will be homogeneous and isotropic. In this case, scaled and randomly perturbed aliasing may be an adequate turbulence model. But in typical engineering flows with high anisotropy, this approach is likely to be inadequate. In any context, it is not ideal to use aliasing error as a turbulence model, unless such error can be controlled, quantified, and properly attenuated.

#### **4.4.4 A new CPMNS-based model**

The specific form of the forcing function employed in this work is inspired by the successful use of linear forcing, first proposed by Lundgren [118], implemented for incompressible turbulence by Rosales and Meneveau [119], and extended to the compressible case by Petersen and Livescu [120] to create a stationary state in homogeneous, isotropic turbulence. This sort of formulation is attractive due to its straightforward implementation and analysis. Originally, it was proposed due to being trivial to implement in physical space rather than the spectral domain. A linear forcing

function for the compressible NSEs simply takes the form

$$f_i = C\rho u_i, \quad (4.35)$$

where  $C$  is a constant, and it can be shown that

$$C = \frac{\varepsilon - \langle (\partial_i u_i) p \rangle}{2K}, \quad (4.36)$$

where  $K$  is mean turbulent kinetic energy, and  $\varepsilon$  is the mean dissipation rate. This shows that as  $C$  increases, the flow must dissipate  $K$  more rapidly in order to maintain equilibrium, and a higher value of  $Re_\lambda$  can be achieved.

Petersen and Livescu [120] found that simple linear forcing is insufficient to fully control the turbulence characteristics of compressible flows due to the distinct solenoidal and dilatational modes. Thus the proposed forcing was of the form

$$f_i = \sqrt{\rho} [C_d(\sqrt{\rho}u)_d + C_s(\sqrt{\rho}u)_s], \quad (4.37)$$

where the  $s$  and  $d$  subscripts denote solenoidal and dilatational modes, respectively. It can be shown that at equilibrium,

$$C_s = \frac{\varepsilon_s}{2K_s} \quad (4.38)$$

and

$$C_d = \frac{\varepsilon_d}{2K_d - \langle (\partial_i u_i) p \rangle}. \quad (4.39)$$

The aforementioned results are, however, of limited applicability to the current situation for several reasons. Foremost among these is the fact that we are not trying to reach an equilibrium, but only to simulate sufficient backscatter to counteract the excess dissipation introduced by filtering. Further, the use of the chaotic CPMNS equations provides an element of unpredictability, so that strict analysis of linear forcing is not directly applicable. Splitting the forcing into dilatational and solenoidal modes appears desirable, but a Helmholtz decomposition of the velocity

field on a large grid consisting of multiple blocks in generalized coordinates with arbitrary boundary conditions is computationally expensive, and developing fast, efficient solvers is an ongoing area of research that is beyond the scope of this work. However, it may be possible to develop a sufficiently fast implementation of the discrete Hodge-Helmholtz decomposition, which has been successfully applied to analyzing experimental fluid data by Guo et al. [121].

Because we are trying to model backscatter rather than achieve stationary turbulence, we apply the forcing only to  $\mathbf{q}_{hi}$  and multiply by  $a_i$  in order to provide chaotic dispersion. Thus the formulas for our forcing terms are

$$f_i = \rho(C_{PMNS})u_{hi,i}(a_i - A_i) \quad (4.40a)$$

$$f_e = f_i u_i \quad (4.40b)$$

where  $f_i$  is the forcing term for the momentum equation,  $f_e$  is the forcing term for the energy equation,  $C_{PMNS}$  is the PMNS model constant, and  $A_i$  is the average of  $a_i$  over the twelve iterations, which again tend to be enough to converge to the system's attractor. This averaging is necessary to ensure that the average kinetic energy induced by the forcing term is zero; *i.e.*, energy should be scattered rather than artificially injected. The forcing term on the energy equation is a simple formulation for maintaining consistency in the governing equations.

We have chosen  $C_{PMNS}$  to be constant on the assumption that the needed backscatter is directly proportional to  $|\mathbf{u}_{hi}|$ . If there is very little high- $k$  content in the solution, this indicates that the flow is locally resolved into the dissipative scale, while significant quantity of energy in the high- $k$  modes suggests that the dissipation scale is not resolved by the mesh. Furthermore, although it is unlikely for the ideal parameter to be a constant (and we will see in Ch. 6 that it indeed is not), the general paradigm of filter-forcing turbulence modeling is not well-studied. Thus, for the present work, we are deliberately keeping the formulation simple. The goal of this present work is to create the theoretical foundation and basic computational evidence necessary for

the development of filter-forcing models as a class, leaving the creation of an ideal forcing function as an open problem (note, for example, that a period of over three decades transpired between Smagorinsky’s original, single-parameter model [1], and the development of the much more effective variable-parameter dynamic model [68]. That said, Eq. (4.36) suggests that increasing  $C_{PMNS}$  will increase the intensity of the backscatter and lead to a more turbulent flow.

Formulas for the bifurcation parameters used in the numerical implementation of Eqs. (4.22a)–(4.22b) are based on the derivations presented in Sec. 4.1. They are given by

$$\beta_i = 1 - \left| \frac{\nu}{\Delta^2 \omega_i} \right| \quad (4.41a)$$

$$\alpha = \tau / (M_{loc})^2 \quad (4.41b)$$

$$\xi_{ij} = \frac{1}{3} \tau k_i k_j (1 - \delta_{ij}) \quad (4.41c)$$

$$\zeta_{ij} = \frac{2}{3} \left( \frac{\tau(\gamma - 1) M_{loc}^2 \epsilon_i \epsilon_j k_i k_j}{Re_{loc}} \right) \quad (4.41d)$$

$$\epsilon_i = \frac{\beta_i}{\tau} \quad (4.41e)$$

$$\eta_{ij} = k_i \epsilon_j \sqrt{\frac{\tau(\gamma - 1) M_{loc}^2}{Re_{loc}}} \quad (4.41f)$$

$$Re_i = \frac{\Delta \sqrt{\nu |\omega_i|}}{\nu} \quad (4.41g)$$

$$Re_{loc} = \frac{1}{3} (Re_1 + Re_2 + Re_3), \quad (4.41h)$$

where all flow variables have been appropriately scaled with local quantities as mentioned previously. Here,  $M_{loc}$  is local Mach number,  $k_i$  is the wavenumber associated with the length of the grid cell in the  $i^{\text{th}}$  direction,  $\omega_i$  is the  $i^{\text{th}}$  component of vorticity,  $\Delta$  is the filter width (here taken to be the average length of a grid cell),  $\tau = 1/|\omega|$ , and  $\nu$  is kinematic viscosity. Note that the formulation of  $Re_i$  is similar to that of  $y^+$ , the dimensionless turbulent wall distance, although with an instantaneous vorticity component in place of mean strain rate. With the exception of elements of  $\beta$ ,

the formulas for the bifurcation parameters are taken directly from the derivations. At each time step, the bifurcation parameters are constructed and, if the DDS is in the quasiperiodic or chaotic regime, iterated 12 times, which is generally sufficient for the system to exhibit its characteristic behavior. If the bifurcation parameters correspond to a non-broadband regime, the map is not iterated and the SGS forcing at the node for the given time step is set to zero.

#### **4.5 Summary and conclusions**

The CPMNS equations exhibit the kinds of properties that are desirable for a DDS to be used as the core of a turbulence model. They exhibit bifurcation behavior similar to that of physical turbulence, and they have the spectral characteristics of deterministic chaos. They have been incorporated in a single-parameter forcing function adapted from a linear forcing method used in DNS of forced turbulence. This forcing function, when combined with a dissipative filter, should be capable of providing the backscatter necessary for LES of turbulent flows.

## Chapter 5. OVERFLOW

The CPMNS model is implemented in the context of an existing compressible flow code, OVERFLOW, which is developed by NASA Ames. While the distribution of OVERFLOW is limited by United States export control regulations, the hybrid C/FORTRAN source code is distributed free of charge within the USA. OVERFLOW is a three-dimensional, implicit, finite volume, structured overset grid CFD code employed widely within the NASA community and academia, and with limited use in industry. Because it is a mature code, it has good stability characteristics, a wide variety of boundary condition and turbulence model options, and features advanced shock-capturing routines and multispecies models. It uses domain decomposition in parallel mode, employing both MPI and OpenMP. Decomposition and reassembly are fully automated processes, leaving the entire parallelization process invisible to the user.

In Sec. 5.1, we outline the governing equations and key numerical features of OVERFLOW. In Sec. 5.2, the chimera interpolation method for overset grids is defined, and its strengths and shortcomings are explained. In Sec. 5.3, the WENOM shock capturing method is explained. This high-order shock capturing method is much preferable to TVD schemes for use in LES. In Sec.5.4, the parallelization scheme used by the code is explained, details of the computational hardware are given, and the results of numerical performance tests are presented. Finally, in Sec. 5.5, we summarize our conclusions on OVERFLOW's pros and cons for use in the present investigation.



## 5.1 Governing equations and features

OVERFLOW solves the dimensionless, compressible Navier–Stokes equations in generalized coordinates  $(\xi, \eta, \zeta)$ . The dimensionless CNSEs without body force or heat source terms are given in rectangular coordinates by

$$\partial_t \rho + \nabla \cdot (\rho \mathbf{u}) = 0, \quad (5.1a)$$

$$\partial_t(\rho \mathbf{u}) + \nabla \cdot (\rho \mathbf{u} \otimes \mathbf{u}) - \nabla p + \frac{1}{Re} \nabla \cdot \tau \quad (5.1b)$$

$$\partial_t(\rho e_0) + \nabla \cdot (\rho e_0 \mathbf{u}) = \frac{1}{Re Pr(\gamma - 1)} \nabla \cdot \mu \nabla T = \nabla \cdot p \mathbf{u} + \frac{1}{Re} \nabla \cdot \tau \mathbf{u}. \quad (5.1c)$$

In these equations,  $\mathbf{u}$  is the velocity vector,  $\rho$  is density,  $T$  is temperature,  $e_0$  is the total energy,  $\gamma$  is the specific heat ratio,  $\mu$  is the dynamic viscosity,  $Re$  is the Reynolds number,  $Pr$  is the Prandtl number,  $\tau = \mu(\nabla \mathbf{u} + \nabla \mathbf{u}^T) - 2/3(\nabla \cdot \mathbf{u})I$ , and  $I$  is the identity matrix. Flow quantities are scaled using the free stream speed of sound, dynamic viscosity, gas constant, and density, and by the length of one grid unit.

Viscosity is computed using Sutherland’s law, implemented in the code as

$$\mu = C_1 \left( \frac{T^{3/2}}{C_2 + T} \right), \quad (5.2)$$

where  $\mu$  and  $T$  are scaled by the freestream reference quantities,  $\mu_\infty$  and  $T_\infty$ , and the two parameters are given by

$$C_1 = \frac{S}{T_\infty} + 1 \quad (5.3)$$

$$C_2 = \frac{S}{T_\infty}, \quad (5.4)$$

where  $S = 199^\circ \text{ R}$ .

Transforming the CNSEs to generalized coordinates is done by selecting a differentiable coordinate transformation  $\boldsymbol{\xi} = (\xi(\mathbf{x}), \eta(\mathbf{x}), \zeta(\mathbf{x}))$  and applying the chain rule, i.e.,

$$\partial_i = \partial_i \boldsymbol{\xi} \cdot \nabla_{\boldsymbol{\xi}}, \quad (5.5)$$

where  $\nabla_{\xi}$  is the gradient operator with respect to  $\xi$ . The transformed CNSEs can then be written in the general form

$$\partial_t \mathbf{q} + \partial_{\xi} \mathbf{E} + \partial_{\eta} \mathbf{F} + \partial_{\zeta} \mathbf{G} = 0, \quad (5.6)$$

where  $\mathbf{q} = [\rho, \rho u_1, \rho u_2, \rho u_3, \rho e_0]$ . Here,  $\mathbf{E}$ ,  $\mathbf{F}$ , and  $\mathbf{G}$  contain the advection, pressure, and dissipation terms. The specific form of the discretization and splitting is specified by the user, and the code offers a wide range of options, such as Yee symmetric total variation diminishing (TVD) [122], third-order Roe upwind [123], and fifth-order weighted essentially non-oscillatory (WENO) [124] schemes for shock capturing, and alternating direction implicit (ADI) Beam–Warming [125], and Steger–Warming [126] for the implicit solver, to list a few examples. Turbulence models are much more limited, by contrast. The only modern Reynolds averaged Navier–Stokes (RANS) models in the code are Spalart–Allmaras [57],  $k-\omega$  [127], and Menter’s shear stress transport (SST) [128] methods. There are no pure large-eddy simulation (LES) models, but there are several detached eddy simulation (DES) options available that use either the SA or SST models for the RANS component.

Either first or second order implicit Euler time advancement is available, and this can be further enhanced with either Newton or dual-time sub-iteration. While these sub-iteration is not formally required by the code, it is recommended due to being less computationally expensive than merely shrinking the time step, and because it enhances convergence in the overlap regions.

## 5.2 Chimera overset interpolation

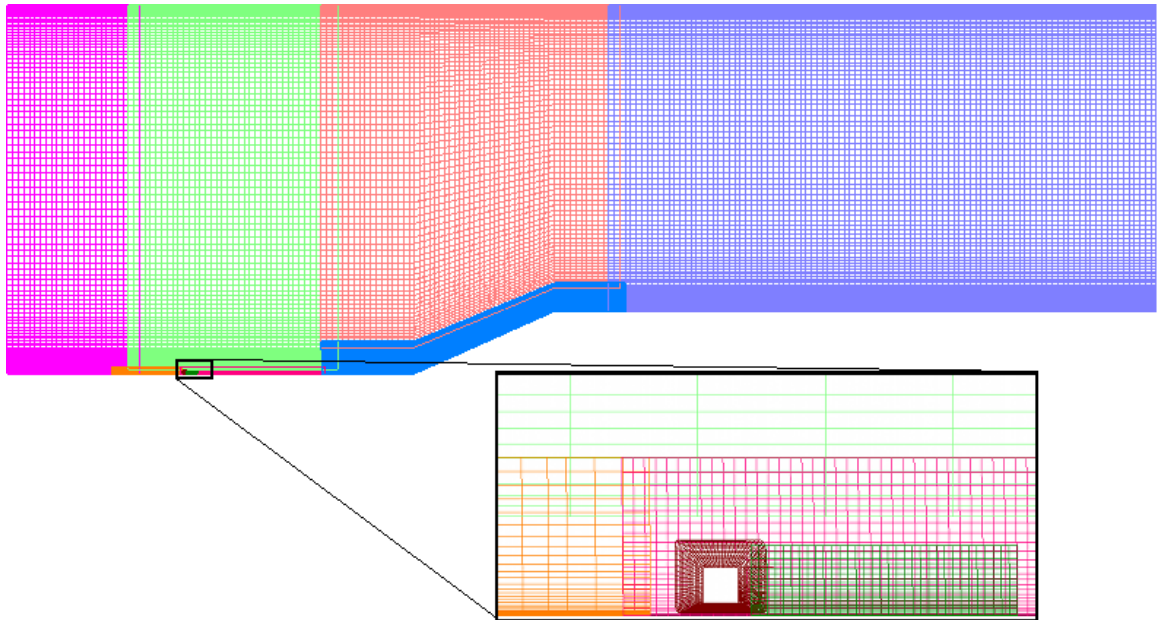
One of the more interesting features of OVERFLOW is its use of overset grids, which represent a unique approach to grid construction developed by Benek, Buning, and Steger [129] in order to allow structured grids to be easily built for complex geometry. Today, overset grids are seldom used outside of academic and government research,

although there are a few commercial tools available that employ them, such as ESI's FASTRAN, Metacomp's CFD++ and Cradle's STREAM. Overset grids are composed of multiple overlapping structured grids. Figure 5.1 illustrates the overlapping nature of the overset grids used in numerical experiments. Hole-cutting is used to discard points inside 3-D objects, while high-order interpolation is used to transition between grids in overlap regions. The advantages to this technique are that it makes grid generation much simpler, as refining or changing one grid does not require changing every other grid connected to it, adjacent grids do not need to conform, and it allows the use of structured grid solvers on hexahedral meshes, which do not have the truncation issues associated with tetrahedral meshes.

Because of the simplicity of construction, a structured mesh can be designed for OVERFLOW in a fraction of the time required to make a mesh for use in Fluent or similar software. OVERFLOW additionally features an automatic mesh generator for off-body grids used in simulating external flows around aircraft and the like, further simplifying mesh generation. Furthermore, because the grids are stored in PLOT3D format, they can be constructed using any of a variety of commercial tools, and results can be viewed in common visualization applications such as Tecplot and FieldView. Further, unlike contiguous-mesh codes, overset meshes allow for easy meshing and fast computation of moving objects, such as ailerons and flapping wings, since the capability of mesh overlap simplifies the movement of different mesh blocks. Of course, structured meshes cause fewer cache misses than unstructured meshes, leading to overall faster computation times.

In the "chimera" scheme [130], each sub-mesh is treated as a separate entity and thus requires a closed set of boundary conditions. Obviously, boundaries that coincide with the boundary of the computational domain simply use the boundary condition assigned by the user. But boundaries that lie in overlap regions within the interior of the flow must inherit information via interpolation from nearby points from

Figure 5.1: Close-up of overset grid features for a 24 degree shock ramp featuring a trip wire



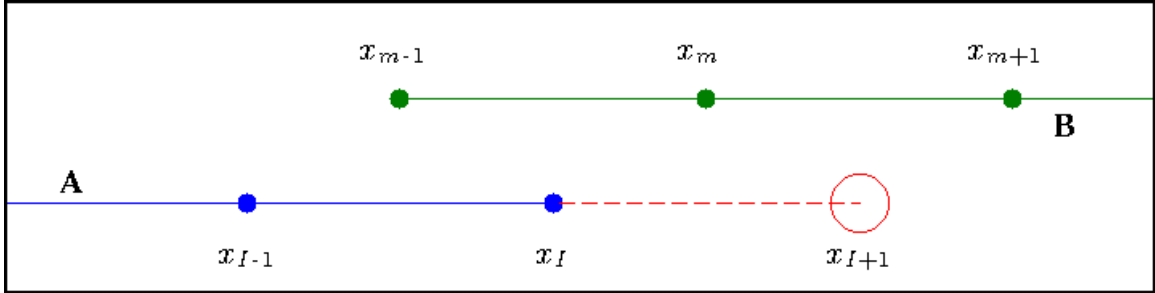
overlapped grids. This interpolation is performed by constructing “ghost points” as depicted in Fig. 5.2, which shows an overset mesh for a 1-D problem. Suppose that the boundary of grid A lies inside grid B. For the interpolated velocity,  $u_{I+1}$ , at a ghost point,  $x_{I+1}$ , where  $I$  is the maximum index of grid A, the value is given by second-order linear interpolation,

$$u_{I+1} = \alpha u_m + (1 - \alpha) u_{m+1} \quad (5.7)$$

$$\alpha = \frac{x_{m+1} - x_{I+1}}{x_{m+1} - x_m}, \quad (5.8)$$

where the  $m$  index denotes the cell of B containing the boundary point of A. Higher orders of accuracy can be obtained by using more points and polynomial rather than linear interpolation. However, this scheme results in non-conservative flux formulations. Wang et al. [131] proved that for a steady-state solution with second-order finite volume scheme, the conservation error induced by the chimera formulation is first-order, suggesting that the conservation error will always be at least an order of magnitude larger than the discretization error. This can cause significant errors when

Figure 5.2: Overlapping 1-D grids with a ghost point (red) created by chimera interpolation



steep gradients or shock waves transverse overlap regions. As we will see in Sec. 6.3 this can cause problems in boundary layers. Furthermore, because large-eddy simulation in general results in transient, highly irregular fluid structures, the traditional chimera formulation will likely induce additional errors. Therefore, it is helpful to keep overlap regions away from critical areas in the flow, though this may not always be possible.

There is currently an active debate over the construction of conservative schemes for OVERFLOW. The problem is that while conservative schemes obviously have some desirable properties, they also tend to be unstable and induce errors of their own. Tang and Zhou [132] showed that the undesirable properties of non-conservative schemes disappear as the mesh resolution increases, but this is to be expected of any method with error based on the mesh resolution. More recently, Tramel et al. [133] have proposed an interpolation scheme based on volumes rather than points, although this scheme is not mature and has not been implemented in OVERFLOW. Currently, there is a tradeoff between stability and obeying conservation laws, and OVERFLOW takes the former approach. As a result, it is important to limit the influence of overset interpolation errors on any computational mesh, and the cases presented in this work are degraded by overset phenomena to varying degrees.

Due to the aforementioned difficulties, the most widely used commercial solvers do not support overset grids. Because of this, it is often impossible to convert results

obtained using overset grids to a format usable by other solvers. This significantly limits the usefulness of overset CFD codes.

### 5.3 WENOM shock capturing

As mentioned in Sec. 5.1, there are a variety of shock-capturing options available in OVERFLOW that eliminate Gibbs phenomena. In the supersonic experiments performed in this work, we have used the mapped weighted essentially non-oscillatory scheme (WENOM) of Hendrick et al. [134]. WENOM is a correction to the original WENO5 scheme of Jiang and Shu [124] that maintains 5<sup>th</sup>-order accuracy near critical points, defined as points where the 1<sup>st</sup> derivatives of the solution vanishes, but the 3<sup>rd</sup> derivatives do not. The original scheme can drop to as low as 3<sup>rd</sup>-order accurate at critical points, hence the need for the WENOM correction to maintain global 5<sup>th</sup>-order accuracy.

To construct a WENO-type scheme, numerical fluxes are first computed across several stencils each containing the point at which the derivative is desired. The derivative is then computed from a weighted average of the fluxes, where each flux is weighted according to a smoothness function, which is defined by the particular scheme. Depending on the stencil size, this allows high orders of accuracy and low dissipation comparable to what can be obtained with centered differencing, yet with the stabilizing, shock-capturing behavior typically associated with much lower-order TVD schemes.

Following Hendrick et al. [134], we explain the WENOM scheme in terms of a scalar conservation law,

$$\partial_t u + \partial_x f(x) = 0, \tag{5.9}$$

which is then spatially discretized on a uniform mesh of  $N + 1$  points,  $\{x_j = j/N\}$ , where the points lie at the center of finite volumes. This is then discretized in space,

yielding

$$\partial_t u(x_j) = \frac{h_{j+1/2} - h_{j-1/2}}{\Delta x}, \quad (5.10)$$

where  $\Delta x = 1/j$  in this case, and  $h \approx f$  is the conservative numerical flux function.

The formula for  $h$  is given by

$$h_{j+1/2} = \sum_{k=0}^2 w_k h_{j+1/2}^k, \quad (5.11)$$

where  $h_{j+1/2}^k$  is the 3<sup>rd</sup>-order stencil approximation of  $h_{j+1/2}$  on  $(x_{j+k-2}, x_{j+k-1}, x_{j+k})$ , and the  $w_k$ s are weights. The WENOM scheme has a fairly complex formulation of weights. First, preliminary weights from the original WENO5 [124] formulation are computed,

$$w_k^* = \frac{\alpha_k}{\sum_{i=0}^2 \alpha_i} \quad (5.12)$$

$$\alpha_k = \frac{a_k}{\varepsilon + \beta_k} \quad (5.13)$$

$$\mathbf{a} = [1/10, 6/10, 3/10], \quad (5.14)$$

where  $\beta_k$  is a smoothness indicator based on local differences (details of the differencing and the formulas for  $\beta_k$  can be found in Hendrick et al. [134]), and  $\varepsilon$  is a small, user-selected value that prevents division by zero. The accuracy of this original formulation exhibits significant dependence on  $\varepsilon$ , which led to the modification of the weights with a continuous mapping,

$$g_k = \frac{w_k^*(a_k + a_k^2 - 3a_k w_k^* + (w_k^*)^2)}{a_k^2 + w_k^*(1 - 2a_k)}. \quad (5.15)$$

The final weights are then computed by

$$w_k = \frac{g_k}{\sum_{i=0}^2 g_i}, \quad (5.16)$$

which provides a system that is 5<sup>th</sup> order accurate everywhere. Not only is WENOM more formally more accurate than WENO5 schemes, but it shows excellent ability to preserve oscillating waves passing through a shock wave, a behavior that TVD

schemes tend to eliminate entirely, thus making the WENOM scheme much better suited for LES.

The main advantages of this scheme are its high accuracy, its non-total variation diminishing (TVD) character, and low dissipation. In the context of LES, excessive dissipation can significantly inhibit or even totally eliminate resolved-scale turbulent behavior. TVD is a non-physical condition when imposed on transient and turbulent flows. To see why, imagine a point downstream of a vortex-shedding obstacle. As the vortices pass through the point, the variation will increase, and as the smooth regions of the flow pass through it, the variation will decrease. In the numerical experiments performed in the course of preparing this work, it was found that TVD schemes tend to completely suppress the development of turbulence, and dissipation near the shock needed to be minimized in order to preserve the shock-turbulent interaction.

#### **5.4 Parallelization and performance tests**

Parallelization of OVERFLOW is done on two levels. First is domain decomposition, which is a fully automated process that splits the grid into hexahedral regions with an approximately equal number of points on each generalized coordinate axis, one per each core specified, with parallelization handled via an MPI abstraction layer. While there is no hard-coded limit on the number of processors, there appear to be computational problems associated with domains that are too small (although this may be due to bugs introduced by our heavy modification of OVERFLOW in this work). It appears that approximately 150k points per subdomain are needed to prevent floating-point overflows in the iterative solution procedure. The second level is the use of OpenMP on any loops through the arrays associated with each of the domains, which requires no sophisticated programming. The hybrid MPI/OpenMP approach allows the strengths of each to be leveraged within the code, resulting in a high level of parallel efficiency on a massively parallel machine featuring multi-core



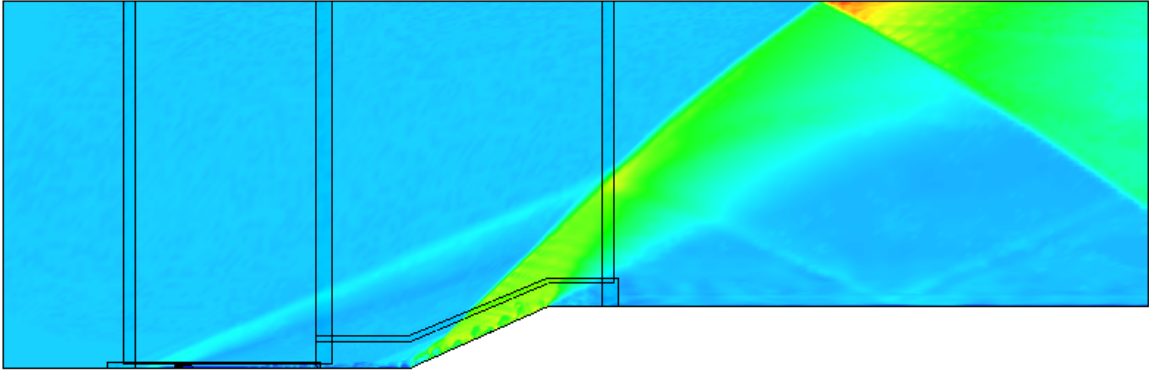
processors.

### 5.4.1 Model problem

To test the parallel efficiency of OVERFLOW on the hardware used for the present investigation, a model problem was constructed for a 24 degree shock ramp experiment with uniform air inlet conditions of Mach 2.9 and  $T_\infty = 109.26K$ . The shock ramp was 454 mm from the inlet and had a height of 68 mm. A trip wire was placed 192 mm from the inlet in order to induce turbulence. The maximum height of the geometry was 400 mm, the width was 500 mm, and the total length was 1396 mm. The floor of the simulated test section was set to the adiabatic no-slip condition, and the other walls were inviscid with pressure extrapolation. This problem was chosen to model the test section of a wind tunnel in a physical experiment performed by Ringuette et al. [135], for which there exists detailed physical data. Additionally, detailed DNS data were obtained by Wu et al. [136]. This model problem and the grids in this section were used for early iterations of the final mesh ultimately used for the simulations found in Sec. 6.3, although they ultimately proved to need significant modification.

Three different meshes were used for simulation, here referred to as the coarse, medium, and fine meshes. The coarse mesh had  $\sim 6.7$  million nodes, the medium mesh had  $\sim 11.8$  million nodes. and the fine mesh had  $\sim 22.4$  million nodes. Each mesh had the same basic structure as seen in Figure 5.1. The ARC3D diagonalized Beam–Warming scheme [137] was used for the implicit solves, and WENOM was used for shock-capturing. Discretization was second order in time, with a dimensionless time step of 0.01. Fifth-order spatial discretization combined with 2<sup>nd</sup>-order simple time discretization achieved high-quality LES resolution in the boundary layer behind the trip wire. No explicit turbulence model was used, nor had any explicit filtering been implemented for these tests, so built-in dissipation parameters were adjusted in

Figure 5.3: Density contours for the initial condition



order to stabilize the computations. Flow was initialized using the  $k - \omega$  turbulence model to achieve a converged solution, and implicit LES (ILES) was run for 200,000 or more time steps (depending on the grid) in order to obtain a fully-developed initial condition.

#### 5.4.2 Results

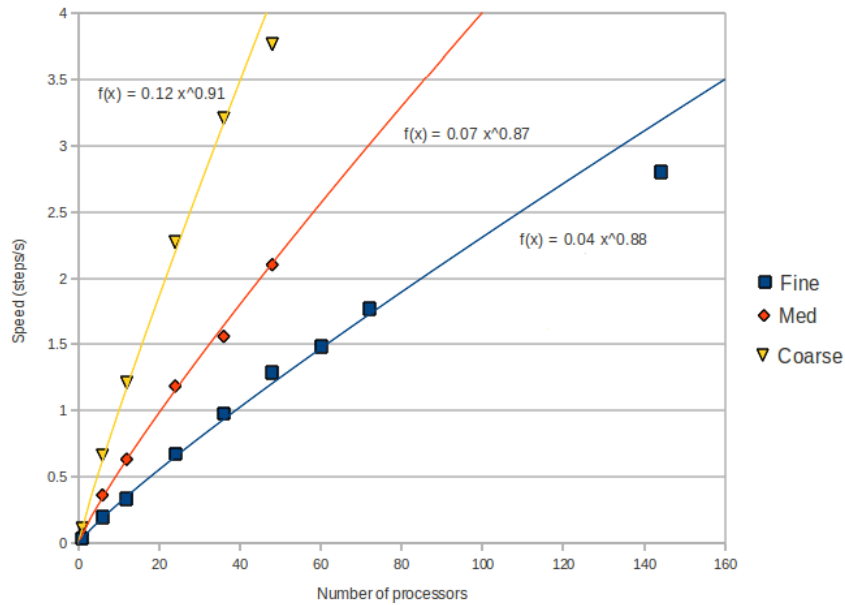
In each case, 500 time steps were computed starting from the statistically stationary, fully-developed initial condition depicted in Figure 5.3, and the average computation time per time step was taken from the output file generated by OVERFLOW. Because the flow was fully developed for the initial condition, the final condition after 500 time steps was nearly identical except for instantaneous details of fluctuations in the boundary layer. Observe that the initial condition exhibits a strong oblique shock at the ramp, which reflects off the ceiling of the wind tunnel and continues to the outlet. There is a system of weaker shocks at the trip wire and near the boundary layer; this is because the boundary layer is unstable and features time-dependent, irregular structures.

Parallel computations for this result and all other computations in this work were performed using from 1 to 200 cores on the University of Kentucky's DLX cluster, which has 376 nodes with two 2.66 GHz Xeon X5650 processors at each node, for a

Table 5.1: Time per step in seconds for the coarse, medium, and fine meshes

N. Cores	Coarse	Med	Fine
1	8.53	14.3	26.7
6	1.50	2.74	4.99
12	0.826	1.58	2.97
24	0.441	0.843	1.48
36	0.312	0.641	1.02
48	0.266	0.476	0.776
60			0.673
72			0.565
144			0.357

Figure 5.4: Processing speed versus number of cores



total of twelve cores and 36 GB of RAM per node. The fine mesh has been run on as many as 144 cores in order to demonstrate the high scalability of the code. The average time per flow solution step is recorded in Table 5.1. OVERFLOW provides a detailed breakdown of the entire computation time, so we have here recorded only the time spent in the solution process, as time spent reading from and writing to files can be minimized by reducing the number of times save states are written. The machine used for computations was experiencing problems with its file system at the time of experimentation, resulting in an undue impact on overall time (as much as

80% of total run time could be consumed by file I/O). Figure 5.4 shows the data for computation speed with a power law curve fit. For the coarse grid,  $f(x) = 0.12x^{0.91}$ , for the medium grid,  $f(x) = 0.07x^{0.87}$ , and for the fine grid,  $f(x) = 0.04x^{0.88}$ , where  $x$  is the number of cores. As can be seen in Figure 5.4, computation time follows an approximate power law. Ideal behavior is a doubling of speed with a doubling of processors, which corresponds to an exponent of 1 in the power law curve fit. The figure shows that this exponent does approach 1 as the grid size decreases, although it should be noted that even the coarse grid at 6.7 million nodes is not particularly small by current engineering CFD standards. Further, for all three grids, the exponent is still close to 0.9—in fact, it is approximately the same for both medium and fine grids, despite the latter grid having about twice as many points as the former.

## 5.5 Summary and conclusions

OVERFLOW is a highly efficient parallel CFD code, exhibiting an approximate power law behavior for computation speed with an exponent close to 0.9 . This behavior persists for grids as large as 22 million nodes and for as many as 144 cores. The hybrid MPI/OpenMP structure of the code combined with the use of structured overset meshes provides excellent, consistent scalability. Computationally optimal decomposition of a structured grid is relatively simple, since the grid is simply a rectangular prism in computational space; this makes structured grids a good choice for parallel CFD. Because the use of overset grids makes the construction of structured meshes much simpler, OVERFLOW is an excellent code for computationally intensive compressible CFD calculations. However, the limitations of overset meshes, especially when high-gradient, turbulent structures and shock waves pass through overlap regions, should not be disregarded when examining computational results.

In the context of LES, we recommend using second-order time advancement with Newton subiterations. In the context of LES, high-order shock capturing is necessary,

and so we recommend the WENOM scheme due to the fact that it is 5<sup>th</sup>-order accurate everywhere in the flow. And because OVERFLOW is so highly efficient, as many cores as are available should be used while keeping the number of grid points per core to  $\sim 150k$ .

## Chapter 6. Computations

In order to validate the potential of the PMNS model for use in LES, three test cases were simulated and compared to DNS or experimental results: homogeneous, isotropic, decaying turbulence on a periodic cube with at rms Mach 0.3, a 24 degree shock ramp at Mach 2.9, and an open cavity with  $L/H = 6$  at Mach 0.8. The form of the model used was based on Lundgren's linear forcing ??, using the output of the CPMNS equations to scatter the energy, with a single adjustable constant used to change the intensity of the SGS velocity field.

In this chapter, we will see that the model's influence on macroscopic flow quantities are marginal. This is in fact desirable, as purely dissipative turbulence models tend to be quite effective at predicting wall pressures to within engineering tolerances. See, for example, the simulations of Kim et al. [138] of a NACA-0018 airfoil using a modification of the dynamic model [68], which show excellent agreement with experimental results. Therefore a backscatter model should not have order-of-magnitude effects on these kinds of quantities. With that in mind, the chief goal of the CPMNS model is providing small-scale structures in the flow field that a purely dissipative model would typically eliminate. Such structures may not have a large effect on quantities such as mean wall pressure, but they have a significant effect on the dispersion of Lagrangian particles in multiphase flows and the mixing rate of chemical species in combusting flows. We have constructed the filter-forcing model with this problem in mind, although we have not at this time begun to investigate the model's effects on Lagrangian particles or chemical kinetics. The forcing scheme in this chapter is implemented as follows:

1. Compute a single time step as usual, including all Newton iterations.

2. Apply an explicit, low-pass filter.
3. Extract a high-pass velocity field,  $\mathbf{u}_{hi}$ .
4. Perform local checks to determine whether the flow is locally turbulent.
5. If the check is positive, iterate a chaotic discrete map and construct a pointwise force,  $\mathbf{f}$ .
6. Incorporate this force into the right-hand side vector to be used in the next time step.
7. Return to step 1.

In Sec. 6.1, the filtering scheme used throughout this work is explained, and the shock-detection routine used to avoid introducing the near-shock oscillations associated with high-order filtering schemes is discussed. In Sec. 6.2, we compare DNS and LES results for homogeneous, isotropic, decaying turbulence on a periodic cube with an rms Mach number of 0.3. These results show the filter-forcing model’s ability to improve CFD results via induced backscatter. In Sec. 6.3, we compare LES of a Mach 2.9 compression ramp to the DNS of Wu [139] and the measurements of Ringuette et al. [135]. In Sec. 6.4, we compare the results of different LES simulations of a Mach 0.8 flow over an open cavity to the classic measurements of Plentovich et al. [140].

## 6.1 HAMR filtering

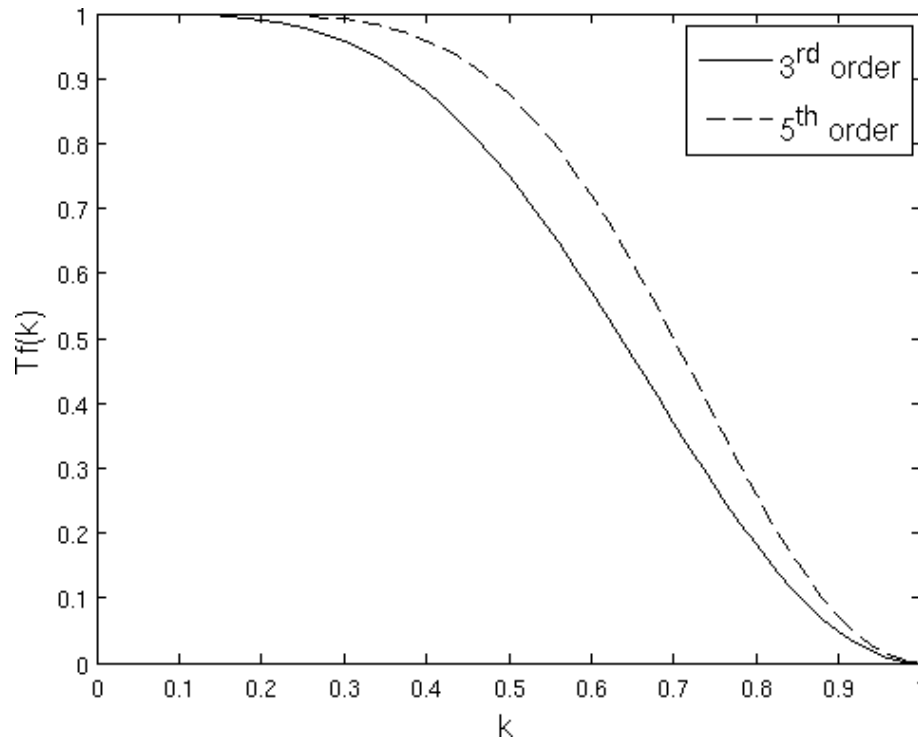
As argued in Section 3.2.3, explicit filtering is superior to relying on dissipation introduced by the numerical method and the turbulence model to act as a kind of implicit filter due to the former’s mathematically straightforward connection to filtering the governing equations. OVERFLOW features two built-in filters, a 3<sup>rd</sup>-order filter employing 4<sup>th</sup> differencing and a 5<sup>th</sup>-order filter employing 6<sup>th</sup> differencing.

If  $n$  is the number of 2<sup>nd</sup> differences applied, the OVERFLOW filtering scheme takes the form

$$\bar{\mathbf{q}} = \mathbf{q} + \left[ \left( -\frac{1}{4} \right)^n \left( (d_j^2)^n + (d_k^2)^n + (d_l^2)^n \right) \right] \mathbf{q}, \quad (6.1)$$

where  $d_j^2$  is the 2<sup>nd</sup> difference operator in the  $j^{\text{th}}$  direction. While this class of filters has  $2n - 1$  vanishing moments and thus can be considered as a class of high-order commutative filters, they are excessively dissipative. As can be seen from the transfer functions for the OVERFLOW filters plotted in Fig. 6.1, the high attenuation region begins at  $k \approx 0.25$  for the 3<sup>rd</sup>-order filter and  $k \approx 0.35$  for the 5<sup>th</sup>-order filter. Numerical experiments revealed that both filters are simply far too dissipative to be used in the context of LES. In fact, even the 5<sup>th</sup>-order filter completely damped all the turbulent fluctuations in the case of the Mach 2.9 compression ramp. Thus it is clear that the particular choice of filter is critical for successful LES computations.

Figure 6.1: Transfer functions for the  $(d^2)^n$  filters featured in OVERFLOW versus scaled wavenumber  $k$





Padé filters take the form

$$G_2 \bar{\phi} = G_1 \phi, \quad (6.2)$$

where  $G_1$  and  $G_2$  are filtering operations using weighted averaging. The transfer function for the filter operation  $G = G_1^{-1}G_2$  is thus given by

$$T_G(k) = \frac{T_{G_1}(k)}{T_{G_2}(k)}. \quad (6.3)$$

By constructing the left-hand and right-hand filter matrices such that  $T_{G_1} \approx T_{G_2}$  for  $k < k_{cutoff}$ , then

$$T_G(k) \approx 1, \quad k < k_{cutoff}. \quad (6.4)$$

This allows the construction of filters that closely approximate spectral cutoff filters without the expense of transforming the solution to the spectral domain. However, because the numerical method solves Eq. (6.2) rather than directly constructing  $G$ , one must avoid having too many coefficients in the banded  $G_2$  matrix in order to not increase solution time too much.

### 6.1.1 Low-pass filtering

Explicit filtering was performed on the conserved variables at the end of each time step using an optimized high-accuracy and maximum-resolution (HAMR) scheme, which is an asymptotically stable Padé filter featuring low dispersion, introduced by Liu et al. [112]. The unique ability of Padé filtering to avoid attenuating low-wavenumber modes resulted in superior solution accuracy compared to a classical 10<sup>th</sup>-order filter as demonstrated in numerical experiments performed by the same authors in a second paper [141]. To filter a variable,  $\phi$ , and obtain  $\bar{\phi}$ , the HAMR formula is given by

$$\bar{\phi}_i + \alpha(\bar{\phi}_{i-2} + \bar{\phi}_{i+2}) + \beta(\bar{\phi}_{i-1} + \bar{\phi}_{i+1}) = \sum_{\ell=0}^3 \frac{p_\ell}{2} (\phi_{i+\ell} + \phi_{i-\ell}) \quad (6.5)$$

for interior points, with the values for the filter coefficients taken from the aforementioned second paper [141]. These are given as

$$\alpha = 0.5673952755$$

$$\beta = 0.1209216774$$

$$p_0 = 0.9665459988$$

$$p_1 = 1.1849715528$$

$$p_2 = 0.2217709541$$

$$p_3 = 0.0033454001.$$

Near the boundary, an asymmetric scheme of the form,

$$\mathbf{a} \cdot [\bar{\phi}_1, \dots, \bar{\phi}_5] = \mathbf{b} \cdot [\phi_1, \dots, \phi_6], \quad (6.6)$$

is used. The coefficients for the second and third points near the boundary are given respectively as

$$\mathbf{a}_2 = (0.3217547156, 1.0, 1.2703966706, \\ 0.4689158656, 0.0)$$

$$\mathbf{b}_2 = (0.317036053, 1.0192555517, 1.2318855773, \\ 0.5074269689, -0.0192555517, 0.003851103),$$

and

$$\mathbf{a}_3 = (0.1346835856, 0.5779871517, 1.0, 0.577987157, \\ 0.1346835856, 0.1346835856)$$

$$\mathbf{b}_3 = (0.13114000585, 0.5957047873, 0.9645646288, \\ 0.6134224229, 0.1169659500, 0.0035435271).$$

Observe that this scheme has only five filter coefficients in the left-hand  $G_2$  matrix, requiring the solution of a pentadiagonal system at each time step. The interior filter

has five vanishing moments, so the commutation error is  $\mathcal{O}(\Delta^6)$ . The boundary filters possess only four vanishing moments, so the commutation error for them is  $\mathcal{O}(\Delta^5)$ . Since OVERFLOW's most highly resolved flux discretizations are 6<sup>th</sup> order accurate in the interior of the flow domain, this makes the HAMR scheme an ideal choice for the computations in this work. This set of filters possess the transfer functions seen in Figs 6.2–6.4. As can be seen, all three filter kernels possess a steep, smooth spectral cutoff and very little attenuation of the low wavenumbers. This makes them an ideal choice for LES, since as the mesh size approaches zero, we expect the high-wavenumber content to be negligible and the error introduced by the filter to be on the order of the discretization error. Since the vector of conserved variables,  $\mathbf{q}$ , is filtered at every time step, we will drop the overbar notation for filtered variables in this chapter.

Figure 6.2: Transfer function for low-pass (solid) and high-pass (dashed) filters versus scaled wavenumber  $\omega$

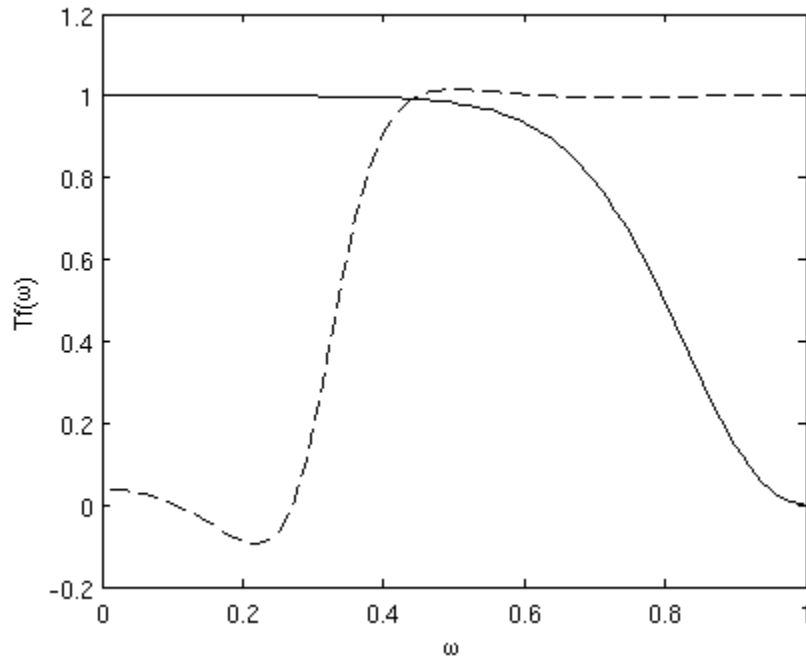
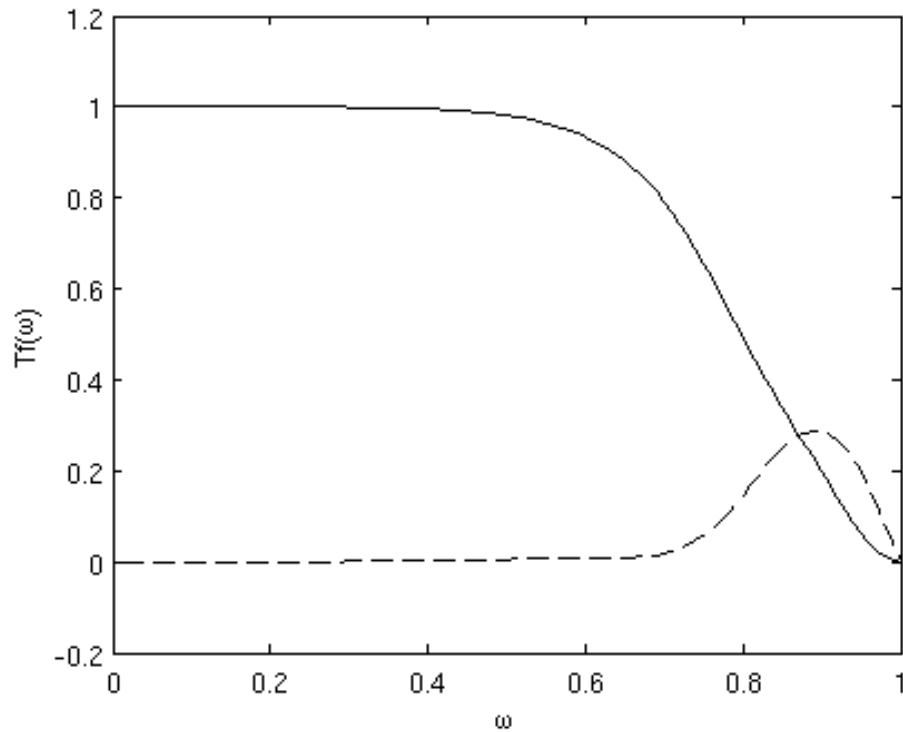


Figure 6.3: Real (solid) and imaginary (dashed) components of the transfer function for the 2<sup>nd</sup> point away from the boundary versus scaled wavenumber  $\omega$



### 6.1.2 High-pass filtering

To calculate the high-pass velocity components for the backscatter model, we obtained filter coefficients by doing a least-squares fit to a sharp spectral cutoff at  $\omega = 0.3$  as seen in Fig. 6.4. While this method proved to sufficiently isolate high-wavenumber content for the purpose of structural turbulence modeling, the filter coefficients do not exactly satisfy the relations necessary to be used as a low-pass filter for mollifying a PDE solution as part of a numerical procedure, so we caution any reader away from using these coefficients in that manner. The filter coefficients for the interior points

are given by

$$\alpha = -0.6275872367$$

$$\beta = 0.2691885228$$

$$p_0 = 0.06314459948$$

$$p_1 = 0.1096411682$$

$$p_2 = 0.0701432898$$

$$p_3 = 0.02940528862,$$

and the same least-squares procedure was used to obtain coefficients for the boundary points, which are given by

$$\mathbf{a}_2 = (0.3096256995, 1.0, 1.1380646293, \\ 0.4106696169, 0.0)$$

$$\mathbf{b}_2 = (0.3084688023, 1.0057844862, 1.1264956568, \\ 0.4222385894, -0.0057844862, 0.0011568972),$$

and

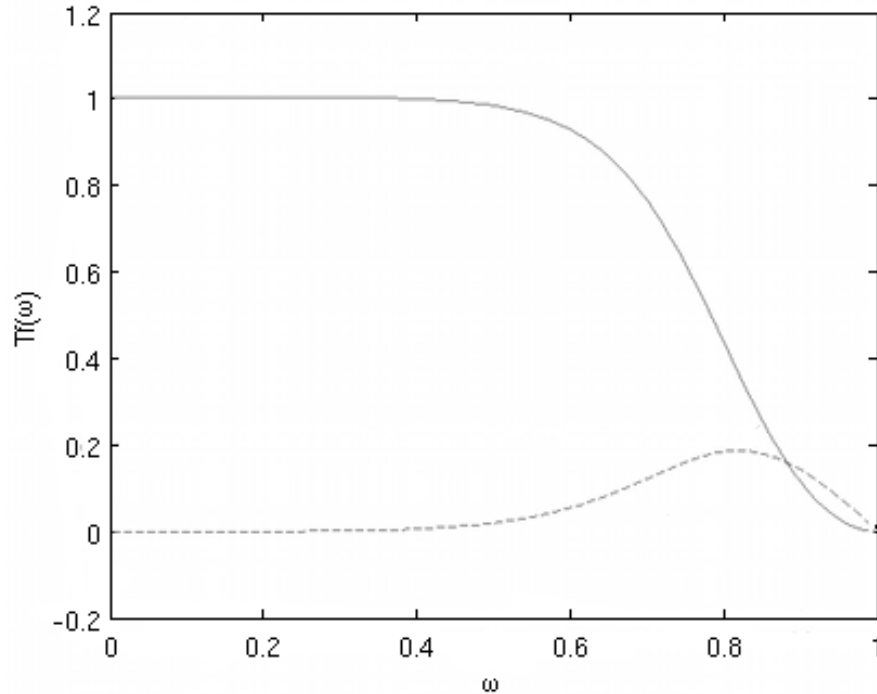
$$\mathbf{a}_3 = (0.1477868412, 1.0, 1.1264956568, \\ 0.6357553622, 0.1477868412)$$

$$\mathbf{b}_3 = (0.1470348738, 0.6395151994, 0.9924803256, \\ 0.6532750366, 0.1440270040, 0.0007519674).$$

By using these coefficients in a high-pass filter, we obtain small-scale conserved variable field  $\mathbf{q}_{hi}$ . The high-pass primitive velocities are found by

$$u_{hi,i} = \frac{(\rho u_i)_{hi}}{\rho}. \quad (6.7)$$

Figure 6.4: Real (solid) and imaginary (dashed) components of the transfer function for the 3<sup>rd</sup> point away from the boundary versus scaled wavenumber  $\omega$



### 6.1.3 Shock detection

Care must be taken regarding shocks. While a HAMR scheme attenuates high- $k$  modes, it does not dissipate in a Gaussian-like manner. The smooth, sharp shocks created by shock capturing schemes depend on high- $k$  modes in order to locally eliminate the Gibbs phenomenon. By attenuating primarily these modes, the HAMR scheme actually counteracts the shock-capturing scheme and reintroduces near-shock oscillations. Additional filtering at each time step compounds the oscillations until they cause critical instability or nonphysical quantities, such as negative densities or pressures. In addition, construction of  $\mathbf{u}_{hi}$  will also create undesired velocities in the vicinity of the shock, which will cause spurious activation of the turbulence model. We illustrate this phenomenon using a simple 256-point scalar jump function smoothed with a single pass of the Shuman filter [142],

$$u_i = \frac{u_{i-1}^* + 2u_i^* + u_{i+1}^*}{4}, \quad (6.8)$$

which creates a signal analogous to the kinds of oscillation-free smoothed shock waves found in CFD simulations using classical shock-capturing routines. This function is depicted in Fig. 6.5. Application of the filter, however, introduces oscillations around the shock, as seen in Fig. 6.6, which depicts the difference between the filtered and unfiltered signals, analogous to  $u_{hi}$  in the LES model. Clearly, this necessitates special treatment at the shock.

The approach to shock treatment taken in this work is to simply avoid filtering near the shock. If we have a discrete signal,  $\{u_i | 1 < i < n\}$ , we will represent the  $n \times n$  HAMR filtering matrix by  $H_n$ . If we have near-discontinuities at  $\{u_{i_1}, \dots, u_{i_m}\}$  we wish to apply the filtering operation only to the “smooth” sections of  $u$  and ignore the discontinuous regions, i.e.,

$$\bar{u} = \left( [H_{i_1-1}(u_1, \dots, u_{i_1-1})^T]^T, u_{i_1}, \dots, u_{i_m}, [H_{n-i_m}(u_{i_m+1}, \dots, u_n)^T]^T \right). \quad (6.9)$$

Although this introduces  $\mathcal{O}(\Delta^5)$  commutation error associated with the boundary filter at places in the interior of the flow, this is preferable to the solution-stopping instabilities caused by allowing Gibbs phenomena to accumulate. Further, the WENOM scheme used for the cavity and the ramp is 5<sup>th</sup>-order, so this will have no effect on global solution accuracy.

Shock detection is a nontrivial problem and currently an area of active research, although the main focus of literature on this topic is visualization of shock waves rather than computing CFD solutions. Because of this, many of the methods are too slow to be incorporated into a CFD solver. The HAMR scheme requires the solution of pentadiagonal systems in each spatial direction, so additional computations should be kept to a minimum. Kanamori and Suzuki [143] identify two main classes of shock detection in current use: those based on the assumption that local gradients are perpendicular to the shock, and those based on solving the local Riemann problem, of which their method is an example. However, this latter class of methods tends to be too computationally expensive to be included as a method of shock detection in

Figure 6.5: Discrete signal  $u$  featuring a smoothed, discontinuous jump.

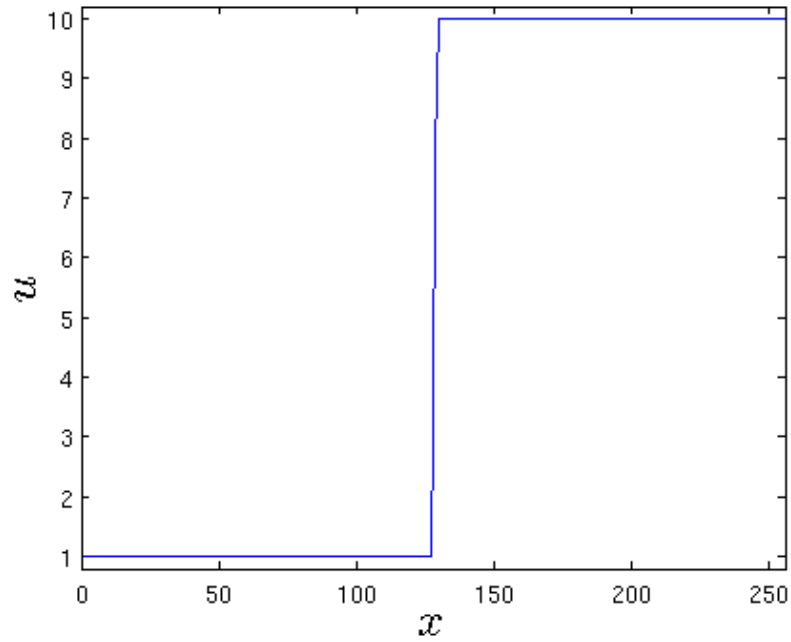
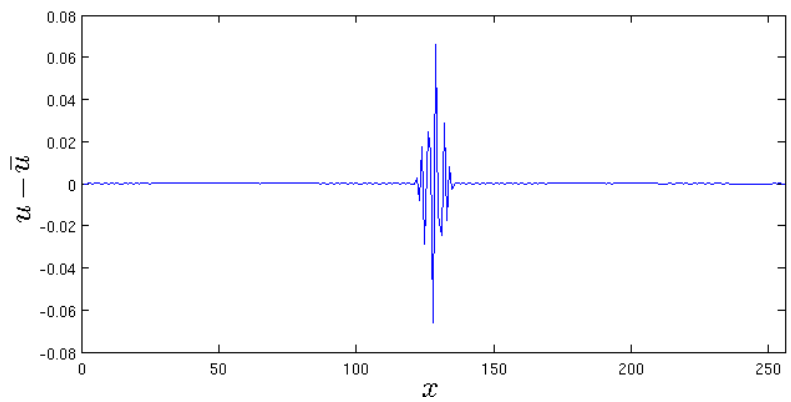


Figure 6.6: Difference between  $u$  and  $\bar{u}$ , where  $\bar{u}$  is filtered with the HAMR scheme without any shock detection





CFD.

The first method investigated was the pressure gradient method of Lovely and Haimes [144]. They introduce a shock detection function,

$$F_{shock} = \frac{\mathbf{u} \cdot \nabla p}{a|\nabla p|} - \frac{a\nabla \cdot (\rho\mathbf{u})}{|\nabla p|}, \quad (6.10)$$

where  $a$  is the speed of sound, and  $F_{shock} \geq 1$  in the presence of a shock. Eliminating all points from the filtering routine where  $F_{shock} \geq 0.9$  proved to be adequate for preventing Gibbs phenomena from arising while still providing filtering in the turbulent regions of the flow. But because OVERFLOW does not store the pressure or its gradient at each time step, the additional memory and computational costs associated with this method were something we wished to avoid. However, it was used in early numerical experiments and proved to be effective in a range of situations without needing to adjust any parameters, so we recommend its use in any compressible CFD code employing high-order filtering.

In the present work, we employed a density smoothness indicator similar to the smoothness functions employed in WENO shock capturing. The formula is given by

$$F_{smooth} = \frac{\frac{13}{12}(\rho_{i-1} - 2\rho_i + \rho_{i+1})^2 + \frac{3}{2}\rho_i(\rho_{i+1} - \rho_{i-1})}{\rho_i^2}. \quad (6.11)$$

This is computationally inexpensive and does not require the creation of whole new variable arrays, since it can be computed only for the vector currently being filtered. But in this formula, there is no reason to expect a universal value of  $F_{smooth}$ . For the shock ramp studied in the present work, cutting out points for  $F_{smooth} > 0.2$  proved to be adequate and returned results close to using the pressure-gradient scheme [144]. Figs 6.7 and 6.8 show  $|\mathbf{u}_{hi}|$  for a Mach 2.9 compression ramp with and without shock detection, respectively.

Figure 6.7: Contours of  $|\mathbf{u}_{hi}|$  for a Mach 2.9 compression ramp with no shock detection. Note the pronounced oscillations on both sides of the shock wave and its reflection.

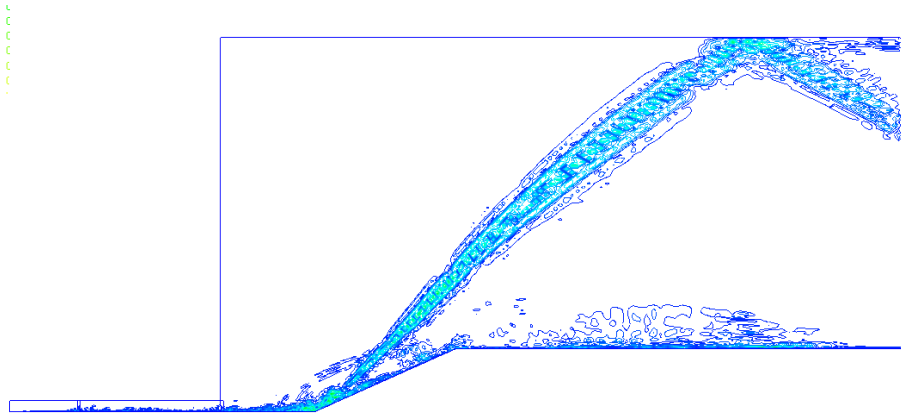
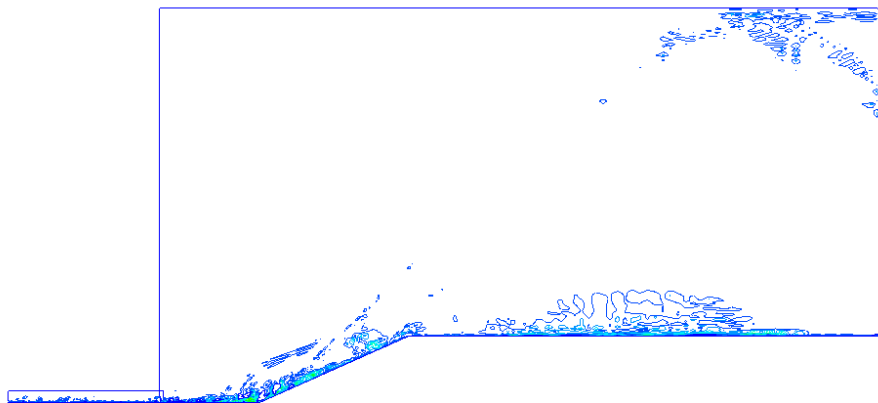


Figure 6.8: Contours of  $|\mathbf{u}_{hi}|$  for a Mach 2.9 compression ramp with simple shock detection using  $F_{smooth} = 0.2$ . Note the elimination of oscillations near the shock wave, although turbulent regions are still effectively captured.



## 6.2 Homogeneous, isotropic, decaying turbulence

Direct numerical simulation of homogeneous, isotropic turbulence on a cube is a popular method of studying features of turbulence and validating theoretical hypotheses that cannot be easily simulated by experiment. Because the goal of LES is to accurately simulate the important large-scale dynamics of turbulence without fully resolving the mesh, validating the turbulence model against DNS results is an ideal place to begin. For example, Schmidt et al. [5] validated their ODT simulations against the DNS results of Kang et al. [145]. This work is based on the DNS results of Samtaney et al. [146]. However, unlike incompressible turbulence, the behavior of compressible turbulence is influenced by shocklets, pressure waves, and dilatational effects, so that compressible turbulence does not currently have a well-established, universal law analogous to Kolmogorov's  $k^{-5/3}$  law for incompressible turbulence. The attempts of Shivamoggi to derive a universal scaling law for fully developed compressible, isotropic turbulence resulted in a scaling law that depends on  $\gamma$ , but is not thermodynamically consistent [147, 148]. More recent theoretical work by Aluie [149] has argued that energy transfers in compressible turbulence occur via a local cascade process; therefore an inertial subrange should exist with a power law behavior decaying faster than  $k^{-1}$ . The numerical experiments of Kritsuk et al. [150] exhibit a power spectral scaling behavior of  $k^{-1.9}$ ; however, introducing a density-weighted velocity,  $\tilde{v} = \rho^{1/3}v$ , returns a scaling close to  $k^{-5/3}$  [150]. Schmidt et al. [151] have found via numerical experiment that Kritsuk's density-weighted velocity correlations of forced, compressible turbulence do not follow a universal scaling law and vary with large-scale forcing (which implies that the inertial subrange does not follow a universal law either). Because of these considerations, we make no attempt here to relate our results to any universal laws. However, we do in part base them on the specific DNS results of Samtaney et al. [146], as they provide detailed information on the setup of the problem and comprehensive information on the time evolution of

the system. We approximate those conditions for the numerical experiments in this section.

### 6.2.1 Initial and boundary conditions

Simulations were carried out for air ( $\gamma = 1.4$ ,  $\text{Pr} = 0.72$ ) in the cube  $[0, 2\pi]^3$  with periodic boundary conditions. A divergence-free, randomized initial condition was generated following the formulation of Samtaney et al. [146]. In our specific implementation, the initial condition had a spectrum given by

$$E(k) = Ak^4 \exp\left(-2\left(\frac{k}{k_0}\right)^2\right), \quad (6.12)$$

with peak wavenumber  $k_0 = 8$ , and initial stagnation energy and density were constant. The desired initial condition can then be generated by randomly generating Fourier coefficients under the constraints

$$\widehat{w}_{jkl} = \frac{-j\widehat{u}_{jkl} - k\widehat{v}_{jkl}}{l}, \quad (6.13)$$

$$\widehat{u}_{jkl}^2 + \widehat{v}_{jkl}^2 + \widehat{w}_{jkl}^2 = E(\mathbf{k}), \quad (6.14)$$

$$|\mathbf{k}|^2 \leq 32, \quad (6.15)$$

The Taylor microscale  $\lambda$  and Reynolds number  $Re_\lambda$  are defined here as

$$\lambda^2 = \frac{u'^2}{\langle(\partial_1 u_1)^2\rangle}, \quad Re_\lambda = \frac{u'\lambda\langle\rho\rangle}{\langle\mu\rangle}, \quad (6.16)$$

where  $\langle \cdot \rangle$  denotes the volume average over the entire domain and

$$u' = \left\langle \frac{u_i u_i}{3} \right\rangle^{(1/2)} \quad (6.17)$$

We further define the turbulent Mach number by

$$M' = \left\langle \frac{u_i u_i}{c^2} \right\rangle^{(1/2)}, \quad (6.18)$$

where  $c$  is local speed of sound. Values of  $A$ ,  $e_0$ , and  $\rho$  were chosen such that  $M' = 0.3$  and  $Re_\lambda = 72$ . Simulations were run on  $129^3$ ,  $65^3$ , and  $33^3$  grids using values of

$C_{PMNS} = 0, 10, 50,$  and  $100$ . The initial conditions for the coarse grids were obtained by downsampling the initial condition for the fine grid and applying the Padé filter. Detailed results from the  $33^3$  grid are not included due to significant divergence from the DNS results. With the peak wavenumber equal to the Nyquist wavenumber of 8, the inertial subrange is not sufficiently resolved, so dissipation dominated the results, and no turbulent behavior was observed. The turbulence model resulted in only very small changes of  $\mathcal{O}(10^{-2})$  between the statistical quantities computed for the different runs. This confirmed that the inertial subrange must be at least partially resolved in order for the backscatter model to be viable.

### 6.2.2 Numerical method

Discretization in space was done using 6<sup>th</sup>-order centered differencing, while time discretization used a 2<sup>nd</sup>-order linearized implicit method with Newton subiterations. A sufficiently small time step and six Newton iterations were sufficient for RHS residuals to drop eight orders of magnitude at each time step. No shock capturing was necessary, as no shock waves were present in the solution field. For this set of experiments, we avoided a high Mach number because shock-turbulent interactions pose additional difficulties for LES due to the fact that length scales necessary to resolve shock corrugation are typically on the order of the Taylor or Kolmogorov scales. Because eddy shocklets can cause a significant contribution to enhancing the overall energy dissipation rate, and since we are not currently implementing a shocklet model, a low Mach number is ideal here. The left-hand side matrix of the implicit solution procedure was constructed using the ARC3D Beam-Warming [137] block tridiagonal scheme, and the HAMR scheme was applied at the end of the Newton iterations at each time step.

Table 6.1: Parameters for the DNS and LES runs on the periodic cube. Note that for the runs with filtering, but no explicit CPMNS model,  $C_{PMNS}$  is assigned a value of 0

Resolution	$C_{PMNS}$
129 <sup>3</sup>	0
65 <sup>3</sup>	0
65 <sup>3</sup>	1
65 <sup>3</sup>	10
65 <sup>3</sup>	50
65 <sup>3</sup>	100
33 <sup>3</sup>	0
33 <sup>3</sup>	1
33 <sup>3</sup>	10
33 <sup>3</sup>	50
33 <sup>3</sup>	100

### 6.2.3 Results and analysis

Simulations were run under the conditions given in Table 6.1. To analyze the results, we considered the time-evolution of four statistical quantities: the rms divergence,  $\theta'$ , the normalized mean kinetic energy,  $K$ , the velocity derivative skewness,  $S_3$ , and rms streamline curvature,  $\kappa'$ . We also computed PSDs for total, dilatational, and solenoidal kinetic energy. Due to memory limitations on the machine used for post-processing, averages were computed on the slice  $[0, 2\pi] \times [0, 2\pi] \times [0, \Delta]$ . Derivatives were not directly compared between DNS and LES results. Rather, the DNS results were filtered and downsampled to a 65<sup>3</sup> grid using a simple Shuman [142] filter with the 1-D form

$$\hat{u}_i = \frac{u_{i-1} + 2u_i + u_{i+1}}{4}, \quad (6.19)$$

which is then applied in each spatial direction.

While the first three statistics are common in analyzing turbulence,  $\kappa'$  is not. The motivation for the use of  $\kappa'$  is the visualization of the time-evolution of small-scale turbulent structures. A high level of turbulence should be associated with streamlines of high curvature due to irregular topology in the flow field. Of course, high-order

statistical moments are common, such as flatness and skewness, but as seen below, the rms curvature reveals significantly more fine-scale behavior.

The decay of the mean kinetic energy,  $K = \frac{1}{2} \langle \rho u_i u_i \rangle$ , is normalized by  $K(0)$  and plotted as a function of  $t$  in Fig. 6.9, where  $t$  is the solution time scaled by  $u'_0/L$ , with  $u'_0$  being the initial rms velocity and  $L = 1$ , which is simply OVERFLOW's internal length scaling. As is clear from the plot, the HAMR scheme alone introduces excessive dissipation. The backscatter model ( $C_{PMNS} > 0$ ) improves the energy decay rate, but does not appear to be capable of exactly matching the DNS in time, with the largest discrepancies appearing early in the time evolution of the system. Recall that the turbulence of the initial condition consists exclusively of the solenoidal mode, which is divergence-free by definition. Thus early evolution of the flow field includes net transfers of energy not only from larger to smaller scales, but from solenoidal to dilatational modes. The mechanisms of this transfer are not adequately resolved on the coarse grid, though it is apparent the backscatter model improves them.  $C_{PMNS} = 50$  appears to give the best match overall of those values employed. As seen from the DNS results,  $K$  in the slice should decay monotonically over time, but this is eventually broken by excessive forcing in the backscatter model. A model parameter of  $C_{PMNS} = 100$  introduces excessive, nonphysical kinetic energy fluctuation, with both rapid increases and decreases in  $K$  over time. Thus, in its current formulation, the model limits the range of parameters that can be considered. However, it may be possible that an orthogonal forcing, which would eliminate Eq. (4.40b) from the model, would allow a greater range of parameters, since the energy input from the forcing would be zero in a pointwise rather than a statistical sense.

Figure 6.10 shows the decay of  $\theta'$  versus  $t$ . Here, it is clear that  $C_{PMNS} = 100$  results in complete disagreement between LES and DNS results, while the best agreement is again achieved by  $C_{PMNS} = 50$ . While all LES solutions are all too dissipative compared to DNS, it is clear that the backscatter model counteracts this effect.

Figure 6.9: Decay of mean kinetic energy over time

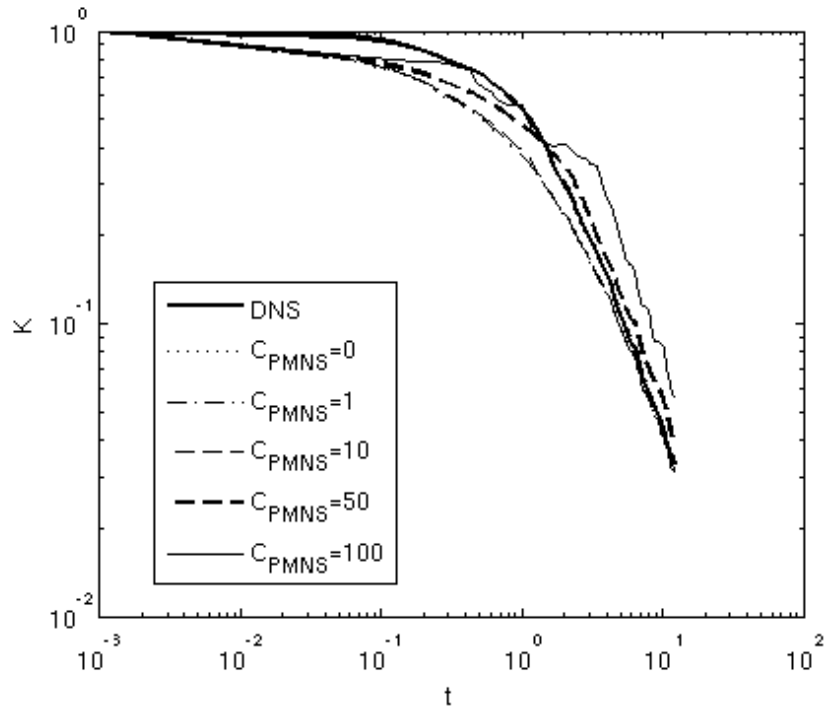
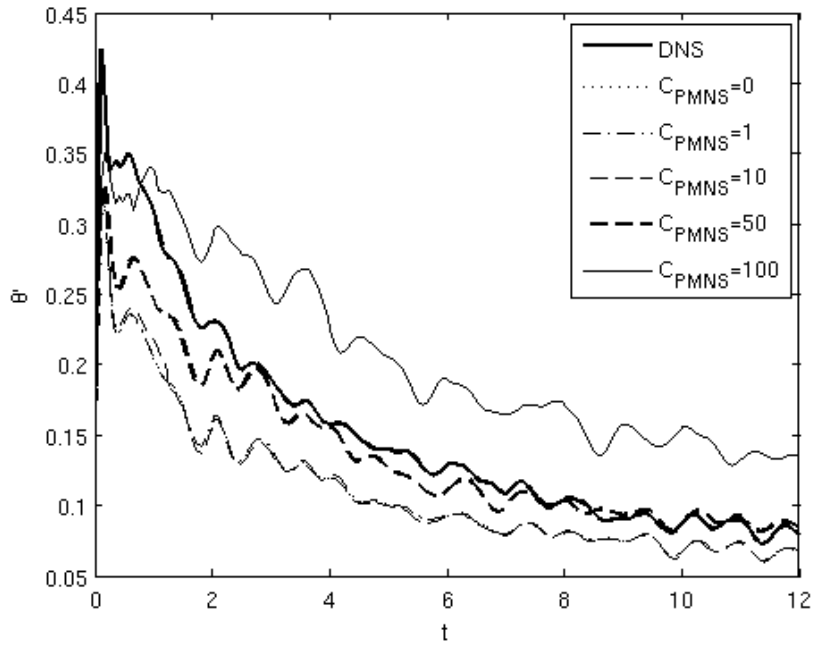


Figure 6.10: Evolution of rms divergence versus time



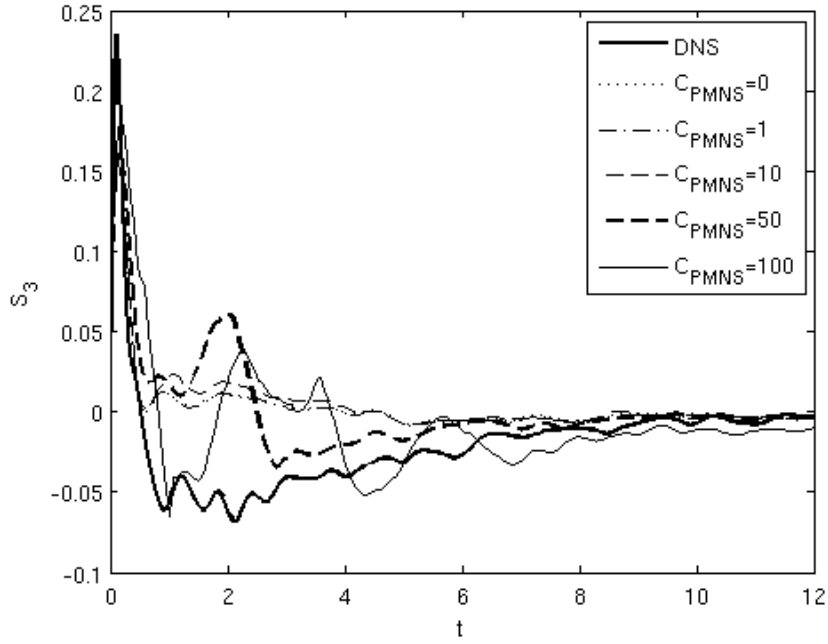


The derivative skewness  $S_3$  is defined by

$$S_3 = \frac{\langle (\partial_x u_1)^3 \rangle}{\langle (\partial_x u_1)^2 \rangle^{3/2}} \quad (6.20)$$

and plotted in Fig. 6.11. Interestingly, the model has significant effects in the early evolution of the system, due largely to the fact that the flow has far larger gradients and overall irregularity. This confirms the model's sensitivity to the irregularity of the resolved flow. While no model parameter creates a good match for the derivative skewness in the slice,  $C_{PMNS} = 50$  provides an overall magnitude comparable to the DNS and a much better match for the decay rate than the lesser values.

Figure 6.11: Evolution of the skewness of  $\partial_x u_1$  in time



In a vector field with well-defined derivatives, the curvature of a streamline through the point  $\mathbf{x}_0$  is given by Weinkauff and Theisal [152] as

$$\kappa(\mathbf{x}_0) = \frac{|\mathbf{u} \times (\nabla \mathbf{u} \cdot \mathbf{u})|}{|\mathbf{u}|^3}, \quad (6.21)$$

leading naturally to the definition of rms curvature,

$$\kappa' = \langle \kappa^2 \rangle^{(1/2)}. \quad (6.22)$$

Numerically, this may lead to singularities, so in practice, the denominator in Eq. (6.21) is replaced by  $\max(|\mathbf{u}|^3, 10^{-8})$ . Figure 6.12 shows the change in  $\kappa'$  over time. Increasing the value of  $C_{PMNS}$  results in the fluctuations in  $\kappa'$  being more frequent and more intense, indicating more creation and destruction of small-scale structures. While none of the curves match the DNS results point by point in time, and we are ignoring  $C_{PMNS} = 100$  due to the aforementioned nonphysical characteristics, the peaks in the curve corresponding to  $C_{PMNS} = 10$  and  $50$  are of a similar frequency and magnitude compared to those of the DNS.

Figure 6.12: Evolution of  $\kappa'$  in time

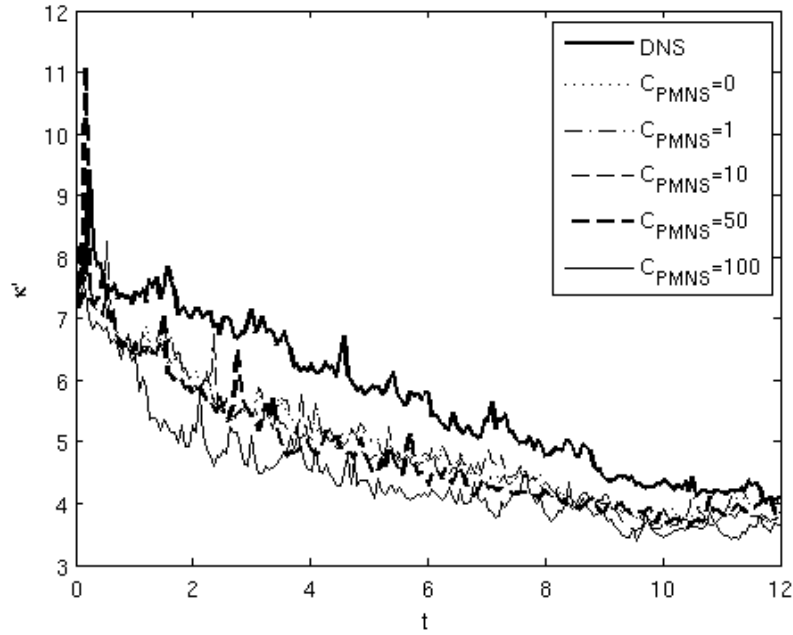
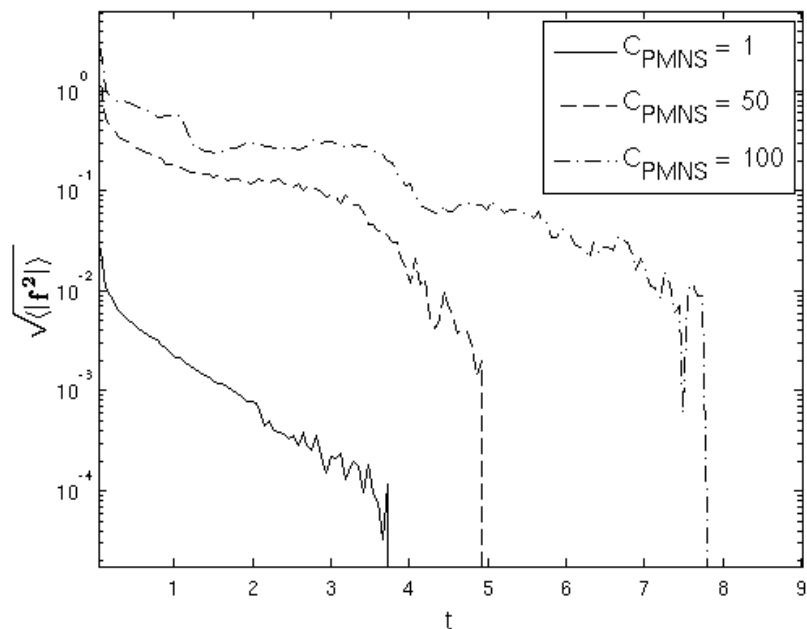


Figure 6.13 shows the rms magnitude of the magnitude of the force vector,  $|\mathbf{f}|$ , versus time. Observe that for any value of  $C_{PMNS}$ , the model eventually deactivates. This is desirable, because as homogeneous, isotropic turbulence decays, the high-wavenumber content decays the most rapidly as energy is permanently dissipated. This manifests itself in the fineness and intensity of small-scale structures decreasing over time. Conserved variable gradients decay as a consequence of this behavior, resulting eventually in a solution that can be well resolved on a coarser mesh, as

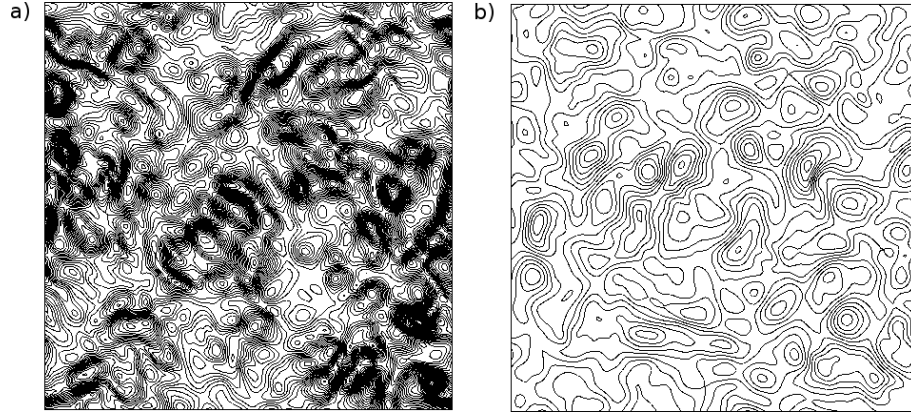
seen in Fig. 6.14. This confirms that the CPMNS turbulence model is unlike traditional Smagorinsky-type models in that it is not continuously active whenever flow is nonuniform. Note that as  $C_{PMNS}$  increases, its decay becomes more and more irregular, until the point where the backscatter model is active well into the range that it is no longer necessary, as seen by comparing the curve for  $C_{PMNS} = 100$  with the KE decay seen in Fig. 6.9.

Figure 6.13: Decay of rms  $|\mathbf{f}|$  versus time.



While the above statistical and spectral analyses give a quantitative appraisal of the model's effect on small-scale behavior, density contour plots of LES and DNS solutions give a qualitative view of how the backscatter model enhances small-scale turbulent structures. Fig. 6.15 shows contours of density at  $t = 2.2$ , which is a value deep in the time-evolution of the flow, but before dissipation dominates the dynamics. All four plots use the same contour levels so that direct comparisons can be made. It is clear that the PMNS model enhances the formation of small-scale turbulent structures, as the results for  $C_{PMNS} = 50$  have a more visible similarity to the DNS results than for  $C_{PMNS} = 0$ . There are more local extrema, more areas of large

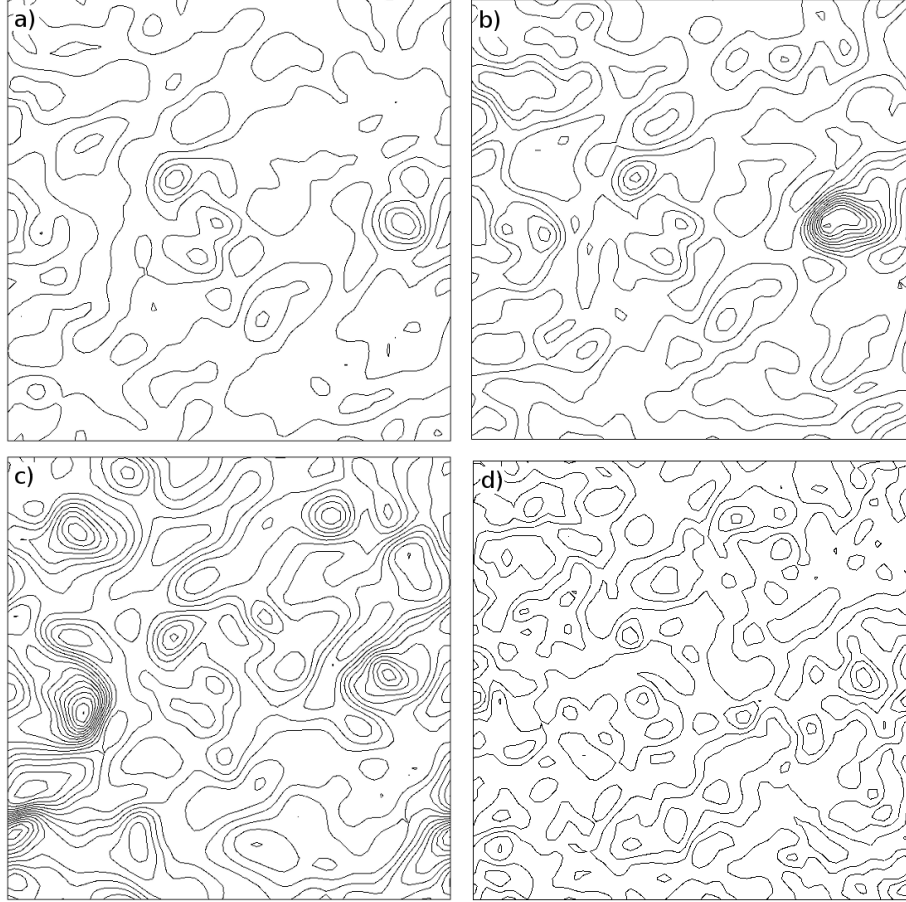
Figure 6.14: Contour plots of  $\rho$  for DNS at  $t = 0.36$  and  $t = 4.02$ . Note the loss of small-scale structure and increase in overall smoothness as the solution evolves in time.



gradients, and more overall small-scale structure, although it still does not have quite as much fine-scale structure in the density field as the filtered DNS exhibits. We can also see that excessive forcing corresponding to  $C_{PMNS} = 100$  results in a completely unrealistic solution featuring excessively steep gradients, rather than enhancement of small-scale structures.

Power spectral density (PSD) estimates of the  $u_1$  component of velocity in the  $x$  direction for several experiments at  $t = 2.2$ , corresponding to 2220 time steps, can be seen in Fig. 6.16. Data for  $C_{PMNS}$  values of 1 and 10 are omitted due to their strong similarity with the  $C_{PMNS} = 0$  series. These estimates were found by averaging the PSDs computed from a discrete Fourier transform (DFT) of the velocity for each row of the slice. Both downsampled  $65^3$  and  $129^3$  DNS results are included for comparison purposes. On the  $65^3$  grid, the steep decay begins at  $k \approx 10$ , while it begins at  $k \approx 25$  for the DNS. After 2220 time steps, the filter has created a significant attenuation of the high wavenumbers in addition to any numerical dissipation. It appears that  $C_{PMNS} = 50$  and  $C_{PMNS} = 100$  produce a slightly better match with the slope of the high-wavenumber decay for the DNS (both filtered and unfiltered) than filtering alone. Note that the results for  $C_{PMNS} = 100$  match the results for  $C_{PMNS} = 50$ , showing that spectral energy decay alone is not enough to establish physically realistic results.

Figure 6.15: Contour plots of density at  $t = 2.2$  for (a)  $C_{PMNS} = 0$ , (b)  $C_{PMNS} = 50$ , (c)  $C_{PMNS} = 100$ , and (d) DNS filtered and downsampled to the  $65^3$  grid



The PSDs for the dilatational and solenoidal kinetic energy are given by, respectively,

$$E_d(k) = \frac{1}{2k^2} E_{div}(k) \quad (6.23)$$

and

$$E_s(k) = \frac{1}{2k^2} E_\omega(k), \quad (6.24)$$

where  $E_{div}$  is the PSD of the divergence field,  $E_\omega$  is the PSD of the vorticity field. The gradients used to construct these quantities were computed using Tecplot, which uses second-order centered differencing. The spectra for LES, DNS, and filtered DNS results can be seen in Figs 6.18 and 6.17. Here, the data for  $C_{PMNS} = 100$  is omitted due to the non-physicality of these results. Of particular interest is the fact that

the HAMR scheme has the strongest effect on the solenoidal mode. Because the initial condition is entirely solenoidal, we expect the solenoidal kinetic energy to have substantially more high-wavenumber content than the dilatational mode. Since the HAMR scheme applies the most attenuation to high- $k$  mode, it thus has the most effect on the solenoidal mode. The addition of the backscatter model improves the high wavenumber content of both modes; however, the most significant improvement can be seen in the dilatational spectrum, where the decay rate in the upper part of the range appears to match that of the filtered DNS fairly well. Clearly, to improve the effectiveness of the model, something must be done to correct the excessive dissipation of the solenoidal energy, either by reformulating the filter, or increasing the solenoidal forcing in the model.

Figure 6.16: PSDs of the velocity field  $t = 2.2$  for,  $C_{PMNS} = 0$ ,  $C_{PMNS} = 50$ ,  $C_{PMNS} = 100$ , and both raw and downsampled DNS results

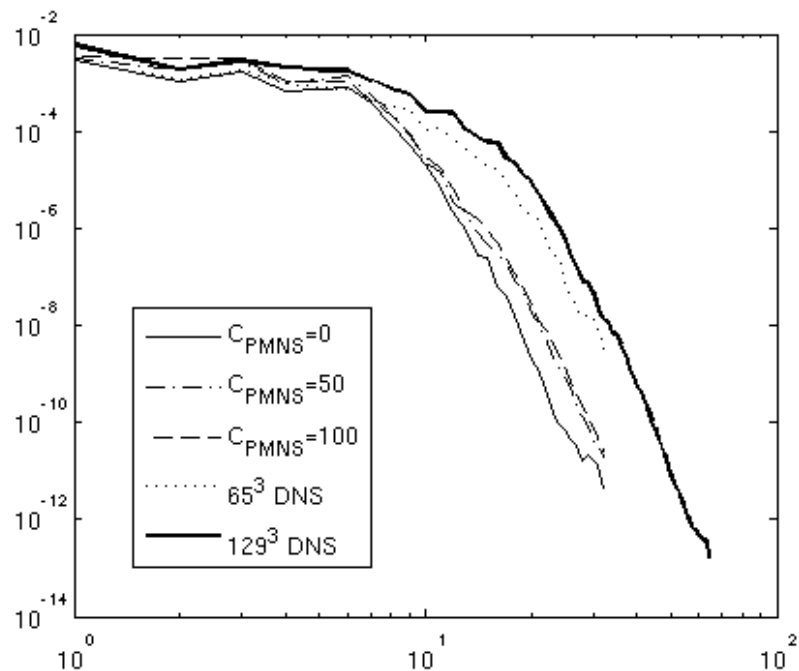


Figure 6.17: PSDs of the solenoidal velocity field  $t = 2.2$  for,  $C_{PMNS} = 0$ ,  $C_{PMNS} = 50$ , and both raw and downsampled DNS results

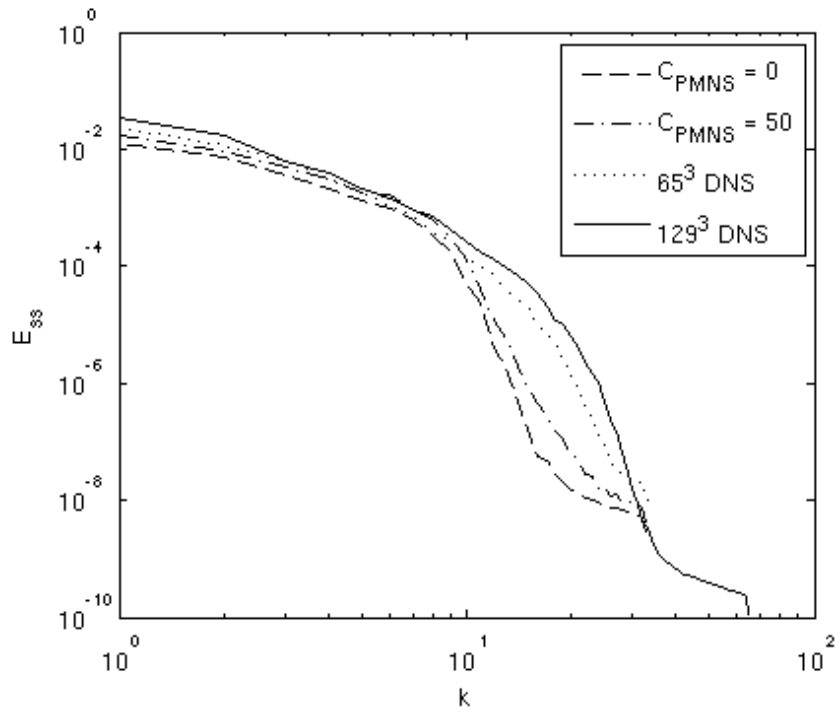
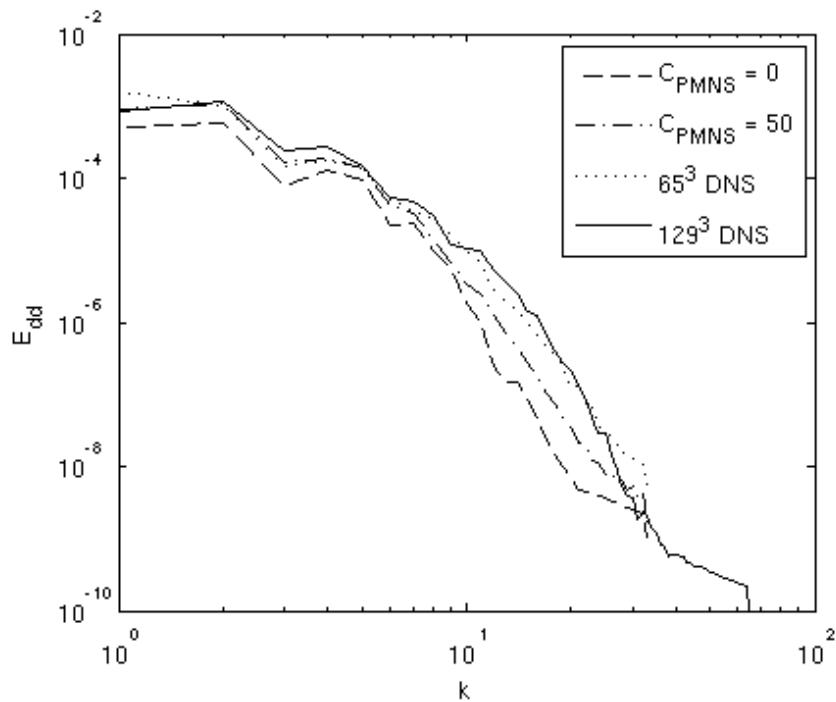


Figure 6.18: PSDs of the dilatational velocity field  $t = 2.2$  for,  $C_{PMNS} = 0$ ,  $C_{PMNS} = 50$ , and both raw and downsampled DNS results



### 6.3 Mach 2.9 compression ramp with turbulent boundary layer

Due to geometric simplicity, two-dimensional compression ramps have been popular tools for studying the interaction of turbulent boundary layers with strong, oblique shock waves at high Mach numbers. This flow is of particular interest because the boundary layer interaction creates a large separation bubble when the ramp angle and Mach number are sufficiently high; thus it is an ideal context for studying interactions of shock waves with turbulent boundary layers. An early comprehensive study was done by Settles et al. [153], which provided detailed results for compression ramps ranging from 8 to 24 degree angles, and for momentum thickness Reynolds number  $Re_\theta = 67,200$ . Later experiments by Selig et al. at a slightly lower Reynolds number [154] gave more insight into effects deeper in the boundary layer. These experiments established four critical features of the turbulent compression ramp flow:

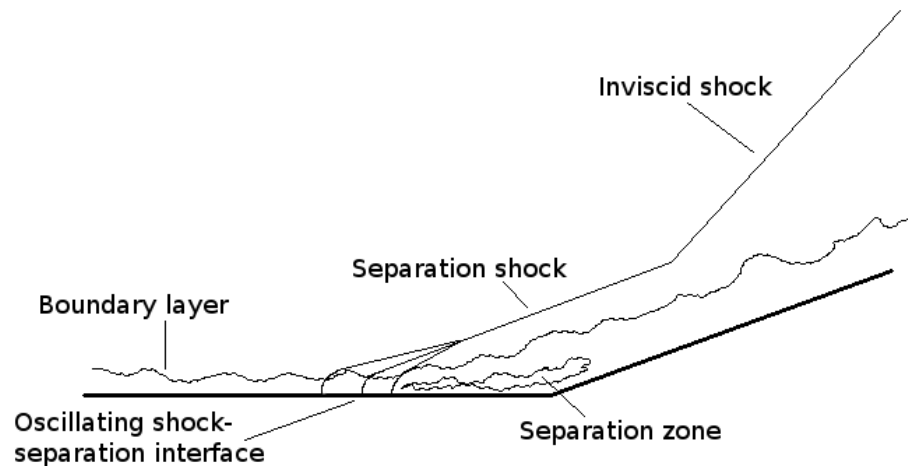
1. The boundary layer thickness  $\delta$ , defined as the point where  $U/U_\infty = 0.99$ , where  $U$  denotes time averaging.
2. The dimensionless separation length,  $X/\delta$ , where  $X$  is the average length of the separation zone. Settles et al. [153] found that  $X/\delta$  increases with decreasing Reynolds number.
3. The separation shock, which occurs at the separation point and has approximately the same angle as the shock ramp due to the shape of the separation zone.
4. The main ramp shock, which obeys the inviscid, oblique shock relations.

All of these structures exhibit significant unsteady behavior, as illustrated in the general profile of the shock-turbulent interaction in Fig. 6.19. The separation bubble's size and shape fluctuate, small turbulent structures arise within the separation, the separation shock oscillates in streamwise location, and it exhibits corrugations as it



interacts with the incoming turbulent flow. Because of this, time-average quantities are determined not just by the strength of the shock, but also by the proportion of time it spends upstream or downstream of a given location.

Figure 6.19: Sketch of the key features of the shock structure near a compression ramp



While the aforementioned physical experiments are important and shed a great deal of light on the nature of shock-ramp/boundary-layer interactions, the Reynolds numbers are simply too high for DNS comparisons. For DNS to be tractable on such a geometry, it is necessary to have  $Re_\theta < \sim 10,000$ . See, e.g., the computations of Wu and Martín [136]. This constraint led Bookey et al. [155], further expanded upon by Ringuette et al. [135], to perform a series of experiments delivering high quality measurements and characteristics of a Mach 2.9 compression ramp at a 24 degree angle. The DNS of Wu and Martín [136] has excellent agreement with these experimental results, demonstrating that the compressible NSEs do in fact provide an adequate model of compressible, turbulent flow in this regime, and that therefore non-continuum effects in the shock wave have minimal effects on the macroscopic flow behavior. This validates the assertion in Sec. 3.3 that the purpose of a turbulence model is to compensate for mathematical inadequacies of the numerical solution procedure, as opposed to providing physics not captured in the governing equations.

Unsteadiness of the separation shock location is particularly a problem for RANS modeling, since the idea is to predict the time average of the flow. RANS modelers are aware of this and attempt to account for this by modifying their turbulence production and dissipation terms in such a way as to account for shock wave oscillation. See, for example, the volume of work produced by K. Sinha with Candler [156] [157] and Pasha [158]. In these works, Sinha and his various co-authors develop a shock-turbulent interaction correction for existing RANS models based on modifying the turbulence production and dissipation quantities behind the shock wave to match experimental results. However, there is a critical oversight in these works—while the authors discuss the effects of shock oscillation on the mean shock location, they neglect to even mention that mean quantities up and downstream of the shock are determined by the temporal distribution of the shock oscillation. This is an intrinsic shortcoming of the RANS equations with Boussinesq hypothesis, as oscillation and dissipation are completely different mechanisms.

To illustrate the problem, consider a uniform, inviscid flow field in air ( $\gamma = 1.4$ ) at an unspecified Mach number with a normal, oscillating shock at a location described by  $x(t) = \sin(t)$ . To simplify the problem, we will ignore shock corrugation, boundary layer effects, separation, etc. Assume the standard normal shock relations associated with perfect gas,

$$\frac{p_2}{p_1} = 1 + \frac{2\gamma}{\gamma + 1}(M_1^2 - 1) \quad (6.25)$$

where  $p_1$  and  $M_1$  are the upstream pressure and Mach number upstream of the shock. Then pressure in the flow field is described by

$$p(x, t) = \begin{cases} p_1, & x \leq \sin(t) \\ p_2, & x > \sin(t). \end{cases} \quad (6.26)$$

The Reynolds averaged pressure is then found by integrating

$$\begin{aligned}
 P(x) &= \lim_{T \rightarrow \infty} \frac{1}{T} \int_0^T p(x, t) dt \\
 &= \frac{1}{2\pi} \int_0^{2\pi} p(x, t) dt \\
 &= \begin{cases} p_1, & x < -1 \\ \frac{p_1 + p_2}{2} + \frac{\sin^{-1}(x)}{\pi} (p_2 - p_1), & x \in [-1, 1] \\ p_2, & x > 1, \end{cases} \quad (6.27)
 \end{aligned}$$

which is no longer a jump condition. A plot of this function corresponding to  $M = 2$ , i.e.,  $p_2/p_1 = 4.5$ , can be seen in Fig. 6.20. Not only is there no discontinuity anywhere, but the derivatives are all discontinuous at the terminal points of the oscillation region,  $x = \pm 1$ . Similar analysis holds for any truncated Fourier expansion of a time series, although there is likely no general, analytical form.

Because this result is independent of any considerations of turbulence or boundary layer separation, it is incorrect to view the problem with standard RANS models as simply under-predicting the size of the mean separation bubble or the mean shock location. Rather, because time-averaged flow quantities near the shock arise due to the temporal distribution of the shock location, there is no sharp distinction between a time-averaged shock and a time-averaged separation zone. The classic experiments of Gadd confirm this [159]. These experiments explored the interaction of a nearly normal shock wave with an airfoil boundary layer. Even in cases with weaker shocks and negligible separation, significant distributional effects on the wall pressure can be observed. This is in fact even more consequential for the modeling of an oblique shock. In the course of preparing this work, we observed that the entire separation shock is corrugated by the turbulent flow, and both its position and shape vary in time. See, e.g., Figs 6.37–6.36 below. The distributional effects on the local pressure therefore will affect the wall pressure in the entirety of the separation region.

Figure 6.20: Time-averaged pressure for an oscillating shock

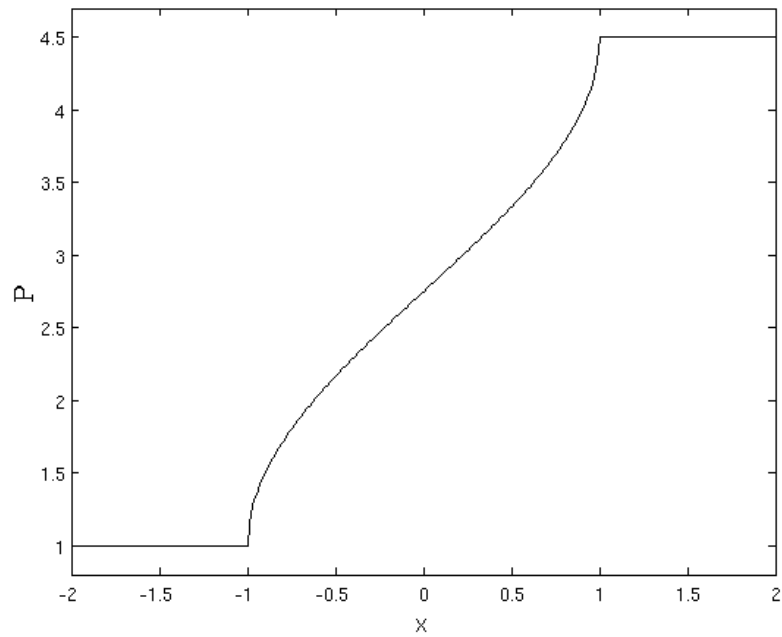
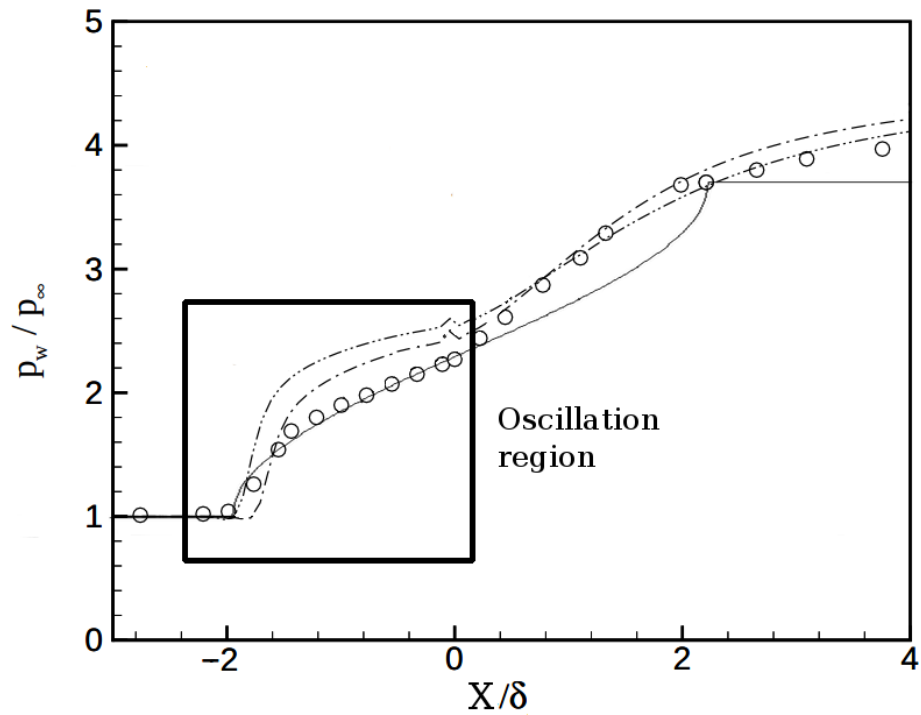


Figure 6.21: Experimental results ( $\circ$ ), Sinha's modified  $k - \epsilon$  ( $- \cdot \cdot -$ ) and  $k - \omega$  ( $- \cdot -$ ), and fit of Eq. (6.27) ( $-$ ). Observe how the shape of the  $\sin^{-1}$  function is a better match to the experimental results than anything produced by the eddy viscosity models. Figure adapted from [157].



So although the boundary layer model of Sinha and Candler [157] manages to obtain wall pressure results close enough to physical experiments for engineering purposes, the overall shape of the curve does not match that of the experiment. Rather, their model produces profile shapes consistent with a well-defined separation with a sharp jump discontinuity at the separation shock. In fact, as can be seen in Fig. 6.21, a fit of Eq. (6.27) provides a better match for experimental results of Settles and Dodson [153] in front of the separation than either of the RANS models (this is probably coincidental, but it is both interesting and surprising). While this model creates improved wall pressure results, likely sufficiently accurate for engineering purposes, the mean velocity profiles contain significant divergence from the experimental results in the separation region. In fact, in some areas, the modified  $k - \omega$  mean velocity profile is a worse match than the standard model. For accurate flow predictions, the shock location and separation bubble length must be predicted in a distributional sense. This may be beyond the capability of RANS models in general; it is almost certainly beyond the capability of eddy viscosity models.

### 6.3.1 Geometry, grid, and methods

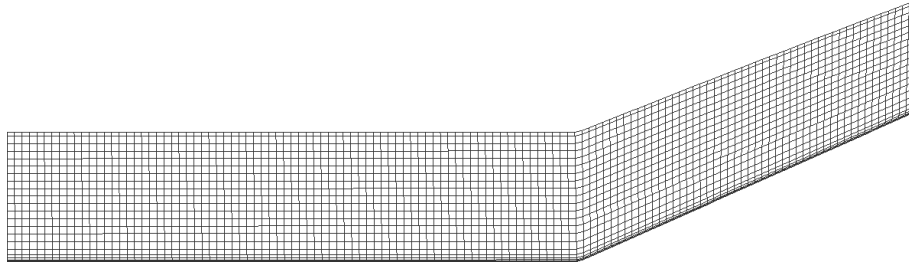
Two sets of numerical experiments have been performed by using two different meshes, which we will denote as Mesh A and Mesh B. These experiments were done to observe how the filter-forcing model behaves at different grid resolutions. The computational geometry and boundary conditions in this first simulation are based on the physical geometry of the 24-degree shock ramp used in the experiments of Ringuette et al. [135]. In both cases, we have modeled the first 120 mm of the ramp. Free stream conditions were imposed at the inlet with  $M_\infty = 2.9$ ,  $T_\infty = 196.67^\circ \text{ R}$ ,  $Re = 5909$  based on a length scale of 1 mm, and  $\gamma = 1.4$  was held constant. Boundary conditions in the spanwise direction were periodic. The lower boundary was a viscous, adiabatic wall with pressure extrapolation, and both the the upper boundary and the outflow

used characteristic extrapolation based on Riemann invariants.

### 6.3.1.1 Mesh A

Mesh A is constructed of a single grid in order to avoid any errors associated with the non-conservative chimera interpolation scheme. In terms of dimensionless wall distance  $y^+$ , the dimensions near the wall were  $(\Delta_x, \Delta_y, \Delta_z) = (25, 1, 25)$  everywhere with a vertical growth rate of  $\frac{\Delta_{y,2}}{\Delta_{y,1}} = 1.28$ . This is a typical resolution for a LES mesh. See, e.g., the experiments of Knight and Yan [160] on the same flow conditions, where they used a mesh with a resolution of  $(24, 1.9, 8.1)$ . This mesh was  $500 \times 87 \times 300$ , with 13.05 million grid points and can be seen in Fig. 6.22.

Figure 6.22: Mesh A for the 24 degree shock ramp. Every 4<sup>th</sup> point is displayed.



### 6.3.1.2 Mesh B

For the second set of experiments, a mesh significantly coarser than typical LES meshes, composed of two overset grids, has been used. The motivation behind this mesh was to construct conditions similar to a typical engineering context, where very fine meshes may not be computationally feasible, and to test the ability of the filter-forcing model to enhance turbulence even in a highly under-resolved situation. Exactly 200 mm in front of the ramp, a high-resolution grid, 160 mm in length and 93 mm in height, was created in order to develop a turbulent incoming boundary layer for the coarse LES region. The near-wall resolution in this region was  $(\Delta_x, \Delta_y, \Delta_z) = (25, 1, 25)$  with a vertical growth rate of  $\frac{\Delta_{y,2}}{\Delta_{y,1}} = 1.28$ . The geometry and grid can

be seen in Figs 6.23–6.25. In the low-resolution grid, the near-wall resolution was  $(\Delta_x, \Delta_y, \Delta_z) = (63, 1, 63)$  with a mesh growth rate again of 1.28. The high-resolution grid was  $318 \times 65 \times 250$  points, and the low-resolution grid was  $247 \times 59 \times 101$  points, for a total of 6.6 million grid points.

Figure 6.23: Mesh B for the 24 degree shock ramp. Note the coarse region containing the ramp. Every 4<sup>th</sup> point is displayed.

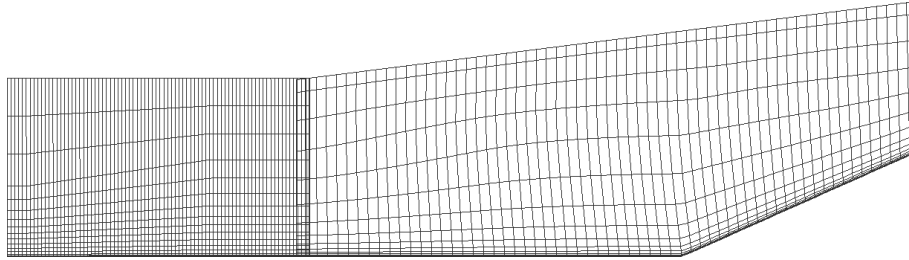


Figure 6.24: Close-up of the overlap zone between the fine and the coarse regions of Mesh B.

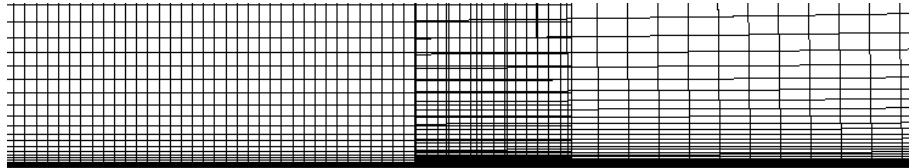
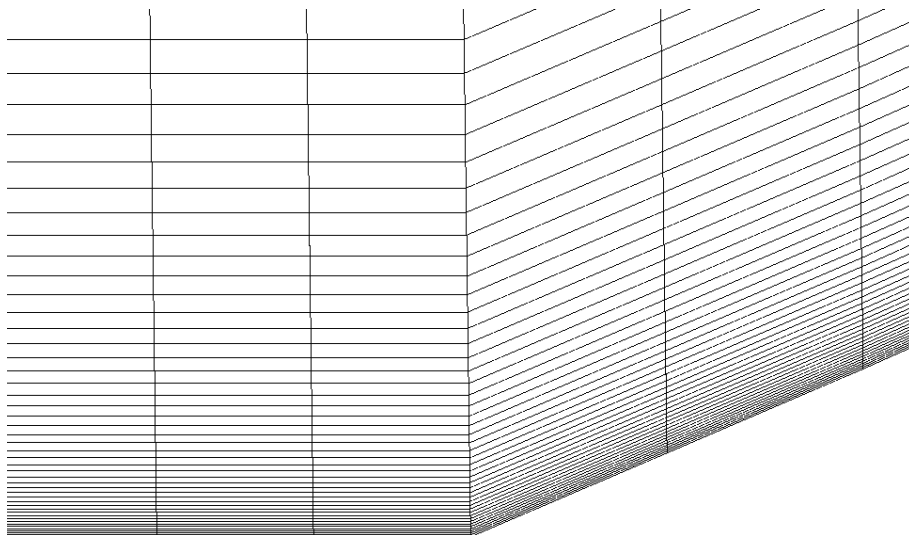


Figure 6.25: Close-up of the shock corner.



### 6.3.1.3 Boundary layer turbulence

Generating a turbulent boundary layer is a non-trivial problem in compressible LES. Unlike in incompressible LES, randomly generated inlet variables tend to be numerically unstable. When using a mature engineering package such as OVERFLOW, the structure of the code itself may prevent straightforward implementation of some popular schemes, such as an inlet forcing function, a boundary impulse, or generating an inlet condition from an entirely separate simulation. For example, the version of OVERFLOW used in the current experiments allowed for a prescribed inlet condition, but because the code was designed with RANS methods in mind, it does not allow an unsteady prescribed condition as some commercial codes do. A spatially irregular, time-constant boundary condition proved to be insufficient to generate turbulence. Attempts to include a trip wire failed to generate turbulence, possibly due to the low Reynolds number of the flow, the nonphysical smoothness of computational walls, and any artificial dissipation induced by filtering and the numerical scheme. Simply lengthening the mesh to the point where turbulence could evolve naturally over a flat plate was computationally prohibitive, besides the fact that modeling transition to turbulence is itself a nontrivial problem.

Because of these concerns, incoming turbulence was generated using a copy-to/copy-from technique already included as a feature of OVERFLOW, where a section of the flow near the ramp is copied to a section upstream. This technique was chosen due to its ability to reduce the size of the mesh needed to achieve turbulence as compared to modeling a trip wire and the ease of controlling the boundary layer thickness by simply adjusting the number of points in the copy-to/copy-from regions. Of course, this method was not without its issues. If the copy regions are too close to overlap regions, they can cause instabilities, and the overall boundary zone must be large enough to resolve all turbulent structures. In addition, boundary layer recycling introduces a harmonic mode based on the length of the recycling zone, so the



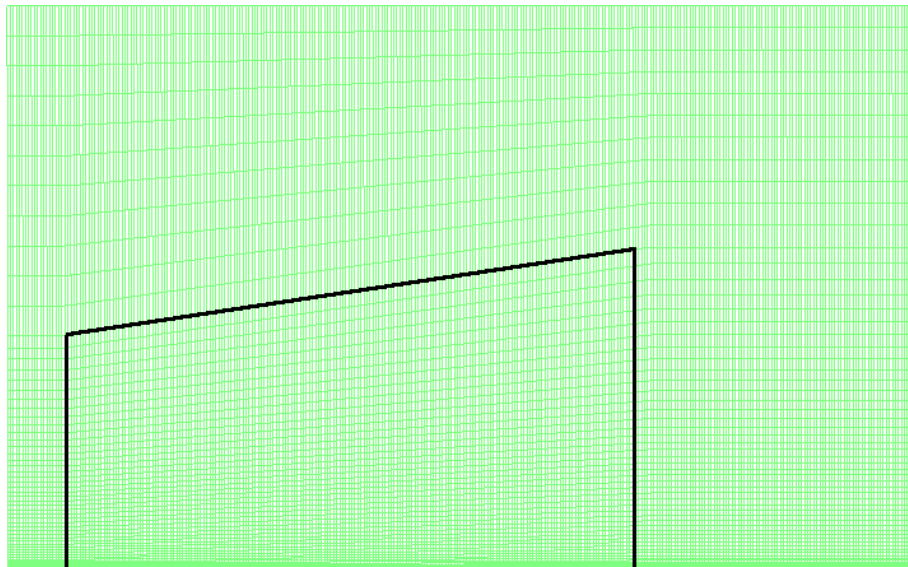
recycling must be long enough that this mode is not adversely affecting the length scales of interest. Further, in order to create a self-similar boundary layer following the usual law of the wall, rescaling must be done in addition to recycling. In the viscous sublayer the scaled velocity obeys the law,

$$u^+ = y^+ = \frac{yu^*}{\nu}, \quad (6.28)$$

where  $u^*$  is the friction velocity. Because  $u^*$  decreases with  $Re_x$ , rescaling the velocity is necessary in order to achieve the canonical self-similarity profile of a typical flat plate boundary layer. Because the version of OVERFLOW used in this investigation lacks the ability to scale copied regions, the equilibrium boundary layer achieved by this method does not have this profile.

The approaches in each case were slightly different, due to the same technique not working on both meshes. In Mesh A, a pure recycling was used, with a small trip placed near the inlet by using OVERFLOW’s hole-cutting feature to remove a small, rectangular “wire” from the grid. In Mesh B, recycling with no trip was used, but the mesh itself was geometrically scaled in order to induce a similarity profile. The geometric scaling can be seen in Fig. 6.26.

Figure 6.26: Fine grid for Mesh A with similarity region outlined.



Discretization was 2<sup>nd</sup>-order in time using the same implicit method with Newton subiterations as before. Six Newton iterations resulted in right-hand side flux residuals dropping at least three orders of magnitude at each step. Spatial discretization used a 5<sup>th</sup>-order HLLC scheme with WENOM interpolation for the shock capturing, and the left-hand side matrix of the implicit solution procedure was again constructed using the ARC3D Beam-Warming block tridiagonal scheme [137]. Experiments were run for  $C_{PMNS} = 0$  (no model), 1, 2, and 5. Note that these values are significantly lower than those used for the periodic cube in Section 6.2. This is due to the fact that large values of the model constant resulted in critical instabilities behind the shock. This shows that, much like the Smagorinsky constant,  $C_{PMNS}$  is not a universal value. This will be elaborated upon in more detail in Section 7.2.

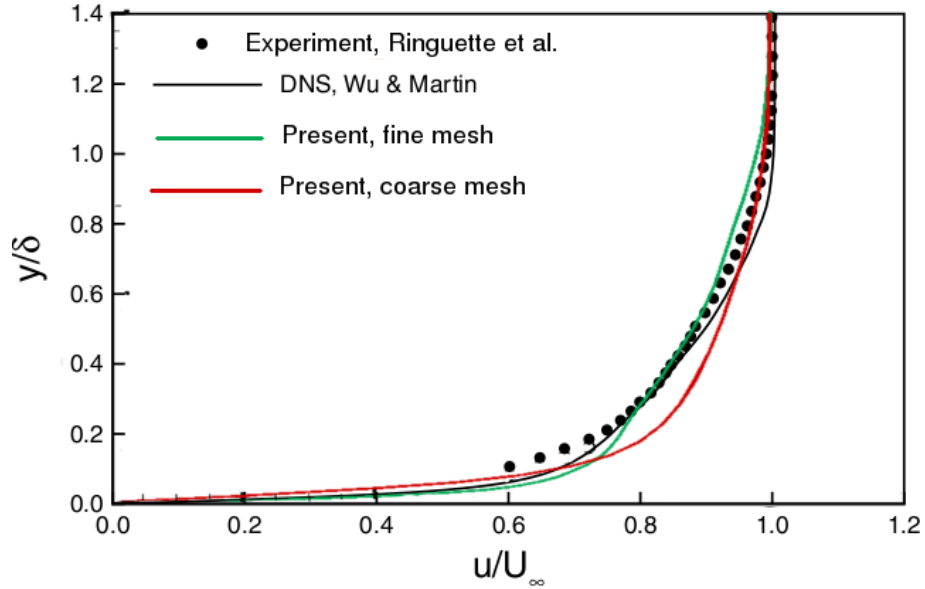
### 6.3.2 Results and analysis

Numerically, there is a fairly significant deviation of all LES results from the experimental results. Settles et al. [153] showed that separation behavior is strongly dependent on  $Re_\theta$ , so we can expect errors due to excessive artificial dissipation, which locally decreases effective  $Re$ , and discrepancies in the boundary layer structure between computational and experimental results.

An issue with both meshes arises due to the recycling technique used to generate the turbulent boundary layer. The profiles are compared with DNS [139] and experiment [135] in Fig. 6.27. In both cases, the viscous layer is clearly larger than in both the physical and DNS experiments. This overshoot is particularly pronounced in the case of the Mesh B. Thus as flow features, such as the separation zone, penetrate upward from the wall into the higher regions of the boundary layer, they will be advected downstream more quickly in this simulation than if the boundary layer had matched the experimental or DNS profiles. As seen in Figs 6.28–6.29, the separation thickness is  $\mathcal{O}(\delta)$ , so it can be expected that the boundary layer profile, and not  $Re_\theta$

alone, will have a significant effect on the separation zone’s shape, size, and location.

Figure 6.27: Velocity profile of incoming boundary layer.



A second issue associated strictly with Mesh B can be traced back in part to the overlap region between the boundary grid and the corner grid. As can be seen in Fig. 6.30, OVERFLOW does not accurately interpolate the pressure between the two meshes, and an adverse pressure gradient is initiated immediately within the overlap region. This was true regardless of the distance between the overlap region and the compression ramp, as several further grid manipulations revealed, although increasing the distance allowed the gradient to settle to some degree and somewhat mitigate early flow separation. Further numerical investigation revealed two influences on the magnitude of this gradient and its influence on the separation point:

1. The artificial dissipation associated with the filter. Early experiments on a mesh that was later discarded revealed that the highly dissipative 5<sup>th</sup>-order differencing filter in OVERFLOW results in an excessively large separation region, as can be seen in Fig. 6.31. Fig. 6.32 shows that the HAMR scheme significantly reduces the severity of this phenomenon. Similarly, increasing other dissipation parameters in the code increased the problem, so they were set to

zero for this investigation. Comparisons without any filtering could not be done due to the instability induced by aliasing.

2. The size of the overlap region. Early on, the overlap region was too small to adequately support the numerical scheme. Increasing its size reduced the severity of the adverse gradient, but did not eliminate it entirely.

This problem may be an interaction between filtering and the overset method. Because filtering is performed in computational space rather than physical space, this results in a discontinuous jump in the physical space filter widths between grids. In addition to these tests, horizontal grid refinement tests were also performed. These had no apparent influence on the adverse pressure gradient, so the horizontal grid resolution can be ruled out as a cause.

Because of these boundary layer discrepancies, there are significant differences between the LES and experimental results. On Mesh A, the large separation zone begins at  $x \approx -0.5\delta$ , whereas the experiments of Ringette et al place it at  $x \approx -4\delta$ , as seen in Fig 6.28. This means that the bulk of the separation is behind rather than in front of the main shock. On Mesh B, we can see in Fig. 6.29 that the separation zone begins at  $x \approx -12$ , due to the nonphysical adverse pressure gradient initiated by the overlap.

Table 6.2 quantifies the difference in boundary layer structure in terms of  $\delta$ , the momentum thickness Reynolds number,  $Re_\theta$ , the displacement thickness,  $\delta^*$ , the momentum thickness,  $\theta$ , and the shape factor,  $H = \delta^*/\theta$ . As can be seen, the fine LES experiment provides the best overall match for the boundary layer profile, but  $Re_\theta$  is about 67% too large. By contrast, the coarse LES runs provide the correct value of  $Re_\theta$ , but the  $H$  is only a third of the value provided by the DNS. To make strict one-to-one comparisons, then, a technique capable of generating the correct boundary profile must be introduced into OVERFLOW, or the CPMNS model needs to be

Table 6.2: Upstream boundary layer properties for the compression ramp

	$M$	$Re_\theta$	$\delta$ , mm	$\delta^*$ , mm	$\theta$ , mm	H
Mesh A	2.9	4000	8.7	2.29	0.678	3.37
Mesh B	2.9	2480	5.3	0.663	0.42	1.58
Experiment [135]	2.9	2400	6.7	2.36	0.43	5.49
DNS [136]	2.9	2300	6.4	1.80	0.38	4.74

tested in a different flow code.

Figure 6.28: Close-up of mean separation zone on Grid A, where coloring is by velocity magnitude.

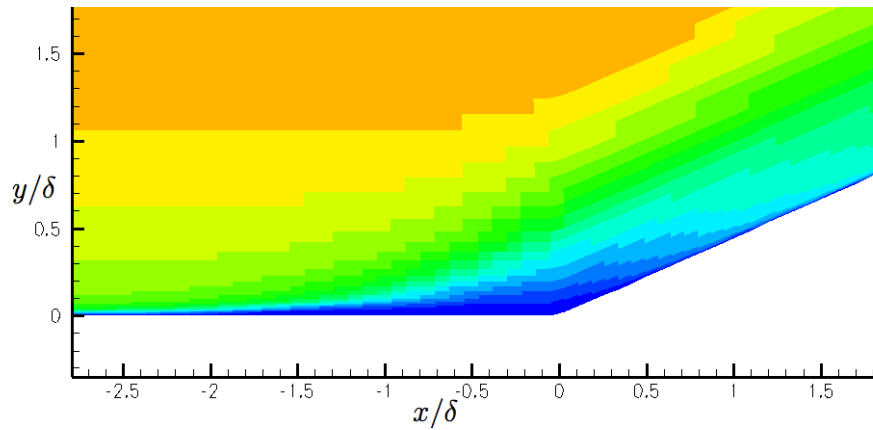


Figure 6.29: Close-up of mean separation zone on Grid B, where coloring is by velocity magnitude.

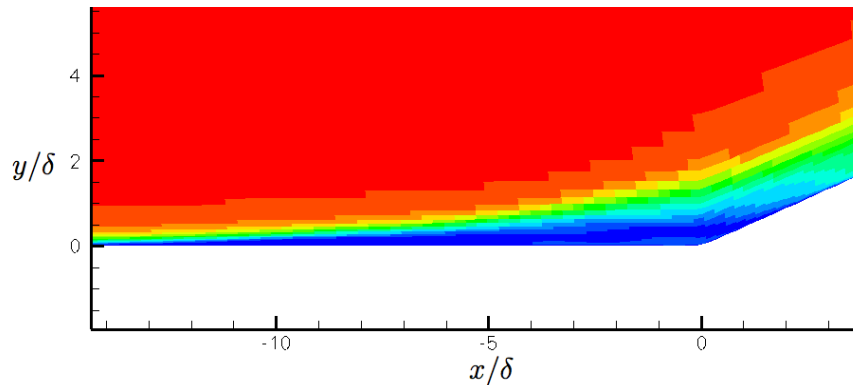


Figure 6.33 is a plot of the density gradient for an instantaneous solution field with the original filter and with the HAMR scheme. From this it is clear just how critical minimizing the dissipation associated with the filter is. The 6<sup>th</sup>-differencing filter results in heavy dissipation of the incoming boundary layer, with the smallest

Figure 6.30: Wall pressure in the interface between the fine grid (blue) and coarse grid (red) for Mesh B. Note the discontinuity between the zones and the immediate beginning of an adverse pressure gradient in the coarse zone.

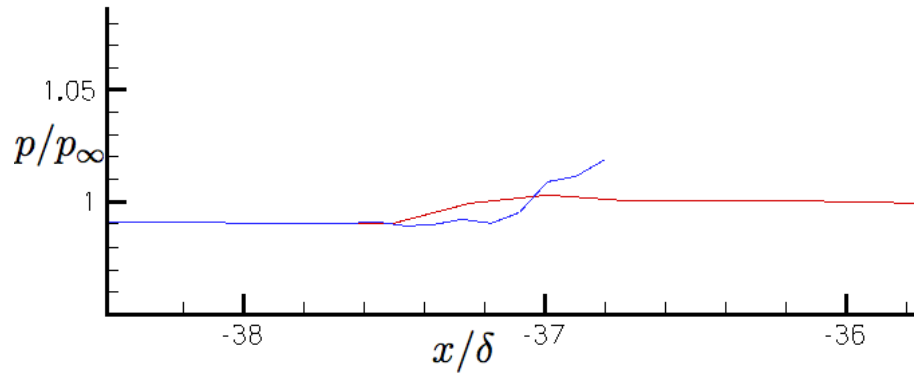


Figure 6.31: Contours of mean velocity for OVERFLOW's 5<sup>th</sup>-order filtering with no turbulence model on an earlier mesh. Note the very long, thin separation zone and Gibbs phenomena upstream of the shock.



turbulent structures being two to three times larger and less frequently occurring than those associated with the HAMR scheme. Further, in the critical shock-turbulent interaction zone, coherent structures are almost entirely absent, especially just downstream of the of the interaction. Finally, the shock waves are not nearly as well defined, and Gibbs phenomena can be seen in front of the shock associated with the differencing filter, illustrating the need for shock-detection schemes when implementing high-order filters in a supersonic flow. What this figure clearly illustrates is that adequate filtering alone is capable of significantly improving the quality of LES results even on highly coarse meshes.

Figure 6.34 is a plot of wall pressure results for the Grid B against the experimental

Figure 6.32: Mean wall pressure for OVERFLOW's 6<sup>th</sup>-difference filtering (black) versus the HAMR scheme (red) on an earlier mesh. The black curve is not as smooth due to being computed with fewer total time steps.

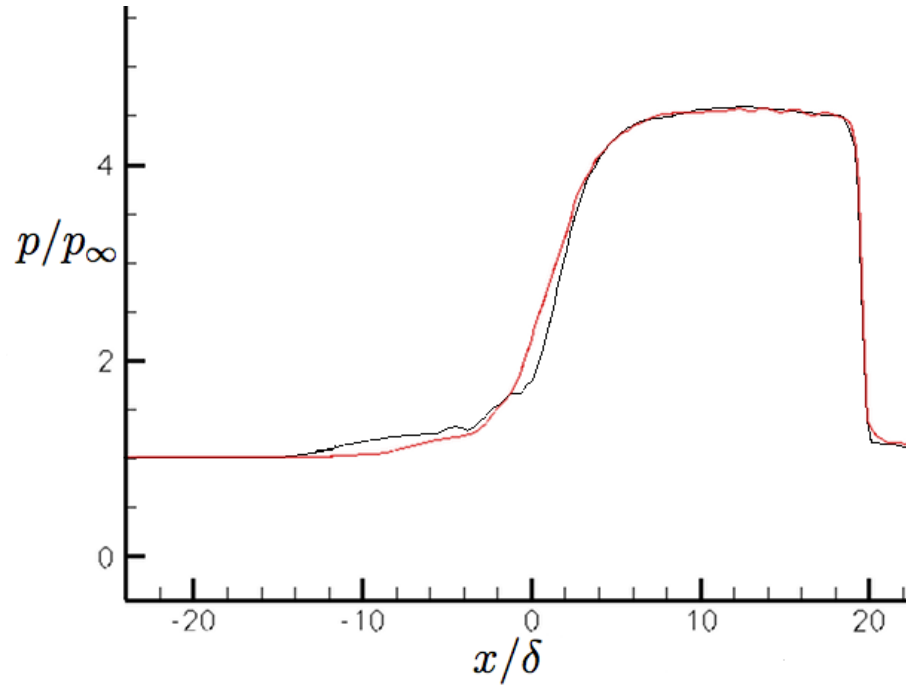
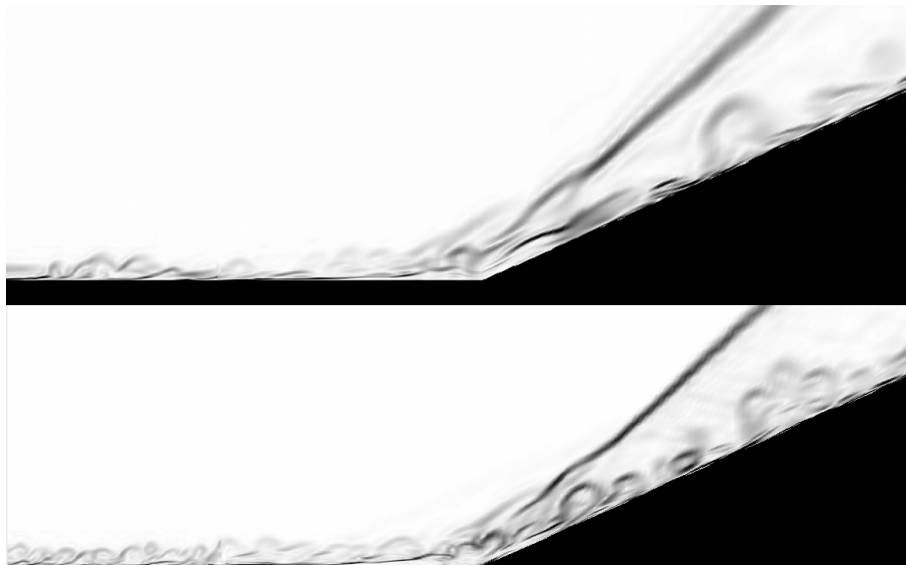


Figure 6.33: Density gradient contours for 6<sup>th</sup>-difference filtering versus the HAMR scheme with shock detection.



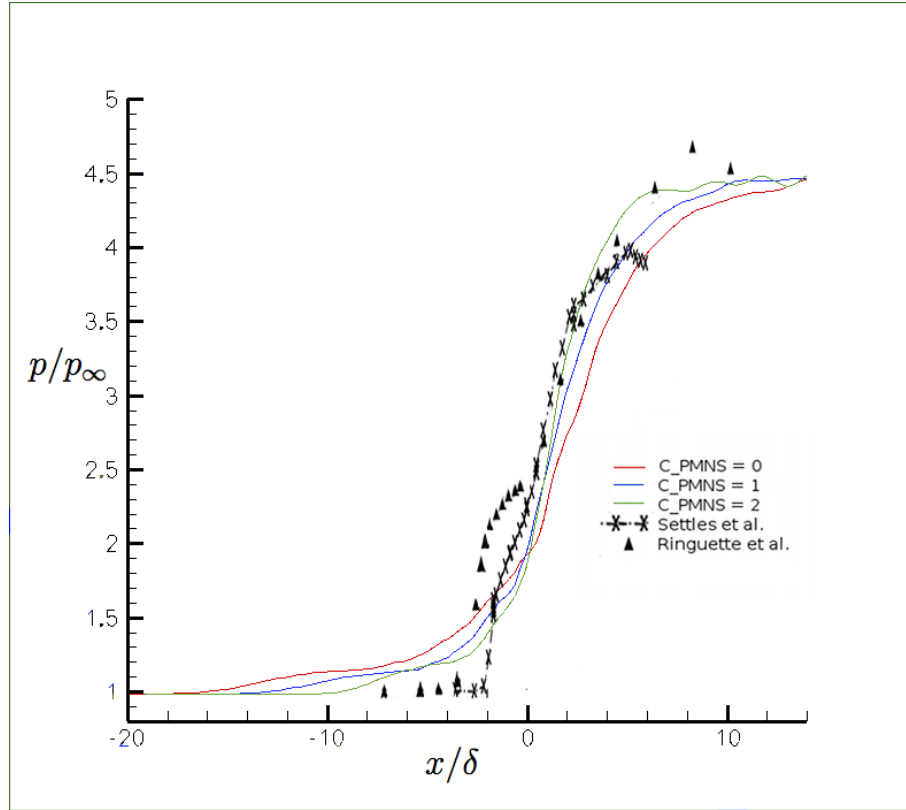
results of Settles et al. [153] and Ringuette et al. [135]. Quite clearly, early separation has a severe effect on the distribution of the wall pressure. Some significant effects of the CPMNS model can be observed. First is that the backscatter supplied by the model tames the adverse gradient and pushes the beginning of this region back from  $X \sim -17$  to  $X \sim -9$ . Given that the results of Ringuette et al. have the adverse region beginning at  $X \sim -4.5$ , this is not sufficient, but it does represent an error reduction of about 35%.

The model also causes some steepening of pressure gradient induced by the main shock, indicating that it does indeed reduce dissipation.  $C_{PMNS} = 2$  gives the best match to the results of Ringuette et al. in the main shock region,  $X \in [0, 8]$ . The difference between the computed and experimental results is probably within the experimental variation in computing the boundary layer thickness and consequent scaling to produce  $X$ . It should also be noted the interface between the inviscid shock and the separation shock is fairly sharp in the Ringuette results, and that the well-definedness of this interface is also improved by increasing  $C_{PMNS}$ . Little effect was observed on the wall pressures for the fine mesh.

As expected from the results discussed in Sec. 6.2, the filter-force model shows a clear ability to induce high-frequency content in the turbulent boundary layer that explicit filtering alone is unable to capture. Figures 6.36 and 6.37 show density gradient contours as  $C_{PMNS}$  is varied. It is quite evident from these images that increasing the value of  $C_{PMNS}$  results in a rising turbulence intensity, with smaller and smaller coherent structures appearing as the parameter increases. Of particular note is that in Fig. 6.36, we can see that small-scale structures on the order of the mesh size arise when  $C_{PMNS} = 5$ , and the turbulent boundary layer looks qualitatively more similar to numerical schlierens of DNS experiments, e.g., those of Wu and Martín [136] as in Fig. 6.35. Physical turbulence is characterized by irregular structures down to the very smallest relevant length scales, as opposed to the large, rolling, coherent



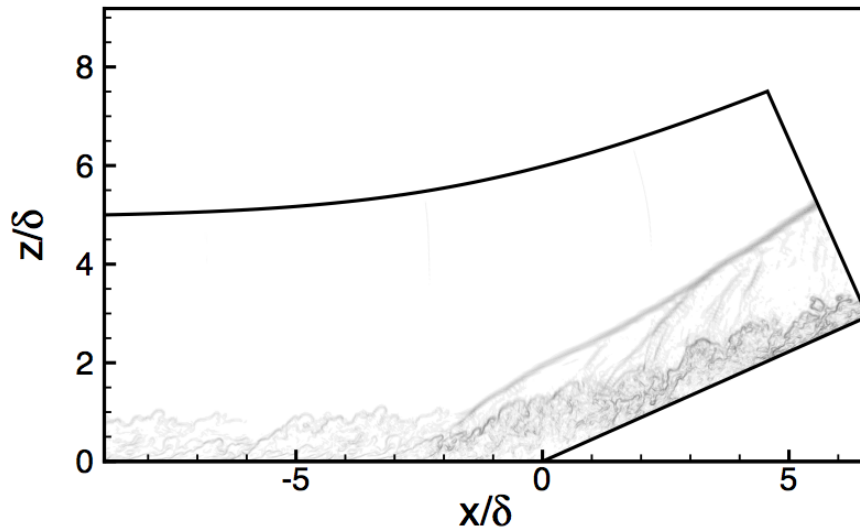
Figure 6.34: Mean wall pressure for the Grid B versus the experimental results of Ringuette et al. ( $Re_\theta = 2400$ ) [135] and Settles et al. ( $Re_\theta = 67,200$ ) [153]. Image adapted from [135] .



structures observed when only filtering is used. While the behavior as  $C_{PMNS}$  is similar between both Mesh A and Mesh B, increasing it all the way to 5 on Mesh B causes a critical instability that results in divergence of the solution. Recall also that the optimal value of  $C_{PMNS}$  was 50 for homogeneous, isotropic, decaying turbulence on the cube, where the grid spacing was only twice as long as that used for DNS. From these plots and those in Sec. 6.2, it appears that the optimal value of  $C_{PMNS}$  varies inversely with the grid spacing—the cube mesh was far more highly resolved than the ramp mesh, and the optimal value of  $C_{PMNS}$  was an order of magnitude larger. This is due to the fact that forcing is proportional to  $q_{hi}$ , which contains a greater percentage of the total kinetic energy on coarser meshes.

The density gradient plots demonstrate that one of the chief values of the CPMNS

Figure 6.35: Numerical schlieren of Mach 2.9 ramp from Wu and Martin. [139] Used with permission.



model has little to do with macroscopic flow quantities, as in the current case of a typically coarse LES mesh, the changes induced in flow integrals by varying  $C_{PMNS}$  are marginal. The fact is that very good predictions of engineering quantities can be obtained with nothing more than a high-quality explicit filter, and we refer once again to the results of Mathew et al. [92] [93] to confirm this. What this model provides is a high level of mixing and overall irregularity into a turbulent flow, so that the flow fields produced by it should be better able to model the kinds of small-scale phenomena needed in multiphase flow simulations and chemical kinetics.

Something should be said about the additional irregularity in the free stream region observable in Figs 6.37–6.36. The exact cause of this is unknown. The model is inactive in this region of the flow, so these fluctuations are not being directly generated. They could be propagated by the HAMR scheme, since it affects the entire domain, or it could be that, since the domain of dependence for a single point is the entire flow field, this is just due to effects of the increasingly fine-structure turbulence propagating throughout the entire domain. We tend toward this latter explanation, especially since the numerical schlierens of Wu and Martín [136] show

such effects downstream of the shock.

Figure 6.36: Density gradient contours for Mesh A with, beginning from the top,  $C_{PMNS} = 0, 1,$  and  $5.$

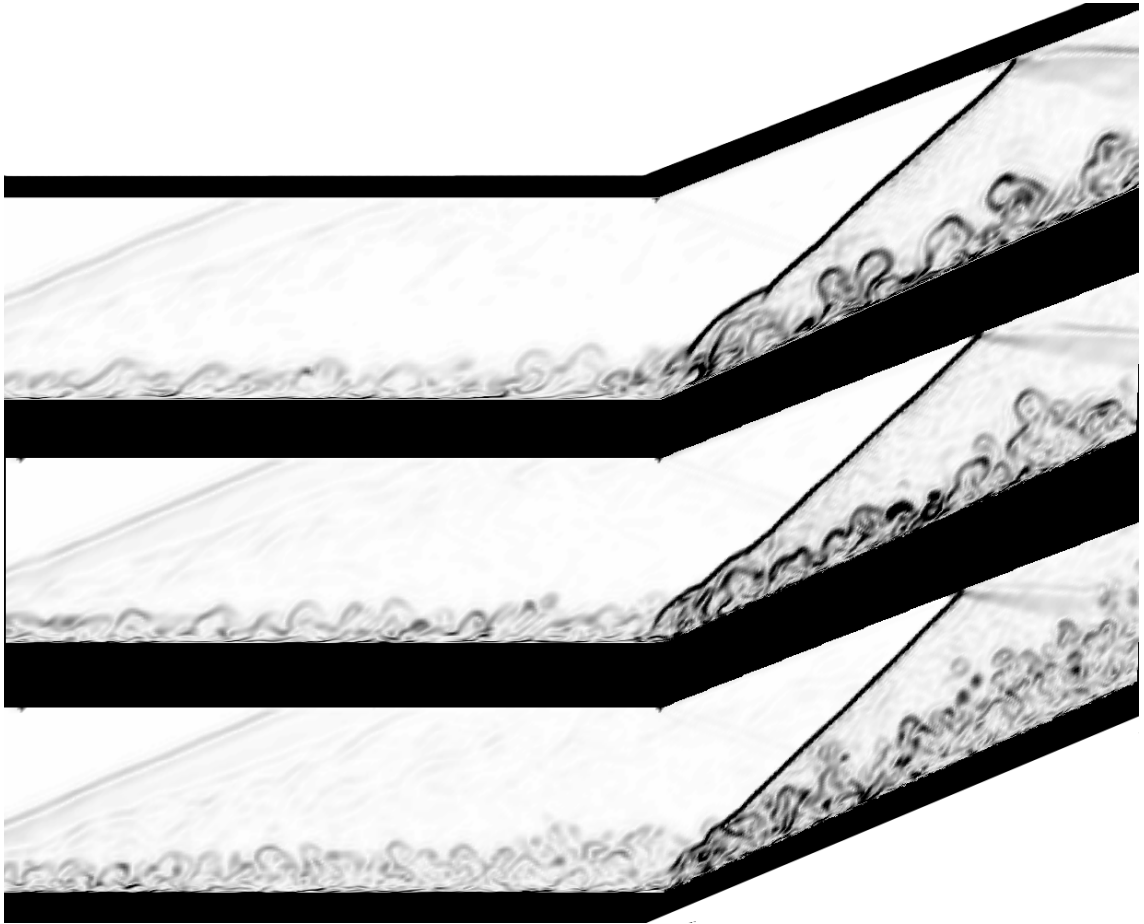
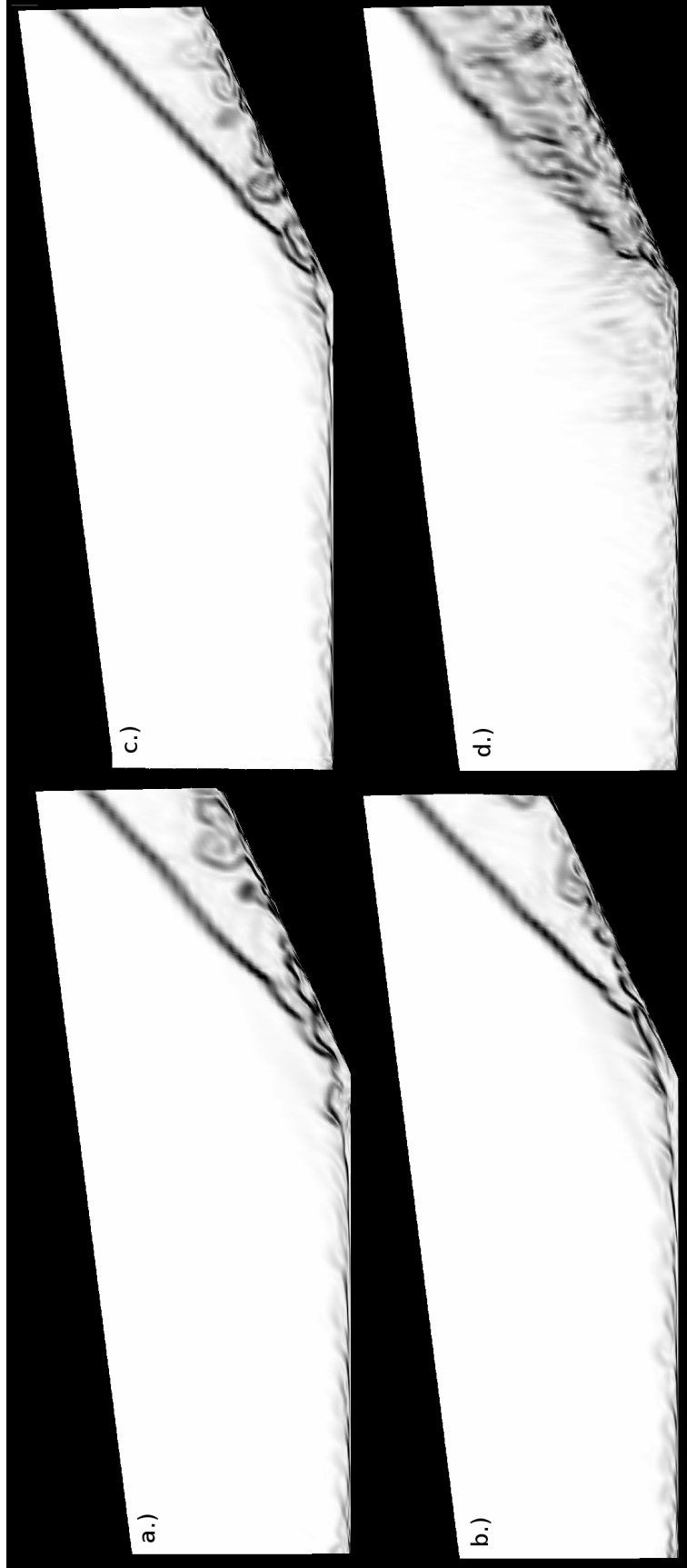


Figure 6.37: Density gradient contours for Mesh B with (a)  $C_{PMNS} = 0$ , (b) 1, (c) 2, and (d) 5, the last of which diverged.



While the results of LES on a Mach 2.9 compression ramp have only limited comparability to the experiments of Ringuette et al. [135] due to discrepancies in the boundary layer structure, there is a great deal of information to be obtained from them. The first is that this model is indeed anti-dissipative, as it tends to reduce or counteract the effects of dissipation on large-scale flow structures such as the separation point. The second is that the model induces the formation of small-scale flow structures on the order of only a few grid cells, something that pure dissipation is completely unable to do on its own. Both of these results are consistent with what we saw in Sec. 6.2. In addition, it gives some insight into the behavior of  $C_{PMNS}$ , namely, that the maximum permitted value of the parameter decreases with increasing mesh spacing,  $\Delta$ . This is likely because as  $\Delta$  increases, so does the filter width, meaning that  $q_{hi}$  is extracted from a lower part of the spectrum, which we naturally can expect to contain more energy.

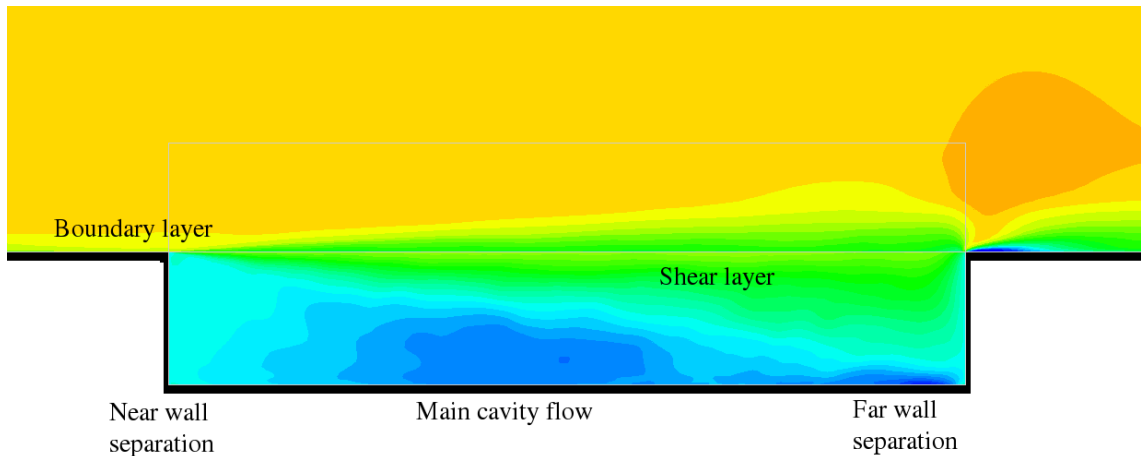
#### 6.4 Turbulent flow over an open cavity

In this section, we demonstrate the feasibility of the turbulence model by comparing numerical results to the detailed wall pressure measurements of Plentovich et al. [140]. Because the authors obtained high-quality data for a wide variety of Reynolds numbers, subsonic and transonic Mach numbers, and geometries, they have been used by a variety of authors as a basis for developing new CFD techniques. Atvars et al. [161] tested a URANS model using a cavity at  $M = 0.85$ , where they found that this model was not capable of capturing some of the significant dynamics. Peng and Leicher [162] had more success by using a hybrid RANS-LES model. However, cavity flows are a natural target for LES rather than RANS methods because the unsteady behavior creates dynamic acoustic phenomena of significant interest to engineers. See, e.g., the experiments of Yang et al. [163], where they found that flow oscillations were dependent on  $L_c/\delta$ . Thus a true RANS simulation, with its lack of any unsteady

information, will not be able to model this important behavior. Indeed, LES has provided good predictions of large-scale flow phenomena in the past, such as the experiments of Larchevêque et al. using an eddy viscosity form of LES [164].

This flow has some similarities with the familiar lid-driven cavity problem, such as separations that occur in the lower corners, but there are some important differences. The key mechanism in an open cavity flow is the shear layer created when the boundary layer suddenly encounters the cavity. But unlike the lid-driven cavity, this shear layer is not fixed to the upper boundary of the cavity; rather, it moves freely and tends to dip toward the cavity floor. Depending on the geometry and the Reynolds number, it can even attach to the cavity floor. Also, when the incoming boundary layer itself is turbulent, it will immediately induce turbulence in the cavity as well, so that the dynamics of the cavity depend on the length of the cavity,  $L_c$ , the free-stream Reynolds, Mach, and Prandtl numbers, and the thickness of the incoming boundary layer. A sketch of the features of an open cavity flow can be seen in Fig. 6.38. Note the separation zones in the corners and the depressed shear layer.

Figure 6.38: Major features of an open cavity flow. Contours are of mean velocity magnitude.



### 6.4.1 Geometry, grid, and methods

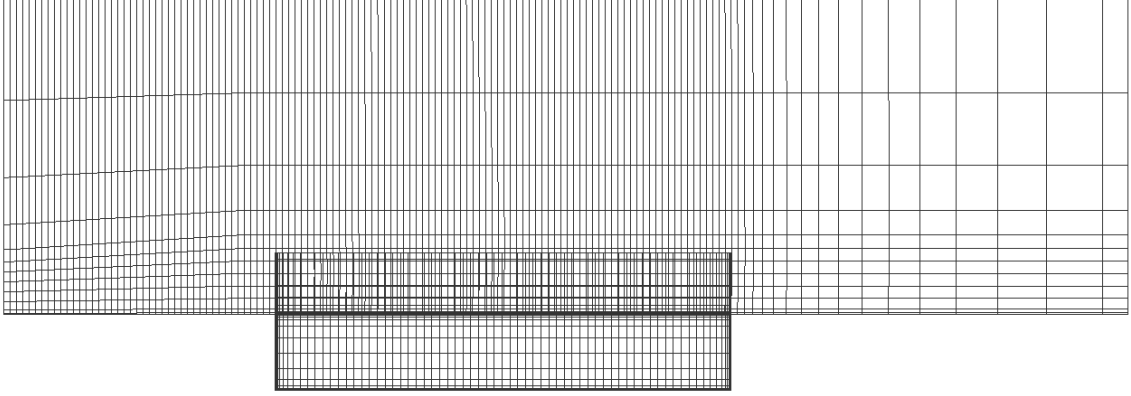
The parameters for these numerical runs are identical to Table 11, Run 31, Point 786 in Plentovich et al. [140]. The cavity here had a depth of 2.4", a length of 14.4", and a width of 2.4". The free stream Mach number was set at 0.8, the free stream temperature at 561.67° R, and the free stream Reynolds number was set at  $3.15 \times 10^5$  based on a length scale of one inch.

At Mach 0.8, a turbulent flow can create local Mach numbers above unity, necessitating shock capturing. Thus the same methods as in the case of the shock ramp were used, ARC3D [137] for the implicit solves, and WENOM [134] for shock-capturing. Discretization was second order in time, with a dimensionless time step of 0.005. Six Newton subiterations were performed, which was sufficient to cause a drop of at least two orders of magnitude in the right-hand side flux residuals at each time step. Free-stream boundary conditions were imposed at the inlet, periodic conditions were imposed on the spanwise boundaries, and the same characteristic extrapolation condition used for the ramp was imposed at the upper boundary and the outlet.

Two overset grids were used to construct the mesh, as seen in Fig. 6.39. In terms of dimensionless wall distance  $y^+$ , the dimensions near the wall in the main flow grid were  $(\Delta_x, \Delta_y, \Delta_z) = (30, 1, 30)$  everywhere with a vertical growth rate of  $\frac{\Delta_{y,2}}{\Delta_{y,1}} = 1.3$ . In the cavity grid, dimensional near-wall spacing was set to  $5 \times 10^{-4}$  in. everywhere, and the interior grid cells were approximately  $0.06'' \times 0.1'' \times 0.06''$ . The main flow grid was  $658 \times 53 \times 211$  points, and the cavity grid was  $298 \times 95 \times 109$  points, for a total of 10.8 million grid points. Note that the turbulent boundary layer crosses the overlap interface. As seen in in the shock ramp problem, we already know from Sec. 6.3 that this causes issues for LES in OVERFLOW, so that should be kept in mind when discussing these results.

As with the shock ramp, generating a turbulent boundary layer proved to be problematic. The recycling method that was successful for Mesh B in the ramp

Figure 6.39: Overset mesh for the open cavity. Every fourth grid point is displayed.



problem proved to be unsuccessful here, likely due to the much higher Reynolds number. For these experiments, a trip constructed by cutting a spanwise hole  $0.16'' \times 0.05''$  in the mesh 8 inches in front of the cavity proved to be effective. The boundary layer thickness induced by this method was estimated at  $\delta = 0.8''$ , which is close to the recorded experimental boundary layer thickness of  $0.5''$  [140]. Since moving the trip requires significant reconstruction of the mesh, this was judged as sufficient for the present investigation. The effect of mesh resolution was tested by increasing the mesh spacing to  $\Delta_{1.5} \equiv 1.5\Delta$  and  $\Delta_{2.5} \equiv 2.25\Delta$  in all directions, and comparing the coefficient of pressure,  $C_p = 2(p - p_\infty)/(\rho u_\infty^2)$ , on the streamwise centerline of the cavity floor. It was found that the quantity,

$$\left( \int_0^{14.4} (C_p(x, \Delta) - C_p(x, \Delta_\alpha) dx)^2 \right)^{1/2}, \quad (6.29)$$

increased nearly linearly with  $\alpha$ , where  $C_p(x, \Delta_\alpha)$  is the centerline floor  $C_p$  associated with mesh spacing  $\Delta_\alpha$ . This confirms that the mesh is significantly under-resolved and is therefore a good candidate for an LES problem.

#### 6.4.2 Results and analysis

One issue with this class of flows arises due to the unsteady harmonics associated with the cavity length. These frequencies are of course much larger than the time scales



associated with turbulence, and therefore it takes a very long time for time averages to converge on this system. Due to the constraints we had on available facilities and computation time, the time averages are not as well converged as they were with the shock ramp, where only a relative few time steps were needed to compute flow averages. The results shown here were computed using 40,000 time steps each, corresponding to a flow time of 3.4 seconds.

Figure 6.40 is a contour plot of the forcing for  $C_{PMNS} = 1$ . Forcing contour plots for other values of  $C_{PMNS}$  look qualitatively similar and have therefore been omitted. What can be seen here is that the model activates in turbulent zones and deactivates in laminar zones, as is desired. This is consistent with the behavior exhibited in Sec. 6.3, and demonstrates that the model does an excellent job detecting turbulent and non-turbulent regions, as no modifications have been made to the model other than adjustment of  $C_{PMNS}$ . As shown by the numerical schlierens in Fig. 6.41, as in the case of the shock ramp, increasing  $C_{PMNS}$  does indeed increase the qualitatively turbulent behavior of the flow and results in the emergence of more small-scale structure than is seen when filtering alone is used.

Figure 6.40: Contours of forcing for  $C_{PMNS} = 1$ .

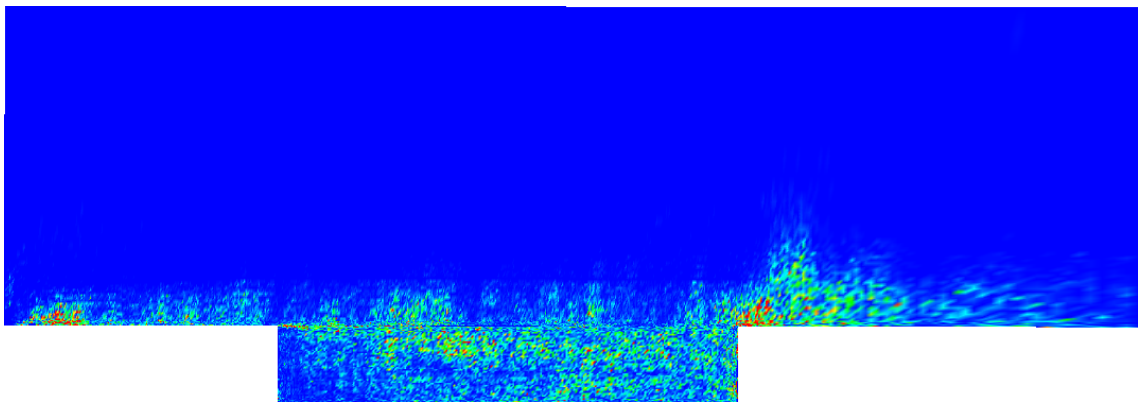


Figure 6.41: Pseudoschlierens of the open cavity simulation for  $C_{PMNS} =$  a) 0, b) 1, c) 5, and d) 10.

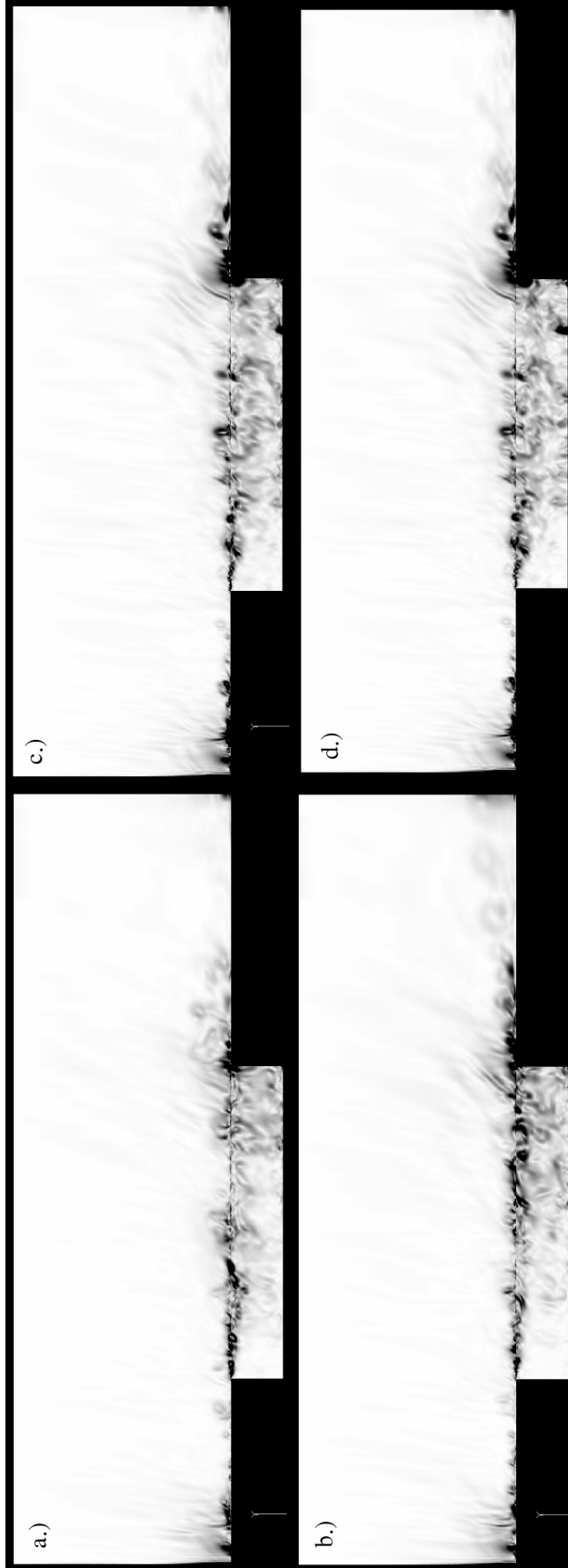
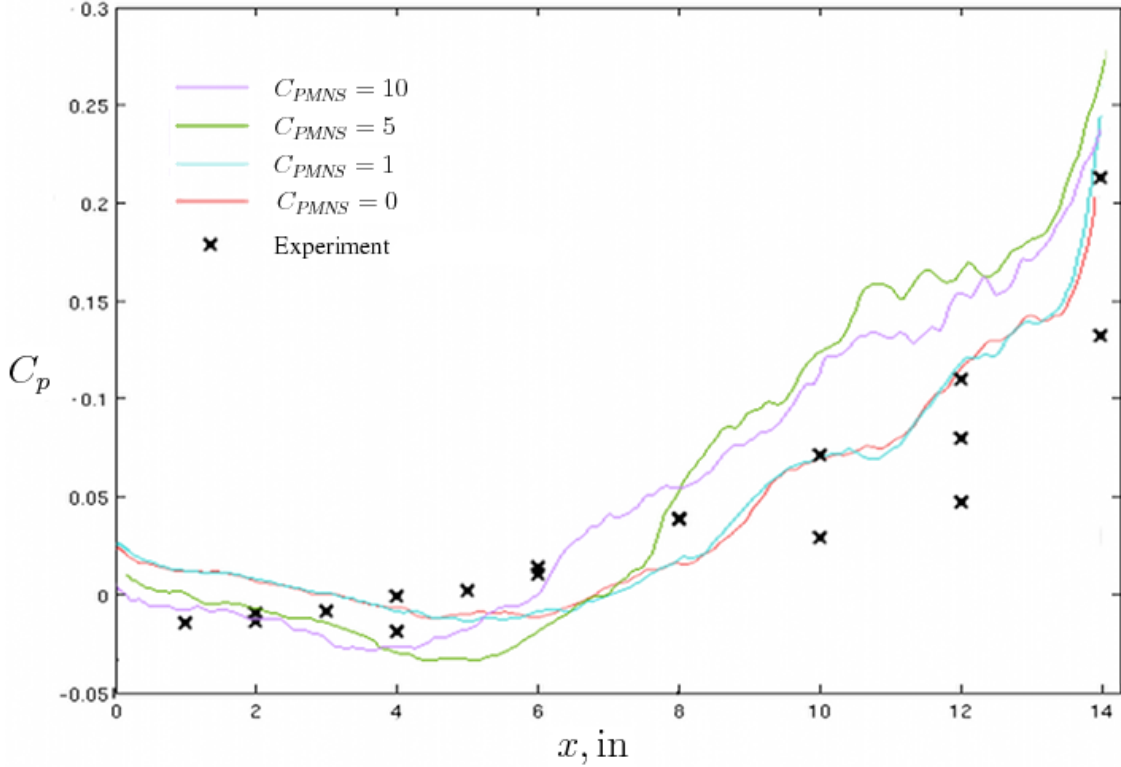


Figure 6.42 depicts wall pressure coefficients,  $C_p$ , for LES and the experiment. The results here are inconclusive. Due to the limitations of available computational resources and the large range of time scales associated with the cavity flow, time averages are not as well-converged for this flow as they were for the shock ramp. As mentioned before, these averages were computed over 3.4 seconds of physical flow time. However, some broad trends can be noted. In particular, while the best agreement with experimental  $C_p$  in the downstream region of the cavity appears to be for  $C_{PMNS} = 0$ , i.e., no backscatter modeling, this over-predicts  $C_p$  in the upstream region. Increasing  $C_{PMNS}$  improves the agreement between the experimental and numerical values of  $C_p$  in the upstream region, but causes a sharper rise in the downstream region. However, note that for  $C_{PMNS} = 10$ ,  $C_p$  in the downstream region is closer to experiment than for  $C_{PMNS} = 5$ . The match for  $x < 8$  is somewhat better for  $C_{PMNS} = 10$  than for  $C_{PMNS} = 0$ . This suggests that some degree of the variation is due to the insufficient convergence of the time averages. The slightly larger values of  $C_{PMNS}$  are consistent with the earlier observation that the ideal value of  $C_{PMNS}$  varies approximately inversely with the grid spacing. The resolution of the grid in this numerical experiment is of the same order as that of the shock ramp, and we see similar values of  $C_{PMNS}$ .

## 6.5 Summary and conclusions

The three cases presented here demonstrate the capabilities and limitations of this simple forcing model. As is expected due to the analysis in Ch. 3, filtering alone proves to be excessively dissipative, and a backscatter model is capable of counteracting these effects. All three cases show that this filter-forcing approach is in general capable of inducing small-scale flow structures and high-wavenumber behavior that is ordinarily lost when using a purely dissipative method. This is a highly desirable characteristic if this model is to be developed for use in conjunction with models of Lagrangian

Figure 6.42: Wall  $C_p$  on the floor of the open cavity for  $C_{PMNS} = 0, 1, 5,$  and  $10$  compared with the experiments of Plentovich et al. [140], where we have assumed the different spanwise locations recorded by Plentovich were obtained by moving the walls of the experimental apparatus.



particle or chemical kinetics. Behaviors associated with dissipation, such as the decay of  $K$  and flow separation, were mitigated by the model and behaviors associated with backscatter, such as skewness and coherent, small-scale structures features of the flow, were enhanced.

The experiments on the cube in Sec. 6.2 show that this model is capable of improving the match between DNS and LES across a broad range of statistical and spectral behavior. However, the more complex geometries in Secs 6.3 and 6.4 reveal that, as is to be expected,  $C_{PMNS}$  is not a universal constant, and that some kind of dynamic model is necessary if the general form of this forcing is to be retained. It does appear that in the case of inlet-forced turbulence, the range of  $C_{PMNS}$  is more consistent, with the ideal value being  $\sim 5$ . As seen on both the shock ramp and the

cavity flow, the “best” value of  $C_{PMNS}$  is  $\mathcal{O}(5)$  across a variety of grid resolutions, Mach numbers, Reynolds numbers, and geometries.

Another conclusion of this investigation is the general unsuitability of OVERFLOW for LES. This conclusion was reached near the end of the preparation of this work. The conservation errors associated with overlap regions cause significant issues in precisely the areas where using overset meshes is desirable from the standpoint of mesh construction. There is active research into developing overset methods suitable for LES. See, e.g., the work of Morgan et al. [165]. Of particular interest is the fact that they used a FD method rather than FV for the main solver. This seems more intrinsically consistent with chimera interpolation, which constructs ghost points rather than ghost volumes or ghost fluxes. Further, the lack of options for inducing turbulence increase this code’s unsuitability, although the recycling ability may be not too difficult to enhance with rescaling. Unfortunately, these discrepancies mean that many of the observations in this work are of the qualitative rather than the quantitative type, as more conclusive work cannot be done without using a completely different code.

## Chapter 7. Final Conclusions and Future Work

The filter-forcing model paradigm proposed in this work not only shows a great deal of promise, but has a fairly rigorous theoretical and mathematical justification. However, there is clearly much additional work to be done in order to develop such models to a state where they can be used in general CFD. In Sec. 7.2 we give a general assessment of the filter-forcing approach presented in this work. In Sec. 7.3, we discuss open problems related to filtering and shock modeling that need to be solved in order to improve compressible LES in general. In Sec. 7.4 and 7.5, we present two alternative proposals for construction of the forcing term. Finally, in Sec. 7.6 we summarize our findings in this dissertation.

### 7.1 Summary

After introducing this dissertation in Ch. 1, we gave an overview of existing turbulence theory to provide a context for the development and investigation of the turbulence model in this work in Ch. 2. Several important mathematical tools were defined: the Kovasznay decomposition, various statistical methods, and spectral analysis. An overview of dynamical systems theory was presented on the ground that turbulent flows behave like chaotic dynamical systems with distinct bifurcation behavior, a characteristic that must be preserved by turbulence models. Shock-turbulence interactions were discussed as well; in particular, it was shown that the local isotropy assumption is not valid behind a shock wave.

Chapter 3 was a thorough overview of the problems associated with CFD and turbulence modeling, with a special attention given to LES. Careful attention was given to aliasing, and it was formally demonstrated that traditional LES formulations are subject to compounding aliasing error that is not avoided with traditional,

unfiltered numerical methods. A thorough critique of eddy viscosity methods was provided as well, and it was shown that the characteristics of eddy viscosity are substantially different from the effects it is intended to model. To address these issues, a dealiased form of the LES equations was derived, and this form served as the basis of the modeling in this work.

The CPMNS equations were completely derived and thoroughly analyzed in Ch. 4. This discrete dynamical system exhibited many of the same characteristics as physical turbulence, such as quasiperiodic behavior and bifurcation to chaos. The overall bifurcation behavior was shown to be qualitatively consistent with physical turbulence, i.e., as changing dimensionless parameters in the NSEs cause transition, corresponding changes in the parameters of the CPMNS equations cause bifurcation. This chapter concluded with constructing the forcing term used to supply backscatter in the simulations in this work.

Chapter 5 was an overview of the features and characteristics of the OVERFLOW compressible flow code. Special attention was given to chimera overset interpolation, which causes conservation errors in overlap regions. A fairly detailed explanation of WENOM shock capturing was given. The original scheme is prone to significant accuracy loss near critical points, and the WENOM scheme corrects this error and maintains 5<sup>th</sup>-order accuracy everywhere. It was shown that the code is highly efficient and maintains near-ideal scaling into the hundreds of cores.

In Ch. 6, computations incorporating the CPMNS filter-forcing model were presented. Details of the HAMR scheme used for filtering were given, and it was shown that this scheme has highly desirable characteristics for use as a filter within the context of LES. Computations were performed on a periodic cube with homogeneous, isotropic, decaying turbulence, on a Mach 2.9 compression ramp with a turbulent boundary layer, and on a Mach 0.8 open cavity. All these cases demonstrated that the model as currently formulated does indeed supply backscatter, tends to enhance

a flow’s behavior to provide a better match with DNS or experiment, and moreover activates only in those regions that appear to be turbulent.

## 7.2 Assessment of the filter-forcing model

We have presented a large-eddy simulation method based on explicit filtering and an explicit, chaotic backscatter forcing term based on the compressible “poor man’s” Navier–Stokes equations and validated it using DNS results computed in OVERFLOW. Explicit filtering rather than eddy viscosity has been rigorously justified in Ch. 3 based on a careful analysis of aliasing and the filtered NSEs. The HAMR scheme implemented in this work exhibits very low dissipation while sufficiently eliminating parasitic modes in order to maintain stability. In addition, the simple shock-detecting scheme proved sufficient to avoid filtering near shocks, which induces Gibbs phenomena, while still applying adequate filtering in turbulent regions.

The forcing term has been demonstrated to enhance backscatter and the formation of small-scale coherent structures. Computations of homogeneous, isotropic, decaying turbulence on a periodic cube showed it to be capable of enhancing LES flow statistics and spectra to provide a closer match to those of the DNS solution than what could be obtained using the filter alone. When applied to a Mach 2.9 compression ramp, the model displayed robustness in being able to sustain turbulent phenomena even on a very under-resolved mesh, created qualitatively realistic small-scale structures on a more resolved mesh, and overall demonstrated anti-dissipative behavior that enhanced the turbulent features of the flow. Application of the model to a Mach 0.8 open cavity confirmed the model behaves consistently across a wide variety of turbulent flow conditions.

The model in its current formulation has a single adjustable parameter,  $C_{PMNS}$ , that controls the intensity of the backscatter model; as with many other turbulence models, *a priori* selection of this parameter is important. The numerical experiments



in this work showed a wide range of ideal parameters, ranging from  $\sim 5$  to  $\sim 50$  depending on the flow. This range, however, is unsurprising. It is well known that Smagorinsky's original model [1] is inadequate due to a global constant, and so the widely-used dynamic model [68] exhibits improved performance by computing a local Smagorinsky parameter. This parameter does not just vary in order of magnitude, but can even be negative. Hence, it is not surprising to expect or see such wide variance in  $C_{PMNS}$ . Also, note that in the two simulations of forced, wall-bounded flow,  $C_{PMNS}$  had approximately the same order of magnitude despite very different Mach numbers, Reynolds numbers, and flow geometries.

It should also be emphasized that there is a great deal of flexibility in the formulation of the model. The particular choice of any individual filter kernel is not intrinsic to the structure of the model; it may very well be that a superior filtering method would enhance the model's overall agreement with DNS and experiment. In fact, the forcing term could just as easily be combined with artificial viscosity rather than filtering, similar to the approaches of Laval and Dubrulle [91], Leith [114], and Chasnov [90], although we recommend explicit filtering due to its more direct mathematical relationship with construction of the LES equations. Further, the forcing function as currently formulated is hardly the only possible choice. Because the PMNS equations return a dimensionless, chaotic set of variables, they could theoretically replace the Gaussian term in any popular method of random forcing.

There were also a number of problems associated with the OVERFLOW code. This code was designed for RANS rather than LES or DNS methods, and the chimera interpolation method poses problems for constructing LES problems. To be able to make strict comparisons to DNS and LES data, either the problems with chimera interpolation and the generation of turbulent boundary layers must be solved within the OVERFLOW code, or the filter-forcing model must be incorporated into a different code.

### 7.3 Open problems

There are two open problems that must be solved to increase the viability of the filtering-forcing paradigm for supersonic, compressible flows. Neither filtering nor shock modeling are directly applicable to any particular forcing formulation, but they are nevertheless essential components of the problem.

#### 7.3.1 Ideal filtering

The HAMR scheme used in this work seemed largely adequate for the flows examined. However, this was based largely on trial-and-error. Less dissipative filters resulted in instability, and more dissipative filters negatively affected the turbulence dynamics. This leaves us with an open question—is there a universal, optimal filter for dealiasing numerical solutions of the NSEs? If such a filter exists, it almost certainly depends on the numerical scheme used. Not only that, but because filtering is generally done in the computational  $(\xi, \eta, \zeta)$  space rather than physical  $(x, y, z)$  space, the filter may need to be formulated in terms of generalized coordinates. What is needed for an ideal filter transfer function is a spectral estimate of aliasing error in generalized coordinates. If a universal estimate can be found, then an optimal transfer function can be formulated, and a Padé-type scheme can be constructed with a transfer function closely matching the optimum.

#### 7.3.2 Shock modeling

It is clear from analytical [36] and numerical work [35] that low-dissipation shock capturing alone is insufficient for accurately capturing shock-turbulent interactions of high Mach flow. It is entirely unknown how the filter-forcing model would interact with any existing shock-thickness model. These models which are often based on Monte Carlo methods (e.g., the hybrid model of Carlson et al. [37]) and may pose additional complications for implementation of a filter-forcing method. It is important

to find out whether a backscatter forcing mechanism would enhance or degrade the performance of such a model in an LES context. Furthermore, because the location of shock waves in an LES context is unsteady, adaptive meshing may be a necessary addition to any method.

#### 7.4 Proposal 1: Helmholtz-decomposed forcing

It is clear from the numerical experiments presented in this work that, much like the Smagorinsky “constant,” the model parameter  $C_{PMNS}$  is not universal. Furthermore, it is suggested by the work of Petersen [120] that a single forcing parameter alone is insufficient in the context of compressible turbulence due to the non-constant distribution of energy between solenoidal and dilatational modes. Recalling Eqs. (4.40a)–(4.40b), the formulation of the forcing used in this work is given by

$$f_i = \rho(C_{PMNS})u_{hi,i}(a_i - A_i)$$

$$f_e = f_i u_i.$$

We propose splitting the momentum forcing into solenoidal and dilatational components. This requires either the development and application of at least an approximate Helmholtz decomposition algorithm fast enough to be used in the context of a CFD simulation. Suppose such a method exists, then let  $\mathcal{H}_s$  be the solenoidal projection operator, and  $\mathcal{H}_d$  be the dilatational projection operator. Then we propose the initial formula

$$f_{i,s} = \rho C_s \mathcal{H}_s (u_{hi,i}(a_i - A_i)) \tag{7.1}$$

$$f_{i,d} = \rho C_d \mathcal{H}_d (u_{hi,i}(a_i - A_i)) \tag{7.2}$$

$$f_e = (f_{i,s} + f_{i,d})u_i. \tag{7.3}$$

The two constants  $C_s$  and  $C_d$  should be computed dynamically from local flow quantities. We propose the formulas based on formulas given by Petersen [120] for the

equilibrium state of linearly forced isotropic turbulence. Here we make the heuristic argument that because the filtering creates “energy-starved” resolved modes, these modes will tend to absorb energy from the resolved modes. Further, because HAMR schemes attenuate all modes, we argue that the attenuation between  $\sim 0.5k_{max}$  and  $\sim 0.75k_{max}$  tends to be excessive, resulting in the over-dissipation seen in Sec. 6.2. So given an appropriate high-pass filter with  $k_{min} \approx 0.5k_{max}$ , we argue that the backscatter model should tend to ameliorate further attenuation of these modes. Hence we propose

$$C_s = \frac{\langle \epsilon_{hi,s} \rangle_{loc}}{2\langle K_{hi,s} \rangle_{loc}} \quad (7.4)$$

$$C_d = \frac{\langle \epsilon_{hi,d} \rangle_{loc}}{2\langle K_{hi,d} \rangle_{loc} - \langle (\partial_i u_{hi,i}) p \rangle}, \quad (7.5)$$

where  $\epsilon_{hi,s}$  and  $\epsilon_{hi,d}$  are computed from the vorticity and divergence of the high-pass velocity field,  $K_{hi,s}$  and  $K_{hi,d}$  are the solenoidal and dilatational kinetic energies of the high-pass field, and  $\langle \cdot \rangle_{loc}$  indicates a local spatial average. In all likelihood, this will not work universally and will still require an adjustable parameter, but dependence on local flow conditions should improve the performance and require less variation from one flow to another.

## 7.5 Proposal 2: Self-similarity

The spectral profile generated by numerical experiments of the spectrally truncated Euler equations in Fig. 2.1 suggests that “missing” backscatter causes significant deterioration only of high- $k$  modes. If we assume that turbulence locally obeys a power law, then suppose we have three wavenumbers,  $k_a < k_b < k_c < k_d$ , where  $k_a$  and  $k_b$  are wavenumbers chosen to be in the inertial subrange,  $k_c$  is the wavenumber at which significant attenuation due to filtering begins, and  $k_d$  is the cutoff wavenumber of the filter. Let  $\mathcal{F}_{a,b}$  be the spectral filter that extracts the modes between  $k_a$  and

$k_b$ , that is,

$$\mathcal{F}_{a,b}(u) = \sum_{j=a}^b \widehat{u}_j \phi_j, \quad (7.6)$$

where  $\{\phi\}$  is a set of Fourier basis functions on a given domain. If we assume that the inertial subrange obeys a power law,

$$E(k) \approx Ck^\alpha,$$

then the energy content between any two can be approximated by the Euler-Maclaurin formula. In particular, assuming the spectrum between  $k_a$  and  $k_c$  has not been significantly dissipated or decayed,

$$K_{ab} = \sum_{j=k_a}^{k_b} E(k) \approx C \left( \frac{1}{2} (k_a^\alpha + k_b^\alpha) + \int_{k_a}^{k_b} x^\alpha dx \right). \quad (7.7)$$

$K_{ab}$  and  $K_{ac}$  can be computed directly from  $\mathcal{F}_{a,b}(\mathbf{q})$  and  $\mathcal{F}_{a,c}(\mathbf{q})$ , so that  $C$  and  $\alpha$  can then be determined algebraically. We now can obtain an estimate for the missing kinetic energy due to excessive dissipation:

$$K_M = K_{cd} - \frac{1}{2} \int_{\Omega} \mathcal{F}_{cd}(u) \cdot \mathcal{F}_{cd}(u). \quad (7.8)$$

This energy can be induced by a forcing term constructed using the CPMNS equations. In the case of a complex geometry, the quantities in Eq. (7.8) should be computed using local integrals. Additionally, this construction should be done in terms of dilatational and solenoidal spectra if a fast Helmholtz decomposition can be found.

## 7.6 Conclusion

The model presented in this work is in an early state. As a general paradigm, filtering and forcing is not well-represented in CFD literature, as explicit filtering has only recently gained traction in the research community, and the few examples of backscatter

forcing functions, despite their successes even when paired with eddy viscosity models, have not gained a great deal of attention. However, in this work, we have provided a comprehensive theoretical argument for the aliasing inherent in the traditional LES formulation, the necessity of explicit filtering in order to formally guarantee resolution on the mesh, and the consequent need for a backscattering model to counteract excess dissipation.

Filter-forcing is a new paradigm in turbulence modeling. This approach is therefore not nearly so well-developed as eddy viscosity modeling, which has had decades of research and development. The study in this work is therefore not the development and presentation of an application-ready turbulence model, but is rather the theoretical investigation and numerical validation of filter-forcing as a general approach, and of the ability of the CPMNS equations to provide a chaotic term in such a model. The results in this work clearly demonstrate the potential and feasibility of this general approach, although they also show that much work remains for filter-forcing to be a viable turbulence model as part of a design process. Because of this, additional proposals for improving this model have been presented here.

The maturity of forcing models at this time can arguably be compared to the maturity of eddy viscosity models when J. Smagorinsky first proposed his model in the mid-20<sup>th</sup> century. The general viability of the approach has been established, and so the current challenge is to develop this basic concept into a technique viable for incorporation into engineering processes. The specific approach presented shows a great deal of promise, as the computational results in this dissertation show, but there is clearly a great deal of work to be done in order to make it viable for industrial CFD. We expect that some modification of the existing scheme, specifically a method dynamically computing local values of  $C_{PMNS}$ , will prove viable as an engineering-quality turbulence model.

## Appendix A. Source Code

```

SUBROUTINE PMITER(Q,QQ,QHI,VOL,XX,XY,XZ,YX,YY,YZ,ZX,ZY,ZZ,
&      IBLANK,VMUL,VGAMMA,VRGAS,DTPHYS,JD,KD,LD,
&      REY,FSMACH,J,K,L,X,Y,Z,GAUSSCO)

C In this sub, we go through all the steps necessary to
C compute the
C bifurcation parameters. We then iterate the PMNS
C equations at
C the point given by (J,K,L).
C CALLED BY: PMNS

#include "precis.h"

integer, intent(IN) :: JD, KD, LD, J, K, L
integer :: JJ, KK, LL, CTR, PMSTEP
c  __REAL, target, DIMENSION(JD,KD,LD,13), INTENT (IN) :: GMET

__REAL, INTENT (IN) :: VOL,XX,XY,XZ,YX,YY,YZ,
\&      ZX,ZY,ZZ
__REAL, DIMENSION(JD,KD,LD,5), INTENT(INOUT) :: QHI,Q,QQ
INTEGER, DIMENSION(JD,KD,LD), INTENT(IN) :: IBLANK
__REAL, DIMENSION(JD,KD,LD), INTENT(IN) :: VMUL,x,y,z
__REAL, DIMENSION(3) :: AA,USTAR,YPLUS,aamean
__REAL, INTENT(IN) :: DTPHYS,VGAMMA,VRGAS,REY,FSMACH
__REAL :: TAU,PI,LAMBDA,MACHTUR,SPEED,SPDOFSND,
\&      KSQ,BETAT,PECLET,REYAVG,EE,EE0,ETATERM,ZETATERM,
\&      CP,VORTMAG,NU,LENGTH,MACHTUR2,SPDSML,
\&      KFIL,KVOL,KDISS,USCALE,SPDLO,E0,EI,RHO
__REAL, DIMENSION(3) :: ALPHA,REYSM,VHI,KVEC,
\&      BETA,EPSILON,AA0,VORT,LENSCALE,QLO
__REAL, DIMENSION(3,3) :: XI,ZETA,ETA,DELTA,D1
__REAL, DIMENSION(-1:1,-1:1,-1:1), INTENT(IN) :: GAUSSCO
__REAL :: u,v,w,r1,r2,r3
real rand

QQ(J,K,L,:) = 0.d0

IF (IBLANK(J,K,L) /= 1) RETURN

```

```

rho = q(j,k,l,1)

PI = ACOS(0.)
LAMBDA = -2./3.*VMUL(J,K,L)
CP = VGAMMA*VRGAS/(VGAMMA - 1.)
NU = VMUL(J,K,L)/RHO

DELTA = 0.
DO JJ = 1,3
    DELTA(JJ,JJ) = 1.
END DO

SPEED = SQRT(DOT_PRODUCT(Q(J,K,L,2:4),Q(J,K,L,2:4)))
SPDSML = SQRT(DOT_PRODUCT(QHI(J,K,L,2:4),QHI(J,K,L,2:4)))

QLO = Q(J,K,L,2:4) - QHI(J,K,L,2:4)
SPDLO = SQRT(DOT_PRODUCT(QLO,QLO))

E0 = Q(J,K,L,5)/RHO
EI = E0 - 0.5*SPEED*SPEED

uscale = DTPHYS
SPDOFSND = SQRT(VGAMMA*(VGAMMA-1)*E0)
MACHTUR = SPDSML/SPDOFSND
MACHTUR2 = MACHTUR*MACHTUR

USTAR = 0.
YPLUS = 0.

C      Do nothing if the flow isn't moving here
      IF (SPEED .EQ. 0.) THEN
          !QQ(J,K,L,:) = 0
          RETURN
      END IF

C      Likewise if hipass is zero
      IF (USCALE .EQ. 0.) THEN
          !QQ(J,K,L,:) = 0
          RETURN
      END IF

c      Compute derivatives and vorticity
c      write(*,*) JD, 'DIFF1'

```



```
CALL DIFF1(Q,IBLANK,D1,VOL,XX,XY,XZ,YX,YY,YZ,ZX,ZY,ZZ,
&      JD,KD,LD,J,K,L)
```

```
LENSCALE(1) = VOL/(ABS(XX) + ABS(YX) + ABS(ZX))
LENSCALE(2) = VOL/(ABS(XY) + ABS(YY) + ABS(ZY))
LENSCALE(3) = VOL/(ABS(XZ) + ABS(YZ) + ABS(ZZ))
LENGTH = SQRT(DOT.PRODUCT(LENSCALE,LENSCALE))
```

```
VORT(1) = D1(3,2) - D1(2,3)
VORT(2) = D1(1,3) - D1(3,1)
VORT(3) = D1(2,1) - D1(1,2)
vortmag = dot_product(vort,vort)
```

```
c Vorticity-based time scale. If we have small vorticity, return.
IF(vortmag < 1D-12) THEN
  !QQ(J,K,L,:) = 0
  RETURN
END IF
TAU = (1/SQRT(VORTMAG))
```

```
KVEC = (1./4.)/LENSCALE
KSQ = DOT.PRODUCT(KVEC,KVEC)
```

```
c Compute our "yplus." If USTAR(KK) = 0 because of a
c zero vorticity component, set YPLUS(KK) to 1. This is
c to avoid divide by zero errors.
```

```
DO KK = 1,3
  USTAR(KK) = SQRT(abs(NU*VORT(KK)/REY))
  YPLUS(KK) = REY*LENSCALE(KK)*USTAR(KK)/NU
c END IF
END DO
```

```
REYAVG = SUM(YPLUS)/3.
```

```
PECLET = 0.72 * REYAVG
C Bifurcation parameters
```

```
C
```

```
C Stuff based on my notes, Tecplot tests, scaling, etc.
```

```
C Smagorinsky-based beta
```

```
do kk = 1,3
  beta(kk) = 1.d0-nu/max(lenscale(kk)**(2.d0)*
&      abs(vort(kk))*rey,1.d-10)
  beta(kk) = max(beta(kk),0.)
```

```

end do

beta = beta*0.955

IF (MAXVAL(BETA) < 0.9 .or. minval(beta) < 0.3 ) then
  QQ(J,K,L,:) = 0
  RETURN
else
end if

IF (MAXVAL(BETA) > 1) THEN
  WRITE(*,*) '**ERROR** BETA > 1'
  WRITE(*,*) BETA
  WRITE(*,*) KVEC
  WRITE(*,*) TAU, KSQ
  WRITE(*,*) YPLUS
  WRITE(*,*) LENSACLE
END IF

IF (TAU .NE. 0.) THEN
  EPSILON = BETA/TAU
ELSE
  !QQ(J,K,L,:) = 0
  RETURN
END IF

ALPHA = TAU/MACHTUR2

DO KK = 1,3
  DO JJ = 1,3
    XI(JJ, KK) = min(TAU*KVEC(JJ)*KVEC(KK)/3., 0.3)
    ZETA(JJ, KK) = 2.*TAU*(VGAMMA-1.)*MACHTUR2*EPSILON(JJ)*
&      EPSILON(KK)*KVEC(KK)*KVEC(JJ)/(3.*REYAVG)
    ETA(JJ, KK) = KVEC(JJ)*EPSILON(KK)*SQRT(TAU*(VGAMMA-1)*
&      MACHTUR2/(2*REYAVG))
  END DO
  XI(KK, KK) = 0.
END DO

BETAT = 1.

C      if (QQ(J,K,L,1).EQ.0) THEN

```

```

ee = qq(j,k,l,5)!/max(qhi(j,k,l,5)*rho*vol*scale,
aa = qq(j,k,l,2:4)

```

```

do ll = 1,3
  if(aa(ll).eq.0) aa = rand(0)/3.d0
end do
if(ee.eq.0) ee = rand(0)/3.d0

```

```

CTR = 12

```

C

```

Apply limiters

```

```

DO LL = 1,3
  IF(ALPHA(LL) > 2.8) ALPHA(LL) = 2.8
  DO KK = 1,3
    IF(XI(KK,LL) > 0.2) XI(KK,LL) = 0.2
    IF(XI(KK,LL) < 0.01) XI(KK,LL) = 0.01
    IF(ETA(KK,LL) > 7.0) ETA(KK,LL) = 7.0
    IF(ETA(KK,LL) < 0.01) ETA(KK,LL) = 0.01
    IF(ZETA(KK,LL) > 300.0) ZETA(KK,LL) = 300.0
    IF(ZETA(KK,LL) < 0.01) ZETA(KK,LL) = 0.01
  END DO
END DO

```

```

END DO

```

```

aamean = 0.d0

```

```

DO PMSTEP = 1,CTR
  ee0 = ee
  aa0 = aa !dd0 - dd0*sum(gammaD*aa0) !+ als
  aa = 4.*beta*aa0*(1.-aa0)
& - aa0*DOT_PRODUCT(beta,aa0)
& - MATMUL(xi,aa0)
& - alpha*ee0 + aa0*beta*aa0
  etaterm = 0.d0
  zetaterm = 0.d0
  do KK=1,3
    do jj=1,3
      etaterm = etaterm + 2.*ETA(JJ,KK)*ETA(KK,JJ)*AA0(JJ)*
& (AA0(JJ)+ AA0(KK))
      zetaterm = zetaterm + zeta(JJ,KK)*
& aa0(JJ)*aa0(KK)
    enddo
    if(aa(kk) > 1.0.or.aa(kk) < 0) aa(kk) = rand(0)
  enddo
enddo

```

```

      ee = (ee0*(1.d0 - VGAMMA*DOTPRODUCT(beta , aa0)
&          )+ etaterm + zetaterm)/(1+betaT)
      if (ee > 1.0.or.ee0 < 0) ee0 = rand(0)

      aamean = aamean+aa
END DO

aamean = aamean/14.d0
aa = aa - aamean

DO JJ = 1,3
  IF (ISNAN(AA(JJ)).or.AA(JJ) > 1.) THEN
    WRITE (*,*) '---> Variable AA contains a NaN value <--'
    write(*,*) 'AA: ', AA
    write(*,*) 'beta: ', beta
    write(*,*) 'xi: ', xi(1,:)
    write(*,*) 'xi: ', xi(2,:)
    write(*,*) 'xi: ', xi(3,:)
    write(*,*) 'eta: ', eta(1,:)
    write(*,*) 'eta: ', eta(2,:)
    write(*,*) 'eta: ', eta(3,:)
    write(*,*) 'zeta: ', eta(1,:)
    write(*,*) 'zeta: ', eta(2,:)
    write(*,*) 'zeta: ', eta(3,:)
    write(*,*) 'alpha:', alpha

    CALL STOP_ALL('PMITER')
  end if
END DO

```

C Scale velocity

```
QQ(J,K,L,1) = TAU !USCALE
```

```
QQ(J,K,L,2) = AA(1)!SIGN(AA(1),QHI(J,K,L,2))
```

```
QQ(J,K,L,3) = AA(2)!SIGN(AA(2),QHI(J,K,L,3))
```

```
QQ(J,K,L,4) = AA(3)!SIGN(AA(3),QHI(J,K,L,4))
```

C Dissipation rate

```
R1 = 0.d0
```

```
do jj = 1,3
```

```
  do kk = 1,3
```

```

                R1 = r1+ ( d1(jj ,kk)+d1(kk , jj) )**2
            end do
                !kk
        end do
                !jj
        r1 = r1*nu
C      kinetic energy
        r2 = q(j ,k ,l ,1)*spdsml*spdsml*0.5 d0
c      time scale
        qq(j ,k ,l ,5) = r2/r1*(REY/FSMACH)

```

END SUBROUTINE

## Bibliography

- [1] Smagorinsky, J., “General circulation experiments with the primitive equations,” *Mon. Weather Rev.*, Vol. 91, No. 3, 1963, pp. 99–164.
- [2] Boris, J. P., Grinstein, F. F., Oran, E. S., and Kolbe, R. L., “New insights into large eddy simulation,” *Fluid Dynamics Research*, Vol. 10, No. 4-6, 1992, pp. 199.
- [3] Domaradzki, J. and Saiki, E., “A subgrid-scale model based on the estimation of unresolved scales of turbulence,” *Phys. Fluids*, Vol. 0, 1997, pp. 2148–2164.
- [4] Berrouk, A. S., Douce, A., Laurence, D., Riley, J. J., and Stock, D. E., “RANS and LES of Particle Dispersion in Turbulent Pipe Flow: Simulations Versus Experimental Results,” *ASME Conference Proceedings*, Vol. 2006, No. 47500, 2006, pp. 1673–1682.
- [5] Schmidt, R., Kerstein, A., and McDermott., R., “ODTLES: A multi-scale model for 3D turbulent flow based on one-dimensional turbulence modeling,” *Comput. Methods Appl. Mech. Engrg.*, Vol. 199, 2010, pp. 865–880.
- [6] Domaradzki, J., Dubois, T., and Honein, A., “A subgrid-scale estimation model applied to large eddy simulations of compressible turbulence,” *Proceedings of the Summer Program 1998*, Center for Turbulence Research, 1998, pp. 351–366.
- [7] Garnier, E., Adams, N., and Sagaut, P., *Large Eddy Simulation for Compressible Flows*, Springer, 2009.
- [8] Schmitt, F., “About Boussinesq’s turbulent viscosity hypothesis: historical remarks and a direct evaluation of its validity,” *C. R. Mecanique*, Vol. 335, 2007, pp. 617–627.
- [9] Kraichnan, R. H., “Convergents to turbulence functions,” *J. Fluid Mech.*, Vol. 41, 1970, pp. 189–217.
- [10] McDonough, J. and Yang, T., “A new LES model applied to an internally-heated, swirling, buoyant plume,” *Proc. 2003 Western States Section/The Combustion Inst.*, Los Angeles, Oct. 20-21 2003, pp. 03F–53.
- [11] Frisch, U., *Turbulence*, Cambridge University Press, Cambridge, 1995.
- [12] Ruelle, D. and Takens, F., “On the Nature of Turbulence,” *Communications in Mathematical Physics*, Vol. 20, 1971, pp. 167–192.
- [13] Lofthouse, A. J., Boyd, I. D., and Wright, M. J., “Effects of continuum breakdown on hypersonic Aerothermodynamics,” *Phys. Fluids*, Vol. 19, 2007, pp. 027105.

- [14] el Hak, M. G., “Questions in Fluid Mechanics: Stokes’ Hypothesis for a Newtonian, Isotropic Fluid,” *J. Fluid. Eng.*, Vol. 117, No. 1, 1995, pp. 3–5.
- [15] Fru, G., Janiga, G., and Thvenin, D., “Impact of Volume Viscosity on the Structure of Turbulent Premixed Flames in the Thin Reaction Zone Regime,” *Flow Turb. Combust.*, Vol. 88, 2012, pp. 451–478.
- [16] Kovaszny, L. S. G., “Turbulence in supersonic flow,” *J. Aero. Sci.*, Vol. 20, 1953, pp. 657–682.
- [17] Chu, B.-T. and Kovaszny, L. S. G., “Non-linear interactions in a viscous heat-conducting compressible gas,” *J. Fluid Mech.*, Vol. 3, No. 05, 1958, pp. 494–514.
- [18] Constantin, P. and Foias, C., *Navier-Stokes Equations*, University of Chicago Press, Chicago, 1988.
- [19] Gatski, T. and Bonnet, J.-P., *Compressibility, Turbulence, and High-Speed Flow*, Elsevier, Oxford, 2009.
- [20] Wilcox, D., *Turbulence Modeling for CFD*, DCW Industries, Inc, La Canada, CA, 1993.
- [21] Evans, L. C., *Partial Differential Equations*, American Mathematical Society, 1998.
- [22] Reynolds, O., “On the Dynamical Theory of Incompressible Viscous Fluids and the Determination of the Criterion,” *Philosophical Transactions of the Royal Society, London, Series A*, Vol. 186, 1895, pp. 123–164.
- [23] Seydel, R., *Practical Bifurcation and Stability Analysis: From Equilibrium to Chaos*, Springer-Verlag, New York, 1996.
- [24] Hopf, E., “Abzweigung einer periodischen Lösung von einer stationären Lösung eines Differentialsystems,” *Bericht der Math.-Phys. Klasse der Sächsischen Akademie der Wissenschaften zu Leipzig*, Vol. 94, 1942.
- [25] Landau, L. and Lifshitz, E., *Fluid Mechanics*, Oxford, Pergamon, 1959.
- [26] Peitgen, H., Jurgens, H., and Saupe, D., *Chaos and Fractals: New Frontiers of Science*, Springer-Verlag, New York, 1992.
- [27] Newhouse, S., Ruelle, D., and Takens, F., “Occurrence of strange Axiom A attractors near quasiperiodic flows on  $T^m$ ,  $m \geq 3$ ,” *Comm. Math. Phys.*, Vol. 64, No. 1, 1978, pp. 35–40.
- [28] Wan, C. and Coney, J., “Transition modes in adiabatic spiral vortex flow in narrow and wide annular gaps,” *Int. J. Heat and Fluid Flow*, Vol. 2, No. 3, 1980, pp. 131–138.

- [29] Yoo, J. and Han, S., “Transitions and chaos in natural convection of a fluid with  $Pr=0.1$  in a horizontal annulus,” *Fluid Dynamics Research*, Vol. 27, No. 4, 2000, pp. 231–245.
- [30] Tennekes, H. and Lumley, J. L., *A First Course in Turbulence*, The MIT Press, Cambridge, 1972.
- [31] Kolmogorov, A., “Local structure of turbulence in an incompressible liquid for ever large Reynolds numbers,” *Dokl. Akad. Nauk SSSR*, Vol. 30, 1941, pp. 229.
- [32] Lighthill, M., “On Sound Generated Aerodynamically. I. General Theory,” *Proc. R. Soc. Lond. A*, Vol. 211, 1952, pp. 564–587.
- [33] Zakharov, V. and Sagdeev, R., “Spectrum of acoustic turbulence,” *Sov. Phys. Dokl.*, Vol. 15, 1971, pp. 439–440.
- [34] Kadomtsev, B. and Petviashvili, V., “On the stability of solitary waves in weakly dispersive media,” *Sov. Phys. Dokl.*, Vol. 15, 1970, pp. 539–541.
- [35] Donzis, D. A., “Amplification factors in shock-turbulence interactions: Effect of shock thickness,” *Phys. Fluids*, Vol. 24, No. 1, 2012, pp. 011705.
- [36] Ruggeri, T., “Breakdown of shock-wave-structure solutions,” *Phys. Rev. E*, Vol. 47, Jun 1993, pp. 4135–4140.
- [37] Carlson, H. A., Roveda, R., Boyd, I. D., and Chandler, G. V., “A hybrid CFD-DSMC method of modeling continuum-rarefied flows,” *42nd AIAA Aerospace Sciences Meeting and Exhibit, Reno, Nevada*, Jan 5-Jan 8 2004, pp. AIAA–2004–1180.
- [38] Wilcox, *Turbulence Modeling for CFD*, chap. 4, DCW Industries, Inc., La Canada CA, 2nd ed., 1994, pp. 73–83.
- [39] Willems, J. C., “Dissipative dynamical systems part I: General theory,” *Arch. for Ration. Mech. and An.*, Vol. 45, Jan. 1972, pp. 321–351.
- [40] Eckmann, J.-P., “Roads to turbulence in dissipative dynamical systems,” *Rev. Mod. Phys.*, Vol. 53, Oct. 1981, pp. 643–654.
- [41] Derks, G., Groesen, E. V., Derks, G., and Groesen, E. V., “Dissipation in Hamiltonian systems: Decaying cnoidal waves,” *SIAM Journ. of Math. Anal.*, Vol. 27, 1996, pp. 1424–1447.
- [42] Olver, P., “A nonlinear Hamiltonian structure for the Euler equations,” *J. Math. Anal. and Appl.*, Vol. 89, No. 1, 1982, pp. 233–250, cited By (since 1996) 20.
- [43] Basdevant, C. and Sadourny, R., “Ergodic properties of inviscid truncated models of two-dimensional incompressible flows,” *J. Fluid Mech.*, Vol. 69, June 1975, pp. 673–688.



- [44] Bos, W. J. T. and Bertoglio, J.-P., “Dynamics of spectrally truncated inviscid turbulence,” *Phys. Fluids*, Vol. 18, No. 7, 2006, pp. 071701.
- [45] Cichowlas, C., Bonaíti, P., Debbasch, F., and Brachet, M., “Effective Dissipation and Turbulence in Spectrally Truncated Euler Flows,” *Phys. Rev. Lett.*, Vol. 95, Dec 2005, pp. 264502.
- [46] Hesselink, L. and Sturtevant, B., “Propagation of weak shocks through a random medium,” *J. Fluid Mech.*, Vol. 196, 1988, pp. 513–553.
- [47] Fabre, D., Jacquin, L., and Sesterhermn, J., “Linear interaction of a cylindrical entropy spot with a shock,” *Phys. Fluids*, Vol. 13, 2001, pp. 2403–2422.
- [48] Jamme, S., Cazalbou, J.-B., Torres, F., and Chassaing, P., “Direct numerical simulation of the interaction between a shock wave and various types of isotropic turbulence,” *Flow Turbul. Combust.*, Vol. 68, 2002, pp. 227–268.
- [49] Papamoschou, D., “Evidence of shocklets in a counterflow supersonic shear layer,” *Phys. Fluids*, Vol. 7, 1995, pp. 233–235.
- [50] Lee, S., Lele, S. K., and Moin, P., “Interaction of isotropic turbulence with shock waves: effect of shock strength,” *J. Fluid Mech.*, Vol. 340, June 1997, pp. 225–247.
- [51] Grube, N. E., Taylor, E. M., and Martín, M. P., “Direct numerical simulation of a shock-wave/isotropic turbulence interaction,” *39th AIAA Fluid Dynamics Conference, San Antonio, TX*, June 2009, pp. AIAA–2009–4165.
- [52] Bermejo-Moreno, I., Larsson, J., and Lele, S. K., “LES of canonical shock-turbulence interaction,” *Annual Research Briefs 2010*, Stanford Center for Turbulence Research, 2010, pp. 209–222.
- [53] Vreman, B., Geurts, B., and Kuerten, H., “Subgrid-Modelling in LES of Compressible Flow,” *Applied Scientific Research*, Vol. 54, No. 3, April 1995, pp. 469–483.
- [54] Domaradzki, J. A., Liu, W., and Brachet, M. E., “An analysis of subgrid-scale interactions in numerically simulated isotropic turbulence,” *Physics of Fluids A: Fluid Dynamics*, Vol. 5, No. 7, 1993, pp. 1747–1759.
- [55] Canuto, C., Hussaini, M., Quarteroni, A., and Zang, T., *Spectral Methods - Fundamentals in Single Domains*, Springer-Verlag, New York, 2006.
- [56] Canuto, C., Hussaini, M., Quarteroni, A., and Zang, T., *Spectral Methods - Evolution to Complex Geometries and Applications to Fluid Dynamics*, Springer-Verlag, New York, 2007.

- [57] Spalart, “A one-equation turbulence model for aerodynamic flows,” *Proceedings of the 30th AIAA Aerospace Sciences Meeting and Exhibit*, Vol. 92-0439, Proceedings of the 30th AIAA Aerospace Sciences Meeting and Exhibit, 1992, pp. AIAA-1992-0439.
- [58] Lilly, D., “On the application of the eddy viscosity concept in the Inertial sub-range of turbulence,” Tech. rep., NCAR, 1966.
- [59] Lien, F. S. and Leschziner, M. A., “Assessment of turbulent transport models including non-linear RNG eddy-viscosity formulation and second-moment closure,” *Computers and Fluids*, Vol. 3, 1994, pp. 983–1004.
- [60] Shafi, H. S. and Antonia, R. A., “Anisotropy of the Reynolds stresses in a turbulent boundary layer on a rough wall,” *Exp. Fluids*, Vol. 18, Jan. 1995, pp. 213–215.
- [61] Djenidi, L., Agrawal, A., and Antonia, R., “Anisotropy measurements in the boundary layer over a flat plate with suction,” *Exp. Therm. Fluid Sci.*, Vol. 33, No. 7, 2009, pp. 1106 – 1111.
- [62] Antonia, R. A., Djenidi, L., and Spalart, P. R., “Anisotropy of the dissipation tensor in a turbulent boundary layer,” *Phys. Fluids*, Vol. 6, No. 7, 1994, pp. 2475–2479.
- [63] Mittal, “Finite Element Computation of Turbulent Flow Past a Multi-Element Airfoil,” *Int. J. of Computational Fluid Dynamics*, Vol. 20, No. 8, 2006, pp. 563–577.
- [64] Kraichnan, R. H., “Eddy Viscosity in Two and Three Dimensions,” *J. Atmos. Sci.*, Vol. 33, No. 8, 2012/08/13 1976, pp. 1521–1536.
- [65] Iaccarino, G., Ooi, A., Durbin, P., and Behnia, M., “Reynolds averaged simulation of unsteady separated flow,” *Int. J. Heat Fluid Flow*, Vol. 24, No. 2, 2003, pp. 147 – 156.
- [66] Johansen, S. T., Wu, J., and Shyy, W., “Filter-based unsteady RANS computations,” *Int. J. Heat Fluid Flow*, Vol. 25, No. 1, 2004, pp. 10 – 21.
- [67] Gatski, T. and Bonnet, J.-P., *Compressibility, Turbulence, and High-Speed Flow*, Elsevier, Oxford, 2009.
- [68] Germano, M., Piomelli, U., Moin, P., and Cabot, W. H., “A dynamic subgrid-scale eddy viscosity model,” *Phys. Fluids A*, Vol. 3, 1991, pp. 1760–1765.
- [69] Nicoud, F. and Ducros, F., “Subgrid-scale stress modelling based on the square of the velocity gradient tensor,” *Flow Turbul. Combust.*, Vol. 62, 1999, pp. 183–200.

- [70] Adams, N. A. and Stolz, S., “Deconvolution methods in subgrid-scale approximations in LES,” *Modern Simulation Strategies for Turbulent Flow*, edited by B. J. Geurts, Vol. 50, R. T. Edwards, Inc., 2001, pp. 21–44.
- [71] Hickel, S., Adams, N. A., and Domaradzki, J. A., “An adaptive local deconvolution method for implicit LES,” *J. Comput. Phys.*, Vol. 213, No. 1, 2006, pp. 413 – 436.
- [72] Thornber, B., Mosedale, A., and Drikakis, D., “On the implicit large eddy simulations of homogeneous decaying turbulence,” *J. Comput. Phys.*, Vol. 226, No. 2, 2007, pp. 1902 – 1929.
- [73] Lund, T., “The use of explicit filters in large eddy simulation,” *Comp. Math. App.*, Vol. 46, No. 4, 2003, pp. 603 – 616, [jce:title;Turbulence Modelling and Simulationj/ce:title;.](#)
- [74] Sagaut, P., *Large Eddy Simulation for Incompressible Flows: An Introduction*, chap. 3, Springer Berlin Heidelberg, 2nd ed., 2006, p. 44.
- [75] Leonard, A., “Energy Cascade in Large-Eddy Simulations of Turbulent Fluid Flows,” *Turbulent Diffusion in Environmental Pollution Proceedings of a Symposium held at Charlottesville*, edited by F. Frenkiel and R. Munn, Vol. 18, Part A of *Advances in Geophysics*, Elsevier, 1975, pp. 237 – 248.
- [76] Germano, M., “A proposal for a redefinition of the turbulent stresses in the filtered Navier-Stokes equations,” *Physics of Fluids*, Vol. 29, July 1986, pp. 2323.
- [77] Sagaut, P., *Large Eddy Simulation for Incompressible Flows: An Introduction*, Springer Berlin Heidelberg, 2006.
- [78] Piomelli, U., Cabot, W., Moin, P., and Lee, S., “Subgrid-scale backscatter in turbulent and transitional flows,” *Phys. Fluids A*, Vol. 3, 1991, pp. 1766–1772.
- [79] Meneveau, C., Lund, T. S., and Cabot, W. H., “A Lagrangian dynamic subgrid-scale model of turbulence,” *J. Fluid Mech.*, Vol. 319, 1996, pp. 353–385.
- [80] Vasilyev, O. V., Lund, T. S., and Moin, P., “A general class of commutative filters for LES in complex geometries,” *J. Comp. Phys.*, Vol. 146, 1998, pp. 82–104.
- [81] Canuto, C., *Spectral methods in fluid dynamics*, Springer series in computational physics, Springer-Verlag, 1988.
- [82] Deardorff, J. W., “A numerical study of three-dimensional turbulent channel flow at large Reynolds numbers,” *J. Fluid Mech.*, Vol. 41, 1970, pp. 453–480.
- [83] Clark, R. A., Ferziger, J. H., and Reynolds, W. C., “Evaluation of subgrid-scale models using an accurately simulated turbulent flow,” *J. Fluid Mech.*, Vol. 91, March 1979, pp. 1–16.

- [84] G. Emanuel, M. C. Cline, & K. H. Witte, editor, *Improved subgrid-scale models for large-eddy simulation*, July 1980.
- [85] Liu, S., Meneveau, C., and Katz, J., “On the properties of similarity subgrid-scale models as deduced from measurements in a turbulent jet,,” *J. Fluid Mech.*, Vol. 275, No. 83, 1994.
- [86] Dehbi, A., “A stochastic Langevin model of turbulent particle dispersion in the presence of thermophoresis,” *Int. J. Multiphas. Flow*, Vol. 35, 2008, pp. 219–226.
- [87] Kerstein, A., “A Linear- Eddy Model of Turbulent Scalar Transport and Mixing,” *Combust. Sci. Tech.*, Vol. 60, 1988, pp. 391–421.
- [88] Kerstein, A., “One-dimensional turbulence: model formulation and application to homogeneous turbulence, shear flows, and buoyant stratified flows,” *J. Fluid Mech.*, Vol. 392, 1999, pp. 277–344.
- [89] Leith, C. E., “Stochastic backscatter in a subgrid-scale model: plane shear mixing layer,” *Phys. Fluids A*, Vol. 2, 1990, pp. 297–299.
- [90] Chasnov, J., “Simulation of the Kolmogorov inertial subrange using an improved subgrid model,” *Phys. Fluids A*, Vol. 3, No. 188-190, 1991.
- [91] Laval, J.-P. and Dubrulle, B., “A LES-Langevin model for turbulence,” *Eur. Phys. J.*, Vol. 49, 2006, pp. 471–481.
- [92] Mathew, J., Lechner, R., Foysi, H., Sesterhenn, J., and Friedrich, R., “An explicit filtering method for large eddy simulation of compressible flows,” *Physics of Fluids*, Vol. 15, No. 8, 2003, pp. 2279–2289, cited By (since 1996) 75.
- [93] Mathew, J., Foysi, H., and Friedrich, R., “A new approach to LES based on explicit filtering,” *Int. J. Heat Fluid Flow*, Vol. 27, 2006, pp. 594–602.
- [94] Brooks, L., “Raindrops on water,” <http://www.public-domain-image.com/nature-landscapes-public-domain-images-pictures/>, Accessed on 24 Aug 2012.
- [95] Stefano, G. D., Vasilyev, O. V., and Goldstein, D. E., “Localized dynamic kinetic-energy-based models for stochastic coherent adaptive large eddy simulation,” *Phys. Fluids*, Vol. 20, No. 4, 2008, pp. 045102.
- [96] Strodtbeck, J., McDonough, J., and Hislop, P., “Characterization of the dynamical behavior of the compressible ‘poor man’s Navier–Stokes equations’,” *Int. J. Bif. Chaos*, Vol. 22, 2012, pp. 1230004S.
- [97] May, R., “Simple mathematical models with very complicated dynamics,” *Nature*, Vol. 261, 1976, pp. 459–467.
- [98] Pulliam, T. and Vastano, J., “Transition to turbulence in an open unforced 2D flow,” *J. Comp. Phys.*, Vol. 105, 1993, pp. 133–149.

- [99] Hylin, E. and McDonough, J., “Chaotic small-scale velocity fields as prospective models for unresolved turbulence in an additive decomposition of the Navier–Stokes equations,” *Int. J. Fluid Mech. Res.*, Vol. 26, 1999, pp. 539–567.
- [100] McDonough, J. and Huang, M., “A ‘poor man’s Navier–Stokes equation’: Derivation and numerical experiments—the 2-D case,” *Int. J. Numer. Methods Fluids*, Vol. 44, 2004, pp. 545–578.
- [101] Lorenz, E., “Deterministic Nonperiodic Flow,” *J. Atmos. Sci.*, Vol. 20, 1962, pp. 130–141.
- [102] Hénon, M., “A Two-Dimensional Mapping With Strange Attractor,” *Commun. Math. Phys.*, Vol. 50, 1976, pp. 69–77.
- [103] Patel, V. and Head, M., “Reversion of turbulent to laminar flow,” *J. Fluid Mech.*, Vol. 34, 1968, pp. 371–392.
- [104] Takeda, Y., “Quasi-periodic state and transition in a rotating Couette system,” *J. Fluid Mech.*, Vol. 389, 1999, pp. 81–99.
- [105] Dyke, M. V., *An Album of Fluid Motion*, The Parabolic Press, Stanford, 1982.
- [106] Gollub, J. P. and Benson, S. V., “Many routes to turbulent convection,” *J. Fluid Mech.*, Vol. 100, 1980, pp. 449–470.
- [107] Demetriades, A., “Transition to Turbulence in Free Shear-Layers,” Tech. Rep. AFOSRTR-80-0056, Ford Aerospace and Communications Corp, Newport Beach, CA Aeronutronic Div, Oct 1979.
- [108] Chen, J. H., Cantwell, B. J., and Mansour, N. N., “The effect of Mach number on the stability of a plane supersonic wake,” *Phys. Fluids*, Vol. 2, 1990, pp. 984–1005.
- [109] H.O. Peitgen, H Jurgens, D. S., *Chaos and Fractals: New Frontiers of Science*, Springer-Verlag, New York, 1992.
- [110] Schwarz, C., Beetz, C., Dreher, J., and Grauer, R., “Lyapunov exponents and information dimension of the mass distribution in turbulent compressible flows,” *Phys. Lett. A*, Vol. 374, 2010, pp. 1039–1042.
- [111] Huang, M.-J. and Leonard, A., “Power-law decay of homogeneous turbulence at low Reynolds numbers,” *Phys. Fluids*, Vol. 6, No. 11, 1994, pp. 3765–3775.
- [112] Liu, Z., Huang, Q., Zhao, Z., and Yuan, J., “Optimized compact finite difference schemes with high accuracy and maximum resolution,” *Int. J. Aeroacous.*, Vol. 7, No. 2, 2008, pp. 123–146.
- [113] Tabor, G. and Baba-Ahmadi, M., “Inlet conditions for large eddy simulation: A review,” *Computers and Fluids*, Vol. 39, No. 4, 2010, pp. 553 – 567.

- [114] Leith, C. E., “Stochastic backscatter formulation for three-dimensional compressible flows,” *Large Eddy Simulation of Complex Engineering and Geophysical Flows*, edited by B. Galperin and S. A. Orszag, Cambridge University Press, 1993, pp. 105–116.
- [115] Leith, C. E., “Stochastic models of chaotic systems,” *Phys. D*, Vol. 98, No. 2-4, Nov. 1996, pp. 481–491.
- [116] Park, N. and Mahesh, K., “Analysis of numerical errors in large eddy simulation using statistical closure theory,” *J. Comput. Phys.*, Vol. 222, March 2007, pp. 194–216.
- [117] E, W., Khanin, K., Mazel, A., and Sinai, Y., “Probability Distribution Functions for the Random Forced Burgers Equation,” *Phys. Rev. Lett.*, Vol. 78, Mar 1997, pp. 1904–1907.
- [118] Lundgren, T. S., “Linearly forced isotropic turbulence,” *Annual Research Briefs*, Center for Turbulence Research, Stanford, 2003, pp. 461–473.
- [119] Rosales, C. and Meneveau, C., “Linear forcing in numerical simulations of isotropic turbulence: Physical space implementations and convergence properties,” *Phys. Fluids*, Vol. 17, No. 9, 2005, pp. 095106.
- [120] Petersen, M. R. and Livescu, D., “Forcing for statistically stationary compressible isotropic turbulence,” *Phys. Fluids*, 2010, pp. 116101.
- [121] Guo, Q., Mandal, M. K., and Li, M. Y., “Efficient Hodge–Helmholtz decomposition of motion fields,” *Pattern Recognition Letters*, Vol. 26, No. 4, 2005, pp. 493 – 501.
- [122] Yee, H., “Construction of explicit and implicit symmetric TVD schemes and their applications,” *J. Comp. Phys.*, Vol. 68, 1987, pp. 151–179.
- [123] Roe, P., “Characteristic based schemes for the Euler equations,” *Ann. Rev. Fluid Mech.*, Vol. 8, 1986, pp. 337–365.
- [124] Liu, X., Osher, S., and Chan, T., “Weighted essentially nonoscillatory schemes,” *J. Comp. Phys.*, 1994, pp. 115, 200–212.
- [125] Warming, R. and Beam, R., “An implicit scheme for the compressible Navier–Stokes equations,” *AIAA J*, Vol. 16, 1978, pp. 393–402.
- [126] Steger, J. and Warming, R., “Flux vector splitting of the inviscid gas dynamics equations with application to finite–difference methods,” *J. Comp. Phys.*, Vol. 40, 1981, pp. 263–293.
- [127] Wilcox, D., *Turbulence Modeling for CFD, 2nd Ed.*, DCW Industries, Inc., 2004.

- [128] Menter, F., “Two-equation eddy-viscosity turbulence models for engineering applications,” *AIAA J.*, Vol. 32, 1994, pp. 1598–1605.
- [129] Benek, J., Buning, P., and Steger, J., “A 3-D CHIMERA Grid embedding technique,” *AIAA-85-1523*, 1985.
- [130] Benek, J., Steger, J., Dougherty, F., Buning, P., and TN., A. E. D. C. A. A., *Chimera. A Grid-Embedding Technique*, Defense Technical Information Center, 1986.
- [131] Wang, Z. J., Hariharan, N., and Chen, R., “Recent Development on the Conservation Property of Chimera,” *Int. J. of Computational Fluid Dynamics*, Vol. 15, Nov. 2001, pp. 265–278.
- [132] Tang, H. S. and Zhou, T., “On Nonconservative Algorithms for Grid Interfaces,” *SIAM J. Numer. Anal.*, Vol. 37, No. 1, Nov. 1999, pp. 173–193.
- [133] Tramel, R., Keeling, S., and Benek, J., “On conservation law based updating schemes for overset mesh communication,” *Presented at the 10th Symposium on Overst Composite Grids and Solution Technology*, Sept 20-23 2010.
- [134] Hendrick, A. K., Aslam, T. D., and Powers, J. M., “Mapped weighted essentially non-oscillatory schemes: Achieving optimal order near critical points,” *J. Comp. Phys.*, Vol. 207, 2005, pp. 542–567.
- [135] Ringuette, M., Bookey, P., Wyckham, C., and Smits, A., “Experimental study of a Mach 3 compression ramp interaction at  $Re_\theta = 2400$ ,” *AIAA J.*, Vol. 47, 2009, pp. 373–385.
- [136] Ringuette, M. J., Wu, M., and Martin, M. P., “Coherent structures in direct numerical simulation of turbulent boundary layers at Mach 3,” *J. Fluid Mech.*, Vol. 594, 2008, pp. 59–69.
- [137] Pulliam, T., *Numerical techniques for viscous flow computation in turbomachinery bladings*, Brussels, Belgium, Jan 20-24 1986.
- [138] Kim, H.-J., Lee, S., and Fujisawa, N., “Computation of unsteady flow and aerodynamic noise of NACA0018 airfoil using large-eddy simulation,” *Int. J. Heat Fluid Flow*, Vol. 27, No. 2, 2006, pp. 229 – 242.
- [139] Wu, M. and Martin, M. P., “Direct Numerical Simulation of Supersonic Turbulent Boundary Layer over a Compression Ramp,” *AIAA J.*, Vol. 45, April 2007, pp. 879–889.
- [140] Plentovich, E. B., R. L. Stallings, J., and Tracy, M. B., “Experimental cavity pressure measurements at subsonic and transonic speeds,” Supplement to nasa technical paper 3358, NASA, 1993.

- [141] Liu, Z., Huang, Q., Zhao, Z., and Yuan, J., “Optimized compact filtering schemes for computational aeroacoustics,” *Int. J. Num. Meth. Fluids*, Vol. 60, No. 8, 2009, pp. 827–845.
- [142] Shuman, F., “Numerical Method in Weather Prediction:oothing and Filtering,” *Monthly Weather Review*, Vol. 85, 1957, pp. 357–361.
- [143] Kanamori, M. and Suzuki, K., “Shock wave detection in two-dimensional flow based on the theory of characteristics from CFD data,” *J. Comput. Phys.*, Vol. 230, 2011, pp. 3085 – 3092.
- [144] Lovely, D. and Haines, R., “Shock detection from computational fluid dynamics results,” *14th Computational Fluid Dynamics Conference, Norfolk, VA*, June 28-July 1 1999, pp. AIAA–1999–3285.
- [145] Kang, H., Chester, S., and Meneveau, C., “Decaying turbulence in an active-grid-generated flow and comparisons with large-eddy simulations,” *J. Fluid Mech.*, Vol. 480, 2003, pp. 129.
- [146] Samtaney, R., Pullin, D. I., and Kosović, B., “Direct numerical simulation of decaying compressible turbulence and shocklet statistics,” *Phys. Fluids*, Vol. 13, 2001, pp. 1415–1430.
- [147] Shivamoggi, B., “Spectral laws for compressible isotropic turbulence,” *Phys. Lett. A*, Vol. 166, 1992, pp. 243–248.
- [148] Shivamoggi, B., “Multifractal aspects of the scaling laws in fully developed compressible turbulence,” *Ann. Phys.*, Vol. 243, 1995, pp. 169–176.
- [149] Aluie, H., “Compressible Turbulence: The Cascade and its Locality,” *Phys. Rev. Lett.*, Vol. 106, Apr 2011, pp. 174502.
- [150] Kritsk, A. G., Norman, M. L., Padoan, P., and Wagner, R., “The statistics of supersonic isothermal turbulence,” *Astrophys. J.*, Vol. 665, 2007, pp. 416–431.
- [151] Schmidt, W., Federrath, C., and Klessen, R., “Is the Scaling of Supersonic Turbulence Universal?” *Phys. Rev. Lett.*, Vol. 101, 2008, pp. 194505.
- [152] Weinkauff, T. and Theisel, H., “Curvature Measures of 3D Vector Fields and their Applications.” *WSCG*, 2002, pp. 507–514.
- [153] Settles, G. S., Bogdonoff, S. M., and Fitzpatrick, T. J., “Detailed Study of Attached and Separated Compression Corner Flowfields in High Reynolds Number Supersonic Flow,” *AIAA J.*, Vol. 17, June 1979, pp. 579–585.
- [154] Selig, M. S., Andreopoulos, J., Muck, K. C., Dussauge, J. P., and Smits, A. J., “Turbulence structure in a shock wave/turbulent boundary-layer interaction,” *AIAA J.*, Vol. 27, 1989, pp. 862–869.



- [155] Bookey, P., Wyckham, C., Smits, A. J., and Martin, M., “New experimental data of STBLI at DNS/LES accessible Reynolds numbers,” *AIAA paper*, Vol. 309, 2005/// 2005, pp. 2005 – 2005.
- [156] Sinha, K. and Candler, G. V., “Modeling shock unsteadiness in shock/turbulence interaction,” *Phys. Fluids*, Vol. 15, 2003, pp. 2290–2297.
- [157] Sinha, K. and Candler, G. V., “Modeling the effect of shock unsteadiness in shock/turbulent boundary layer interactions,” *AIAA J.*, Vol. 43, 2005, pp. 586–594.
- [158] Sinha, K. and Pasha, A. A., “Shock-unsteadiness model applied to oblique shock wave/turbulent boundary-layer interaction,” *Int. J. Comput. Fluid D.*, Vol. 22, 2008, pp. 569–582.
- [159] Gadd, G. E., *Interactions Between Normal Shock Waves and Turbulent Boundary Layers*, Reports and memoranda // Aeronautical Research Council, H.M. Stationary Office, 1962.
- [160] Knight, D. and Yan, H., “Large Eddy Simulation of Supersonic Compression Corner,” *APS Division of Fluid Dynamics Meeting Abstracts*, November 2000, p. D3.
- [161] Atvars, K., Knowles, K., Ritchie, S. A., and Lawson, N. J., “Experimental and computational investigation of an open transonic cavity flow,” *J. Aero. Eng.*, Vol. 224, 2009, pp. 357–368.
- [162] Peng, S.-H. and Leicher, S., “DES and hybrid RANS-LES modelling of unsteady pressure oscillations and flow features in a rectangular cavity,” *Notes on Numerical Fluid Mechanics Advances in Hybrid RANS-LES Modelling*, Vol. 97, 2008, pp. 132–141.
- [163] Yang, D.-G., Fan, Z.-L., Li, J.-Q., and Yao, D., “Effects of Boundary-Layer Thickness on Flow Oscillations Inside Open Cavities at Supersonic Speeds,” *Mod. Phy. Lett. B*, Vol. 24, 2010, pp. 487–493.
- [164] Larchevêque, L., Sagaut, P., Lê, T.-H., and Comte, P., “Large-eddy simulation of a compressible flow in a three-dimensional open cavity at high Reynolds number,” *J. Fluid Mech.*, Vol. 516, 2004, pp. 265–301.
- [165] Morgan, P., Visbal, M., and Rizzetta, D., “A Parallel Overset Grid High-Order Flow Solver for Large Eddy Simulation,” *J. Sci. Comput.*, Vol. 29, 2006, pp. 165–200.

## Vita

Joshua Strodbeck was born on 28<sup>th</sup> of July, 1981 in Frankfurt am Main, Germany. He earned his BS in Mathematics at the Rose–Hulman Institute of Technology. He published “Characterization of the dynamical behavior of the compressible ‘poor man’s Navier–Stokes equations’” with Peter Hislop and James McDonough in the *International Journal of Bifurcation and Chaos* in 2012, and he delivered annual presentations at the Dayton-Cincinnati Aerospace Sciences Symposium between 2009 and 2012.